DISTRIBUTION OF EXCITATION-CONTRACTION COUPLING PROTEINS AS A FUNCTION OF DEVELOPMENT

by

TSAI JING ERIC LIN

A THESIS SUBMITTED IN PARTIAL FULFILLMENT OF THE REQUIREMENTS FOR THE DEGREE OF

DOCTOR OF PHILOSOPHY

in

THE FACULTY OF GRADUATE STUDIES

(Physiology)

THE UNIVERSITY OF BRITISH COLUMBIA

(Vancouver)

February 2010

Abstract

Excitation-contraction (EC) coupling in the neonatal rabbit heart has been previously shown to be mediated predominately by reverse-mode activity of the sodium-calcium exchanger (NCX). Thus the regulation of NCX is a primary determinant of neonatal cardiac contractility. It is proposed that in neonate hearts, a restricted domain allows a sodium current (I_{Na}) to mediate a large elevation in subsarcolemmal sodium concentration which then drives calcium entry through reverse-mode NCX. Functional data suggest that calcium influx through NCX can also trigger calcium induced calcium release (CICR).

Traditionally, neonatal myocytes are thought to mediate EC coupling exclusively through trans-sarcolemma calcium influx. This model of EC coupling is distinct from the adult model of EC coupling in that it does not involve a significant CICR component. Traditionally, CICR processes are thought to be a hallmark of adult EC coupling processes where CICR is triggered exclusively by the L-type calcium current. Neonatal myocytes were previously believed to be too immature to sustain physiologically significant levels of CICR. Yet recent functional data suggest that not only are neonatal myocytes able to sustain CICR but that neonatal myocytes trigger CICR independently of the calcium current. Neonatal myocytes appear to trigger CICR exclusively though reverse-mode NCX activity (NCX-CICR).

The phenomenon of NCX-CICR, prominent in early developmental stages and declining with further development, suggest that the neonatal myocardium contains specialized microdomains that allow NCX-CICR to occur. To investigate this unique EC coupling phenotype, three-dimensional confocal microscopy and advanced digital image analysis techniques are utilized to quantify the presence of these specialized microdomains and to determine the changes in these microdomains that occur with development.

Table of Contents

List of Tables

List of Figures

List of Abbreviations

EC	excitation contraction
CICR	calcium induced calcium release
RyR	ryanodine receptor
SR	sarcoplasmic reticulum
SL	sarcolemma
I_{Ca}	calcium current
Ca_V	voltage-gated calcium channel
$[Ca^{2+}]_i$	intracellular calcium concentration
$[Ca^{2+}]_o$	extracellular calcium concentration
Ca^{2+}	calcium ion
DHPR	dihydropyridine receptor
I_{Na}	sodium current
Na_V	voltage-gated sodium channel
$[Na^+]_i$	intracellular sodium concentration
$[Na^+]_o$	extracellular sodium concentration
Na^+	sodium ion
TTX	tetrodotoxin
NCX	sodium calcium exchanger
ATP	adenosine triphosphate
E_{NCX}	equilibrium potential of sodium calcium exchanger
E_{Na}	sodium Nernst potential
E_{Ca}	calcium Nernst potential
FRET	Förster resonance energy transfer
PSF	point spread function
FWHM	the full width at half-maximum amplitude

Acknowledgments

I would like to express my heartfelt gratitude to the multitude of people, who have invested the time and effort to make this thesis possible. Regretfully, due the abundance of grace shown to me in the course of my studies, I cannot adequately express my appreciation to each of you in words or in speech. I can only hope that each of you will realize the significance of your contributions in shaping me and my PhD experience. My PhD experience, although difficult at times, has been undeniably delightful. No other collection of experiences has brought me such joy and personal growth.

This opportunity to pursue knowledge with near reckless abandonment has been a great indulgence; however, it is not without significant cost. Without the commitment and support of my family and friends such a positive experience would have undoubtedly been lost. My parents, in particular, were instrumental in providing me an environment where failure can be answered with renewed vigour and where success can still prevail, even if it takes a couple of tries. To my grandparents, who supported this adventure long before I even existed, thank you for loving and supporting my parents so that they could love and support me. To my tolerant and long suffering wife Joyce, who has travelled on this journey of mine since the beginning, cheering all along the way. Thanks for being my favourite travel partner and for sharing the joys and burdens of this adventure.

Without the dedication of my co-workers, especially Cynthia Gershome, Vivian Hung, Pauline Dan, Jingbo Huang, and Haruyo Kashihara, this indulgent adventure of mine would almost certainly have ended in disaster. Without the advice, encouragement and dedication of my supervisory, comprehensive, and dissertation examination committee members (Dr. Ed Moore, Dr. Chris Ahern, Dr. Eric Accili, Dr. Thomas Claydon, Dr. Hakima Moukhles, Dr. Peter Ruben and Dr. Leighton Izu) such an involved process of education would simply not be possible.

Lastly, I would like to thank my senior supervisor Dr. Glen Tibbits. It is his dedication to his craft, his commitment to the scientific process and his generosity of spirit that allowed me to embark on this scientific foray. Thanks Glen, it's been fun.

Thanks for reading,

Eric Lin

Co-Authorship Statement

The manuscripts included in this thesis were co-authored; collaborators provided unprocessed images that were instrumental in the development of novel image analysis techniques. In chapter 2, Eric Lin contributed manuscript preparation and Franklin Sedarat contributed primary data collection. In chapter 3, Eric Lin contributed image analysis technique development, data analysis and manuscript preparation while Pauline Dan contributed primary data collection and manuscript preparation. In chapter 4, Eric Lin contributed image analysis technique development, data analysis and manuscript preparation while Vivian Hung contributed primary data collection. In chapter 5, Eric Lin contributed image analysis technique development, data analysis and manuscript preparation while Cynthia Gershome contributed to primary data collection and manuscript preparation.

1. BACKGROUND LITERATURE

1.1. INTRODUCTION

It is generally well accepted that excitation-contraction (EC) coupling in mature adult cardiomyocytes occurs through calcium-induced calcium release (CICR)[1]. At rest, myocytes have a resting membrane potential of about -80 mV[2] and can be passively depolarized via gap junctions by neighbouring cells[3]. When myocytes are depolarized to about -60 mV, voltage gated sodium channels are activated, further depolarizing the cell membrane[2]. At approximately -35 mV, the L-type voltage-gated calcium channels ($Ca_v1.2$) are activated and calcium ions permeate into the cell[2]. This calcium influx then causes the ryanodine receptor (RyR), a calcium release channel located on the sarcoplasmic reticulum (SR), to release calcium stored in the SR[1]. Only ~30% of the calcium transient flows across the sarcolemma and the majority of calcium necessary for contraction comes from SR release[4-6], although the absolute values show substantial species variation. Elevations in cytosolic calcium increases Ca^{2+} binding to cardiac troponin C (cTnC) thereby reducing the inhibition by the troponin-tropomyosin complex and activates the myofilaments. For relaxation to occur cytosolic free calcium ($[Ca^{2+}]_i$) must be returned to the resting levels of ~100 nM. Cytosolic calcium falls as calcium is sequestered into the SR by SR-Ca^{2+} ATPase (SERCA) and as calcium is extruded from the cell by NCX and to a much lesser extent by the sarcolemmal calcium pump.

Functional data suggest that neonatal myocytes, but not adult myocytes, exhibit the ability to induce CICR via reverse-mode NCX activity (NCX-CICR)[7]. Calcium transients in neonatal myocytes are highly sensitive to KB-R7943 (KB-R), an inhibitor of NCX activity, suggesting that NCX is the predominant calcium influx mechanism. Consistent with the hypothesis, is that neonatal myocytes are also insensitive to nifedipine, an L-type calcium channel blocker[7]. The reverse relationship is found in adult myocytes; insensitivity to KB-R and sensitivity to nifedipine[7]. The sensitivity of neonatal myocytes to KB-R is consistent with the significantly higher NCX expression and activity in neonatal myocytes in comparison to adult myocytes[6-10]. An L-type calcium current ($I_{Ca,L}$) is present in neonatal myocytes. Although neonatal $I_{Ca,\,L}$ density is generally thought to be lower than that of adult $I_{Ca,\,L}$, the developmental stages used

in these studies are associated with a similar range of $I_{Ca,\,L}$ densities[11].Despite this, however, neonatal $I_{Ca,\,L}$ does not appear to be able to mediate a CICR response. Analysis of L-type voltage-gated Ca^{2+} channel calcium-dependent inactivation (CDI) as an indicator of RyR calcium release and as an indicator of the proximity between calcium channels and RyR, find that the time course of I_{Ca} in neonatal myocytes is unaffected by the presence or absence of SR calcium load[11] and is consistent with the absence of L-type mediated CICR (I_{Ca}-CICR) in the neonate. Furthermore, even in the presence of nifedipine, the remaining NCX related calcium transient has been shown to be dependent on SR calcium, suggesting that NCX is mediating a CICR response in early developmental stages.

NCX-mediated CICR has been extensively investigated in adult myocytes. The notion of a 'fuzzy space' was proposed as a putative mechanism underlying the ability of a sodium current (I_{Na}) to induce SR calcium release in adult guinea pig myocytes by LeBlanc and Hume[12]. In the absence of calcium influx through voltage-gated calcium channels, membrane depolarization via voltage clamp resulted in the activation of a large I_{Na}, leading to the release of SR calcium. This SR calcium release appeared to be mediated by the sodium-calcium exchanger operating in reverse or calcium influx mode. Although the I_{Na} is large, with peak currents estimated at 50 nA for a typical guinea pig myocyte, the rapid inactivation of the I_{Na} (1 ms) limits the total amount of sodium entering per action potential[12]. For a cell measuring 10x20x100 μm, this I_{Na} would likely increase $[Na^+]_i$ by only 25 μM. Therefore, the ability of sodium influx to induce reverse-mode NCX activity must imply that sodium enters into a shared and restricted diffusional space. The 'fuzzy space' hypothesis is reliant on four key assumptions[13]. First, the hypothesis requires a large I_{Na}. Second, it requires a diffusional barrier to create elevated ion concentrations. Third, NCX flux must be sufficiently large to activate calcium release. Fourth, the relevant channels and exchangers must be functionally colocalized.

This thesis investigates the presence of these four assumptions in the context of the neonatal myocardium. The first assumption of a large I_{Na} is investigated by determining the expression and localization of sodium channel isoforms. The second assumption of a diffusional barrier is investigated by determining the physical proximity between NCX and the SR membrane by the colocalization relationship between NCX and RyR. The third assumption of a large NCX flux is investigated by determining the organization of NCX and the possibility that

NCX is organized in multi-exchanger functional units. The colocalization of these multi-exchanger units with the presence of a sodium influx mechanism is expected to regulate NCX exchange rates. The fourth assumption of functional colocalization is investigated by the use of confocal microscopy and advanced image analysis.

1.2. VOLTAGE-GATED SODIUM CHANNELS

Na_v channels are expected to be a key element in the regulation of NCX activity, through membrane depolarization and or sub-membrane sodium accumulation. With high channel expression and permeability, activation of Na_v channels rapidly drives the membrane potential towards the E_{Na} of ~+67mV. There are currently nine identified and expressed mammalian voltage-gated sodium channel isoforms ($Na_v1.x$) which are often categorized based on their sensitivities to channel block by the neurotoxin tetrodotoxin (TTX). $Na_v1.1$, 1.2, 1.4, 1.6 and 1.7 are broadly expressed in neurons and have EC_{50} values of less than 12 nM[14]. Skeletal $Na_v1.4$ (EC_{50} = 5 nM) also displays high TTX sensitivity and, together with the neuronal isotypes, these channels are considered as being TTX-sensitive sodium channels[14]. $Na_v1.5$ (EC_{50} = 1-2 mM), the primary sodium channel found in cardiac myocytes, as well as $Na_v1.8$ (EC_{50} = 60 mM) and $Na_v1.9$ (EC_{50} = 40 mM) are considered to be TTX-resistant sodium channels[14].

While $Na_v1.5$ is the predominant cardiac form, other $Na_v1.x$ more commonly associated with neuronal tissue have also been found in cardiac myocytes; consistent with early reports of a mixed I_{Na}[15]. However, the subcellular localization and functional roles have not yet been firmly established. Some studies have reported Na_v 1.1, Na_v 1.3 and Na_v 1.6 to be found within the t-tubular membrane in mouse ventricular myocytes while $Na_v1.5$ is expressed predominantly in the intercalated discs[16, 17]. It was suggested by the localization of $Na_v1.5$ that its primary purpose was to transmit the action potential from cell-to-cell while the localization of the non-cardiac/neuronal channels suggested a role in conducting membrane depolarization into the interior of the cell; coupling membrane excitation to cell contraction[16, 17]. Neuronal isoforms have also been reported in canine heart where $Na_v1.1$ was found predominately in the intercalated discs while $Na_v1.2$ was found at the z-lines and surface membrane[18]. This study did not find either $Na_v1.3$ or $Na_v1.6$ to be expressed in the canine heart but did find $Na_v1.5$ at the

intercalated discs[18]. Some of the disparity between these results may be due to species variation. Isoform expression in cultured neonatal myocytes suggest at all Na_V isoforms (Na_v1.1-6) are present, however expression of Na_v1.5 is apparently more robust that the other isoforms[19]. Immunolabelling using non-specific Na_v antibodies suggests that the membrane may be contiguously labelled with sodium channels[20, 21].

The heterogeneity of Na_v isotype expression suggests differential roles for specific isotypes during the action potential. Of the Na_v channel isotypes, Na_v1.5, 1.7 and 1.9 have more negative $V_{a\ 0.5}$ values (~ -47 mV) while the other isotypes have considerably more positive $V_{a\ 0.5}$ values at around -20 mV[14]. Na_v1.5 can be expected to be activated at lower levels of depolarization however since the peak of the action potential normally crosses 0 mV, presumably all Na_v isotypes are activated and the roles of specific isotypes have yet to be elucidated. The majority of these studies investigated Na_v distributions in fully mature myocytes and it is unclear how Na_v isotypes will be developmentally regulated, especially given the lack of an extensive t-tubular network in immature myocytes.

1.3. DIFFUSIONAL BARRIER

It is not yet clear how sodium mobility is impeded in the subsarcolemmal space. There are some estimates of sodium mobility using the sodium indicator dye SBFI to measure the global sodium concentration. Radial diffusion coefficients have been estimated to be 10^3-10^4 times lower than aqueous diffusion[22] and longitudinal diffusional coefficients have been estimated to be 100-200 times lower than aqueous solutions [23]. One possible source of reduced sodium mobility is the dyadic cleft itself[24] where a restricted space reduces the effective diffusional coefficient. Modeling results indicated that a single sodium channel could activate reverse-mode NCX 5 ms prior to activation of the L-type current given sufficiently reduced sodium diffusion; at least several orders of magnitude less than aqueous rates. If sodium diffusion is restricted to this degree then the total area with this level of restriction must be small since sodium buffering is reportedly low[22]. Electron micrographs have identified 300 nm sheets of SR membrane located ~20 nm beneath the sarcolemma in neonatal rabbit myocytes[25] and may reduce sodium mobility in neonatal myocytes. The diffusional coefficient as predicted by Lines et al.[24] may not be

required for significant reverse-NCX if sodium channels and NCX are not homogenously distributed along the membranes.

The peak I_{Na} has been estimated at 50 nA, which reflects the rapid and concerted activation of the sodium channels[12]. Rapid activation allows a relatively few sodium channels, density estimates ranging from 2 to 10 channels/μm^2, to mediate the rapid upstroke of the action potential[15]. However the effect of the I_{Na} on subsarcolemmal Na^+ levels will depend on the peak channel density rather than average channel density. Such that, if multiple Na_v channels are localized together, significant localized elevations in subsarcolemmal sodium are expected. If the diffusional volume is restricted to 10 nm beneath the membrane then 50 nA would raise the sub membrane concentration by 8 mM. However if Na_v channels exist in clusters, as hypothesized, then the diffusional volume will be further restricted and is expected to mediate a larger localized $[Na]_i$ transient. Previously, NCX has been shown to be distributed in clusters at a periodicity of ~1 micron in both transverse and longitudinal directions[26], suggesting that I_{Na} need not homogeneously elevate subsarcolemmal sodium concentrations to potentiate reverse-mode NCX activity.

Neonatal myocytes express large amounts of NCX and it is hypothesized that these myocytes have specific adaptations to allow theses myocytes to mediate calcium-induced calcium release in an efficient and effective manner. The NCX-CICR mechanism suggests that the I_{Na}–NCX microdomain is shared by a NCX-RyR microdomain. Colocalization between NCX and RyR ensures that the SR membrane is in close vicinity to NCX. The corresponding colocalization of $Na_V1.x$ with this NCX-RyR complex would then be expected to mediate the observed NCX-CICR phenomenon.

1.4. THE SODIUM-CALCIUM EXCHANGER (NCX)

The accepted stoichiometry of NCX is 3 Na^+ per 1 Ca^{2+} and as an antiporter, that does not directly consume ATP, its direction and rate is dictated by the sodium and calcium electrochemical gradients. Since these electrochemical gradients exist relative to the cell membrane potential, the membrane potential also has a direct effect on both the rate and direction of NCX activity. NCX is electrogenic and ion transport results in a net gain or loss of charge. When operating in forward mode, or calcium efflux mode, the exchanger passes an inward current. Likewise, when operating in reverse-mode, or calcium influx mode, the

exchanger passes an outward current. The reversal potential of NCX is given by: $E_{NCX} = 3E_{Na} - 2E_{Ca}$ where E_{Na} and E_{Ca} are the Nernst potentials for sodium and calcium, respectively[27].

Because of the stoichiometry of NCX, its reversal potential is intensely sensitive to intracellular sodium levels. For example, during quiescence, $[Na^+]_i$ in rabbits myocytes is ~4.5 mM and stimulation at 1 Hz / 60 bpm results in a ~3 mM rise in $[Na^+]_i$[28]. This relatively small change in internal $[Na^+]$ is predicted to decrease the reversal potential of the exchanger by ~37 mV, thereby increasing the driving force for calcium entry. If one assumes $[Na^+]_o$ = 140 mM with calcium $[Ca^{2+}]_o$ = 2 mM and $[Ca^{2+}]_i$ = 150 nM during diastole, a $[Na^+]_i$ = 4.5 mM gives a E_{NCX} of +18 mV while a 7.0 mM gives a E_{NCX} of -19 mV. Therefore even small changes in intracellular sodium can have large effects on exchanger activity.

Although it is established that rabbit neonatal myocytes have sufficiently high levels of NCX expression to mediate CICR, it is not yet clear how the myocardium regulates the activity of such a large pool of NCX. The regulation of NCX activity is especially important because NCX can mediate both calcium entry and calcium efflux as well as depolarize and repolarize the cell membrane. The fuzzy space hypothesis focuses on the initiation of contraction; however the role of NCX in relaxation imposes some limitations on both the density of NCX as well as the resting levels of sodium inside the cell. Certainly high NCX density is favourable regarding calcium entry however large amounts of expression is also expected to reduce SR calcium load since forward mode NCX competes directly with SERCA activity. The converse relationship is expected with tonic elevations in $[Na]_i$. While elevated intracellular Na^+ can increase calcium influx, it also depresses calcium efflux during diastole impairing relaxation as well as elevating SR load.

1.5. INTRODUCTION TO COLOCALIZATION ANALYSIS

The emphasis of this thesis is on understanding EC coupling in the developing heart and the process has necessitated significant advances in our ability to utilize confocal microscopy to study protein distributions. In a short time confocal microscopy, and other improved resolution imaging techniques (spinning disk, wide-field deconvolution, structured illumination) have

become increasingly “turn-key” with commercial offerings spanning a large range of budgets and capabilities. The popularity of these instruments is undoubtedly linked to their flexibility and improved resolution over basic wide-field techniques as well as the ease-of-use. By in large, the largest technical offering of these advanced microscopes is the ability to utilize optical-sectioning to acquire 3-dimensional (3D) images. These 3D images contain a wealth of information however the development of the analysis tools necessary to extract this information has been limited. Thus current investigators are not only limited not by the capabilities of the microscopes but also by the capabilities of the available analysis techniques.

These improved-resolution techniques are considered diffraction-limited techniques. Diffraction-limited instruments are limited by the inherent properties of the wavelength of light (λ) used for excitation and or emission and by the numerical aperture ($NA = n \sin \theta$) of the objective lens. The NA is dependent on *n*, the index-of-refraction and on θ, the half maximal angle of the objective lens. Diffraction limited resolution is summarized by Abbe’s law of limiting resolution ($D = \frac{1}{2} \lambda / NA$). In confocal microscopy, axial resolution is estimated by $z_{min}=2\lambda\eta / NA^2$, thus axial resolution increases with the square of the NA while lateral resolution increases linearly with the NA. There are alternative definitions of resolution such as Raleigh resolution ($D = 0.61 \lambda / NA$) or Full-Width-Half-Maximum (FWHM) resolution, with the later often used due to its simplicity in real world images. In practice, a confocal microscope has a typical FWHM lateral resolution of ~300 nm and an axial resolution of ~850 nm using a 1.4 NA oil-immersion lens and refractive index matched mounting medium[29]. Although image restoration techniques, such as deconvolution, are able to improve image quality the resolution of the confocal microscope is still up to an order of magnitude lower than distances found in the dyadic cleft (15-20 nm). Colocalization, in the context of confocal microscopy, describes the localization of two fluorescent signals at sub-resolution dimensions while actual colocalization would describe an actual direct protein-protein interaction. Colocalization analysis then, as a general rule, always overestimates the true colocalization interaction. The degree of overestimation, however, can be reduced by careful experimental design and is minimized by increased imaging resolution.

The dyadic cleft is perhaps the smallest defined EC coupling structure to date and represents the juxtaposition between voltage-gated calcium channels on the sarcolemma (SL)

and RyR channels on the SR membrane. The distance between these two membranes has been measured to be 15 to 20 nm using electron microscopy (EM) and is an important physical dimension because it represents a well established yet non-direct interaction between two EC coupling proteins. This distance is below the resolution of a confocal microscope yet is a distance undetectable by high-resolution single molecule techniques such as Förster resonance energy transfer (FRET). FRET describes the potential interaction between two chromophore/fluorophores, where one chromophore is able to transfer its energy to another chromophore through nonradiative transfer of energy. The amount of energy transferred is strongly dependent on distance and is an effective 'molecular ruler' technique at separation distances of less than 10 nanometers[30]. However FRET has a limited dynamic range since separation distances longer than 10 nanometers will generate little to no FRET signal. This suggests that, even if antibodies/fluorophores could be positioned within the dyadic cleft, FRET-pairs are unlikely to return a FRET signal. Therefore, confocal microscopy and other traditional fluorescent techniques remain important tools.

Colocalization analysis varies in sophistication and the level of sophistication required depends on the needs of the investigator. In some applications colocalization between proteins in the same general cellular compartment is sufficient for the hypothesis being tested. Perhaps the most prevalent analysis approach for general compartment colocalization is 'merge analysis', where typically one protein distribution is indicated in green, another distribution in red, and colocalization indicated by yellow. Large areas of 'yellow' are then interpreted as areas within the cell where the two proteins exist and possibly function together. When 'merge analysis' is applied to wide-field microscopy images with relatively thin specimens, the inherently 2-dimensional nature of this style of analysis is acceptable due to the limited axial resolution present in the acquired images. However, in confocal images, with its optical-sectioning abilities 'merge analysis' is counter-productive since it effectively reduces a 3D dataset into a 2D image. Any axial resolution gained by the use of a confocal microscope is lost by the merge approach and one can expect vertically resolved events to be erroneously colocalized.

Published colocalization results using this 'merge analysis' approach often do not include the technical details on how the results are generated. However, it is likely that a consumer level image editing software as Adobe Photoshop is used. In order for these types of programs to

return a yellow ‘channel’, the intensities of the red and green display channels must be manipulated to highlight specific areas of interest and is effectively a thresholding procedure. Thresholding of the imaging channels in tandem may inadvertently introduce a biased result. Interpretation of ‘merge analysis’, like the interpretation of many measures of colocalization, is simply positive or negative. This binary result makes it difficult to report any biological or statistical variations in the relationship between the proteins of interest. Thus the ‘merge analysis’ technique, while easily accessible to all investigators, has significant attributes that can be improved upon.

An improvement over ‘merge analysis’ is voxel-based colocalization analysis. These techniques consider the contents of individual voxel units and avoid the ‘merge’ techniques loss of axial information by retaining the 3D nature of the original images. In general, these approaches either calculate the probability of colocalization on thresholded images or they calculate the correlation between image intensities within the two imaging channels. Probability of colocalization calculations (colocalization index) are easier to interpret but are highly sensitive to the initial thresholding inputs. Analysis techniques that utilize correlation coefficients circumvent some of the difficulties associated with image thresholding however is more liable to differences in labelling and acquisition efficiency between the two fluorescent labels. For this reason, colocalization index calculations were used as a starting point for colocalization analysis in these studies.

The colocalization index of A with B is calculated from the number of voxels containing both A and B events (colocalization events) compared with the number of voxels containing just A. Thus, 33% colocalization would mean that one third of all A events also contain B events. Colocalization analysis is inherently dependent on the imaging system’s resolution and as such, this technique is more definitive in indicating non-colocalization since the relatively poor resolution available from confocal microscopy is expected to result in false colocalization events.

One method of reducing the probability of false colocalization events is to use image restoration techniques such as deconvolution. Deconvolution is the statistical modeling of the original specimen, which generated the acquired image, using information gathered from the

microscope's point spread function (PSF). The PSF of a microscope can be estimated from images acquired of a sub-resolution object, most commonly 100-200 nm fluorescent latex beads. The image of this sub-resolution spot is purposefully blurry since it is this blurring that characterizes the image properties of the microscope. Deconvolution assumes that every image is composed of numerous sub-resolution spots therefore the PSF contains much of the necessary information to reverse the image degradation process.

To examine the effects of deconvolution in a more controlled setting, bead images can be positioned at different lateral and axial separation distances to create a model system[29]. Because application of the Nyquist sampling theorem results in super-sampling, signals emitted from a sub-resolution spot are distributed across multiple pixels in all dimensions. Although a point source is a finite spot, it is represented in the image has a hazy cluster of pixels. Thus, when calculating the colocalization index, a wide range of colocalization index values are possible even from a singular pair of objects. Rather than a yes or no result, as one might expect, a continuum of values is found. As lateral and axial separation distances increase the colocalization index decreases from 100% at zero separation to 0% at a characteristic distance. In the lateral direction 800 nm of separation is required in raw confocal images to reach 0% colocalization and only 500 nm is required after deconvolution. In the axial direction, a separation of 1500 nm is required in raw confocal images and 750 nm is required in deconvolved images. Thus deconvolution is an effective means of decreasing false colocalization events and should be adopted as standard practice for high resolution microscopy.

Nevertheless, false colocalization events will exist even in deconvolved images. At a 100 nm bead separation, a full 5 times larger than the dyadic cleft, even deconvolved bead pairs had a colocalization index of 70%. Alarmingly, this value is quite similar to values gathered for DHPR-RyR colocalization. This type of colocalization analysis, while an improvement over 'merge analysis' is not specific enough to indicate whether colocalization events occur due to true colocalization events or whether colocalization occurs by image blurring.

The interpretation of colocalization indices is further complicated by in situ measurements of maximal colocalization inside the cell. Maximal colocalization measured in a more natural environment, using two different antibodies for the same antigen, found a maximum

colocalization index of 65%. However, maximum colocalization measured in the bead model was 100%. Although some differences are expected from experiment to experiment, it is likely that in this case the simple bead model did not contain the complexity necessary to reproduce cellular labelling. In any real imaging system the requirement for different excitation and emission wavelengths for each fluorophore necessitates different combinations of optical components, each of which will have a downstream effect on the acquired image. As a result, in real imaging, PSF's differ for each imaging channel and are not expected to overlap completely. The bead model returns 100% colocalization because both images are identical in composition and intensity. Real images contain noise and different levels of background noise require different thresholding parameters. When thresholding is applied to remove non-specific signal the shape and size of image features will be affected. Thus, even if two antibodies are used to label the same protein they should not be expected to return identical images.

Thresholding is an integral part of colocalization analysis and effectively designates what is real and what is noise. The number of voxel events attributed to a protein distribution is dependent on the labelling density of the protein (the physical distribution), the resolution/sampling of the microscope and the thresholding intensity. Arbitrary thresholding can, in fact, return any colocalization value regardless of the physical distribution and imaging resolution. A common thresholding approach is to identify the amount of background noise present in the dataset. Two common sources of background noise are electronic noise and labelling or antibody noise. Electronic noise originates from the light detectors themselves, such as dark counts or electronic offsets, and antibody noise originates from non-specific antibody interactions. Thus 'noise' thresholding identifies the minimal thresholding value necessary to exclude these factors.

Noise thresholding may overestimate the number of voxel events due to the laser scanning imaging process. Due to diffraction, the laser beam has an approximately Gaussian profile and the leading and trailing edges of the laser beam are really not edges at all but rather have a gradually increasing or decreasing quality. Thus, all imaged objects contain bright and dim pixels/voxels that are completely unrelated to noise processes. The key implication is that, if imaged objects are bright, then the signal intensity associated with these leading and trailing edges may be higher than the noise floor. In this scenario, noise thresholding will overestimate

the number of voxel events attributed to a protein distribution. The effects of this 'under-thresholding' will be magnified when labelling density is high. Because fluorescent signals are additive, the leading and trailing edges of neighbouring objects are summed. Pixels located in between two closely positioned point sources are thus 'blurred together'. In fact, the summation of leading and trailing edges is what limits the imaging resolution.

When thresholding is applied to an image it results in a binary image; the image is reduced to 'lit' and 'dark' pixels represented by 0's and 1's respectively. Many EC coupling proteins are distributed in punctate clusters. When thresholding is applied to these punctate clusters the resulting binary image contains islands of 'lit' pixels surrounded by a sea of 'dark' pixels. Each of these islands is considered to be an independent object and the number of pixels contained in each object is intimately connected with the thresholding parameter. Lower thresholding values have the tendency to inflate object sizes whereas higher thresholding values have the tendency to deflate object sizes.

Conceptually, images that are under-thresholded are expected to clump together neighbouring objects and images that are over-thresholded are expected to be missing objects. Therefore, both under-thresholding and over-thresholding values decrease the number of found objects. At some intermediate thresholding value, a 'peak' number of objects is expected, where the selected thresholding value effectively segments neighbouring objects but is not so aggressive as to delete legitimate objects. This usage of a 'peak' thresholding value is the underlying principle behind the iterative thresholding procedures.

Instead of using a single thresholding value, estimated from control experiments, iterative thresholding procedures apply multiple thresholding values to each image to determine how the image 'reacts' to different thresholding values. Images are intentionally under and over-thresholded to examine the effects of each. When the thresholding value is too low for an image the overall object count will be very low. When the thresholding value is very high the overall object count will also be very low. However, in between these under and over thresholding values you expect a peak value in the number of objects, where the gain in object count via segmentation of neighbouring clusters balances out the losses in object count via the deletion of objects. The thresholding value that produces this peak object count offers an objective estimate

of the true thresholding value. The thresholding parameter is determined on a cell-by-cell basis, rather than a batch thresholding procedure relying on primary antibody omission controls. In all cases, a segmenting thresholding is more stringent than a background threshold value since antibody dilutions are already optimized to suppress labelling noise.

Iterative thresholding procedures explicitly segment cellular fluorescence into small discrete objects. The bead modeling results indicated that non-colocalized objects can nevertheless produce colocalization events due to limited imaging resolution. The amount of colocalization events produced is correlated with the separation distance between two object pairs, with larger colocalization indices being correlated with smaller separation distances and vice versa. This correlation between the colocalization index and the separation distance suggests that colocalization events can be categorized into high and low probability events. In object-specific colocalization analysis, the colocalization indices within individual pairs of objects are determined, making the analysis analogous to the bead modeling experiments.

Object-specific colocalization analysis effectively quantifies the number of ‘fringe’ colocalization events and is especially useful when dealing with lower colocalization indices. Low colocalization indices can occur either due the presence of a non-colocalized protein relationship (i.e. the two proteins are never found together) or because the colocalization only occurs some of the time. Object-specific analysis allows a distinction to be made between these two subtly different organizations.

Both colocalization analysis and object-specific colocalization analysis are very sensitive to object size. Object sizes as estimated by iterative thresholding procedures are affected by the overall density of the punctate distribution. When clusters of fluorescence are spatially well separated, iterative thresholding will estimate a lower thresholding value because neighbouring objects are more easily segmented from each other. The lower thresholding value retains more of the ‘shoulder regions’ of leading and trailing edges of the sub-resolution spot. Object sizes grow quickly with reduced thresholding values since these shoulder regions extend in all three-dimensions.

To counteract this tendency of iterative thresholding, a secondary thresholding procedure can be applied to each object. Object size should be independent of object densities and should only depend on imaging resolution. The Full-Width-Half-Maximum (FWHM) definition of resolution estimates the size of an object by the width of the object at 50% of the maximum intensity of the object. Thus, the FWHM definition can be applied to each individual object. Application of this secondary thresholding procedure normalizes object sizes and limits the effects of under-thresholding on object size.

The secondary thresholding procedure has little effect on very dense object densities. When objects are separated by distances just above the limit of resolution, relatively high thresholding values are estimated by iterative thresholding procedures. This is because high thresholding values are required to segment neighbouring objects. The estimated thresholding value can be so high, in fact, that is approaches the 50% maximum as implied by the FWHM definition. Thus the application of the secondary thresholding procedures has little effect if the object density is high.

Object sizing also has a direct effect on the maximum amount of colocalization that can occur. If a pair of objects have mismatched object sizes then the smaller object will limit the maximum colocalization index. If object A is 10 pixels large and object B is 6 pixels large then the colocalization of A with B is only 60% even if the two objects are perfectly colocalized. In the reverse relationship, the colocalization of B with A, maximum colocalization will be 100% since object A is expected to envelope object B if they are perfectly colocalized. Because the maximum possible colocalization index may be significantly lower than 100%, quantification of the objects' sizes for each protein distribution can aid interpretation. Both voxels-based and object-based calculations are affected by object size. In object-based colocalization, there is a possibility that a small object will pair with a large object. Thus even if the two objects are in fact perfectly colocalized, the object pair will return a small object-specific colocalization index.

Object-specific colocalization sought to correlate the colocalization index between two isolated objects with the distance of separation between these two objects. However, this distance of separation can also be determined more directly. Positional resolution, the ability to describe the location of an object differs from the ability to resolve the presence of two

juxtaposed objects. Diffraction-limited resolution dictates how closely two objects can approach each other while still being able to visualize the presence of two objects. As discussed, the leading and trailing edges of each object eventually blur together until it is not clear whether the object being examined is a single elongated object or two point sources. However, if the two objects are located in different imaging channels then leading and trailing edges are never optically combined and remain distinct in the acquired images.

The position of a single sub-resolution object can be localized to a much higher precision than the diffraction limit resolution would suggest. This is because the position of an object can be estimated from the intensity profile of the imaged object and groups have reported the ability to positionally resolve sub-resolution objects down in to the singular nanometer range, albeit in two dimensions[31-33]. With symmetrical point-spread-functions, or the assumption thereof, the position of an object can be estimated from the centroid, the center-of-mass co-ordinate.

Direct distance calculations then provide a third indicator of colocalization. Voxel-based colocalization and object-specific colocalization, as have been shown, are both dependent on object size and are thus more dependent on the thresholding parameter. However, centroid calculations are less affected by thresholding because low pixel/voxel values associated with object edges contribute little to the total 'mass' of the object. Nevertheless, direct distance calculations are dependent on the assumption of punctate point sources. Because objects are reduced to centroid co-ordinates, there is the distinct possibility that non-symmetrical objects will be misrepresented by a centroid reduction.

These three indicators of colocalization can be effectively used together to investigate age-related changes in colocalization. A good example of the potential of these techniques can be found in the Na_V-NCX study (chapter 5). With development NCX-Na_V1.4 colocalization drops by 42% from 17% to 12%.This decrease could be mediated by an increase in the number of NCX labelling events or it could be mediated by a decrease in colocalization events. It is known that the periodicity of NCX labelling events does not change with development, suggesting that if there is an increase in the number of NCX labelling events, it must be occurring through an increase in object size. However, size analysis indicates that NCX objects do not change with

development. Thus a change in NCX labelling does not appear to be a factor and suggests that the number of colocalization events must be changing.

The number of identified colocalization events can change due to increased object separation, decreased object size and or through decreased object density. Each of these factors differ in their physiological implications and although the colocalization index may increase or decrease with development, it is more physiologically relevant to consider the mechanism or mechanisms behind any changes in the colocalization index.

Distance analysis indicates that NCX and $Na_v1.4$ objects have similar separation profiles during development which suggests that individual pairs of NCX and $Na_v1.4$ objects maintain their spatial relationships as the cells develop. However, if the apparent size of $Na_V1.4$ objects decreases with development then the colocalization index will still decrease even though the physical separation between NCX and $Na_V1.4$ objects does not change. To control for this effect, the size of $Na_V1.4$ object sizes were determined and the results indicate that $Na_V1.4$ object sizes are constant with development. These results indirectly suggest that the decreased colocalization index is the result of decreased $Na_v1.4$ object density. When $Na_v1.4$ density was further quantified, it was determined that the $Na_v1.4$ density drops from 42% to 35% relative to NCX labelling density. This analysis approach indicates that the change in $Na_v1.4$-NCX colocalization decreases with development as a result of decreased $Na_v1.4$ density. When $Na_v1.4$-NCX objects do associate, there is no developmental distinction between neonatal and adult coupling events.

Colocalization analysis for $Na_V1.5$ and NCX colocalization also indicated that the colocalization between these two proteins decreases with development. Like the $Na_v1.4$-NCX results age related changes in object sizes were minimal. However, the $Na_V1.5$ object density does not change with development and the colocalization index does not decrease due to decreased $Na_V1.5$ expression. Rather, the colocalization index falls because the individual relationships between $Na_V1.5$ and NCX objects become increasingly distant. This increased separation between objects is apparent in the object-specific colocalization analysis and direct measurements of the separation distances.

In the following chapters, confocal microscopy and image analysis techniques are used to investigate the developmental expression and distribution of cardiac EC coupling proteins. Chapter 2 investigates the spatial relationship between calcium channels and RyR as a function of development. Included in chapter 2 is an investigation on the effects of image restoration on colocalization analysis, both in a physiological context and in a modeling environment. In chapter 3, the relationship between NCX and RyR is investigated and presents novel cell outline extraction techniques necessary for compartmental colocalization analysis. Compartmental colocalization analysis and a novel automated objective thresholding technique are used in Chapter 4 in the investigation of NCX organization by caveolin-3 (cav-3). The relationship between NCX and cav-3 is also investigated using the "object-specific" colocalization analysis technique, a supplementary analysis technique to the traditional colocalization index. Chapter 5 investigates the relationship between NCX and various sodium channel isoforms and represents the summation of the preceding image analysis techniques. The separation distances between individual labelling clusters are included into a third measure of protein-protein colocalization. Finally, chapter 6 discusses the findings of these previous chapters in light of the current literature, where further experiments are also proposed.

1.6. REFERENCES

1. Callewaert G. Excitation-contraction coupling in mammalian cardiac cells. *Cardiovascular research.* 1992;26(10):923-932.

2. Luo CH, Rudy Y. A dynamic model of the cardiac ventricular action potential. I. Simulations of ionic currents and concentration changes. *Circ Res.* 1994;74(6):1071-1096.

3. Rohr S. Role of gap junctions in the propagation of the cardiac action potential. *Cardiovascular research.* 2004;62(2):309-322.

4. Delbridge LM, Bassani JW, Bers DM. Steady-state twitch Ca2+ fluxes and cytosolic Ca2+ buffering in rabbit ventricular myocytes. *Am J Physiol.* 1996;270(1 Pt 1):C192-199.

5. Hryshko LV, Stiffel V, Bers DM. Rapid cooling contractures as an index of sarcoplasmic reticulum calcium content in rabbit ventricular myocytes. *Am J Physiol.* 1989;257(5 Pt 2):H1369-1377.

6. Huang J, Hove-Madsen L, Tibbits GF. Na+/Ca2+ exchange activity in neonatal rabbit ventricular myocytes. *American journal of physiology.* 2005;288(1):C195-203.

7. Huang J, Hove-Madsen L, Tibbits GF. Ontogeny of Ca2+-induced Ca2+ release in rabbit ventricular myocytes. *American journal of physiology.* 2008;294(2):C516-525.

8. Artman M. Sarcolemmal Na(+)-Ca2+ exchange activity and exchanger immunoreactivity in developing rabbit hearts. *The American journal of physiology.* 1992;263(5 Pt 2):H1506-1513.

9. Boerth SR, Zimmer DB, Artman M. Steady-state mRNA levels of the sarcolemmal Na(+)-Ca2+ exchanger peak near birth in developing rabbit and rat hearts. *Circulation research.* 1994;74(2):354-359.

10. Qu Y, Ghatpande A, el-Sherif N, Boutjdir M. Gene expression of Na+/Ca2+ exchanger during development in human heart. *Cardiovascular research.* 2000;45(4):866-873.

11. Huang J, Xu L, Thomas M, Whitaker K, Hove-Madsen L, Tibbits GF. L-type Ca2+ channel function and expression in neonatal rabbit ventricular myocytes. *Am J Physiol Heart Circ Physiol.* 2006;290(6):H2267-2276.

12. Lederer WJ, Niggli E, Hadley RW. Sodium-calcium exchange in excitable cells: fuzzy space. *Science (New York, N.Y.* 1990;248(4953):283.

13. Sham JS, Cleemann L, Morad M. Gating of the cardiac Ca2+ release channel: the role of Na+ current and Na(+)-Ca2+ exchange. *Science (New York, N.Y.* 1992;255(5046):850-853.

14. Catterall WA, Goldin AL, Waxman SG. International Union of Pharmacology. XLVII. Nomenclature and structure-function relationships of voltage-gated sodium channels. *Pharmacological reviews.* 2005;57(4):397-409.

15. Fozzard HA, January CT, Makielski JC. New studies of the excitatory sodium currents in heart muscle. *Circulation research.* 1985;56(4):475-485.

16. Maier SK, Westenbroek RE, McCormick KA, Curtis R, Scheuer T, Catterall WA. Distinct subcellular localization of different sodium channel alpha and beta subunits in single ventricular myocytes from mouse heart. *Circulation.* 2004;109(11):1421-1427.

17. Maier SK, Westenbroek RE, Schenkman KA, Feigl EO, Scheuer T, Catterall WA. An unexpected role for brain-type sodium channels in coupling of cell surface depolarization to contraction in the heart. *Proceedings of the National Academy of Sciences of the United States of America.* 2002;99(6):4073-4078.

18. Haufe V, Cordeiro JM, Zimmer T, Wu YS, Schiccitano S, Benndorf K, Dumaine R. Contribution of neuronal sodium channels to the cardiac fast sodium current INa is greater in dog heart Purkinje fibers than in ventricles. *Cardiovascular research.* 2005;65(1):117-127.

19. Kaufmann SG, Westenbroek RE, Zechner C, Maass AH, Bischoff S, Muck J, Wischmeyer E, Scheuer T, Maier SK. Functional protein expression of multiple sodium channel alpha- and beta-subunit isoforms in neonatal cardiomyocytes. *J Mol Cell Cardiol.* 2009.

20. Scriven DR, Dan P, Moore ED. Distribution of proteins implicated in excitation-contraction coupling in rat ventricular myocytes. *Biophys J.* 2000;79(5):2682-2691.

21. Cohen SA. Immunocytochemical localization of rH1 sodium channel in adult rat heart atria and ventricle. Presence in terminal intercalated disks. *Circulation.* 1996;94(12):3083-3086.

22. Despa S, Bers DM. Na/K pump current and [Na](i) in rabbit ventricular myocytes: local [Na](i) depletion and Na buffering. *Biophys J.* 2003;84(6):4157-4166.

23. Despa S, Kockskamper J, Blatter LA, Bers DM. Na/K pump-induced [Na](i) gradients in rat ventricular myocytes measured with two-photon microscopy. *Biophys J.* 2004;87(2):1360-1368.

24. Lines GT, Sande JB, Louch WE, Mork HK, Grottum P, Sejersted OM. Contribution of the Na+/Ca2+ exchanger to rapid Ca2+ release in cardiomyocytes. *Biophys J.* 2006;91(3):779-792.

25. Huang J, van Breemen C, Kuo KH, Hove-Madsen L, Tibbits GF. Store-operated Ca2+ entry modulates sarcoplasmic reticulum Ca2+ loading in neonatal rabbit cardiac ventricular myocytes. *Am J Physiol Cell Physiol.* 2006;290(6):C1572-1582.

26. Dan P, Lin E, Huang J, Biln P, Tibbits GF. Three-dimensional distribution of cardiac Na+-Ca2+ exchanger and ryanodine receptor during development. *Biophysical journal.* 2007;93(7):2504-2518.

27. Mullins LJ. A mechanism for Na/Ca transport. *The Journal of general physiology.* 1977;70(6):681-695.

28. Despa S, Islam MA, Weber CR, Pogwizd SM, Bers DM. Intracellular Na(+) concentration is elevated in heart failure but Na/K pump function is unchanged. *Circulation.* 2002;105(21):2543-2548.

29. Sedarat F, Lin E, Moore ED, Tibbits GF. Deconvolution of confocal images of dihydropyridine and ryanodine receptors in developing cardiomyocytes. *J Appl Physiol.* 2004;97(3):1098-1103.

30. Selvin PR. The renaissance of fluorescence resonance energy transfer. *Nat Struct Biol.* 2000;7(9):730-734.

31. Toprak E, Selvin PR. New fluorescent tools for watching nanometer-scale conformational changes of single molecules. *Annu Rev Biophys Biomol Struct.* 2007;36:349-369.

32. Cheezum MK, Walker WF, Guilford WH. Quantitative comparison of algorithms for tracking single fluorescent particles. *Biophys J.* 2001;81(4):2378-2388.

33. Thompson RE, Larson DR, Webb WW. Precise nanometer localization analysis for individual fluorescent probes. *Biophys J.* 2002;82(5):2775-2783.

2. DECONVOLUTION OF CONFOCAL IMAGES OF DIHYDROPYRIDINE AND RYANODINE RECEPTORS IN DEVELOPING CARDIOMYOCYTES[1]

2.1. INTRODUCTION

Excitation-contraction coupling in cardiac muscle requires Ca^{2+} influx through sarcolemmal DHPR, followed by Ca^{2+}-induced Ca^{2+}release (CICR) through the sarcoplasmic reticulum (SR) Ca^{2+} release channels also known as RyR [1-5]. Dyadic couplings in cardiac muscle cells are formed between RyRs and either sarcolemmal or T-tubular DHPR [6-8]. The juxtaposition of DHPR and RyR in these couplings is crucial for both CICR and excitation-contraction coupling in adult myocardial cells. In newborn rabbits, myocytes have sparse SR and do not develop T-tubules until 8-10 days of age, therefore the spatial relationship between DHPR and RyR is different from the adult heart [9-11]. Using confocal microscopy and immunofluorescent labelling, we previously showed a significant increase in the degree the colocalization of DHPR-RyR as well as changes in colocalization distribution inside the cell during development. All imaging systems distort object information and/or introduce imaging artefacts that subsequently affect quantitative analysis. We expected that this distortion would lead to an over-estimation of protein/fluorophore colocalization. In this study we quantified the effects of deconvolution on colocalization analysis using a fluorescence model and then applied the same deconvolution algorithms to our previously collected data.

Colocalization is a resolution-dependent descriptor and it is often used to indicate possible protein-protein interactions. A colocalization event is defined as when one fluorophore is found in the same voxel as another fluorophore, implying that the proteins attached to the fluorophores are also within the same voxel. A colocalization event, where two fluorophores are found together, actually refers to a range of possible separation distances. Because deconvolution

[1] A version of this chapter has been published. Sedarat F, Lin E, Moore ED, Tibbits GF. Deconvolution of confocal images of dihydropyridine and ryanodine receptors in developing cardiomyocytes. *J Appl Physiol*. 2004 Sep;97(3):1098-103.

increases resolution, it increases the power of colocalization analysis by limiting the range of possible separation distances. In addition to increasing the likelihood of an actual protein-protein relationship, deconvolution also decreases the probability of false colocalization events. Confocal microscopy attenuates the majority of out-of-plane fluorescence emission but does not remove it completely. Such that, two sub-resolution point sources (fluorophore clusters) may generate colocalization events even if the center of masses of the two points are well separated. These pseudo-colocalization events arise due to the point spread function (PSF) of the microscope. Sub-resolution objects do not appear simply as blurry spheres but as blurry hourglasses, due to the numerical aperture (NA) of the objective and the pinhole radius. Because deconvolution fundamentally changes how sub-resolution objects appear, by transforming the hourglass shape into a bead shape, the results can not be duplicated via other image processing techniques such as aggressive thresholding (which affect size more so than the shape of objects).

Colocalization is a function of resolution and separation distance and physiological systems, in general, can not be used to characterize the effects of deconvolution because of their complexity and irregularity. Hence, a non-physiological model is required to evaluate the effects of image restoration regarding colocalization.

In order to quantify the effects of deconvolution, multiple PSF images were positioned at a variety of axial and lateral separation distances to simulated fluorophore colocalization interactions inside a cell. Deconvolution algorithms strive to effectively reassign out-of-focus light (by conserving total flux) back to its original location within the image volume and reverse many of the aberrations introduced by the optics [12, 13]. Colocalization was calculated pre- and post-deconvolution in the fluorescence interaction model. Results from the fluorescence model showed that colocalization analysis without deconvolution tended to over-estimate fluorophore interactions. We examined raw confocal and deconvolved confocal images of DHPR and RyR to determine the extent that colocalization might be overestimated due to out-of-focus light in confocal images. The data clearly show that deconvolution of confocal images is essential for colocalization analysis and should be adopted as a standard procedure in studies of this nature.

2.2. METHODS

2.2.1. DECONVOLUTION

Deconvolution was performed by *Huygens Professional* (Version 2.18 Scientific Volume Imaging, Hilversum, Netherlands) software. The point spread function (PSF) of the Zeiss 410 confocal microscope was measured using images of 200 nm diameter fluorescent latex beads captured at the same image parameters as the cardiomyocyte images (see below – Biological Samples). The beads were appropriately diluted, plated on a glass slide and embedded in DABCO mounting medium to minimize the refractive index mismatch. Singular beads, beads with no neighbours in the field of view, were imaged on the Zeiss 410 and then aligned (centered) and averaged in Huygens Professional. Multiple bead (~10) images were acquired to provide sufficient signal-to-noise ratio for the reconstruction of the PSF. The averaged bead image was utilized as the PSF for deconvolution as well as for FWHM measurements pre- and post-deconvolution. In addition, this average bead image was also utilized as the foundational image for the fluorescence interaction's model. Images were recorded at the Nyquist rate (100 nm lateral and 250 nm axial sampling interval) to prevent aliasing. We applied a Maximum Likelihood Estimation (MLE) algorithm to deconvolve the confocal images. The Huygens implementation of MLE takes the following factors into consideration: the numerical aperture (NA) of the microscope objective; refractive index of the medium; excitation wavelength; emission wavelength; confocal pinhole radius; pixel size; Z axis interval; microscope type (i.e. wide field, confocal or 4π) and the number of excitation photons.

Under low light-level conditions, the detector in a confocal microscope (normally a photomultiplier tube) behaves essentially as a photon counter. This conversion of fluorescence intensity to a discrete number of detected photons is described statistically as a Poisson process. The MLE algorithm computes the maximum likelihood estimate for the intensity of a Poisson process [14]. This iterative process is based on the work done about 3 decades ago by Richardson [15] and Lucy [16] for astronomical imaging processing and is frequently referred to as R-L iteration.

The relevant iterative equation for MLE is:

$$f_{new} = f_{old} \Sigma g_i \frac{h(i|j)}{\Sigma\left[h(i|j) f_{old,j}\right]}$$

where f is the object function

g is the image

h(i | j) is the PSF (the fraction of light from true location j that gets scattered into observed pixel i)

The R-L iterative algorithm was shown by Shepp and Vardi [17] to converge to the maximum likelihood solution for Poisson statistics of optical data with noise from counting statistics. The number of iterations may serve as a regularization factor. In general, the remaining restoration error decreases with an increasing number of iterations. At the same time, the error due to noise amplification increases. The procedure should be stopped at an iteration number in which the sum of both errors is minimal [18].

2.2.2. MODELING

Previous experiments have demonstrated that the DHPR and RyR are largely co-distributed in distinct clusters throughout the membranes of T-tubules and the SR, respectively. The 3D images of these clusters were found to be indistinguishable from that of a point source object [19]. Therefore, a microscope's recorded PSF can be used to simulate a cluster of molecules. Using Optimas 5.2 image processing software, a macro was written in ALI (analytic language of imaging) to create multiple copies of the Alexa488 and Alexa594 fluorophores PSFs. These PSFs were placed a variety of lateral and axial separation distances in order to analysis the effects of hourglass shaped PSFs (raw confocal) verses spherical shaped PSFs (deconvolved) on colocalization. The distance between the centers of mass of the two bead images (PSF images) were varied in 100 nm increments between 0 to 1000 nm in the x-axis and varied in 250nm increments from 0 to 1500 nm in the z-axis (see results – Figure 2.2). Note that

because colocalization calculations were performed on 3D stacks, colocalization events were still generated even if the spheres were well separated, especially when looking at the raw confocal beads. The colocalization index was calculated as a function of distance before and after deconvolution.

2.2.3. BIOLOGICAL SAMPLES

Neonatal New Zealand white rabbits were used from four age groups: 3, 6, 10 and 20-day old. The method of myocardial cell isolation and immunofluorescent labelling has been previously described [20]. Briefly, single cardiac myocytes were isolated from neonatal rabbit hearts by enzymatic digestion. Double labelling was performed on fixed and permeabilized cardiomyocytes with anti-RyR and anti-DHPR primary antibodies. The cells were then incubated with Alexa-conjugated secondary antibodies (Alexa488 for DHPR and Alexa594 for RyR). After applying secondary antibodies, the cells were mounted on a glass slide and embedded in DABCO mounting medium (90% glycerol, refractive index (n) = 1.47) to minimize the refractive index mismatch of the lens immersion liquid (oil, n = 1.52) to that of the specimen. The labelled cardiomyocytes were examined using a Zeiss LSM 410 laser scanning confocal microscope equipped with a Zeiss Plan-Apochromat 63x / NA 1.40 oil objective. An Ar-Kr 488/568 laser provided the excitation light. The confocal pinhole aperture was set to the diameter of the Airy disk. Stacks of 50 to 70 focal planes were captured at 0.25 μm Z intervals through the depth of the cell. 3-dimensional images of the cells were reconstructed using the image stacks. The Nyquist theorem, which utilizes the limitation of the microscope optics (FWHM) to dictate adequate sampling, was used to determined that pixel dimensions of 100 nm by 100 nm by 250 nm (x, y, z) were required to properly sample the data. Using Optimas 5.2 image processing software, 3-dimensional images of myocardial cells were examined to determine the degree of colocalization, or colocalization index (CI), of DHPR and RyR in each age group before and after image restoration. Before measuring CI, a threshold was applied to the images to exclude ~99% of the signal found in the images captured from control samples (stained with secondary antibodies without applying primary antibodies). Typically, thresholding resulted in about a 10-15% reduction in the total signal and a signal to noise ratio of about 15.

2.3. RESULTS

2.3.1. MODELING

Figure 2.1 shows that the measurement of the full width at half-maximum amplitude (FWHM) of the PSF and demonstrates significant enhancement of both lateral and axial resolution after deconvolution of confocal images. Lateral resolution improved two-fold (FWHM = 310 nm before and 150 nm after restoration). Axial resolution improved almost four-fold (FWHM = 850 nm before and 230 nm after restoration).

Figure 2.2 illustrates the arrays of fluorescent beads used for the modeling before and after restoration. By increasing the distance between the bead arrays, the colocalization index decreased in both x and z-axes. In raw confocal images the separation distance along the x-axis was increased to 800-900 nm before reaching zero colocalization. Only 400-500 nm of separation was needed to reach zero colocalization in the deconvolved images. In the z-axis, a 1500 nm separation resulted in almost zero colocalization in the raw images as opposed to 500 nm for restored confocal images.

In Figure 2.3 the upper panel shows decreasing colocalization as a function of separation distance along the x-axis. The lower panel shows decreasing colocalization with increasing z-distance. Both graphs show the comparison of the effects of separation distance on colocalization index before and after restoration of confocal images. Note the significant reduction in colocalization index in both axes after deconvolution. Using Origin 6.0 software, the data were fit with a first order exponential decay equation: $CI = Ae^{-x/\lambda}$, where CI is the colocalization index, A is the maximum amplitude (with x equal to 0 and was set to 100%) and x is the separation distance in nm. The derived correlation coefficient, r^2 was ≥ 0.98 for all curves. We used λ as a parameter to describe colocalization index as function of separation distance. The value of λ significantly decreased after restoration in both axes (x-axis: $\lambda = 332 \pm 18$ nm before and 205 ± 13 nm after deconvolution, z-axis: $\lambda = 845 \pm 50$ before nm and 248 ± 23 nm after deconvolution).

2.3.2. BIOLOGICAL SAMPLES

Applying the MLE restoration deconvolution produced images of DHPR and RyR distribution with enhanced resolution and reduced out-of-focus light (fig 2.4) and the image improvement was particularly clear in cross-sectional images (fig 2.5).

The overall staining pattern of DHPR and RyR remained unchanged after deconvolution. The staining pattern of RyR was similar in all age groups and included striations, spaced at regular intervals of ~2 μm. In myocytes from young animals (3 and 6 day), prior to the development of T-tubules, DHPRs associated fluorescence was seen only on the periphery of the cell. In 10-day and 20-day animals DHPR fluorescence could be seen on the periphery as well as in the cell interior.

The degree of colocalization in restored images was different from non-restored images. DHPR colocalization with RyR decreased after deconvolution in all age groups (Table 2.1). However, both before and after restoration, the colocalization index of DHPR and RyR increased significantly from 3 to 20-day old rabbit hearts. Differences in the absolute degree of colocalization before and after deconvolution are most likely due to out-of-focus light that contributes light to each plane of the optically sectioned images, resulting in the counting of co-incident pixels which are artifactual as shown in Figure 2.6.

2.4. DISCUSSION

The data presented in this paper clearly show that deconvolution of confocal images can have a profound impact on the quantification of colocalization. For example, the colocalization index (CI) of DHPR with RyR in the 3 day old group was overestimated by ~50% in the raw confocal images in relation to CI calculated from deconvolved images. In addition, this effect has now been demonstrated in other physiological systems [21]. This significant difference can affect the biological interpretation of the data and, therefore, cannot be ignored. In practice, however, very few confocal images published in physiological journals are deconvolved prior to image analyses and interpretation.

When light passes through a microscope it interacts with a number of optical components such as lenses, mirrors and prisms, before reaching the PMT. In mathematical terms, the light from the sample is said to be convolved by the point spread function of the optical system. Deconvolution aims to correct diffraction-induced distortions and results in images that exceed diffraction-limited resolution (where resolution is only dependent on the excitation wavelength and numerical aperture). At the heart of deconvolution are two assumptions/approximations: 1) objects are composed of many point sources and 2) that each point source is subjected to the same diffraction induced distortions. These assumptions imply that if one knows how the image of a point source is degraded then one knows how the image of an object is degraded as well. Therefore by capturing the effects of the optical pathway (blurring) for a point source, the image degradation can then be reversed for a whole object/sample. The point spread function was found by imaging a 200 nm fluorescent bead (sub-resolution bead) and the distortion was particularly obvious in the axial direction (Figure 2.1).

Although the imaging properties in a confocal microscopy give rise to much less blurring than a conventional microscope, the distortions will still significantly skew subsequent quantitative analyses. Colocalization without deconvolution will tend to describe a looser protein-protein relationship due to more limited resolution as well as over-estimate the actual number of colocalization events due to image blurring.

2.4.1. MODELING

An important issue in image restoration is the quantitative assessment of the gains in resolution and the corresponding gains in the reliability of the deconvolved image as compared with the original image. Physiological systems are difficult to characterize and always carry a level of uncertainty. This uncertainty prevents the accurate assessment of the effects of deconvolution on physiological systems. Due to the quantitative nature of deconvolution, the effects of deconvolution on physiological systems can be modeled computationally because clusters of DHPR or RyR appear the same as sub-resolution points. Therefore, the effects of deconvolution can be accurately modeled by sub-resolution fluorescent beads. By constructing a series of bead images with varying separation distances from 0 to 1000 nm laterally and 0 to 1500 nm axially, we measured the benefits of deconvolution and the corresponding changes in colocalization indices. Our model demonstrated that deconvolution increases the power of colocalization calculations by increasing image resolution while simultaneously decreasing the likelihood of false-positives by limiting out-of-focus light.

2.4.2. BIOLOGICAL SAMPLES

We re-examined our confocal images of dyadic couplings formation in rabbit ventricular myocytes during the first 20 days after birth [20]. Deconvolved data emphasizes the importance of microstructural changes in relation to DHPR and RyR association during ontogeny. In each age group, the degree of colocalization for DHPR decreased after deconvolution, due to the redistribution of out-of-focus light as established with bead models (see above). We have previously shown that DHPR-RyR colocalization increases with age (6 – 20 days) and deconvolution does not appear to change the overall distribution pattern of DHPR and RyR. This study shows that deconvolution has a positive effect on the reliably of quantitative measurements by increasing resolution and decreasing false colocalization events. We conclude that, in order to optimize colocalization's predictive power of protein-protein in confocal microscopy, resolution must be maximized and false-positives must be minimized by deconvolving prior to quantitative analysis.

2.5. FIGURES

Figure 2.1 Microscope point spread function

Point spread function of a 63X / NA 1.40 oil Zeiss Plan-Apochromat objective obtained from a 200 nm fluorescent bead. (A) Image of fluorescent bead used to measure the FWHM before and after restoration. (B) The graph shows significant improvement in both lateral and axial resolutions.

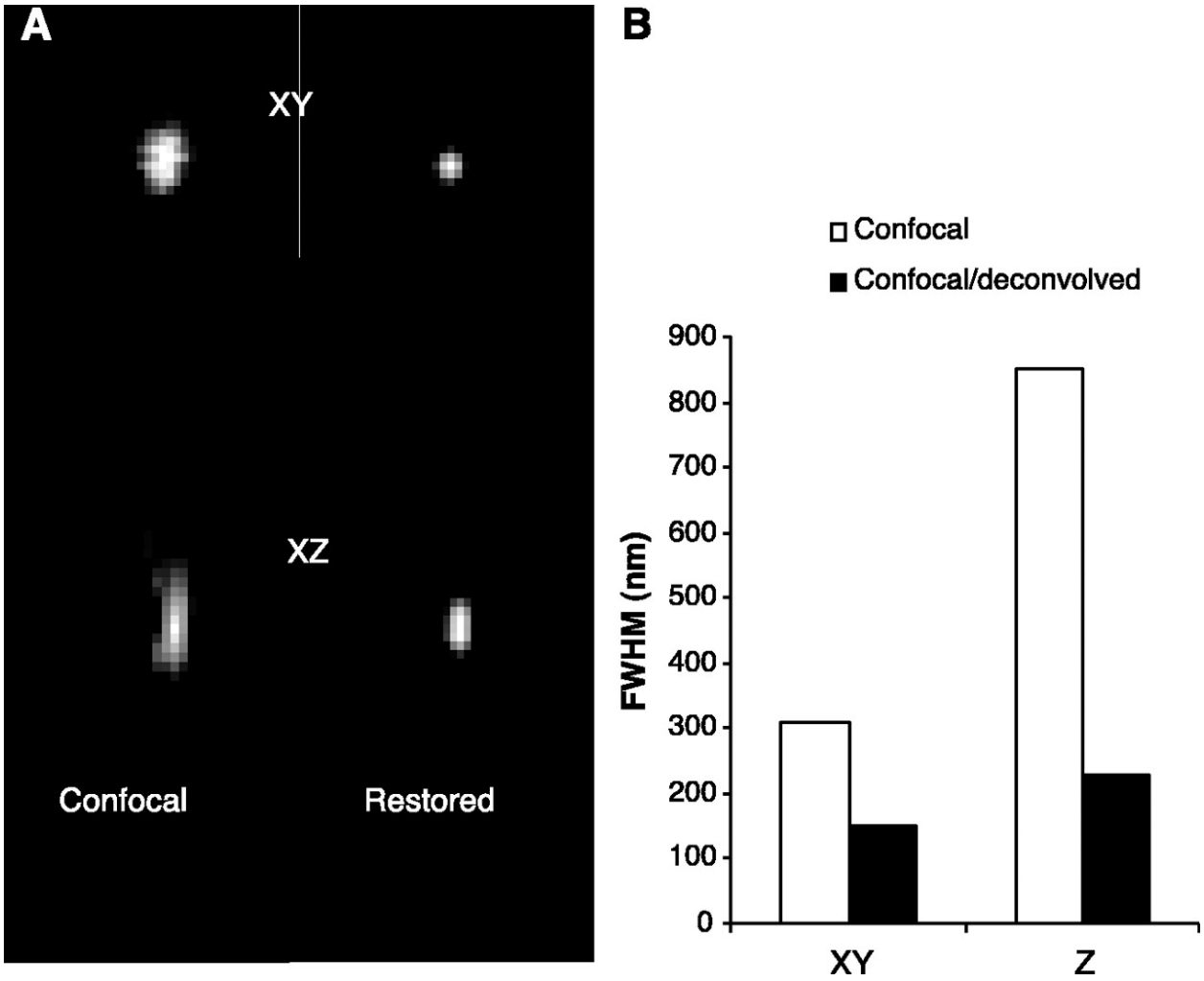

Figure 2.2 Fluorescence interaction model

The left panel shows the degree of colocalization pre- and post-deconvolution with increasing x-axis separation. The right panel shows changes in colocalization index pre- and post-deconvolution with increasing z-axis separation. Deconvolved images are shown on the left side and confocal images on the right. Colocalization indices are indicated below each image.

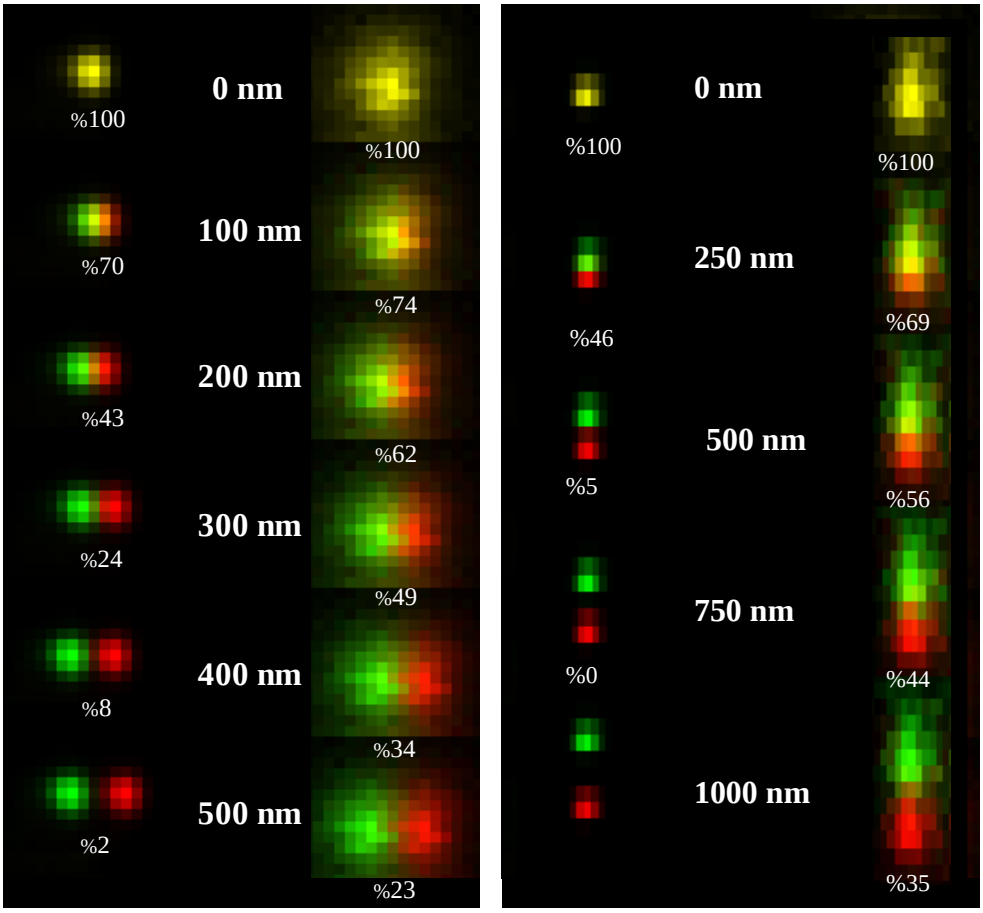

Figure 2.3 Colocalization index as a function of distance

Graphs of colocalization index versus distance of bead separation.

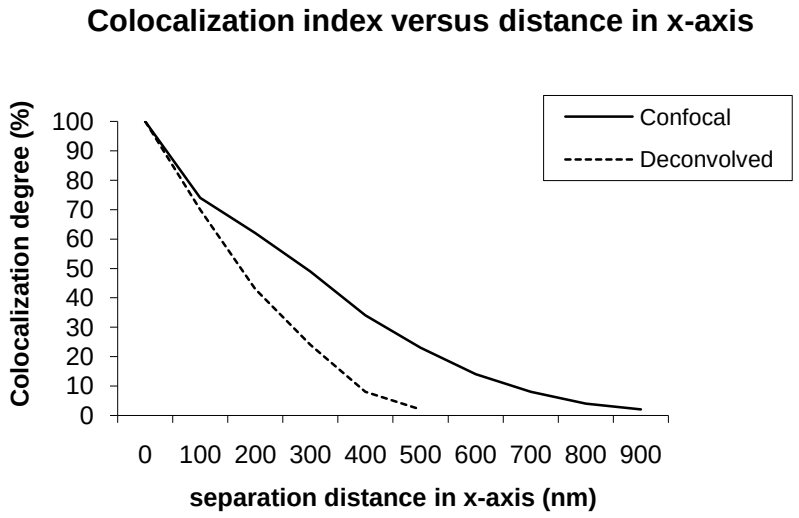

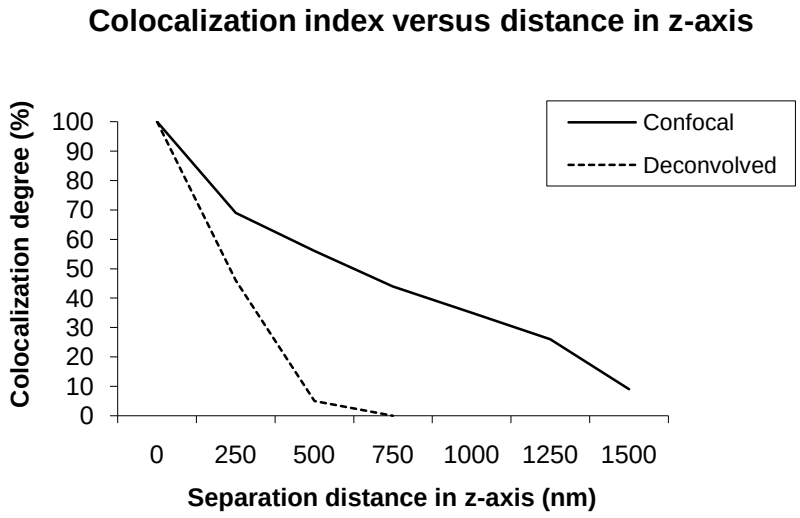

Figure 2.4 Confocal images of DHPR and RyR

(A, B and C) Confocal images (x-y) of the DHPR staining pattern (pseudo-coloured green), RyR staining pattern (pseudo-coloured red) and colocalization pattern (pseudo-coloured yellow) in myocardial cells isolated from a 10-day old rabbit heart. Data are shown by superposition (summation projection) of a series of optical sections through the z-axis from the front to back surfaces of the cell. The images have been scaled by adjusting both the intensity and contrast to highlight all pixels containing signal. This adjustment makes it possible to display out-of-focus light readily but because of the intensity scaling the background noise is also exaggerated. Note that for the purpose of colocalization analysis these images were corrected for the background and thresholded to exclude ~99% of signal found in control images related to nonspecific binding of secondary antibody. (A1, B1 and C1) Confocal images restored by MLE algorithm. Note increased clarity, and significant reduction in dispersion of the signal in the deconvolved images. Scale bars indicate 5 μm.

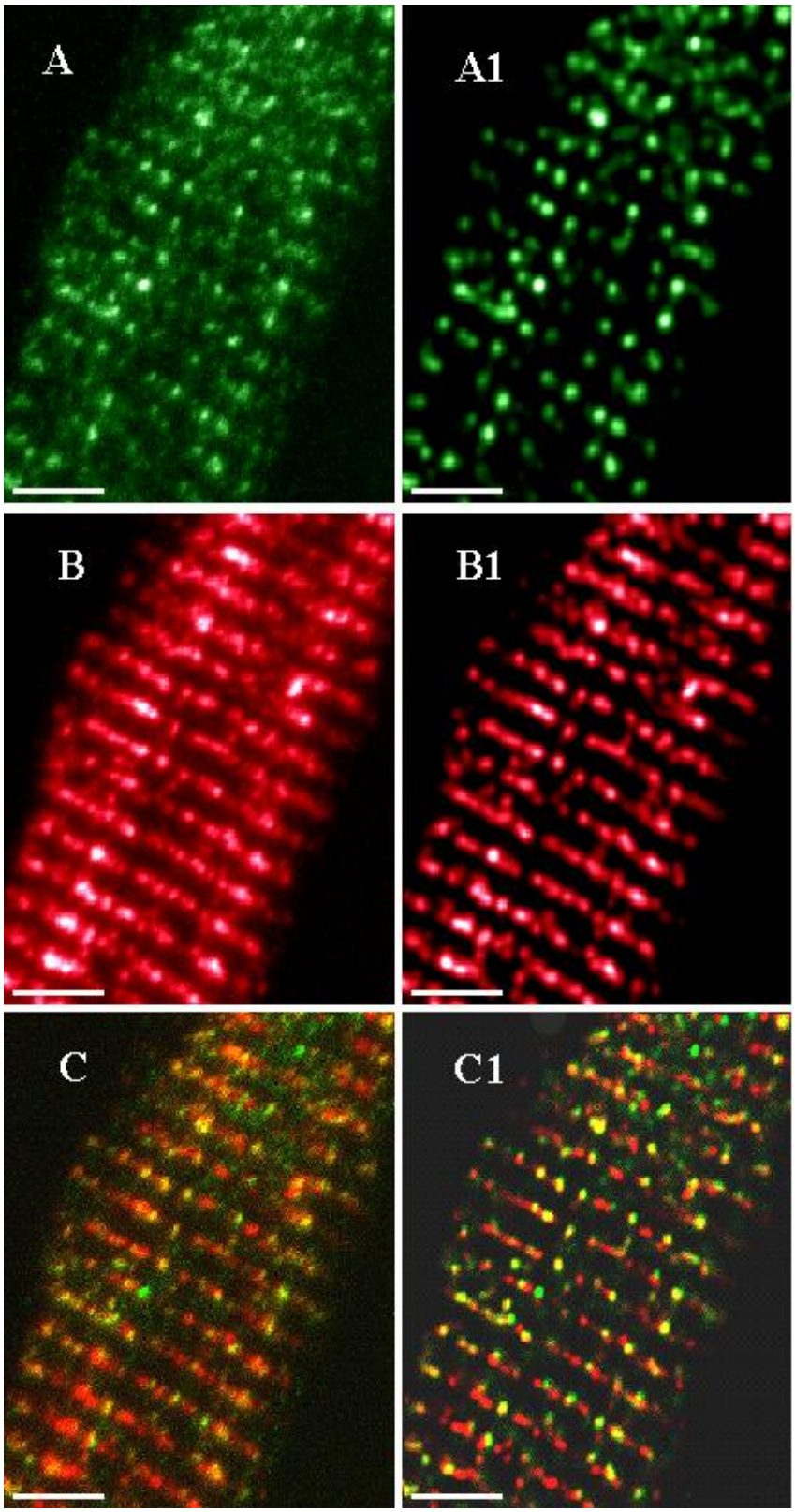
A
A1
B
B1
C
C1

Figure 2.5 Cross-sectional (x-z) images of a rabbit myocardial cell.

Cross-sectional (x-z) images of a rabbit myocardial cell. (A) Confocal image before restoration (DHPR in green, RyR in red, and colocalization in yellow). See Figure 2.4 for image display information. Note the elongation of distribution patterns along the z-axis due to the lower axial (z) resolution. (B) Same image as above after deconvolution. Note that there are significant improvements in z-axis elongation and noise after restoration. Scale bars for both images indicate 5 μm.

A

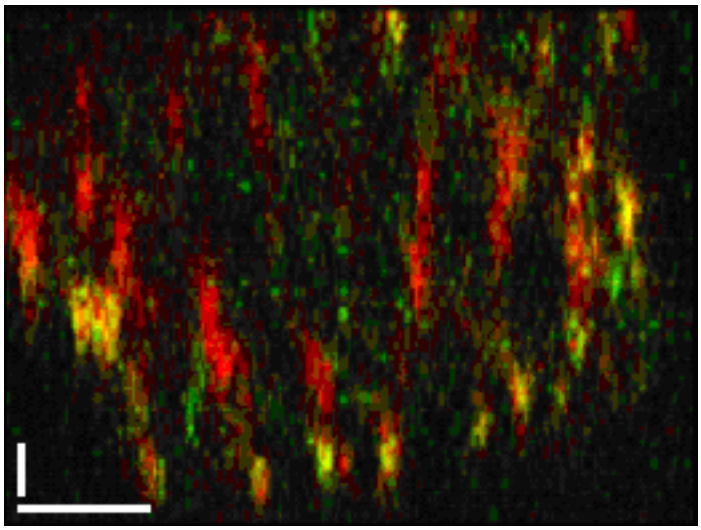

B

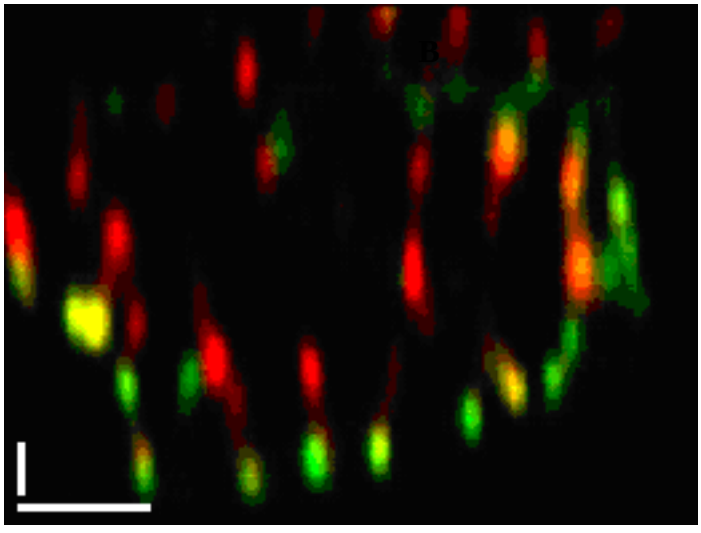

Figure 2.6 Pictorial of interacting airy discs

Pictorial representation of two 3-dimensional bead images and the corresponding airy disk patterns. Note the well separated bead centers (red and green spheres) and false colocalization events (yellow) that occur axially away from the focal plane.

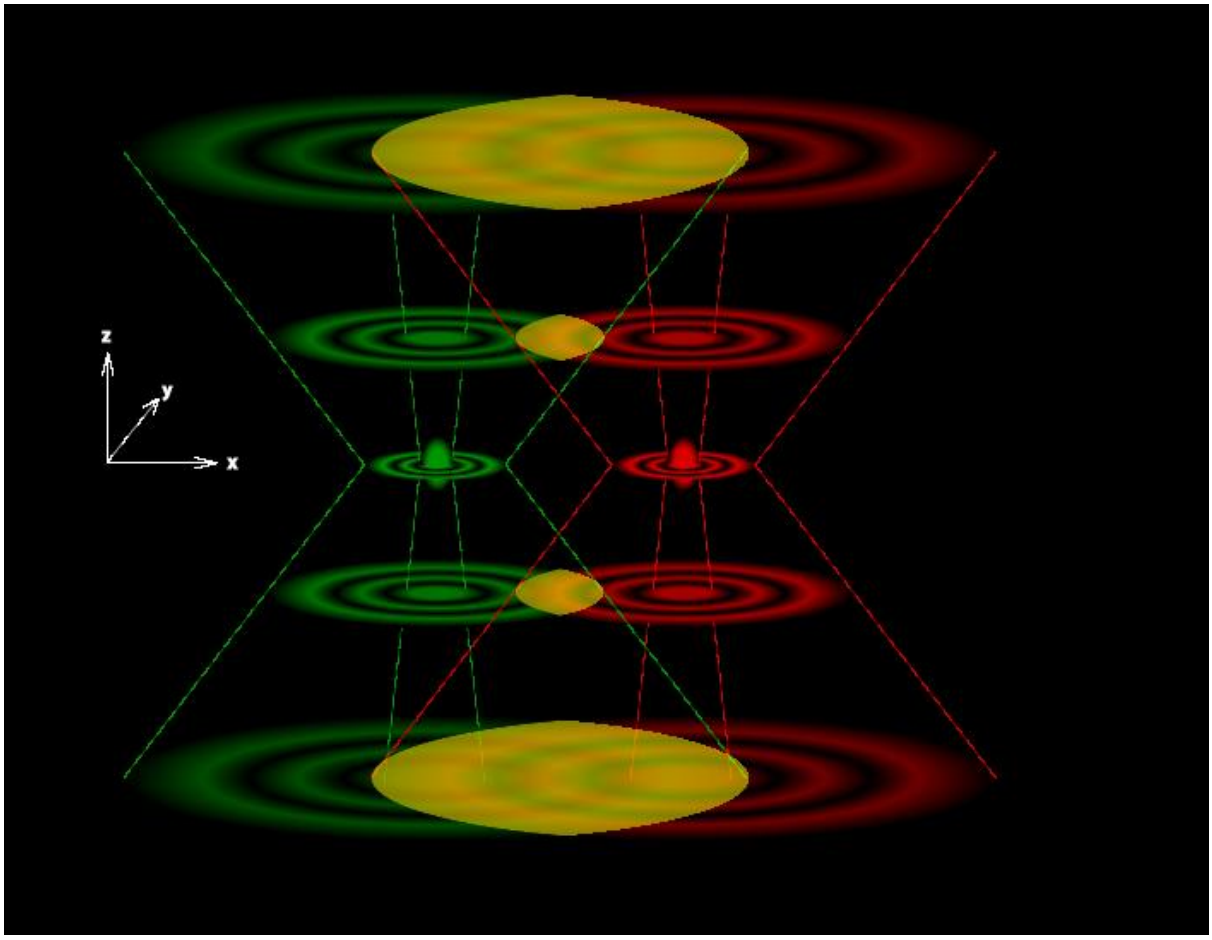

2.6. TABLES

Table 2.1 Colocalization index (CI) of DHPR and RyR

Colocalization index (CI) of DHPR and RyR before and after restoration of confocal images. The CI is calculated by the number of colocalized voxels divided by the total number of DHPR voxels and expressed as a percentage. All CI values are means ± S.E.M. The effect of restoration on CI is the CI after deconvolution divided by the CI in the confocal image prior to deconvolution expressed as a percentage.

Age (days)	CI of DHPR with RyR		Effect of restoration on CI
	Confocal	Deconvolution	
3	62 ± 2	44 ± 3	70.9
6	76 ± 1	52 ± 3	68.4
10	75 ± 1	55 ± 2	73.3
20	79 ± 1	63 ± 2	79.7

2.7. REFERENCES

1. Fabiato A. Appraisal of the physiological relevance of two hypothesis for the mechanism of calcium release from the mammalian cardiac sarcoplasmic reticulum: calcium-induced release versus charge-coupled release. *Mol Cell Biochem.* 1989;89(2):135-140.

2. Fabiato A. Calcium-induced release of calcium from the cardiac sarcoplasmic reticulum. *Am J Physiol.* 1983;245(1):C1-14.

3. Fozzard HA. Excitation-contraction coupling in the heart. *Adv Exp Med Biol.* 1991;308:135-142.

4. Nabauer M, Callewaert G, Cleemann L, Morad M. Regulation of calcium release is gated by calcium current, not gating charge, in cardiac myocytes. *Science.* 1989;244(4906):800-803.

5. Cleemann L, Morad M. Role of Ca^{2+} channel in cardiac excitation-contraction coupling in the rat: evidence from Ca^{2+} transients and contraction. *J Physiol (Lond).* 1991;432:283-312.

6. Rardon DP, D.C. Cefali, R.D. Mitchell. High molecular weight proteins purified from cardiac junctional sarcoplasmic reticulum vesicles are ryanodine-sensitive calcium channels. *Circ. Res.* 1989;64:779-789.

7. Inui M, Saito A, Fleischer S. Isolation of the ryanodine receptor from cardiac sarcoplasmic reticulum and identity with the feet structures. *Journal of Biological Chemistry.* 1987;262(32):15637-15642.

8. Brandt N, Bassett A. Separation of dihydropyridine binding sites from cardiac junctional sarcoplasmic reticulum. *Archives of Biochemistry & Biophysics.* 1986;244(2):872-875.

9. Fabiato A, Fabiato F. Calcium-induced release of calcium from the sarcoplasmic reticulum of skinned cells from adult human, dog, cat, rabbit, rat, and frog hearts and from fetal and new-born rat ventricles. *Annals of the New York Academy of Sciences.* 1978;307:491-522.

10. Maylie JG. Excitation-contraction coupling in neonatal and adult myocardium of cat. *American Journal of Physiology.* 1982;242(5):H834-843.

11. Nakanishi T, Jarmakani JM. Developmental changes in myocardial mechanical function and subcellular organelles. *American Journal of Physiology.* 1984;246(4 Pt 2):H615-625.

12. Shaw P. Deconvolution in 3-D optical microscopy. *Histochem J.* 1994;26(9):687-694.

13. Carrington WA, Lynch RM, Moore ED, Isenberg G, Fogarty KE, Fay FS. Superresolution three-dimensional images of fluorescence in cells with minimal light exposure. *Science.* 1995;268(5216):1483-1487.

14. Van Kempen GMP, Van der Voort HTM, Bauman JGJ, Strasters KC. Comparing maximum likelihood estimation and constrained Tikhonov-Miller restoration. *IEEE Engineering in Medicine and Biology.* 1996:76-83.

15. Richardson BH. Bayesian-based iterative method of restoration. *Journal of the Optical Society of America.* 1972;62:55-59.

16. Lucy LB. An iterative technique for the rectification of observed distributions. *Astronomical Journal.* 1974;74:745-754.

17. Shepp LA, Vardi Y. Maximum-liklihood reconstruction for emission tomography. *IEEE Transactions on Medical Imaging.* 1982;1:113-121.

18. Van Der Voort HTM, Strasters KC. Restoration of confocal images for quantitative image analysis. *Journal of Microscopy.* 1995;178:165-181.

19. Scriven DR, Dan P, Moore ED. Distribution of proteins implicated in excitation-contraction coupling in rat ventricular myocytes. *Biophys J.* 2000;79(5):2682-2691.

20. Sedarat F, Xu L, Moore ED, Tibbits GF. Colocalization of dihydropyridine and ryanodine receptors in neonate rabbit heart using confocal microscopy. *Am J Physiol Heart Circ Physiol.* 2000;279(1):H202-209.

21. Landmann L. Deconvolution improves colocalization analysis of multiple fluorochromes in 3D confocal data sets more than filtering techniques. *J Microsc.* 2002;208(Pt 2):134-147.

3. THREE DIMENSIONAL DISTRIBUTION OF CARDIAC NA^+- CA^{2+} EXCHANGER AND RYANODINE RECEPTOR DURING DEVELOPMENT[2]

3.1. INTRODUCTION

In adult mammalian ventricular myocytes, excitation-contraction (E-C) coupling occurs primarily through Ca^{2+}-induced-Ca^{2+} release (CICR) [1], which is initiated by membrane depolarization, causing a Ca^{2+} influx via the opening of dihydropyridine receptors (DHPR; or L-type Ca^{2+} channels). This influx in turn acts as a trigger to activate a greater and graded release of Ca^{2+} from the sarcoplasmic reticulum (SR) via the ryanodine receptors (RyR), resulting in a rapid rise in free cytosolic Ca^{2+} concentration and contraction.

The functional coupling of DHPR and RyR hinges upon a close spatial relationship. At the dyad, DHPR in the T-tubular membrane and RyR in the junctional sarcoplasmic reticulum (SR) membrane are directly apposed, separated only by a diffusion-limited space of <20 nm [2]. Their juxtaposition ensures that when DHPR open, RyR in the immediate vicinity sense a substantially large and rapid rise in free local Ca^{2+} concentration, critical to RyR activation [3]. This organization permits SR Ca^{2+} release at each junction to be tightly regulated by only local DHPR, underpinning the local control theory of cardiac E-C coupling.

Mechanisms of E-C coupling in neonatal hearts are still not clearly defined. At early stages, the myocardium undergoes rapid growth, accompanied by morphological changes that markedly impact contractile function; T-tubules are either absent or poorly developed. Neonatal myocytes appear to have a different mechanism of E-C coupling than that in the adult. Unlike adults, Ca^{2+} influx via DHPR and DHPR-mediated CICR contributes little to E-C coupling.

---

[2] A version of this chapter has been published. Dan P, Lin E, Huang J, Biln P, Tibbits GF. Three-dimensional distribution of cardiac Na+-Ca2+ exchanger and ryanodine receptor during development. Biophys J. 2007 Oct 1;93(7):2504-18.

DHPR blockers have negligible effects on both Ca^{2+} transients [4] and muscle contractions [5] in newborn ventricular myocytes. However, DHPR blockers applied to adult cells results in cessation of Ca^{2+} transients.

Investigations into the role of SR Ca^{2+} release on neonatal E-C coupling have yielded conflicting results. Some indicate SR blockers to decrease neither the activator Ca^{2+} transient nor the contractile force in newborn ventricles [6-8], while others demonstrate these responses to be significantly diminished upon SR blockade [9, 10]. Recent work shows the neonatal ventricular SR to have at least the same capability as that of adults in both storing and releasing Ca^{2+} [4, 6, 11] when normalized per unit cell volume. Furthermore, RyR from both newborn and mature cardiomyocytes exhibit similar gating, permeation and ligand binding properties [6] in planar lipid bilayers.

In studies of neonatal E-C coupling, there is a general consensus that reverse-mode Na^{+}-Ca^{2+} exchange (NCX) is the main route of entry for activator Ca^{2+} during systole [5, 12, 13]. Depolarization-induced Ca^{2+} influx via NCX could directly elicit contractions in neonatal ventricular myocytes [5, 12]. Consistent with this observation NCX mRNA, protein expression, and current density are maximal near birth, being 2.5- to 6-fold greater than those observed in mature cells, and decline postnatally to adult levels by ~3 weeks of age [13-15].

We recently reported a novel finding in the mechanism of newborn cardiac E-C coupling. Using electrophysiological and Ca^{2+} imaging techniques, we demonstrated in neonatal rabbit ventricular myocytes that reverse-mode NCX was functionally coupled to RyR to initiate CICR, the efficacy of which attenuated with development [16]. We hypothesized, therefore, that NCX colocalizes with RyR in the neonatal heart and that this colocalization declines with ontogeny. To test this, we used immunofluorescence, confocal microscopy, deconvolution, and digital image analysis to measure the regional distribution and colocalization of NCX and RyR in developing rabbit ventricular myocytes.

3.2. MATERIAL AND METHODS

All chemicals used were obtained from Sigma unless otherwise stated. Animal handling was done in compliance with the guidelines of the Canadian Council on Animal Care.

3.2.1. CELL ISOLATION AND PREPARATION

Ventricular myocytes were isolated from the hearts of New Zealand White rabbits (of either sex) from 5 age groups [3 (3d; N=15 cells), 6 (6d: N=10 cells), 10 (10d; N=25 cells), 20 (20d; N=22 cells), and 56 (56d; N=14 cells) days postpartum; 4 animals per group] using an age-specific collagenase-based digestion technique described previously [4]. Freshly isolated myocytes were fixed in 2% paraformaldehyde (10 minutes (min)), quenched by 100 mM glycine (10 min), permeabilized with 0.1% Triton X-100 (10 min), and washed 3 × 10 min in PBS. Fixed cells were adhered to poly-L-lysine coated coverslips and subsequently labelled.

3.2.2. IMMUNOCYTOCHEMISTRY

Fixed cells were incubated with primary antibodies raised against the cardiac NCX1 (0.23 μg/ml; mouse anti-NCX1 (C2C12); IgM; Affinity Bioreagent, Golden, CO) and RyR2 (5 μg/ml; mouse anti-RyR2 (C3-33); IgG_1; Affinity Bioreagent) overnight at 4^oC. The specificity of both antibodies in cardiac ventricular myocytes has been extensively described [7, 17-20]. After incubation, cells were washed for 3 × 10 min, and incubated in fluorophore-conjugated, secondary antibodies (4 μg/ml; Alexa Fluor 488 goat anti-mouse IgG_1 and Alexa Fluor 555 goat anti-mouse IgM) for 1 hour at room temperature. Then cells were washed for 3 × 10 min and mounted onto coverslips with Molecular Probes Slow Fade Gold anti-fade reagent (Invitrogen Canada, Burlington, ON). Coverslips were fixed onto the slide with nail polish.

Two sets of control experiments were performed. First, cells were labelled with an irrelevant, isotype-specific (IgG_1 or IgM), primary antibody and its corresponding secondary antibody. Second, cells that had been labelled with the primary monoclonal IgM directed against NCX were incubated with an anti-mouse IgG_1 secondary antibody; cells that had been labelled

with the primary monoclonal IgG_1 directed against RyR were incubated with an anti-mouse IgM secondary antibody. Images of these control experiments showed only dim, diffuse, non-specific staining.

3.2.3. IMAGE ACQUISITION AND DECONVOLUTION

Images of labelled cells were acquired with a Zeiss LSM 5 Pascal laser scanning confocal microscope equipped with a Zeiss 63X/1.4 Plan-Apochromat oil immersion objective. The acquisition software was LSM5 Pascal version 2.8 SP1. The 543 nm and 488 nm excitation beams were supplied by Helium-Neon and Argon lasers (Zeiss LSM5 Pascal laser module), respectively. A series of two dimensional images were acquired through the depth of the cell, using a voxel dimension of 100 nm by 100 nm by 200 nm (axial). A typical image stack contained 40-80 images. Emission was captured sequentially to minimize signal bleed-through and the confocal pinhole was set at one Airy disk.

To increase the resolution of the data, images were deconvolved using a maximum likelihood estimation algorithm (Huygens Pro 2.4.1 Linux based software; Scientific Volume Imaging, Hilversum, Netherlands). The PSF for deconvolution was determined empirically using 100 nm diameter fluorescent beads (Invitrogen Canada; [21]). Representative images are shown in Fig 3.1 – 4.

The full-width at half-maximum intensity (FWHM) of a deconvolved image of a fluorescent bead labelled with Texas Red was 250 nm in both *x* and *y* dimensions. In the z-direction, the FWHM was 620 nm. Comparable FWHM values were obtained for fluorescein beads. Therefore, the voxel dimensions used for this study satisfied the Nyquist criterion for sampling.

3.2.4. IMAGE ANALYSIS

Colocalization in whole cell

To measure NCX and RyR colocalization in the whole cell, deconvolved images were processed using Imaris 4.0 (Bitplane Inc., Saint Paul, MN) software. Images of control cells, dual labelled with irrelevant primary antibodies and appropriate secondary antibodies were used to determine a threshold value that eliminated > 99% of the voxels in these control images[18,22,23]. This threshold was applied to images of fully labelled cells; voxels with intensities lower than the threshold were set to zero, whereas voxels containing intensities greater than the threshold remained unaltered. After thresholding, only those voxels with identical x, y, and z coordinates were considered to be colocalized.

Cell layering - *Cell outline estimation*

Using intensity thresholds derived from the control experiments, two binary images were created for each cell, one for the NCX label and the other, the RyR label. The two binary volumes were combined to form a rough outline of the cell. To obtain a cell outline, morphological closing was used to extrapolate the cell outline between clusters of label (see Figure 3.10). A morphological closing operation (dilation followed by erosion) was applied to each 2-dimensional (2D) X-Y slice using a circular kernel with a radius similar to the cell's radius. A morphological dilation operation grows or expands each element of the image proportional to the size and shape of the kernel. Visually, dilation returns a larger version of the input image. Because we used a circular kernel, the resultant image grows in all directions equally. In effect, dilation fills in gaps between objects as well as the gaps within objects. Because this dilation makes the image bigger, the resultant outline is much larger than the rough outline. Therefore, in order to obtain an appropriate cell outline, the image must be eroded or shrunk with morphological erosion. The erosion function trims the edges of the previously dilated image and effectively makes the outline smaller. Because the dilation kernel is the same as the erosion kernel, the combination of these two operations returns an outline that encompasses the original rough outline. The multiple closed 2D slices are then combined to form a binary 3D cell outline.

There exists the possibility that the closing operation on a given x-y slice may leave small areas undefined, essentially leaving holes in the cell outline. These holes are filled by applying morphological closing across the cell's cross-section, in 2D, with a radius of 10-15 pixels. This second application of morphological closing refines the description of the cell outline. We calculated the number of voxels contained in the cell volume by calculating the sum of the cell outline (since this binary volume equals 1 wherever there is cell, the sum of the cell outline will equal the number of pixels contained in the cell volume).

Layering operations

Once the cell outline for an image volume was obtained, the images were broken down into individual peels or layers by sequentially trimming a 1 pixel thick sheet away from the cell outline. This was accomplished by repeatedly applying an erosion function on each cross-sectional image with a circular kernel (r=1). Therefore, the n^{th} peel layer was equal to the difference between the cell outline eroded n-1 times and the cell outline image eroded n times. The XYZ co-ordinates for each peel layer were then used to reference the intensity values found in original images.

Segmentation of the cell outlines into layers is illustrated by Fig. 3.5A. The outermost layer, the cell boundary, was designated as layer 1. Each successive inward layer was one voxel thick (layers not drawn to scale) and numbered in ascending order. An additional layer, denoted layer 0, was included just outside the surface to account for the uncertainty in identifying the cell boundary. The volume (in picoliter, pL) of each cell layer was determined by calculating the number of voxels contained within that layer.

After layering, the fully labelled cell was thresholded according to values obtained from control images. The number of pixels of a given label per peel layer was calculated by counting the number of pixels that contained intensity values equal to or greater than the applicable threshold value. For each cell the number of events above threshold as well as the maximum number of possible events, equivalent to the area of each peel layer, was recorded. Each cell was normalized to the total number of events in that cell.

3.2.5. INTER-CLUSTER DISTANCE ANALYSIS

The inter-cluster spacing of peripheral NCX or RyR clusters was determined by measuring the longitudinal distance between fluorescent clusters at the boundary of the myocyte. Periodicity analysis was performed on individual XY images of each cell, including all middle slices that were independent (resolvable) from the top and bottom of the cell. The analysis was performed on 18-35 central optical planes, depending on cell size, of each cell. For peripheral periodicity the entire length of the image was considered for analysis. Two regions of interest (ROI) were defined based on the cell outline, one for each side of the cell membrane, by eroding the cell outline image (XY) by 3 pixels forming a ROI that follows the curvature of the cell (Fig. 3.5B red; not drawn to scale**)**. Definitions of ROI's were done automatically by the analysis program to limit bias in the analysis.

For a given region of interest, sub-threshold pixels were set to zero, leaving behind clusters of label. These clusters of label were then reduced to a single point by calculating the center-of-fluorescence, akin to a center of mass calculation. Point-to-point separation distance in each ROI was calculated by first finding the pair of points with the longest separation distance. Distances between intermediate points were then determined starting from one of these end points. For each individual cell, separation distances were recorded and normalized to the total number of distances found for that cell. The probability of observing a particular inter-cluster spacing in each cell was calculated by "the frequency of observing a particular inter-cluster distance" divided by "the total number of inter-cluster distances recorded" in that cell.

Measurements of NCX-labelled vesicular structures or longitudinal periodicity of transverse rows of NCX or RyR labelling

NCX-labelled vesicular structures in 10d (N=70 cells from 4 animals) and 20d cells (N=56 cells from 4 animals) were manually counted under the microscope by focusing through the depth of each cell. The longitudinal periodicity of transverse rows of NCX or RyR labelling was determined using the measurement probe from Imaris 4.0 (Bitplane Inc., Saint Paul, MN) software. Sample size for each measurement is shown with data.

Fitting peripheral RyR inter-cluster distance data

Results of peripheral RyR periodicity from each of the five age groups exhibited a bimodal distribution and was well described by the sum of two Gaussian functions (Origin 7 SR1 software, OriginLab Corporation, Northampton, MA),

$$\text{Probability} = \frac{A_1}{\sqrt{2\pi}\sigma_1} e^{-\frac{1}{2}\left(\frac{x-x_1}{\sigma_1}\right)^2} + \frac{A_2}{\sqrt{2\pi}\sigma_2} e^{-\frac{1}{2}\left(\frac{x-x_2}{\sigma_2}\right)^2},$$

where A_1 and A_2 are the amplitudes, σ_1 and σ_2 are the widths of the Gaussian functions, and x_1 and x_2 are the two most probable inter-cluster distances. Quality fits were achieved for all age groups, as indicated by values of the correlation coefficient, ranging from 0.86 to 0.98.

3.2.6. STATISTICAL ANALYSIS

All data expressed in the form of percentages or proportions had undergone arcsine transformation prior to performing statistical analyses [24]. Statistical significance of results was determined by Student's *t*-test for paired samples or one-way analysis of variance (SPSS 13.0 software; SPSS Inc., Chicago, IL). Multiple comparisons were performed using the Gabriel or the Games-Howell test (SPSS). All values were expressed as mean ± SE, unless otherwise stated.

3.3. RESULTS

We measured the regional distribution and colocalization of NCX and RyR in developing ventricular myocytes. Confocal images of dual-labelled cells were acquired, deconvolved, and digitally analyzed. Since a cardiomyocyte is too long to be imaged in its full length under high magnification, we selected only the central cell region for both analysis and projection. All images are representative of each age group, although developmental variations existed within each group; some myocytes were either less or further developed than the majority within the same heart.

NCX immunolabelling

3d (neonate)

Figure 3.1A displays images of NCX distribution in a 3d myocyte dual-stained for both NCX and RyR (images of RyR labelling are shown in Fig. 3.3A). The 3D reconstruction of NCX label shows a relatively slender cell exhibiting an abundance of immunofluorescence (Fig. 3.1Aa, top). Since newborn rabbit ventricles do not have T-tubules [25], cross-sectional images confirm that the observed staining is restricted to the surface membrane (Fig. 3.1Aa, bottom). A magnified view of only the surface label illustrates NCX being organized in closely spaced, discrete clusters (Fig. 3.1Ab).

Images acquired from the cell center revealed a punctate NCX distribution (Fig. 3.1Ac). NCX clusters were arranged at periodical intervals along the cell edge; the inset provides a magnified view of this orderly spacing, observed in all 3d cells examined and occurred throughout much of the cell.

An identical series of experiments were performed on 6d myocytes; the data obtained were virtually identical to that of 3d. Therefore, the 6d data are only graphically presented and not described in the text hereinafter.

10d and 20d (adolescent)

Surface distribution of NCX in 10d and 20d cells appeared similar to the 3d distribution. At 10d, most NCX was still orderly distributed at the cell surface, but the majority of cells had a low to moderate level of labelling at the cell interior (Fig. 3.1Ba and Fig. 3.1Bb). A notable feature of this interior staining is that there were two patterns. In one, NCX label projected as short extensions from the surface membrane into the cytoplasm (Fig. 3.1Ba, bottom, single arrow). T-tubule formation in rabbit ventricles occurs postnatally at ~10 days of age [25], consistent with the pattern just described.

In the other pattern, NCX was distributed on the periphery, or the surface, of small vesicular-like structures, located near the outer zone of the cytoplasm (Fig. 3.1Bb, single arrow). The majority of cells expressed these structures, ranging from ~5 to ~30 per cell. One of the structures within the cell was isolated and magnified (Fig. 3.1Bb, bottom). Some structures had no obvious connection to the surface membrane and appeared suspended in the cytoplasm; Fig. 3.1Bc, top, shows a side (*xz*) view of a structure (single arrow) having no visible link to the surface membrane (double arrows), although it is possible that the labelling of potential connections were too dim for our system to detect. Yet, other structures appeared connected to the surface sarcolemma; Fig. 3.1Bc, bottom, illustrating a side view of another structure, shows an apparent link between the edge of the structure and the cytoplasmic end of a surface membrane invagination.

At 20d, NCX distribution appeared similar to that of 10d. Surface NCX clusters were closely spaced in some, but not all, regions (Fig. 3.2Ab). Internal NCX label became more abundant and extended further into the cytoplasm (Fig. 3.2Aa bottom), single arrow; Fig. 3.2Ab, double arrows). As in 10d, myocytes from this group also expressed NCX-labelled vesicular-like structures at the outer zones of the cytoplasm (Fig. 3.2Ab, single arrow).

56d (adult)

Images of adult myocytes display a clear shift in the pattern of NCX distribution; most staining was at the cell interior. However, the regular periodicity of NCX distribution on the surface remained consistent with younger age groups. A magnified view of only the surface label (Fig. 3.2Bc) from the 3D reconstruction (Fig. 3.2Ba) illustrates some clusters to be spaced further apart than those observed for 3d. Some surface labels were still closely distributed at some regions (Fig. 3.2Bb, single arrow), but larger gaps emerged (double arrows). Interior clusters mainly organized in a series of transverse rows running perpendicular to the long axis of the cell. The longitudinal spacing of these rows concentrated at ~2.1 μm (N=6 cells). Some label was also observed between the transverse rows (Fig. 3.2Bb, triple arrows). A cell cross-section reveals internal NCX labels forming tubular projections extending radially inward from the surface membrane (Fig. 3.2Ba, bottom). Of interest, there was a complete absence of NCX-labelled vesicular-like structures, seen in 10d and 20d, in these mature cells.

RyR immunolabelling

3d

Figure 3.3A displays images of the corresponding RyR staining for the 3d myocyte previously analyzed for NCX distribution. The 3D reconstruction (Fig. 3.3Aa, top) and its cross-section (bottom) illustrate RyR labels being organized in discrete clusters, distributed in both the periphery (bottom, single arrow) and the interior (double arrows) of the cell. A magnified view of only the surface label is shown in Fig. 3.3Ab. Images from the cell center revealed a highly organized RyR distribution along the cell edge (Fig. 3.3Ac). The magnified region (the inset) shows the receptor clusters closely spaced at periodic intervals, much like the 3d surface NCX.

At the interior, shown in Fig. 3.3Ac, RyR distribution did not appear as highly organized as that seen at the periphery. In some places, RyR clusters distributed in a series of short transverse rows orientated perpendicularly to the cell's long axis (single arrow). The longitudinal distance of these rows was 1.97 ± 0.01 μm (N=10 cells), which coincides with the sarcomeric spacing of myofibrils. At other regions, RyR clusters were less orderly spaced

(double arrows). The black void (marked "n") at the cell center indicates an absence of antibody staining. In immature rabbit cardiomyocytes, myofibrils are generally confined to the cell periphery [26]. A thin shell of myofibrils, only a few myofibrils deep, surrounds a central mass of nuclei and mitochondria, occupying a large fraction of the cell. This indicates that the void was not attributed to inaccessibility of anti-RyR, but represented the location of the cell nuclei and mitochondria.

10d and 20d

Unlike 3d, RyR clusters in the 10d (Fig. 3.3Ba) and 20d (Fig. 3.4Aa) cells localized mainly to the cell interior. Peripheral RyR staining became progressively sparse; some clusters were still narrowly spaced in some regions (*10d*: Fig. 3.3Bb and *20d*: Fig. 3.4Ab, single arrow), but in other places, larger gaps emerged (double arrows).

Interior RyR clusters assumed a more orderly distribution than the 3d, arranged in a series of short transverse rows orientated perpendicularly to the cell's long axis (10d: Fig. 3.3Bb; 20d: Fig. 3.4Ab). The longitudinal periodicity of these rows were 2.02 ± 0.02 μm (N = 8 cells) for 10d and 2.04 ± 0.01 μm (N = 8 cells) for 20d.

56d

In mature myocytes (Fig. 3.4Ba), the vast majority of RyR appeared to be in the interior; those located at the periphery had assumed a different distribution. Only a small fraction of the peripheral clusters remained closely spaced (Fig. 3.4Bc, single arrow); the majority of them exhibited relatively longer inter-cluster distances (double arrows). Interior RyR label became highly organized, distributed in a series of transverse rows periodically spaced at 2.04 ± 0.01 μm (N=8 cells), in agreement with previous findings [18, 19, 27].

Measurements of NCX distribution

NCX fraction - surface vs. interior

With development, the bulk of NCX label re-distributed from the cell surface to the cell interior. To quantify this spatial transition, we mathematically divided each labelled cell into two cellular compartments – the surface and the interior. To achieve this, we digitally segmented each cell into cylindrical layers across its diameter, as shown in the NCX-labelled (red) 3d cell in Fig. 3.5A (see Materials and Methods under "Cell layering"). The outermost layer of the surface label was layer 1; each successive inward layer was 1 voxel thick and numbered in ascending order. An additional layer was added just outside of layer 1 to account for the uncertainty in finding the surface.

A plot of the NCX fraction at each cell layer for all groups is shown in Fig. 3.6A. In 3d cells, virtually all (94.2% ± 0.7%) of the NCX voxels resided within layers 1, 2, and 3. The lack of T-tubules in neonatal cells indicates these three layers collectively approximate the cell surface. Based on this, cells from all groups were additionally divided into two compartments, the surface (layers 1, 2, and 3) and the interior (remaining internal layers). The fraction of NCX located in each compartment is display in Fig. 3.6C, showing that 3d cells expressed the highest surface proportion. With growth, the surface fraction declined steadily while the interior fraction gradually increased. The surface fractions for the 6d, 10d, 20d and 56d were 92.5% ± 0.9%, 84% ± 1.0%, 77.0% ± 1.1%, and 32.8% ± 0.7%, respectively. In Fig. 3.6A, the 56d curve shows a progressively drop in percent for the innermost cell layers. This drop reflects the progressive decrease in the layers' diameter while transitioning into the cell center.

Surface NCX inter-cluster distance

Our images show that NCX clusters at the cell surface were distributed in an orderly fashion in the neonate, but became increasing irregular with age. To mathematically capture this change, we measured the longitudinal distance between each pair of clusters along the cell boundary, which was delineated by a 3-pixel thick band (red, Fig. 3.5B; see Materials and

Methods). Our calculation indicated at 3d, the most commonly observed inter-cluster spacing of surface NCX label occurred at ~0.7 μm (Fig. 3.7A, single arrow). Further development to 6d, 10d and 20d did not change the length of this dominant spacing. At maturity (56d), the inter-cluster distance was still most commonly registered at ~0.7 μm, but the probability of observing this spacing decreased significantly from younger groups ($p < 0.05$). Longer intervals were commonly seen; a second, smaller peak emerged at ~1.9 μm (Fig. 3.7A, double arrows).

Measurements of RyR distribution

RyR fraction - surface vs. interior

RyR distribution was prominent both in the cell periphery and the cell interior in the neonate, but by adulthood, most localized to the latter compartment. To quantify this age-dependent transition, the cell was divided into the same surface and interior volumes as previously described for the corresponding NCX label. Figs. 3.6B and D indicate the majority (60.7% ± 1.3%) of RyR at 3d was localized to the surface. We assume the peripheral receptors resided at the peripheral SR, but our optical system could not resolve the distance between the surface and the peripheral SR membranes; hence, receptors at the periphery were captured in the surface layers. Surface fractions for 6d, 10d, 20d and 56d declined progressively with age; their values were 56.7% ± 2.3%, 38.2% ± 1.4%, 26.5% ± 1.2%, and 9.0% ± 1.8%, respectively. In Fig. 3.6B, the progressive decline in percent for the innermost layers, shown in all groups, signifies a progressive decrease in the diameter of the inner layers.

Peripheral RyR inter-cluster distance

At 3d, RyR clusters near the cell surface were distributed at orderly, periodic intervals. With development, the interval between clusters appeared to lengthen. We measured the age-dependent change in peripheral RyR periodicity, applying the same method used for calculating the corresponding surface NCX inter-cluster distances.

Figure 3.7B shows the RyR periodicity data in all groups to exhibit a bimodal distribution, which was well described by the sum of two Gaussian functions (see Materials and Methods). The Gaussian fits indicate the most probable inter-cluster spacing for 3d cells occurred at 0.72 ± 0.01 μm (left peak; Figs. 3.7B and C), almost identical to the corresponding NCX value. A second, smaller, peak probability occurred at 1.36 ± 0.07 μm (right peak, Figs. 3.7B and C). With development, the left peak remained concentrated at ~0.69 to ~0.81 μm, but the probability of recording these narrow spacings in a given cell dropped considerably with age. In contrast, the probability of observing the right peak increased with growth, along with a gradual increase in the length of spacing. By 20d, both the left (0.73 ± 0.12 μm) and right (1.75 ± 0.04 μm) peaks had almost equal probabilities. At adulthood, the left peak (0.81 ± 0.08 μm) diminished considerably while the right peak became dominant (2.02 ± 0.03 μm).

Colocalization

Whole cell and compartmental colocalization

In Fig. 3.8, top, the merged 3D reconstruction of NCX (red) and RyR (green) label in the 3d myocyte shows a considerable number of colocalized voxels (white) dispersed throughout the cell length. Colocalization analysis in the whole cell indicated 14.2% ± 0.7% of the voxels containing NCX also contained RyR (Fig. 3.9A). Almost all of the colocalization (91.9% ± 1.0%, Fig. 3.6E) occurred at the surface, further confirmed by a cell cross-section (Fig. 3.8, bottom). We also measured colocalization in each cellular compartment; 13.0% ± 0.5% at the surface and only 1.0% ± 0.1% at the interior (Fig. 3.9A).

At 10d and 20d (Fig. 3.9A), colocalization in the whole cell declined significantly to 8.2% ± 0.4% and 8.0% ± 0.5%, respectively. Colocalization was no longer restricted to the surface, but was also at the interior (Fig. 3.6E). The compartmental breakdown of colocalization further confirmed this transition. At 56d, colocalization in the whole cell was 10.0% ± 0.6% (Fig. 3.9A), significantly lower than that observed in 3d; the vast majority (91.4% ± 0.8%; Fig. 3.6E) of colocalized voxels resided within the interior.

Colocalized voxel density

Although NCX and RyR colocalization in the whole cell decreased significantly from 3d to 56d, the percentage difference was small, giving an impression that their spatial relationship underwent little change with growth. Two crucial points that a colocalization percentage fails to convey in this study are the drastic developmental changes occurring in both cell size and NCX protein expression. The sarcolemmal area of neonatal rabbit ventricular myocytes is ~4.6-fold smaller than that of adults [28]. Despite having a smaller surface, newborn NCX protein expression is ~2.5-fold greater than concentrations measured in adults [14]. Given these age-dependent changes, having comparable colocalization percentages between newborns and adults does not necessarily translate into a similar distribution. Quite the contrary, the density of colocalized voxels (number of colocalized voxels per unit area cell compartment) in newborns appears to be substantially higher than that observed in adults, which could have important implications on cardiac E-C coupling.

To incorporate developmental changes (cell size and NCX expression level) into the colocalization equation, we normalized "the number of colocalized voxels in a cell" to "the sarcolemmal volume of that cell", which is the "colocalized voxel density" in a given cell. The reason we selected to normalize to the sarcolemma was because NCX distribution is largely restricted to the surface membrane and T-tubules of ventricular myocytes. However, we did not have measurements for the T-tubular volume because it was technically difficult to reliably stain for tubules, NCX and RyR in the same cell. Thus, we normalized "the number of colocalized voxels in a cell" to only the surface compartment (in pL, delineated by layers 1, 2, and 3) of that cell. This method is the most appropriate for newborn myocytes exhibiting little or no T-tubules, but in 56d cells, T-tubules constitute ~42% of the total sarcolemmal area [29], indicating that this approach would grossly overestimate the colocalized voxel density in adults.

In Fig. 3.9B, the 3d colocalized voxel density was 6,403 ± 487 colocalized voxels per pL surface compartment, which is significantly higher than other groups. Values for 6d, 10d, 20d, and 56d (in colocalized voxels per pL surface compartment) were 6000 ± 585, 3504 ± 839, 2808 ± 996, and 2085 ± 215, respectively. Despite its overestimation, the adult measurement was only

one third of the neonatal value. This large disparity was masked when colocalization was expressed in percentages.

3.4. DISCUSSION

We provide the first quantitative report of NCX and RyR distribution in developing ventricular myocytes using immunocytochemistry, confocal imaging and digital image analysis. Programs used for image analyses in this study could potentially have wide spread applications. The layering and inter-cluster distance analyses can be used in combination to quantify protein distribution at different cell regions in a variety of cell types. In addition, most of the analyses were automated to provide high throughput.

Our principal findings are: 1) NCX was largely localized to the surface sarcolemma in newborns; by adulthood, NCX also resided at the cell interior. 2) RyR was prominent both at the cell periphery and at the cell interior in neonates; at maturity, the receptors were concentrated mainly at the interior. 3) NCX and RyR distribution was highly organized in neonates and adults. 4) A relatively stable fraction (8 – 14%) of NCX colocalized with RyR in the whole cell during growth, but the colocalized voxel density in the adult was only one-third of the neonatal value.

NCX distribution

3d

The abundance of NCX label observed in the neonatal 3d cells is consistent with previous reports, which show that NCX expression is maximal near birth [13-15]. This observation also highlights the exchanger's importance in delivering contractile Ca^{2+} to neonatal myofibrils. Virtually all of the fluorescent labelling was concentrated at the cell surface, demonstrating a lack of T-tubules in the newborns, as well as the specificity of the anti-NCX used in this study.

In addition, we uncovered a novel NCX distribution in these young cells; NCX clusters at the cell surface were spaced orderly at ~0.7 μm, about one-third the length of a relaxed sarcomere [26]. This surprisingly organized pattern stands in sharp contrast with all past reports, which immunocytochemically show that NCX is apparently distributed homogeneously at the surfaces of neonatal rabbit ventricular myocytes [7, 30]. One of these studies [7] used the same anti-

NCX employed in our work; indicating the differences likely did not arise from labelling with a different antibody clone. We ascribe this discrepancy to variations in cell isolation, fixation, and labelling procedures, all of which critically impact the staining pattern. The highly ordered and specific location of the exchanger may be of importance for understanding Ca^{2+} fluxes associated with E-C coupling in the neonate, as discussed further below.

The small fraction (~ 9%) of NCX voxels detected in the interior likely arose from two sources. First, the small amount of internal staining may signify NCX molecules undergoing posttranslational modifications at the SR and Golgi, subcellular trafficking or degradation. Second, there may be errors in identifying the cell surface layers due to the nature of the plasma membrane. The sarcolemma of a cardiomyocyte has uneven edges, steps and folds [25]; all of which decreases the accuracy in identifying the cell surface. A small fraction of the steps and folds of the cell surface may be included in the subsarcolemmal interior layers.

10d, 20d and 56d

As development progresses to 10d and 20d, most NCX was still distributed at the cell surface, but the interior fraction increased significantly from the 3d value, coincident with the onset of T-tubule development. Of interest, NCX label was observed on the surface or the periphery of vesicular-like structures located at the outer zone of the cytoplasm. These structures were present only in cells undergoing T-tubule biogenesis; they were completely absent in cells without T-tubules (3d) and in cells with fully developed T-tubules (56d). Further work is required to uncover the function of these vesicular-like structures in ventricular myocytes undergoing T-tubule development.

At 56d, the majority (67.2% ± 2.7%) of NCX was located at the cell interior. The internal staining pattern closely resembled the complex morphology of a mature T-tubule network containing both transverse and axial elements [31], and is in good agreement with past immunocytochemical findings [5, 7, 18, 30, 32, 33]. The primary function of NCX in adult ventricular myocytes is Ca^{2+} extrusion. The vast majority of Ca^{2+} entering the cell via DHPR during systole is removed by the exchanger [34]. In adult rabbit ventricles, most of the dyadic junctions are concentrated in T-tubules, with relatively few dyadic sites at the surface membrane [29]. Our

measurements indicate that most NCX, responsible for Ca^{2+} extrusion, was likely localized to T-tubules where major calcium release sites reside, consistent with previous functional work [35].

RyR distribution

3d

The few studies examining RyR distribution in neonatal ventricular myocytes qualitatively show the receptors to locate mainly at the cell interior [7, 19], where they arrange in an array of rows parallel to the level of the Z-line [19]. We observed a similar interior RyR organization, based on the longitudinal spacing of short transverse rows of labelling, but additionally noted a highly organized distribution near the surface membrane. At the cell periphery where the majority (60.7% ± 1.3%) resided, RyR clusters were orderly spaced at narrow intervals of ~0.7 μm. This new finding implicates that there was a dense network of Ca^{2+} release sites at the subsarcolemma of newborn myocytes.

In both developing [36] and mature [37] ventricular myocytes, RyR molecules are largely clustered at specialized SR junctions, closely apposing either the surface membrane (forming peripheral couplings) or T-tubules (forming dyads). RyR clusters are also found in specialized SR domains that do not form junctions with the sarcolemma, known as corbular SR. These specialized junctions, including corbular SR, are functionally equivalent and are named Ca^{2+} release units (CRUs) [37]. Ultrastructural studies show that peripheral couplings are the first to occur during cardiac development, followed by the formation of corbular SR. With the development of T-tubules, the dyads appear [36].

In this study, the narrowly spaced peripheral RyR clusters were likely located at the peripheral SR, where they juxtaposed the surface membrane to form peripheral couplings. In congruence with this view, our previous ultrastructural work demonstrated that the subsarcolemmal SR in 3d rabbit ventricular myocytes appear to form sheet like structures extending along the apposing sarcolemma and were determined to be ~3 times longer than those in adult cells [38]. The RyR fraction we observed at the interior maybe localized to the corbular SR, since T-tubules had not yet been formed.

10d, 20d and 56d

With development to 10d and 20d, RyR distribution shifted progressively from the periphery to the interior. By adulthood, the vast majority (91.0% ± 0.7%) of RyR was at the interior, where they were mainly organized in transverse rows periodically spaced at ~2.0 μm, coinciding with the sarcomeric Z-line pattern of myofibrils. RyR molecules are known to locate largely in the SR membrane adjacent to the T-tubules of adult cardiac myocytes [27, 37], indicating the receptor staining was likely localized to the dyadic junctions along the Z-lines.

At the cell periphery, the most probable RyR inter-cluster distance rose gradually from ~0.7 μm at 3d, to ~2.0 μm at 56d (Fig. 3.7B and C). If the longitudinal spacing of interior clusters were used to infer the Z-line's position, then the peripheral labels, which once interspersed between Z-lines or at a peri-M-line position, of young cells were largely absent in adults. Since the predominant inter-cluster spacing in matured myocytes is comparable to the length of a relaxed sarcomere [26], some of the subsarcolemmal receptor clusters may be distributed near the mouth of T-tubules, which have been shown to have a similar longitudinal spacing of ~1.8 μm [31]. A word of caution is required for the estimate of inter-cluster distances. Two dimensional techniques are highly dependent on the corresponding alignment between the imaging plane of the microscope and the alignment of the cellular structure being investigated. This relationship, coupled with finite limitations in resolution, allows clusters above and below the analysis plane to interfere. Given the z-axis resolution (~620 nm) of the confocal microscope, applying deconvolution to all our images prior to analyses could only minimize, but not completely eliminate, the out-of-focus fluorescence emitting from adjacent planes. This out-of-focus signal could lead to a systematic underestimation of the apparent inter-cluster distances for peripheral NCX or RyR [20].

A recent study shows intense peripheral RyR staining between the Z lines of rat adult ventricular myocytes and indicates these labels are absent in over-permeabilized myocytes [20]. We, on the other hand, commonly observed peripheral RyR label between the Z lines of neonatal myocytes, but not in mature cells. Newborn cardiomyocytes are far more fragile than those of adults; yet we consistently generated clean, reproducible staining in this age group. Hence, the

paucity of peripheral RyR label in the 56d myocytes we studied could not be ascribed to cell over-permeabilization. Ventricular contractions in rats have been shown to have a greater reliance on SR Ca^{2+} release than that observed in rabbits [39]. Hence, the discrepancy may be attributed, in part, to the use of a different animal species.

Peripheral vs. interior subpopulation

Based on their regional distribution, we postulate that there are two subpopulations of RyR in rabbit ventricular myocytes; the interior and the periphery. The expression patterns of the two subgroups appear to be reciprocal with development. In neonatal cells, peripheral clusters were highly expressed and narrowly spaced; internal clusters, although abundant, are less organized. At maturity, the peripheral clusters became less closely spaced, assuming a similar inter-cluster distance as that of their interior counterparts, which were highly organized at the Z-lines. Consonant to this view, functional studies have shown that Ca^{2+} sparks, elementary events of SR Ca^{2+} release [40], occur primarily at the periphery of neonatal rabbit and rat ventricular myocytes [7, 41]. When these cells reached maturity, sparks were detected throughout the width of the cell, mainly along the Z lines at the cell interior [41]. In adult rat ventricular myocytes, Ca^{2+} sparks at the cell interior has been shown to originate specifically from the T-tubules [42].

On a cautionary note, we cannot completely rule out the possibility that NCX or RyR distribution differences observed between groups may be attributed to differences in epitope accessibility. We did, however, devote extensive effort to optimizing our fixative and labelling protocols for epitope accessibility. We tested different concentrations of fixative, triton X-100, primary antibodies, and secondary antibodies, as well as different lengths of incubation period for each reagent concentration. In our selected protocol, the fixative and permeability agents were kept to a minimal to avoid excessive cross-linking and extraction of antigens, respectively. This approach produced labelling of the highest contrast and reproducibility and concomitantly optimized epitope accessibility.

Colocalization: A potential link to E-C coupling

We observed three distinguishing features in neonatal (3d) NCX and RyR distributions that make them likely candidates for functional coupling. First, both were highly expressed at or near the cell surface. Second, their distribution at or near the cell surface was highly organized with the identical predominant inter-cluster spacing. Third, their colocalized voxel density was maximal in 3d cells. Taken together, neonatal myocytes contain the largest number of potential coupling sites per pL cell surface, all of which concentrated in one compartment, the surface membrane.

Like the 3d cells studied, adult atrial myocytes of most mammalian species do not exhibit T-tubules [27, 43], and have a network of Ca^{2+} stores both close to the sarcolemma and deep inside the cell [44]. A depolarization-induced Ca^{2+} influx via sarcolemmal DHPR triggers Ca^{2+} release only from those RyR clusters located at the peripheral SR [43, 45, 46]. Initially, discrete release sites at the periphery are activated; the signal spreads quickly to adjacent peripheral sites to form a subsarcolemmal ring of elevated cytosolic Ca^{2+}. This signal spreads inward and evokes a centripetally propagating Ca^{2+} wave, simultaneously eliciting peripheral and central myofibril contraction.

An analogous event could occur in neonatal ventricular myocytes, which express a high density of surface NCX and have a dense network of both peripheral and internal Ca^{2+} release sites. Previous work shows Ca^{2+} influx through reverse-mode NCX is sufficient to directly stimulate contraction in neonatal, but not adult, rabbit ventricular myocytes [12, 13]. This age-dependent difference was attributed to neonatal cells having a larger (~6 fold) NCX current density and a greater (~2- to 3-fold) surface area-to-volume ratio. On a similar note, our laboratory [28] and others [6] recently show that the neonatal rabbit SR has a larger (~3-fold) Ca^{2+} store (normalized per unit cell volume) than that of adult, and that neonatal and adult cardiac RyR have similar gating and kinetic properties in planar lipid bilayers.

In addition, we recently demonstrated in neonatal rabbit ventricular myocytes that calcium influx via NCX could stimulate CICR, which accounted for ~40% of the Ca^{2+} transient; the process diminished with development [16]. Imaging data presented in this study provide a

potential structural basis for this functional finding. In the neonate, Ca^{2+} influx via reverse-mode NCX during systole could trigger Ca^{2+} release from the dense population of peripheral RyR clusters and generate an inward propagating Ca^{2+} wave. Although whole cell colocalization in 3d cells was only a moderate ~14%, the narrow spacing of both NCX and RyR at the cell surface and their relatively high colocalized voxel density may be important in attaining the CICR component. The colocalized sites could represent discrete sites of Ca^{2+} signal initiation, which rapidly spreads to adjacent peripheral Ca^{2+} release sites to create a subsarcolemmal ring of elevated Ca^{2+}.

In support of this view, a recent study of adult cardiac E-C coupling, using mathematical modeling, shows peripheral RyR clusters (or CRUs) located between the Z-lines to be responsible for increasing the likelihood of Ca^{2+} wave generation in adult atrial cardiomyocytes [47]; the closer the CRUs, the higher the probability of wave initiation. This suggests that the narrow spacing (~0.7 μm) of RyR clusters at the neonatal cell periphery could be of importance in sufficiently elevating Ca^{2+} concentration at the subsarcolemma to initiate an inward propagating Ca^{2+} wave. We calculated the distance between the peripheral and the first interior rows of RyR clusters to be 1.06 ± 0.07 μm (N = 10 cells).

The remaining NCX population (~86%) that was not colocalized, or potentially coupled, with RyR in the neonate was likely responsible for only transporting Ca^{2+} inward the cell during systole, without eliciting SR Ca^{2+} release. Influx via uncoupled exchangers may mainly activate myofibrils that are located directly under the cell membrane, whereas the coupled exchangers could elicit CICR and initiate an inward propagating Ca^{2+} wave to activate interior myofibrils. In neonatal ventricular myocytes, myofibrils are mainly located at the cell periphery, which may explain why only a moderate fraction of NCX is needed to mediate CICR.

It is well established that DHPR-mediated CICR is the dominant mode of E-C coupling in the mature mammalian myocardium [1]. In adult rabbit myocytes (56d), whole cell NCX and RyR colocalization was ~10% and their colocalized voxel density was 2085 voxels per pL surface compartment; the latter was only one-third of the neonatal value, suggesting that adult cells contained the lowest number of potential coupling sites. Our colocalization percentage was slightly higher than the value reported by Scriven *et al* (2000) [18], although these authors

performed their studies in adult rat. Despite these low values, there is electron microscopy data to show that in the adult rat ventricle, some NCX gold particles are in close proximity to RyR particles, at distances comparable to those measured between RyR and DHPR particles [48]. The importance of NCX in initiating CICR in adult ventricular myocytes during systole is still debated. Some studies show the depolarization-induced Ca^{2+} influx via reverse-mode NCX could trigger SR Ca^{2+} release [49-56], whereas others measured little or no response [57-60].

Summary and Conclusions

In this study, we found NCX to be organized in a punctuate pattern at the cell surface throughout development. Our data also indicate the distribution of NCX and RyR to vary considerably with age. NCX located largely at the surface sarcolemma in newborns and re-distributed to the cell interior at adulthood. RyR was prominent at both the cell periphery and the cell interior but concentrated at the interior upon maturity. Neonatal NCX or RyR clusters located at or near the surface sarcolemma were orderly spaced at narrow intervals; two-dimensional image analysis showed the longitudinal periodicity of these clusters to be concentrated at ~0.7 μm. Because of the previously-described confounding factors, the peak periodicity value of ~0.7 μm may be underestimated. The spacing of surface NCX clusters did not vary appreciably with age, but the periodicity of peripheral RyR clusters underwent a significant change, occurring mainly at ~2.0 μm in adults. At maturity, interior NCX and RyR clusters were distributed primarily in transverse rows periodically spaced at ~2.0 μm. If the interior RyR labelling were consistent with the position of Z-lines in all groups, then the neonatal myocytes have a more prominent peri-M-line distribution in comparison to adults. Therefore, there may be a subpopulation of RyR that is prominent in the newborn heart and gradually decreases with development.

The colocalized voxel density in the neonate was ~3-fold greater than that observed in adults, suggesting the young cells expressed the highest number of potential coupling sites. Taken together, Ca^{2+} influx via NCX in the neonate could activate the dense network of peripheral SR Ca^{2+} stores via peripheral coupling, and evoke Ca^{2+}-induced Ca^{2+} release, eliciting the contraction of myofibrils located near the cell center. Ca^{2+} influx via the exchangers that were not colocalized with RyR may mainly activate subsarcolemmal myofibrils. In sum, NCX has multiple potential roles in neonatal E-C coupling: Ca^{2+} influx via the reverse mode to trigger CICR and to contribute to the Ca^{2+} transient; Ca^{2+} efflux via the forward mode to maintain low diastolic Ca^{2+} concentration.

3.5. FIGURES

Figure 3.1 NCX distribution in 3d and 10d ventricular myocytes

(A) 3d: (Aa) *Top*, 3D reconstruction of NCX distribution; *bottom*, a cross-section of top image; section thickness = 5 μm; scale bar = 5 μm. (Ab) Magnified NCX label at cell surface, scale bar = 2 μm. (Ac) Single optical section, scale bar = 5 μm; inset =magnified region of surface label. (B) 10d myocyte: (Ba) *Top*, 3D reconstruction of NCX distribution; *bottom*, a cross-section of top image, single arrows point to surface invagination, scale bar = 5 μm. (Bb) *Top*, single optical section (single arrow points to vesicular-like structures); *bottom*, a magnified view of vesicular-like structure; (Bc) *Top*, magnified side view (*yz*) of a vesicular structure with no link to sarcolemma (single arrow=structure, double arrow=surface membrane, scale bar = 2 μm); *bottom*, magnified side view (*yz*) of a structure with an apparent link to sarcolemmal invagination (single arrow=structure, double arrow=surface membrane invagination, triple arrow=surface membrane).

3d NCX

A

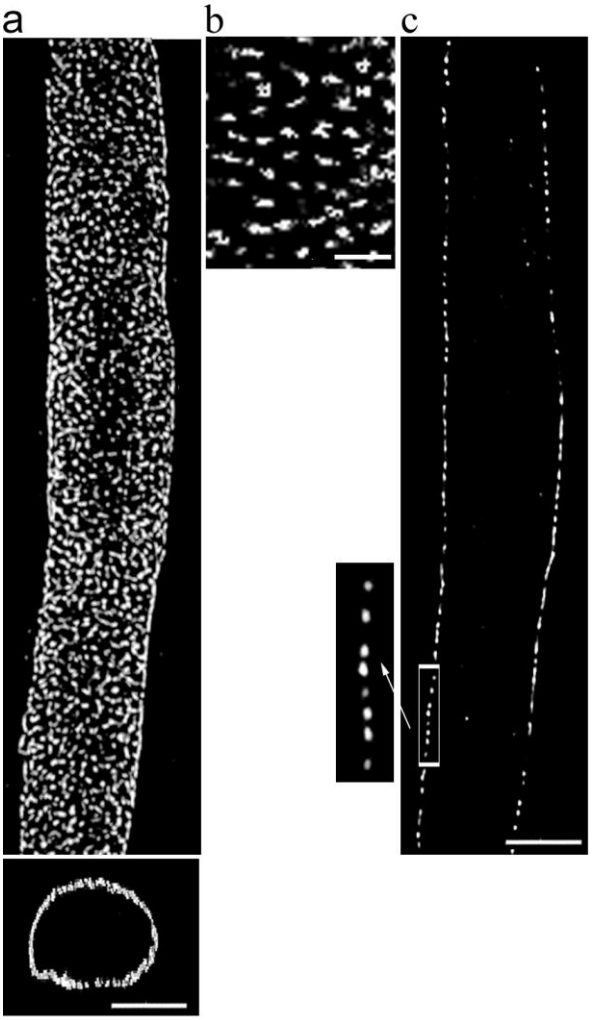

10d NCX

B

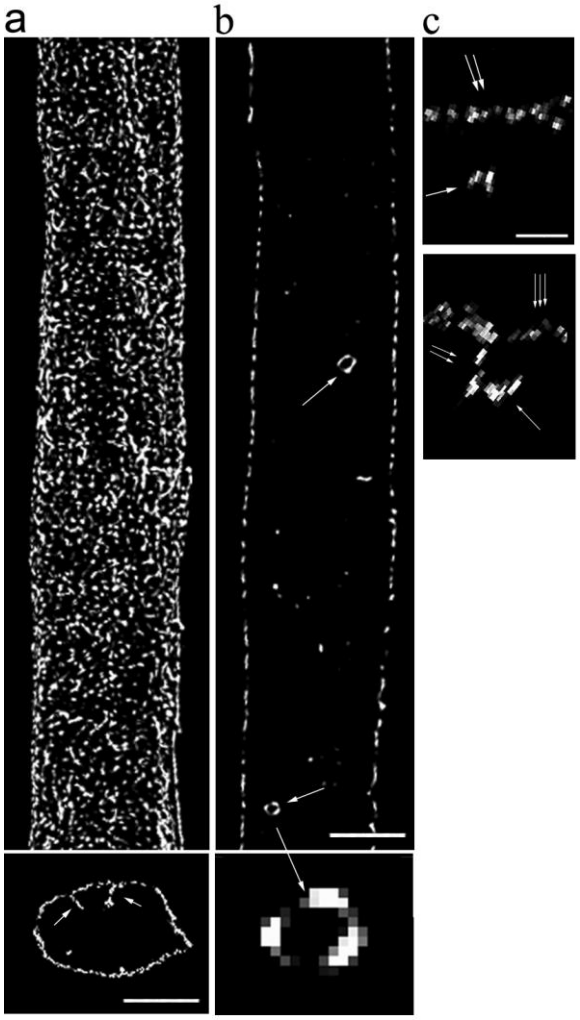

Figure 3.2 NCX distribution in 20d and 56d ventricular myocytes

(A) 20d myocyte: (Aa) *Top*, 3D reconstruction of NCX distribution; *bottom*, a cross-section of top image (single arrow points to surface membrane invaginations), scale bar = 5 μm. (Ab) Single optical section (single arrow = vesicular-like structures; double arrows = surface membrane invaginations; scale bar =5 μm). (B) 56d myocyte: (Ba) *Top*, 3D reconstruction of NCX distribution; *bottom*, a cross-section of top image, scale bar = 5 μm. (Bb) Single optical section at cell center (single arrow=closely spaced clusters; double arrows=widely spaced clusters; triple arrows=NCX label between the Z-lines, scale bar = 5 μm. (Bc) A magnified view of surface NCX label, scale bar = 2 μm.

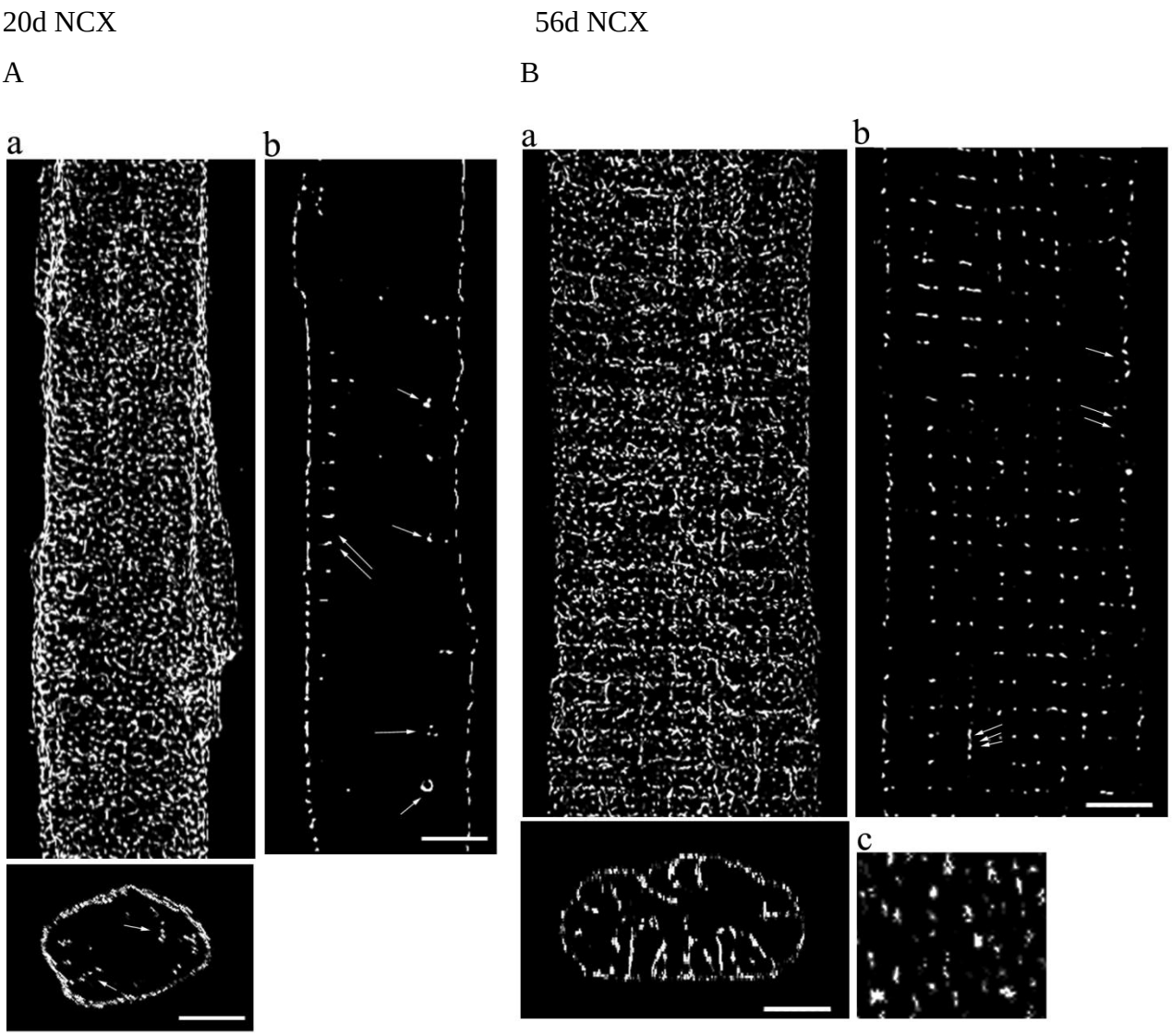

Figure 3.3 RyR distribution in 3d and 10d ventricular myocytes

(A) 3d myocyte: (Aa) *Top*, 3D reconstruction of RyR distribution; *bottom*, a cross-section of top image; single arrow=peripheral label; double arrows=internal label; scale bar = 5 μm. (Ab) Magnified RyR label at cell surface, scale bar = 2 μm. (Ac) Single optical section (single arrow=orderly spaced internal RyR; double arrows=sparsely spaced internal RyR; n=nuclear region); inset=magnified view of surface label. (B) 10d myocyte: (Ba) *Top*, 3D reconstruction of RyR distribution; *bottom*, a cross-section of top image; scale bar = 5 μm. (Bb) Single optical section at cell center (single arrow=closely spaced peripheral RyR; double arrows=widely spaced peripheral RyR; n=nuclear region; scale bar=5 μm).

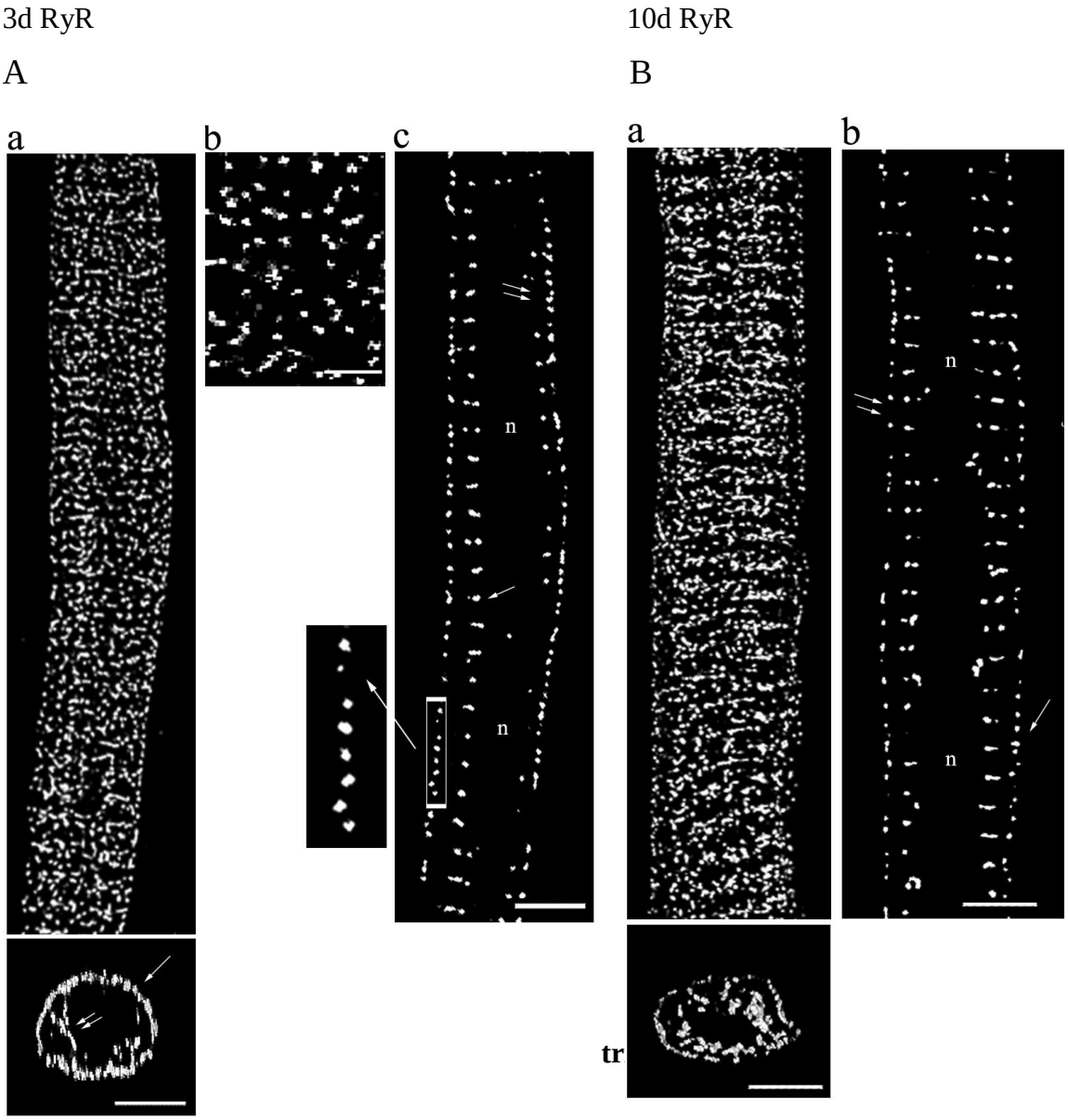

20d myocyte: (Aa) *Top*, 3D reconstruction of RyR distribution; *bottom*, a cross-section of top image, scale bar = 5 μm. (Ab) Single optical section (single arrow=label between the Z-line; double arrows=absence of label between Z-line; scale bar = 5 μm. (B) 56d myocyte: (Ba) *Top*, 3D reconstruction of RyR distribution; *bottom*, a cross-section of top image, scale bar = 5 μm; (Bb) Magnified RyR label at cell surface, scale bar = 2 μm. (Bc) Single optical section (single arrow = label between Z-line; double arrows = absence of label between Z-line, scale bar = 5 μm).

20d RyR 56d RyR

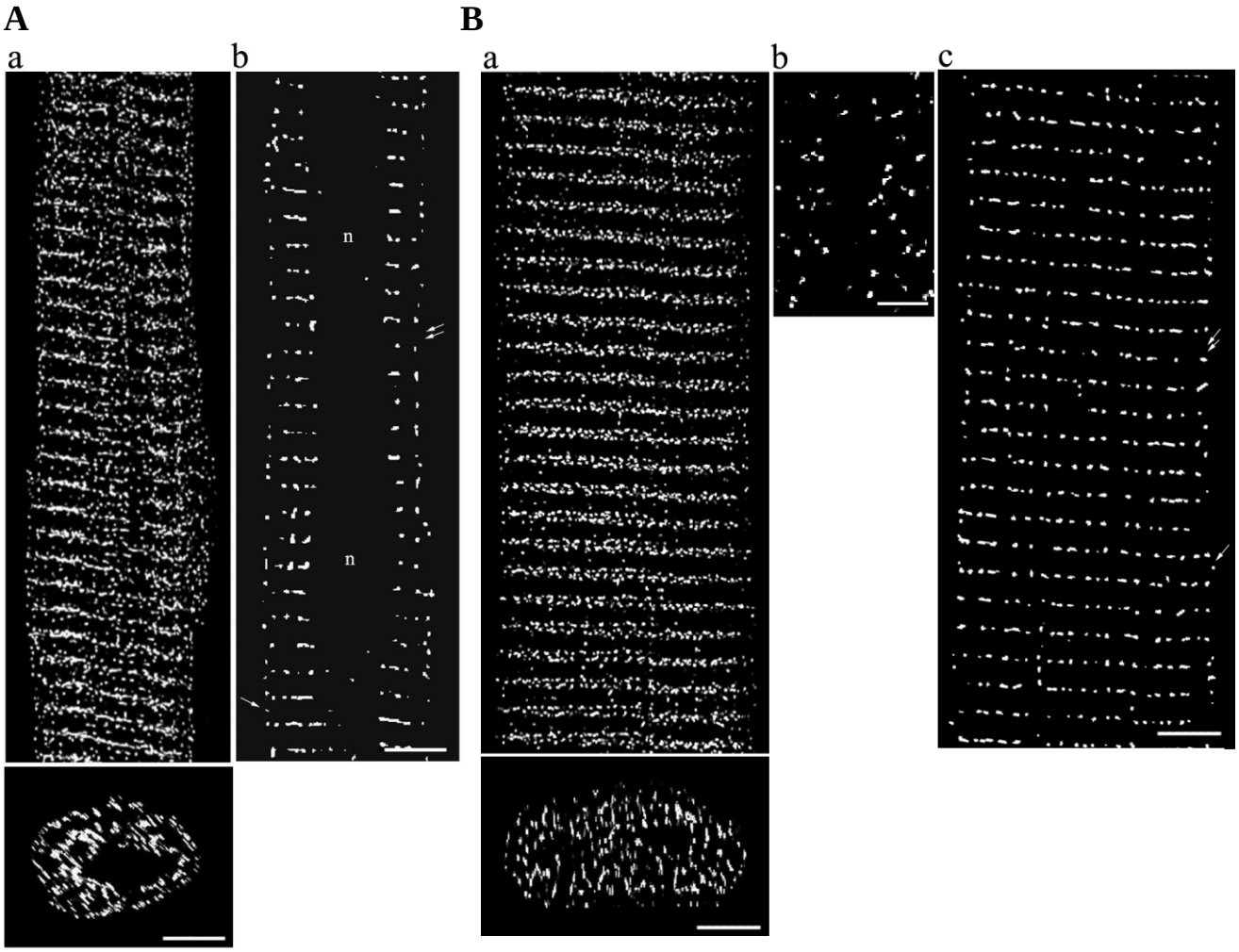

Figure 3.5 Cell layering and outline delineation

(A) Cross-section of a 3d myocyte labelled for NCX (red) divided into layers (white lines; not drawn to scale) across the cell diameter; scale bar = 5 μm. (B) Single optical plane of a 3d ventricular myocyte stained for NCX (white). A 3-pixel thick band (red; not drawn to scale) outlines the cell boundary.

A

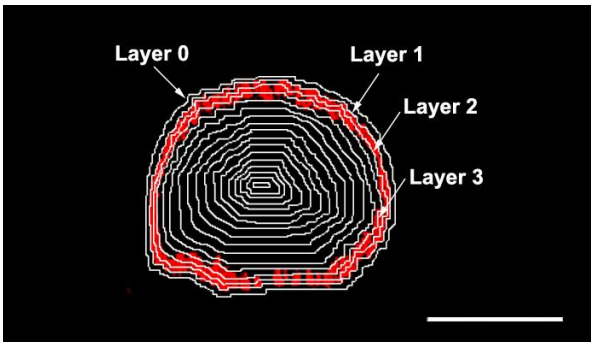

B

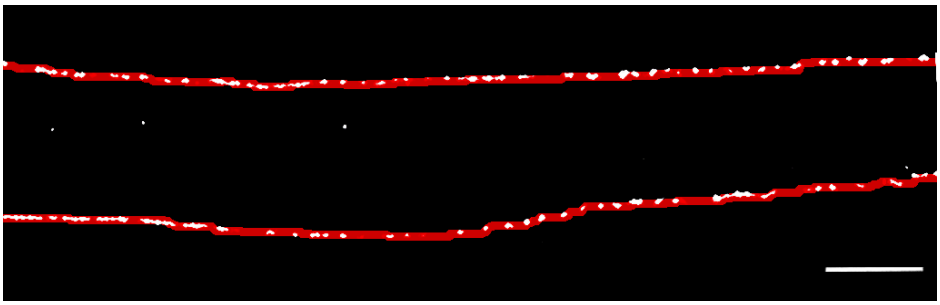

Figure 3.6 NCX or RyR fraction at different cell layers

(A) NCX fraction at different layers. (B) RyR fraction at different layers. (C) NCX, (D) RyR, or (E) Colocalized voxel, fraction at surface (layers 1, 2, and 3) vs. interior (remaining layers) compartment; (*) denotes a significant difference between surface and interior ($p < 0.05$); (#) denotes a significant difference in surface distribution between groups ($p < 0.05$), except for between 3d and 6d; (+) denotes a significant difference in interior distribution between groups ($p < 0.05$), except for between 3d and 6d.

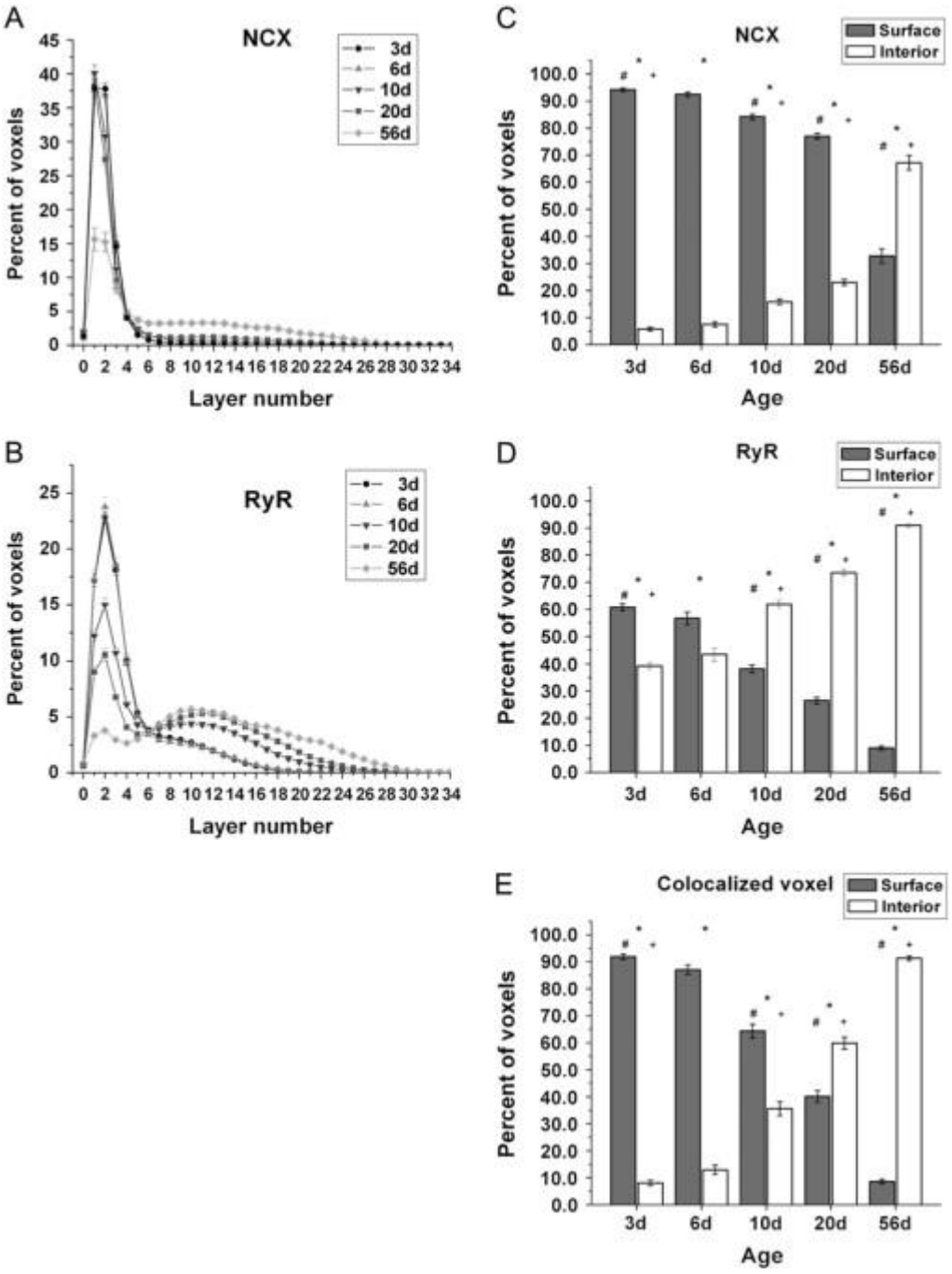
A
NCX
3d
6d
10d
20d
56d
Percent of voxels
Layer number
B
RyR
3d
6d
10d
20d
56d
Percent of voxels
Layer number
C
NCX
Surface
Interior
Percent of voxels
Age
3d
6d
10d
20d
56d
D
RyR
Surface
Interior
Percent of voxels
Age
3d
6d
10d
20d
56d
E
Colocalized voxel
Surface
Interior
Percent of voxels
Age
3d
6d
10d
20d
56d

Figure 3.7 Inter-cluster distance of surface NCX or peripheral RyR

(A) Probability distribution of NCX inter-cluster distances. Y-axis denotes the probability of a particular inter-cluster spacing occurring within a cell; (*) denotes a significant difference between the 56d and the younger groups, ($p < 0.05$). (B) Probability distribution of RyR inter-cluster distances well described by the sum of two Gaussian functions. The fits show each age group has two peak probabilities, denoted as left or right peak. (C) Peripheral RyR inter-cluster distance corresponded to the left or the right peak probability shown in (B).

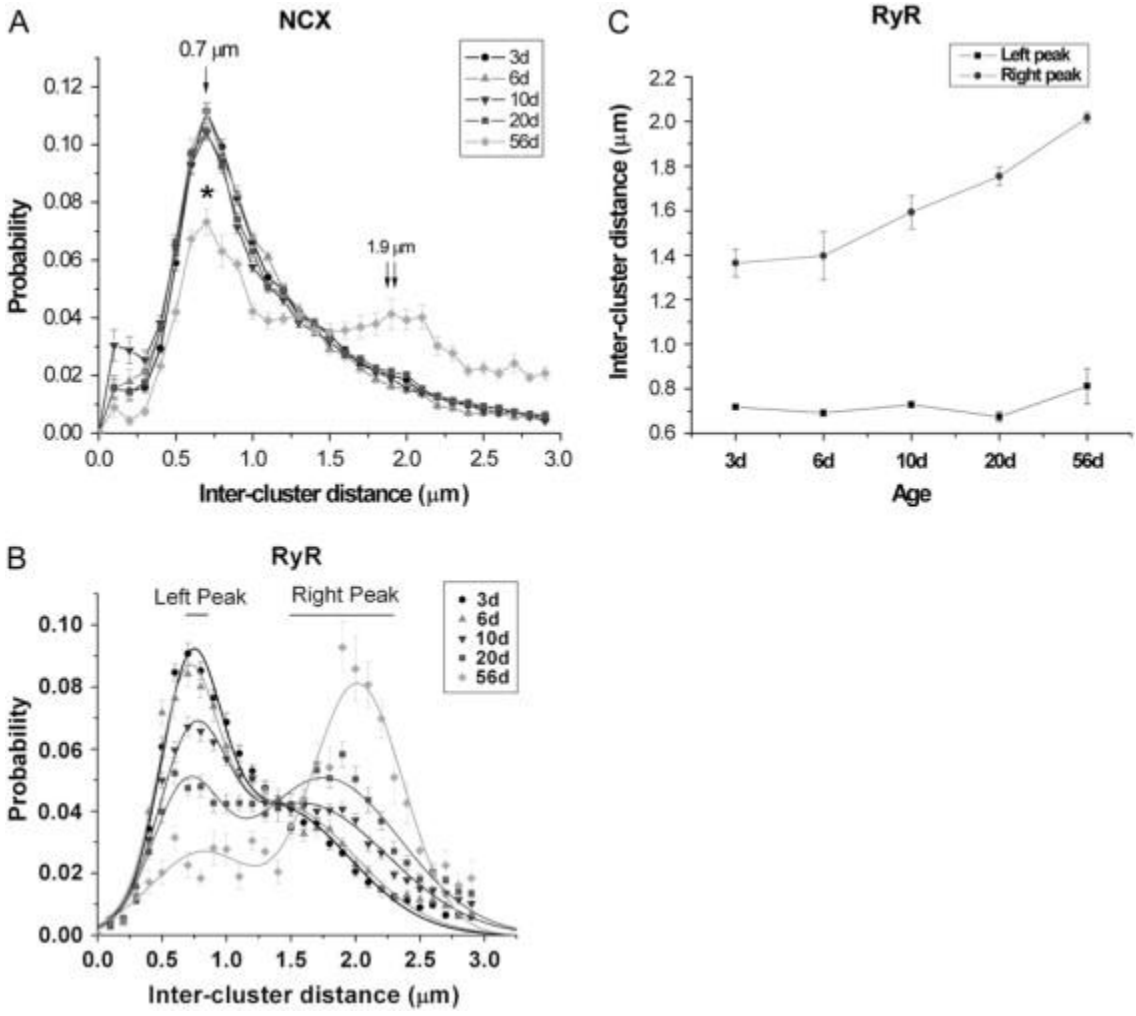

Figure 3.8 NCX and RyR images as a function of development

Merged images of NCX (red) and RyR (green) label previously shown; colocalized voxels are white; scale bar=5 μm.

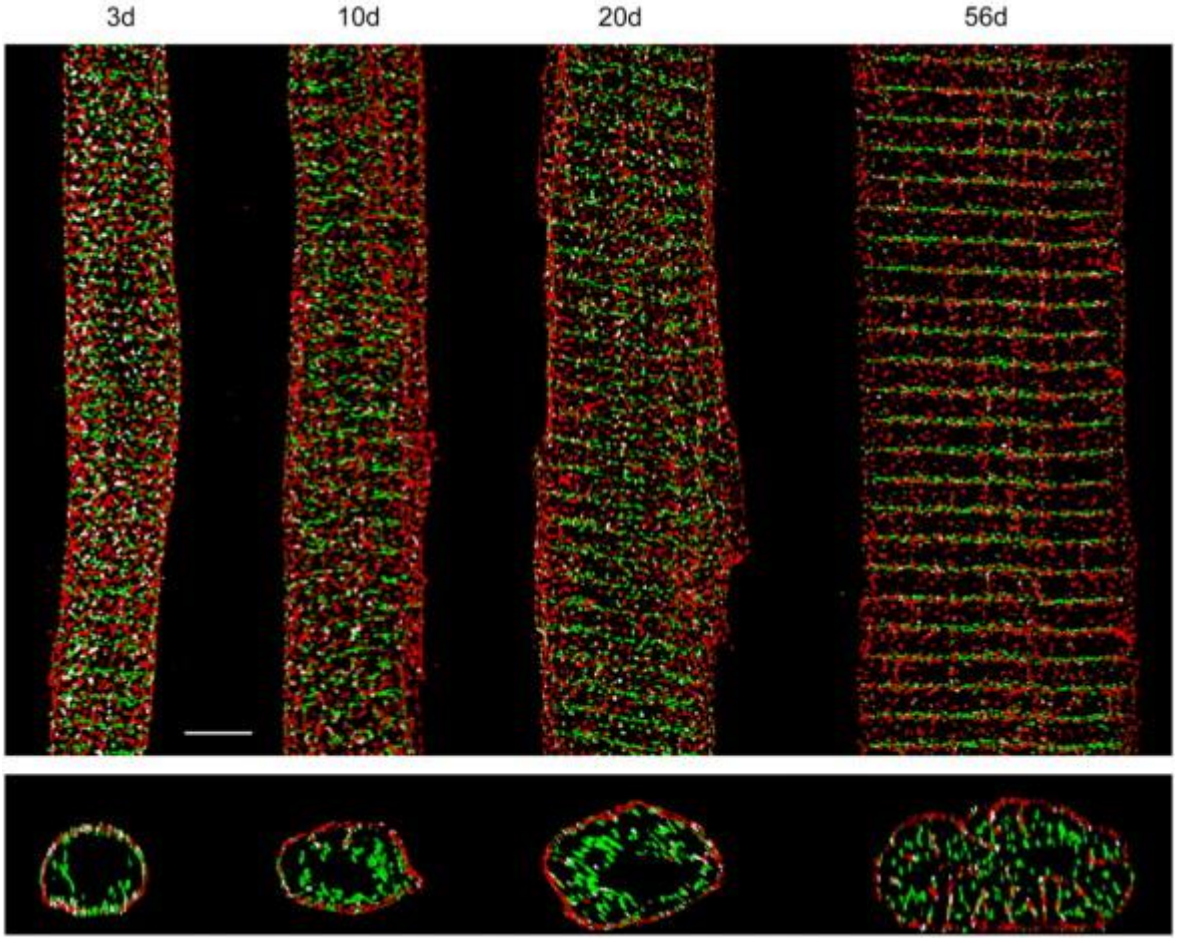

Figure 3.9 NCX and RyR colocalization

Whole cell NCX and RyR colocalization vs. colocalized voxel density in developing and matured ventricular myocytes.(A) Colocalization in whole cell; # denotes a significant difference between 3d vs. 10d, 20d, and 56d ($p < 0.05$); * denotes a significant difference between groups; + denotes a significant difference between groups ($p < 0.05$). (B) Colocalized voxel density (number of colocalized voxels per pL surface compartment); * denotes a significant difference between 3d vs. 10d, 20d, and 56d ($p < 0.05$).

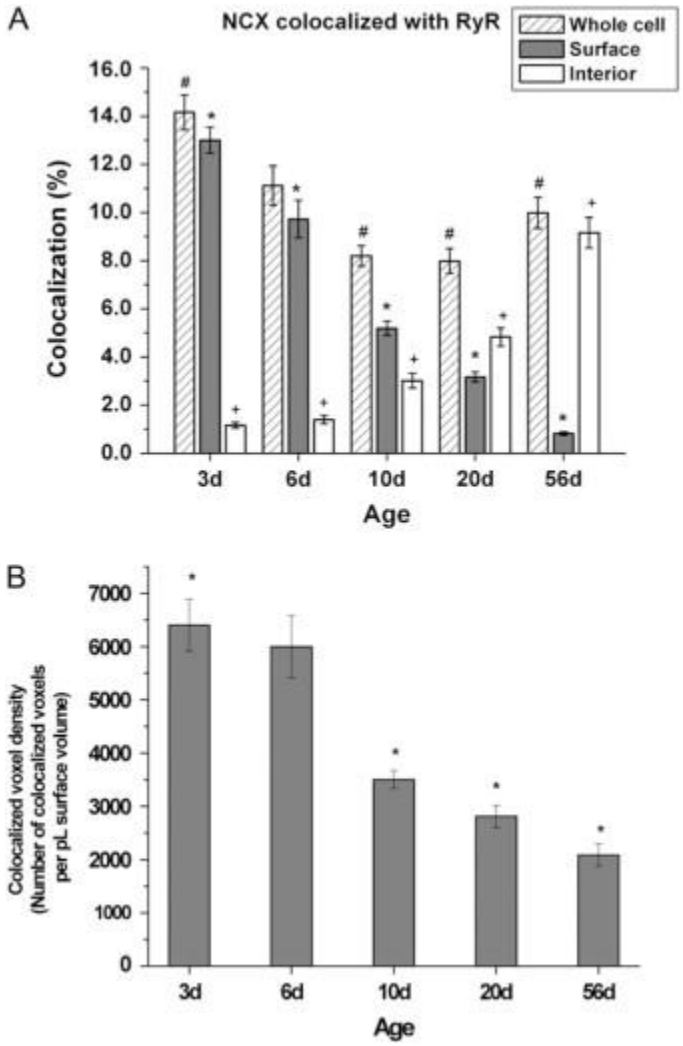

Figure 3.10 Cell outline extraction

A completed cell outline for a single X-Y image. For clarity, the cell area has been marked in black and the non-cell area marked in light grey. Red and green pixels represent NCX and RyR labelling respectively. **Middle:** A simplified schematic representation of the top figure. Gray circles show the result of a dilation operation with a kernel with radius R on some of the points. Outward arrows illustrate the growing and merging effect of dilation. Each point expands by R. **Bottom:** The completed dilation operation shown in gray. Inward arrows illustrate the trimming effect of morphological erosion. Erosion of the dilated image produces the cell outline as per the top figure.

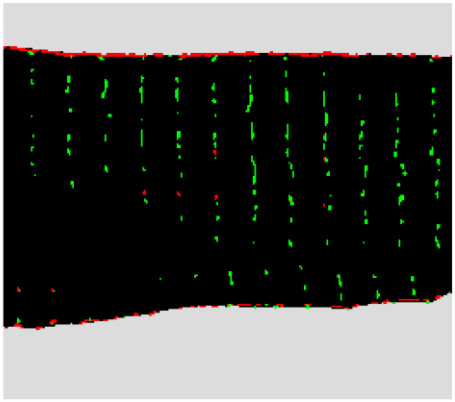

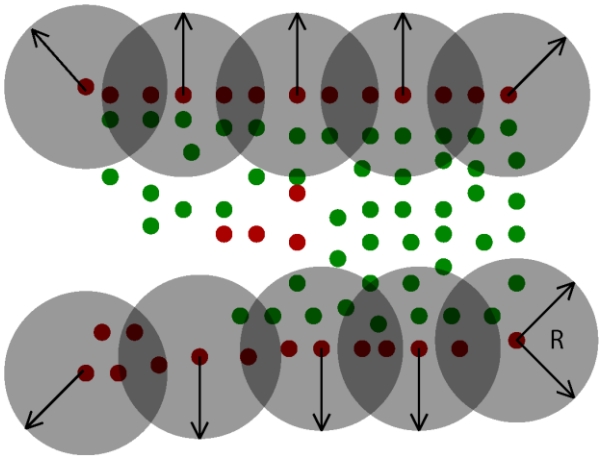
R

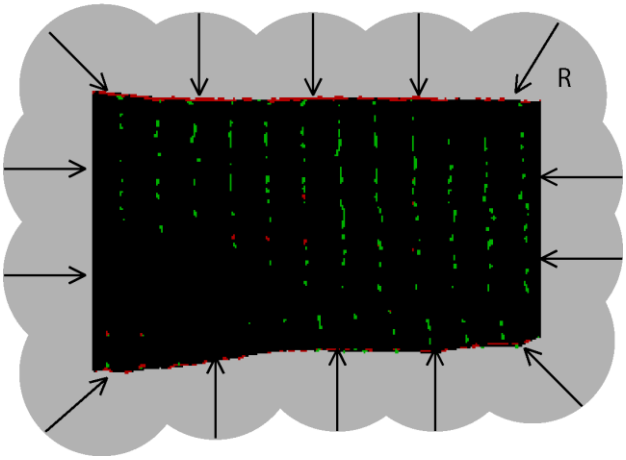
R

3.6. REFERENCES

1. Fabiato A. Calcium-induced release of calcium from the cardiac sarcoplasmic reticulum. *Am J Physiol.* 1983;245(1):C1-14.

2. Langer GA, Peskoff A. Role of the diadic cleft in myocardial contractile control. *Circulation.* 1997;96(10):3761-3765.

3. Stern MD. Theory of excitation-contraction coupling in cardiac muscle. *Biophys J.* 1992;63(2):497-517.

4. Huang J, Hove-Madsen L, Tibbits GF. Na+/Ca2+ exchange activity in neonatal rabbit ventricular myocytes

10.1152/ajpcell.00183.2004. *Am J Physiol Cell Physiol.* 2005;288(1):C195-203.

5. Wetzel GT, Chen F, Klitzner TS. Na+/Ca2+ exchange and cell contraction in isolated neonatal and adult rabbit cardiac myocytes. *Am J Physiol Heart Circ Physiol.* 1995;268(4):H1723-1733.

6. Perez CG, Copello JA, Li Y, Karko KL, Gomez L, Ramos-Franco J, Fill M, Escobar AL, Mejia-Alvarez R. Ryanodine receptor function in newborn rat heart. *Am J Physiol Heart Circ Physiol.* 2005;288(5):H2527-2540.

7. Haddock PS, Coetzee WA, Cho E, Porter L, Katoh H, Bers DM, Jafri MS, Artman M. Subcellular [Ca2+]i gradients during excitation-contraction coupling in newborn rabbit ventricular myocytes. *Circ Res.* 1999;85(5):415-427.

8. Klitzner TS, Chen FH, Raven RR, Wetzel GT, Friedman WF. Calcium current and tension generation in immature mammalian myocardium: effects of diltiazem. *J Mol Cell Cardiol.* 1991;23(7):807-815.

9. Hohl CM, Livingston B, Hensley J, Altschuld RA. Calcium handling by sarcoplasmic reticulum of neonatal swine cardiac myocytes. *Am J Physiol.* 1997;273(1 Pt 2):H192-199.

10. Tanaka H, Sekine T, Nishimaru K, Shigenobu K. Role of sarcoplasmic reticulum in myocardial contraction of neonatal and adult mice. *Comp Biochem Physiol A Mol Integr Physiol.* 1998;120(3):431-438.

11. Balaguru D, Haddock PS, Puglisi JL, Bers DM, Coetzee WA, Artman M. Role of the sarcoplasmic reticulum in contraction and relaxation of immature rabbit ventricular myocytes. *J Mol Cell Cardiol.* 1997;29(10):2747-2757.

12. Haddock PS, Coetzee WA, Artman M. Na+/Ca2+ exchange current and contractions measured under Cl(-)-free conditions in developing rabbit hearts. *Am J Physiol Heart Circ Physiol.* 1997;273(2):H837-846.

13. Artman M, Ichikawa H, Avkiran M, Coetzee WA. Na+/Ca2+ exchange current density in cardiac myocytes from rabbits and guinea pigs during postnatal development. *Am J Physiol Heart Circ Physiol.* 1995;268(4):H1714-1722.

14. Artman M. Sarcolemmal Na(+)-Ca2+ exchange activity and exchanger immunoreactivity in developing rabbit hearts. *Am J Physiol.* 1992;263(5 Pt 2):H1506-1513.

15. Boerth SR, Zimmer DB, Artman M. Steady-state mRNA levels of the sarcolemmal Na(+)-Ca2+ exchanger peak near birth in developing rabbit and rat hearts. *Circ Res.* 1994;74(2):354-359.

16. Huang J, L. Hove-Madsen, Tibbit G. Ontogeny of Ca^{2+}-induced Ca^{2+} release (CICR) in rabbit ventricular myocytes. *Biophysical J.* 2005;88:483a.

17. Frank JS, Mottino G, Reid D, Molday RS, Philipson KD. Distribution of the Na(+)-Ca2+ exchange protein in mammalian cardiac myocytes: an immunofluorescence and immunocolloidal gold-labeling study. *J Cell Biol.* 1992;117(2):337-345.

18. Scriven DR, Dan P, Moore ED. Distribution of proteins implicated in excitation-contraction coupling in rat ventricular myocytes. *Biophys J.* 2000;79(5):2682-2691.

19. Sedarat F, Xu L, Moore ED, Tibbits GF. Colocalization of dihydropyridine and ryanodine receptors in neonate rabbit heart using confocal microscopy. *Am J Physiol Heart Circ Physiol.* 2000;279(1):H202-209.

20. Chen-Izu Y, McCulle SL, Ward CW, Soeller C, Allen BM, Rabang C, Cannell MB, Balke CW, Izu LT. Three-dimensional distribution of ryanodine receptor clusters in cardiac myocytes. *Biophysical journal.* 2006;91(1):1-13.

21. Sedarat F, Lin E, Moore ED, Tibbits GF. Deconvolution of confocal images of dihydropyridine and ryanodine receptors in developing cardiomyocytes. *J Appl Physiol.* 2004;97(3):1098-1103.

22. Maruoka ND, Steele DF, Au BP, Dan P, Zhang X, Moore ED, Fedida D. alpha-actinin-2 couples to cardiac Kv1.5 channels, regulating current density and channel localization in HEK cells. *FEBS Lett.* 2000;473(2):188-194.

23. Dan P, Cheung JC, Scriven DR, Moore ED. Epitope-dependent localization of estrogen receptor-alpha, but not -beta, in en face arterial endothelium. *Am J Physiol Heart Circ Physiol.* 2003;284(4):H1295-1306.

24. Anscombe FJ. The transformation of poisson, binomial, and negative binomial data. *Biometrika.* 1948;35:246-254.

25. Smolich JJ. Ultrastructural and functional features of the developing mammalian heart: a brief overview. *Reprod Fertil Dev.* 1995;7(3):451-461.

26. Nassar R, Reedy MC, Anderson PA. Developmental changes in the ultrastructure and sarcomere shortening of the isolated rabbit ventricular myocyte. *Circ Res.* 1987;61(3):465-483.

27. Carl SL, Felix K, Caswell AH, Brandt NR, Ball WJ, Jr., Vaghy PL, Meissner G, Ferguson DG. Immunolocalization of sarcolemmal dihydropyridine receptor and sarcoplasmic reticular triadin and ryanodine receptor in rabbit ventricle and atrium. *J Cell Biol.* 1995;129(3):672-682.

28. Huang J, Xu L, Thomas M, Whitaker K, Hove-Madsen L, Tibbits GF. L-type Ca2+ channel function and expression in neonatal rabbit ventricular myocytes. *Am J Physiol Heart Circ Physiol.* 2006;290(6):H2267-2276.

29. Page E, Surdyk-Droske M. Distribution, surface density, and membrane area of diadic junctional contacts between plasma membrane and terminal cisterns in mammalian ventricle. *Circ Res.* 1979;45(2):260-267.

30. Chen F, Mottino G, Shin VY, Frank JS. Subcellular distribution of ankyrin in developing rabbit heart--relationship to the Na+-Ca2+ exchanger. *J Mol Cell Cardiol.* 1997;29(10):2621-2629.

31. Soeller C, Cannell MB. Examination of the transverse tubular system in living cardiac rat myocytes by 2-photon microscopy and digital image-processing techniques. *Circ Res.* 1999;84(3):266-275.

32. Kieval RS, Bloch RJ, Lindenmayer GE, Ambesi A, Lederer WJ. Immunofluorescence localization of the Na-Ca exchanger in heart cells. *Am J Physiol.* 1992;263(2 Pt 1):C545-550.

33. Scriven DR, Klimek A, Lee KL, Moore ED. The molecular architecture of calcium microdomains in rat cardiomyocytes. *Ann N Y Acad Sci.* 2002;976:488-499.

34. Crespo LM, Grantham CJ, Cannell MB. Kinetics, stoichiometry and role of the Na-Ca exchange mechanism in isolated cardiac myocytes. *Nature.* 1990;345(6276):618-621.

35. Yang Z, Pascarel C, Steele DS, Komukai K, Brette F, Orchard CH. Na+-Ca2+ exchange activity is localized in the T-tubules of rat ventricular myocytes. *Circ Res.* 2002;91(4):315-322.

36. Franzini-Armstrong C, Protasi F, Tijskens P. The assembly of calcium release units in cardiac muscle. *Ann N Y Acad Sci.* 2005;1047:76-85.

37. Franzini-Armstrong C, Protasi F, Ramesh V. Shape, size, and distribution of Ca(2+) release units and couplons in skeletal and cardiac muscles. *Biophys J.* 1999;77(3):1528-1539.

38. Huang J, van Breemen C, Kuo KH, Hove-Madsen L, Tibbits GF. Store-operated Ca2+ entry modulates sarcoplasmic reticulum Ca2+ loading in neonatal rabbit cardiac ventricular myocytes. *Am J Physiol Cell Physiol.* 2006;290(6):C1572-1582.

39. Fabiato A, Fabiato F. Calcium-induced release of calcium from the sarcoplasmic reticulum of skinned cells from adult human, dog, cat, rabbit, rat, and frog hearts and from fetal and new-born rat ventricles. *Ann N Y Acad Sci.* 1978;307:491-522.

40. Cheng H, Lederer WJ, Cannell MB. Calcium sparks: elementary events underlying excitation-contraction coupling in heart muscle. *Science.* 1993;262(5134):740-744.

41. Seki S, Nagashima M, Yamada Y, Tsutsuura M, Kobayashi T, Namiki A, Tohse N. Fetal and postnatal development of Ca2+ transients and Ca2+ sparks in rat cardiomyocytes. *Cardiovasc Res.* 2003;58(3):535-548.

42. Shacklock PS, Wier WG, Balke CW. Local Ca2+ transients (Ca2+ sparks) originate at transverse tubules in rat heart cells. *J Physiol.* 1995;487 (Pt 3):601-608.

43. Kockskamper J, Sheehan KA, Bare DJ, Lipsius SL, Mignery GA, Blatter LA. Activation and propagation of Ca(2+) release during excitation-contraction coupling in atrial myocytes. *Biophys J.* 2001;81(5):2590-2605.

44. Michailova A, DelPrincipe F, Egger M, Niggli E. Spatiotemporal features of Ca2+ buffering and diffusion in atrial cardiac myocytes with inhibited sarcoplasmic reticulum. *Biophys J.* 2002;83(6):3134-3151.

45. Bootman MD, Higazi DR, Coombes S, Roderick HL. Calcium signalling during excitation-contraction coupling in mammalian atrial myocytes. *J Cell Sci.* 2006;119(Pt 19):3915-3925.

46. Berlin JR. Spatiotemporal changes of Ca2+ during electrically evoked contractions in atrial and ventricular cells. *Am J Physiol.* 1995;269(3 Pt 2):H1165-1170.

47. Izu LT, Means SA, Shadid JN, Chen-Izu Y, Balke CW. Interplay of Ryanodine Receptor Distribution and Calcium Dynamics. *Biophys J.* 2006.

48. Thomas MJ, Sjaastad I, Andersen K, Helm PJ, Wasserstrom JA, Sejersted OM, Ottersen OP. Localization and function of the Na+/Ca2+-exchanger in normal and detubulated rat cardiomyocytes. *J Mol Cell Cardiol.* 2003;35(11):1325-1337.

49. Leblanc N, Hume JR. Sodium current-induced release of calcium from cardiac sarcoplasmic reticulum. *Science.* 1990;248(4953):372-376.

50. Litwin SE, Li J, Bridge JH. Na-Ca exchange and the trigger for sarcoplasmic reticulum Ca release: studies in adult rabbit ventricular myocytes. *Biophys J.* 1998;75(1):359-371.

51. Levi AJ, Brooksby P, Hancox JC. A role for depolarisation induced calcium entry on the Na-Ca exchange in triggering intracellular calcium release and contraction in rat ventricular myocytes. *Cardiovasc Res.* 1993;27(9):1677-1690.

52. Nuss HB, Houser SR. Sodium-calcium exchange-mediated contractions in feline ventricular myocytes. *Am J Physiol.* 1992;263(4 Pt 2):H1161-1169.

53. Kohomoto O, Levi AJ, Bridge JH. Relation between reverse sodium-calcium exchange and sarcoplasmic reticulum calcium release in guinea pig ventricular cells. *Circ Res.* 1994;74(3):550-554.

54. Vornanen M, Shepherd N, Isenberg G. Tension-voltage relations of single myocytes reflect Ca release triggered by Na/Ca exchange at 35 degrees C but not 23 degrees C. *Am J Physiol.* 1994;267(2 Pt 1):C623-632.

55. Wasserstrom JA, Vites AM. The role of Na(+)-Ca2+ exchange in activation of excitation-contraction coupling in rat ventricular myocytes. *J Physiol.* 1996;493 (Pt 2):529-542.

56. Lines GT, Sande JB, Louch WE, Mork HK, Grottum P, Sejersted OM. Contribution of the Na+/Ca2+ exchanger to rapid Ca2+ release in cardiomyocytes. *Biophys J.* 2006;91(3):779-792.

57. Evans AM, Cannell MB. The role of L-type Ca2+ current and Na+ current-stimulated Na/Ca exchange in triggering SR calcium release in guinea-pig cardiac ventricular myocytes. *Cardiovasc Res.* 1997;35(2):294-302.

58. Sipido KR, Maes M, Van de Werf F. Low efficiency of Ca2+ entry through the Na(+)-Ca2+ exchanger as trigger for Ca2+ release from the sarcoplasmic reticulum. A comparison between L-type Ca2+ current and reverse-mode Na(+)-Ca2+ exchange. *Circ Res.* 1997;81(6):1034-1044.

59. Bouchard RA, Clark RB, Giles WR. Regulation of unloaded cell shortening by sarcolemmal sodium-calcium exchange in isolated rat ventricular myocytes. *J Physiol.* 1993;469:583-599.

60. Sham JS, Cleemann L, Morad M. Gating of the cardiac Ca2+ release channel: the role of Na+ current and Na(+)-Ca2+ exchange. *Science.* 1992;255(5046):850-853.

4. DISTRIBUTION PATTERNS OF THE NA^+-CA^{2+} EXCHANGER AND CAVEOLIN-3 IN DEVELOPING RABBIT CARDIOMYOCYTES[3]

4.1. INTRODUCTION

Excitation-contraction (E-C) coupling via L-type Ca^{2+} channels ($Ca_v1.2$) mediating calcium-induced calcium release (CICR) is the established working model for mature ventricular myocytes. In this process, membrane depolarization activates the voltage-sensitive $Ca_v1.2$, allowing an influx of extracellular Ca^{2+} into the cytosol. This relatively small sarcolemmal Ca^{2+} influx results in a larger release of Ca^{2+} from the sarcoplasmic reticulum (SR) through the ryanodine receptor (RyR2). RyR-mediated release of SR Ca^{2+} raises the cytosolic Ca^{2+} concentration several-fold, thereby initiating contraction. Relaxation occurs as cytosolic Ca^{2+} is removed, mainly by reuptake into the SR via SR Ca^{2+} ATPase (SERCA2a) and extrusion (forward mode) by the sodium calcium exchanger (NCX1.1) into the extracellular space [1]. Under specific conditions, NCX is also capable of operating in reverse mode, resulting in Ca^{2+} influx.

Although Ca^{2+} influx occurs predominantly through $Ca_v1.2$ [1] in adult cardiomyocytes, recent functional data from our laboratory strongly suggests that in neonatal rabbit myocytes Ca^{2+} influx is primarily through reverse mode NCX activity that also results in CICR, termed NCX-mediated CICR (NCX-CICR) [2]. The contribution of NCX Ca^{2+} influx corresponds with developmental expression levels of NCX, which are high at birth and decrease several-fold during maturation [3-8]. Concurrently, L-type mediated CICR contribution increases during development as $Ca_v1.2$ expression and coupling with RyR2 increases [7, 9-11].

[3] A version of this chapter has been published. Lin E, Hung VH, Kashihara H, Dan P, Tibbits GF. Distribution patterns of the Na+-Ca2+ exchanger and caveolin-3 in developing rabbit cardiomyocytes. Cell Calcium**.** 2009 Apr;45(4):369-83. 27.

Considering the reversal potential and the Ca^{2+} transport rate of NCX, it is hypothesized that in the neonate cardiomyocytes, a high local density of NCX, Na^{+} channels, and RyR proteins are organized in a restricted microdomain to allow for effective reverse mode NCX activity leading to NCX-CICR [2, 12]. While previous studies on NCX distribution in the neonate myocytes suggest a homogeneous surface distribution [13, 14], recent immunofluorescence images in rabbit ventricular myocytes showed a punctate peripheral NCX distribution [15]. We proposed that in early developmental stages, a microdomain containing this multi-protein functional unit (couplon) exists in rabbit ventricular myocytes. Several possible candidates may be responsible for structuring this microdomain space including caveolae.

Caveolae are narrowed-neck membrane invaginations (diameters 50-100 nm) with distinct lipid and protein constituents [16, 17]. The principal protein structural component of cardiac caveolae is caveolin-3. Other groups have reported biochemical and morphological data from adult cardiomyocytes suggesting association and colocalization between NCX and caveolin-3 (cav-3) [18, 19] however, more recent studies have challenged this notion [20]. One might hypothesize that a subset of NCX is colocalized with an anchoring molecule such as cav-3 in the early developmental stages, but such colocalization declines as ventricular myocytes mature into adulthood.

In this study, we investigate in detail the distribution of NCX in the cardiomyocyte in a developmental period in which [NCX] decreases several fold. We also determine the spatial relationship between NCX and cav-3 during development using confocal microscopy in conjunction with various image analysis techniques. In all 5 age groups tested (3 day, 6 day, 10 day, 20 day and 56 day old myocytes), we found the majority of NCX and cav-3 to be weakly associated at the cell periphery. In developmental stages (10, 20 and 56 day groups) only limited colocalization was found in the cell interior. However, 3-D image analysis of peripheral NCX and cav-3 objects showed that both proteins appear to be distributed in a highly organized manner but tended to have a mutually exclusive relationship that did not appear to change with age.

4.2. MATERIAL AND METHODS

Isolation of ventricular myocytes

Animals were cared for in accordance with the principles established by the Canadian Council on Animal Care (CCAC). The Simon Fraser University Animal Care Committee approved the use of animals and the experimental protocols used in this study in accordance with the CCAC regulations. Ventricular myocytes were isolated from the hearts of New Zealand White rabbits of either sex from five different age groups (days post-partum): 3d, 6d, 10d, 20d, and 56d as described previously [8].

Antibodies

Primary antibodies used were monoclonal anti-caveolin-3 IgG1 antibody (610420, BD Biosciences, Mississauga, ON, Canada), and monoclonal anti-NCX IgM antibody (MA3-926, Affinity Bioreagents, Golden, CO). These monoclonal antibodies were chosen in order to avoid possible non-specific interactions of rabbit derived polyclonal antibodies with the rabbit myocytes. Secondary antibodies were affinity purified, isotype specific goat polyclonal antibodies that were either anti-mouse IgG1 conjugated to Alexa Fluor 488 (A21121, Invitrogen) or anti-mouse IgM conjugated to Alexa Fluor 555 (A21426, Invitrogen). These secondary antibodies react specifically with the Fc portion of the immunoglobulin heavy chain of the appropriate isotype, thereby allowing for distinction between the two mouse-derived monoclonal antibodies. To minimize cross-reactivity, these antibodies were also highly adsorbed against other antibody isotypes. Control primary antibodies raised against an antigen absent in mammalian cells were obtained from DakoCytomation, Denmark (mouse IgG1, X0931; mouse IgM, X0942).

Labelling

The isolated cells were prepared as described previously [21] before they were adhered to poly-L-lysine (Sigma) coated coverslips at an appropriate density. Antibody solutions were applied directly onto the coverslips. Cells were incubated in anti-caveolin-3 antibody diluted in antibody buffer (75 mM NaCl, 18 mM sodium citrate with 2% goat serum, 1% bovine serum albumin, 0.05% Triton X-100, 0.02% NaN3) at 125 ng/mL for 4 hours at room temperature. Cells were then washed for 3 × 10 min in antibody wash solution (18 mM sodium citrate containing 0.05% Triton X-100) before incubating in anti-mouse IgG1 conjugated to Alexa Fluor 488 (4 ng/mL) for 1 hour at room temperature. After 3 × 10 min washes, cells were incubated with anti-NCX IgM antibody (250 ng/mL) at 4^{o}C overnight. After the overnight incubation, cells were washed with 3 × 10 min washes before the last 1 hour incubation of anti-mouse IgM conjugated to Alexa Fluor 555 (4 ng/mL) at room temperature. After 3 × 10 min washes in antibody buffer, cells were subjected to an additional 5 min wash in PBS before the coverslips were mounted onto glass slides in Slow Fade Gold anti-fade reagent (Invitrogen) and sealed with nail polish.

To determine the level of non-specific staining of the isotype specific secondary antibodies in these cardiomyocytes, control primary antibodies were used. Control cells were stained in the same way as described above but instead of anti-caveolin-3 and anti-NCX antibodies, control primary antibodies of the same isotype were used at the same concentrations as their respective experimental primary antibodies (cav-3, IgG1: 125 ng/mL; NCX, IgM: 250 ng/mL). Control images were acquired under the same settings as the experimental images. Only very dim, diffuse staining was observed from these images. In addition, to determine the specificity of the secondary antibodies used, single stain control experiments with mismatched secondary antibodies were performed (i.e. cav-3 + IgM; NCX + IgG1). The staining pattern was very dim and diffuse, similar to that observed from isotype matched control primary antibodies experiments.

Image Acquisition

Images were acquired on a Zeiss LSM 5 Pascal (software version 2.8) laser scanning confocal microscope equipped with a Zeiss 63X/1.4 Plan-Apochromat oil immersion objective. The 543 nm and 488 nm excitation beams were supplied by Helium-Neon and Argon lasers, respectively. Images were acquired with a voxel dimension of 100 nm×100 nm×200 nm (axial) and the pinhole set to one Airy disc. Sequential acquisition was used to minimize signal bleed-through.

Image Processing and Analysis

After image acquisition, images were deconvolved using a maximum likelihood estimation (MLE) algorithm (Huygens Pro 2.4.1, Scientific Volume Imaging, Hilversum, The Netherlands) using an empirically determined point spread function (PSF). A cell outline was created for each image and was further segmented into individual voxels layers as previously described [15]. This study incorporated an anti-noise mask to refine the cell outline, the details on how these masks were created can be found in the Figure 4.12. This refined cell outline was then used to iteratively determine a threshold value. The peripheral compartment was defined as the first 3 layers of the cell outline and the interior compartment was defined as the volume enclosed by the peripheral compartment.

For each cell, the peripheral compartment was used to determine an appropriate threshold value. The peripheral compartment was subjected to multiple threshold values ranging from 0 to 10000 “intensity values” in 100 point increments (16-bit images with a maximum intensity value of 65535). The number of discrete objects was then determined at each threshold value. Here, an object was defined as an island of voxels above the threshold value surrounded on all sides by sub-threshold values. For each label, the threshold value that resulted in the maximal number of objects was used as the binary threshold for all subsequent analysis.

Colocalization events were defined as voxels that were supra-threshold in analogous positions in the NCX and cav-3. Colocalization for each label was defined as the number of colocalized voxels divided by the total number of voxels containing that particular label per

compartment. For example, peripheral NCX colocalization equals the number of colocalized voxels divided by the number of NCX supra-threshold voxels also in the peripheral compartment. Colocalization analyses were performed at the compartment level, (i.e. whole cell compartment, peripheral compartment and interior compartment) as well as at the individual object level (object specific colocalization).

For object specific colocalization, individual objects were categorized into colocalized and non-colocalized objects within the peripheral and interior compartments. Colocalized objects were defined as objects containing one or more colocalization events (more than 0% colocalization). Non-colocalized objects were defined as objects containing zero colocalization events (0% colocalization). We then analyzed colocalized objects as individual regions of interest and determined their individual colocalization indices. Within these colocalized objects, we determined the overall colocalization index, which is equivalent to defining a region of interest that excludes all non-colocalized objects within a given compartment.

To investigate the effects of development on the spatial distributions of NCX and cav-3 at the cellular level we calculated separations distances connecting each object to its immediate neighbours. Three distance measurements were used: 1) NCX to NCX, 2) cav-3 to cav-3 and 3) NCX to cav-3. Distance analysis was conducted for both peripheral objects and internal objects directly beneath the peripheral compartment.

For this analysis, objects were reduced into single pixel co-ordinates by determining the center-of-mass of each object. Using the above mentioned cell outline the 3D co-ordinates of the center of mass were converted to a 2D equivalent array to reduce the complexity of the calculations. Additional details on the conversion algorithm can be found in the Figure 4.13. Once this conversion to 2D space is complete Delaney triangulation was used to establish connectivity between each NCX and cav-3 cluster as can be seen in Figure 4.7. In analyses that included a directional component distances were calculated along a $\pm 15^{o}$ window along the specified direction. Only distances less than 3 μm in length were included.

Internal separation distances were determined as per the peripheral calculations except distances were measured 3 voxel layers in from the surface. Because of the restricted space

within the t-tubules, the separation distances between NCX objects and cav-3 objects were not measured.

It should be noted that these images are collected using light microscopy with the resolution limitations being well established and the conclusions derived in this and similar studies must be made with this in mind.

Statistics

Two statistical tests were used to establish statistical significances of age related changes. The first test used was the Kruskal-Wallis H-Test, a non-parametric one-way analysis of variance, and was used to establish that at least one of the age groups was significantly different from the rest. This was then followed by pair-wise comparisons using the Mann-Whitney U-Test, a non-parametric test analogous to Student's T-test. For the purposes of the statistical analysis the parameter N represents the number of cells included in the analysis. For 3d, N = 14, from 2 animals; for 6d, N = 36, from 3 animals; for 10d, N = 22, from 3 animals; for 20d, N = 50, from 6 animals; for 56d, N = 23, from 5 animals.

4.3. RESULTS

Iterative Thresholding Technique:

Thresholding is an integral parameter to all imaging studies that essentially defines the minimal signal required to be included in to the analysis. Visually, NCX and cav-3 appeared as punctate objects, an area of bright pixels surrounded by an area of dim pixels. In an effort to find the balance between excluding dim but real objects with the need to limit erroneous connectivity between individual objects, we utilized an iterative thresholding technique that applies multiple threshold values and calculates the number of objects on the cell periphery at each threshold value. Figure 4.1A is a representative plot of the number of independent objects as a function of threshold value. Shown in Figure 4.1B are images of a cell at different thresholding values. As the threshold increased from 0, the number of events increased as dim connective regions were excluded. Each profile contained a peak value in which a threshold value generated a maximal number of events. Any further increases in threshold values began to remove dim objects. The threshold value that generated the maximal number of events was used in this study.

Although it is unlikely that dim objects were excluded from the analysis, it is possible that object size is excessively reduced by the iterative thresholding technique. The median object size is shown in Figure 4.2 panels B-E, as a function of the polar angle in the cross-sectional plane. Notable is the non-homogenous object size along the circumference of the cell for NCX and cav-3. Here, the left and right aspects of the cell align to the 0 and 180 degree marks and the top and bottom aspects of the cell correspond to the +90 and -90 degree marks. The median object size along the top and bottom aspects of the cell are noticeably smaller than object sizes along the left and right aspects of the cell. This indicates that the iterative thresholding technique does not excessively reduce object size. However, the anisotropic object size suggests that the axial resolution may affect where colocalization events are found.

Visual Comparisons

Five age groups were considered in this study and images were collected from 3d, 6d, 10d, 20d, and 56d myocytes post-partum. Figure 4.3 shows surface XY sections (A), middle XY sections (B) and cross-sectionals (C) of representative cells using iteratively determined threshold values. From the cross-sectional images, it is apparent that as the cells develop both NCX and cav-3 labelling increased in the interior of the cell. Images from young cells (3 and 6 day) contain only minimal interior labelling. In the 10 day group interior labelling was seen but did not appear robust. The 20 day and 56 day groups showed increasingly robust NCX and cav-3 labelling in the cell interior. NCX and cav-3 labelling in the cell interior appeared as periodic inward protrusions from the cell surface along what may be t-tubule structures. Although changes in interior labelling were easily seen, we were unable to visualize any large changes in the NCX and cav-3 distribution on the surface of the cell. NCX and cav-3 appeared punctate and evenly distributed along the cell surface. Visually no definite pattern in colocalization was seen on the cell surface but noticeable colocalization was observed in the interior.

Global Colocalization in Various Compartments

Visually the peripheral and interior relationships between NCX and cav-3 appeared to differ. To determine the relationship between these two proteins, the colocalization index for three compartments was calculated. Figure 4.4 shows whole cell (A), peripheral (B) and interior colocalization (C) between NCX and cav-3. Neither whole cell nor peripheral colocalization showed a clear age dependency but colocalization in the cell interior appeared to increase with age. Changes between neighbouring developmental stages up to the 20 day group were found to be statistically non-significant (d3 vs. d6, d6 vs. d10, and d10 vs. d20 but not d20 vs. d56) for the whole cell and peripheral colocalization indices. P-values for the individual tests for all graphed variables are reported in Table 4.1-3. In the interior, the changes in development between the d10 and d20 groups were not significant for interior NCX colocalization but were significant for interior cav-3 colocalization. In all these global colocalization parameters, the 56 day group was found to be statistically different from the other age groups.

Because changes in the interior colocalization did not seem to affect the whole cell colocalization indices, we also quantified the amount of colocalization events in the periphery of the cell. Figure 4.4D shows the relative number of NCX, cav-3 and colocalization events on the periphery as a percentage of total events and all changes between neighbouring developmental stages were found to be statistically significant.

Object Specific Colocalization in the Peripheral Compartments

The low colocalization percentages found above may be due to a small population of highly colocalized objects amidst a lowly colocalized general population. This low or non colocalized population if much larger than the highly colocalized population may dilute the calculations, reducing the derived colocalization index.

To test for a highly colocalized subpopulation, we identified which NCX and cav-3 objects contained one or more colocalization events. This population is referred to as colocalized objects and the remaining objects, containing no colocalization events, are referred to as non-colocalized objects. To quantify the effects of non-colocalized objects, we calculated the overall colocalization percentage for NCX and cav-3 within just the colocalized objects, i.e. with the non-colocalized objects removed. We determined the median object colocalization as well as the proportion of objects that were highly colocalized, with more than 50% colocalization in each object. The number of colocalization events contained in these highly colocalized events was also determined.

In the peripheral compartment, NCX and cav-3 appear to be minimally colocalized. Less than 40% of peripheral objects contain one or more colocalization events (Figure 4.5A). The percentage of NCX objects containing colocalization events were found to be not statistically significant for all neighbouring groups. However percentages of cav-3 objects containing colocalization for d3 vs. d6 and for d20 vs. d56 were found to be statistically significant.

If all NCX and cav-3 objects containing no colocalization events are removed which effectively restricts the region of interest to the colocalized subpopulation, the object specific NCX and cav-3 colocalization indices increase by about 5% (Figure 4.4B versus Figure 4.5B).

However, even with the restricted region of interest to only include colocalized objects, the object specific colocalization was less than 21% for either NCX or cav-3 colocalization (Figure 4.5B).

The small rise (~5%) in overall colocalization, even with the complete removal of all non-colocalized objects indicates that although ~60% of the objects were removed, indicates that these non colocalized objects were relatively small in size. Colocalized objects were found to be roughly 3x larger than non-colocalized objects and these differences were found to be statistically significant at all developmental stages (data not shown). For peripheral NCX object specific colocalization, d3 vs. d6, d6 vs. d10 and d20 vs. d56 were found to be statistically significant. For peripheral cav-3 object specific colocalization, d10 vs. d20 and d20 vs. d56 were found to be statistically significant.

Although non-colocalized objects have been removed for object-specific colocalization calculations there remains a continuum of colocalization indices within the remaining objects. High colocalization indices in individual objects reflect a high degree of overlap between NCX and cav-3 while low colocalization indices reflect a low degree of overlap. Colocalized voxels that result from objects containing large degrees of overlap may have more physiological significance than colocalized voxels resulting from objects that contain only small degrees of colocalization. Therefore, colocalization indices within individual objects were quantified as small isolated regions of interest.

A representative histogram, from the 20 day group, is shown in Figure 4.5C and D for NCX and cav-3 object colocalization, respectively. Histograms from the other age groups revealed a similar shape and trend in their profiles. The median object colocalization was 19% and 17% for NCX and cav-3 objects, respectively, indicating that half of the objects had colocalization indices less than that. The 56 day group had the largest median colocalization index, with a 22% median NCX object colocalization. The large right skew of the cumulated histogram indicates that the majority of colocalization events arise from events that are minimally colocalized.

To quantify the significance of highly colocalized objects, (i.e. objects containing more than 50% colocalization) the proportion and contribution of these events was determined. Of the colocalized objects, each containing at least one colocalized voxel, only ~7% of peripheral colocalized objects contained 50% or greater colocalization (Figure 4.5E). Statistical tests between neighbouring age groups found only the d3 vs. d6 comparison for the proportion of highly colocalized NCX objects to be significantly significant. All other comparisons found no significant differences between neighbouring age groups.

The contribution of these highly colocalized objects, as in the proportion of peripheral colocalization voxels that can be attributed to these highly colocalized objects is reported in Figure 4.5F. The contribution of these highly colocalized objects did not contribute more than 23% of the overall colocalization events in the cell periphery. Except for the comparison between the contributions of highly colocalized NCX objects between d6 vs. d10, all other comparisons between neighbouring age groups were found to be not statistically significant.

Object Specific Colocalization in the Interior Compartment

The analysis approach utilized for the peripheral compartment was also utilized for the interior compartment. In contrast to the peripheral population, levels of colocalization in the cell interior appeared to change with development (Figure 4.6). Because significant t-tubule development only occurs after 10 days post-partum, only the d10, d20 and d56 groups are considered in this section. Within the cell interior, NCX colocalization was greater than cav-3 colocalization partially due to a larger amount of cav-3 voxels. Although the proportion of t-tubule objects containing one or more colocalization events was less than in the periphery, this proportion increased with development (Figure 4.6A). From the 10d group to the 56d group, the percent NCX objects containing colocalization events increased from 20% to 36%. Over the same time frame, the percent of colocalized cav-3 objects increased from 11% to 34%. Statistical tests between d10 vs. d20 and between d20 vs. d56 found these changes to be statistically significant.

NCX and cav-3 object specific colocalization in the cell interior (i.e. interior colocalization with the non-colocalized objects removed) increased with age. NCX object specific

colocalization increased from 20 % to 30% while cav-3 object specific colocalization increased from 16% to 20%. Differences between the d20 vs. d56 groups were found to be statistically significant for both NCX and cav-3 object specific colocalization in the interior.

Similar to the histogram profiles of NCX and cav-3 objects on the periphery, interior histograms indicated large right skews. Note that in the interior, there tend to be more cav-3 object than NCX objects. The percentage of interior objects with colocalization indices greater than 50% is shown in Figure 4.6E. The increases in NCX and cav-3 proportions are statistically significant between d10 vs. d20 and between d20 and d56. The contribution of the highly colocalized objects is shown in Figure 4.6F. Comparisons between d10 vs. d20 and between d20 and d56 found that these changes were not statistically significant.

Peripheral Distributions of NCX and Cav-3

Colocalization measurements are best suited to describing non-resolvable distributions, in which two proteins are distributed within a common voxel space. The large proportion of objects that are either non-colocalized or only lowly colocalized indicates many objects may be separated by a measurable distance.

Figure 4.8 indicates that the overall distributions of NCX and cav-3 on the cell periphery do not appear to change between developmental stages. Figure 4.8A (closed symbols) indicates that NCX objects were separated from other NCX objects most often by a distance of about 1µm. Figure 4.8B (closed symbols) indicates that the separation profiles of cav-3 objects appears to follow a similar pattern, where the most common separation distance is also 1 µm with no changes in the profile with development. The relationship between NCX and cav-3 objects is shown in Figure 4.8A (open symbols) and indicates that NCX and cav-3 objects appear to be well separated with a peak separation distance of about 0.5 µm.

To investigate these separation profiles further, we also calculated the separation profiles in the lateral and longitudinal directions. Figure 4.9 indicates that lateral and longitudinal separation distances for all three measurements do not appear to be developmentally regulated and that lateral separation profiles and longitudinal separation profiles are very similar between developmental stages. Separation profiles shown in Figure 4.9 appear to be more left-skewed in comparison with profiles from Figure 4.8. This shift to finding longer distances when determining lateral and longitudinal separations may be a reflection of the decreased probability of finding a lateral as well as a longitudinal neighbour for each and every node. The lack of an intermediate neighbour allows a pseudo-neighbour to be included (the neighbour's neighbour).

Because NCX to NCX, cav-3 to cav-3 and NCX to cav-3 separation profiles did not appear to change with development, Figure 4.10 summarizes the overall peripheral distribution by cumulating data from all age groups. Figure 4.10A and B summarizes the angular relationship between NCX and NCX objects and between cav-3 and cav-3 objects, respectively. Data points along the $\pm 90^{o}$ positions correspond with longitudinal measurements while data points at 0^{o} and $\pm 180^{o}$ correspond with lateral measurements as per Figure 4.9. About 6000 events were also

found at the intermediate angles at ±45^{o} and at ±135^{o}. Figure 4.10C provides distance profiles for these eight directions.

For the 20 day and 56 day groups, internal separation profiles were also determined (Figure 4.11). For internal measurements, measurements were determined 3 voxels in from the cell surface but otherwise similar to determining peripheral measurements. Relative to measurements of peripheral separation, internal measurements are low probability events. Neither NCX nor cav-3 labels appear to envelope large amounts of t-tubular membrane. As such, the distances to the closest neighbouring object were often greater than 3 µm and are not included in the figures. Lateral separation profiles appear similar with peripheral separation profiles with peak separation at around 1µm. Longitudinal separation profiles, however, are distinctly different than their peripheral counterparts. Although on the periphery, NCX-to-NCX and cav-3-to-cav-3 separation are at 1 µm, interior measurements indicate that the most common separation distances are 2-3 µm in length.

4.4. DISCUSSION

Thresholding criteria are an integral part of every imaging study and in this study we utilized an iterative thresholding technique that determined a threshold value based on the number of objects found at each threshold value between 0 and 10000. To avoid eliminating dim objects, the threshold that generated the maximum number of events was used. Over thresholding was checked for by determining the median object size as a function of polar angle and it was determined that objects along the tops and bottoms of the cells were smaller than objects on the left and right aspects of the cell. Although objects were smaller on the tops and bottoms, median object size was still greater than 10 voxels per object. Therefore, this iterative technique did not appear to result in systematic over thresholding.

Several stages of colocalization analysis were employed in this study, ranging from whole cell measurements to individual object measurements and we did not find the majority of NCX and cav-3 to be colocalized at any age group. Colocalization at the whole cell levels were less than 15% colocalization for all age groups. Analysis of the peripheral and interior compartments indicated that the majority of colocalization events occurred on the periphery. Development brings about increased colocalization in both the peripheral and interior compartments with larger changes occurring in the interior. Statistical analysis reveals that changes in colocalization between 3d vs. 6d vs. 10d vs. 20d groups are not statistic significant. However, the 56d group was found to be statistically different from all other groups. Subsequent removal of non-colocalized objects (object specific colocalization) increased peak levels of peripheral colocalization to 21% and peak levels of interior colocalization to 30%. Interior colocalization increased with development and myocytes may continue to mature after 56 days which may result in further increases in colocalization.

The role of cav-3 in E-C coupling seems unclear given data from this and several other studies. Both imaging and biochemical studies have reported differing relationships between NCX and cav-3. Scriven et al. 2005 showed that on the surface of adult rat myocytes, 30 to 40% of voxels labelled for $Ca_V1.2$, the sodium channel isoform rH1, NCX and RyR also contained cav-3. Since Scriven et al. [21] had already reported that NCX and RyR, and NCX and Na^+

channel do not colocalize in adult rat cardiomyocytes, this suggested that there must be several subpopulations of cav-3 with varying associations with other proteins.

The implications of their NCX and cav-3 colocalization data suggest that the surface distributions of NCX and cav-3 in the rat cardiomyocyte may be fundamentally different from that in the rabbit. In our study, most cells had a similar number of NCX and cav-3 voxels on the cell periphery, an effect that is visible in the similarities between colocalization values for that compartment (Figure 4.4). Because NCX and cav-3 colocalization calculations share the same numerator, similar colocalization percentages indicates a similar sized denominator. Scriven et al. [19] found 30% NCX colocalization with cav-3 and 10 % cav-3 colocalization with NCX which indicates that there is 3 times more cav-3 voxels than NCX voxels on the surface of adult rat myocytes. Whether this difference implicates differing distribution periodicities or differing objects sizes between rat and the rabbit is not yet known.

Bossuyt et al. [18] found that NCX and cav-3 co-immunoprecipitate in bovine cardiac sarcolemmal vesicles. However, a recent study by Cavalli et al. [20] reported NCX and cav-3 to be un-associated by both imaging and biochemical techniques. They found NCX and caveolin to stain the surface and interior compartments strongly but colocalization correlation coefficients did not indicate significant colocalization. The relationship between NCX and cav-3 was also tested using differing lipid raft isolation protocols. Using a "Na_2CO_3, pH 11" protocol to isolate rafts, this protocol found an association between NCX and cav-3. However, when the protocol was changed to a "Triton X-100" protocol, an association between NCX and cav-3 was no longer observed. While biochemical studies are able to make inferences about actual protein associations under different environments or isolation protocols, these results may not reflect differing cav-3 subpopulations that may occur physiologically.

We determined the overall NCX and cav-3 colocalization to be quite low but also found a small population of NCX and cav-3 objects that are highly colocalized. About 6% of peripheral and interior objects were found to have a colocalization index of greater than 50%. However, the functional contributions of these small populations are unknown. Cav-3 is likely to participate in both E-C coupling and non-E-C coupling related roles therefore; overall cellular colocalization between the protein in question and cav-3 may be difficult to interpret in

conditions in which the number of cav-3 voxels is large. In this study, we partially controlled for the effects of lowly colocalized cav-3 voxels by performing colocalization on an object by object basis, thereby separating highly colocalized events from the non-colocalized population. In protein distributions that contain distinct subpopulations, the colocalization indices of individual objects may be more reflective of physiological coupling than a global colocalization measure.

Protein Separation Distances

The distance data suggest that NCX and cav-3 are not rigidly distributed on the periphery of the cell since separation distances vary considerably. However, NCX and cav-3 are likely to be distributed with an underlying pattern that does not appear to change during development. Since the majority of NCX and cav-3 objects do not appear to be colocalized, most of NCX and cav-3 are distributed in a mutually exclusive pattern. Closest neighbour analysis indicates that NCX is often within 0.5 μm of a cav-3 cluster (and vice versa) and that both NCX and cav-3 are separated from other NCX and cav-3 objects often by ~1.0 μm. Angle analysis (Figure 4.10) indicates that NCX and cav-3 objects are likely to have eight neighbouring objects of the same type at every half turn or every $45^{o.}$ Four neighbours are located longitudinally and laterally (positions $\pm 90^{o}$, $\pm 180^{o}$) and four neighbours located diagonally (positions $\pm 45^{o}$, $\pm 135^{o}$). This may suggest that NCX and cav-3 objects are organized in a grid-like manner. Internal separation distances revealed that NCX and cav-3 have a similar lateral separation profile to peripheral measurements but have a 2-fold longer longitudinal periodicity in the cell interior versus the cell surface. The vast majority of interior objects were not contiguous with surface objects and we were unable to register surface events with t-tubule and z-line positions.

Summary

In this study NCX and cav-3 objects categorized into non-colocalized (0%), lowly colocalized (<50%) and highly colocalized (> 50%) subpopulations in both the interior and peripheral compartments. The majority of colocalization events were found to be associated with lowly colocalized objects but a small and possibility physiologically important population of highly colocalized events was also found. Distance analysis revealed that the distribution of NCX and cav-3 does not appear to vary with development and we demonstrate for the first time

that these two proteins appear to be distributed in an alternating checker pattern with a common lateral and longitudinal periodicity.

4.5. FIGURES

Figure 4.1 An iterative approach to image thresholding

In the peripheral volume, the number of objects was determined at multiple threshold values for each label. Values ranging from 0 to 10000, in 100 point increments, were used. The peak value, where the maximal number of events occurred, was used as the binary threshold for all subsequent analysis. In this example, "2000" is the peak value with the maximal number of events. Images of the periphery at 5 different thresholding intensities are also shown. Note the connectivity between objects in "0" and "1000" and the loss of some objects at "3000" and "4000".

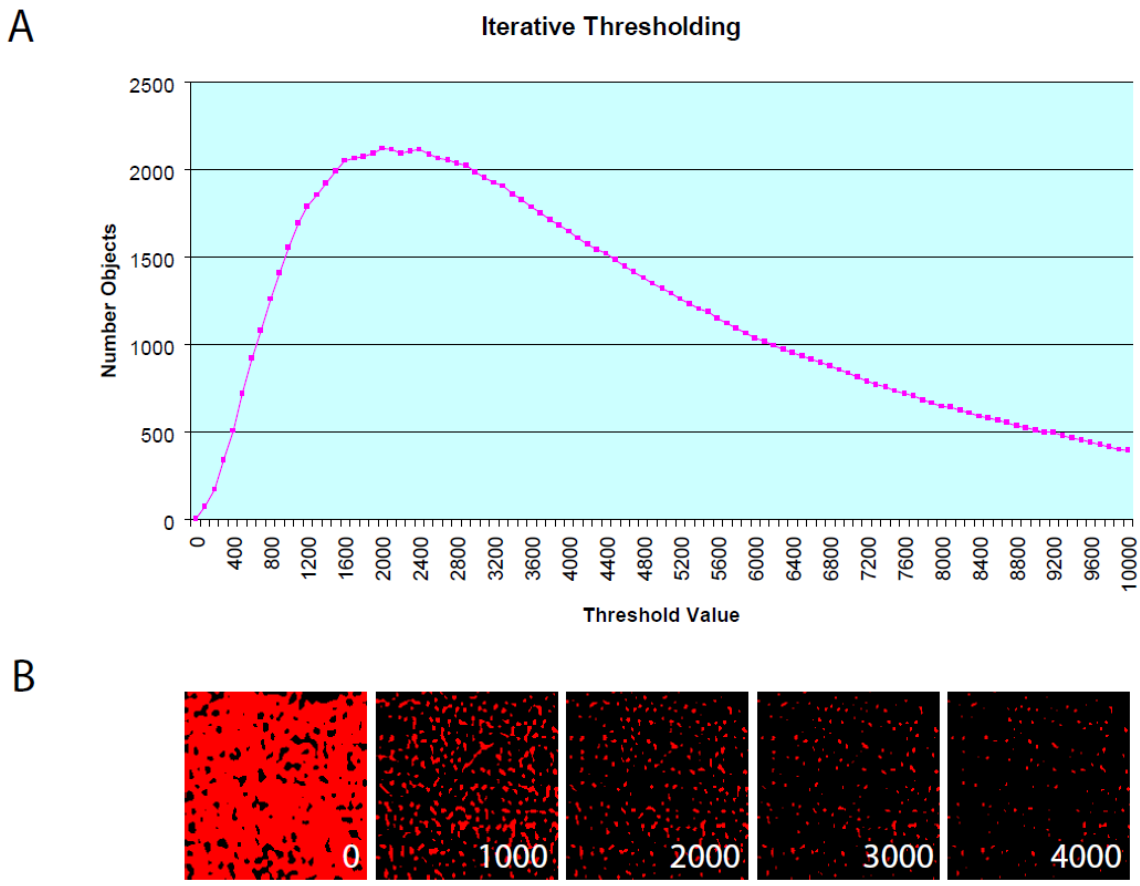

Figure 4.2 Object size as a function of circumference

To test the influence of differential lateral and axial resolutions on apparent protein localization, object size (number of voxels) and object locations were determined along the cell circumference. Because cell circumference varies with age, object positions were described by their angular relation to the center line of the cell. The center-line of the cell was determined by taking the center of mass of the equivalent cross-section of the determined cell outline. Therefore, the positioning of each object was described by the angle of the line connecting the center-line of the cell outline and the object's center-of-mass. Orientation of the cells is shown in Figure 4.2A. Median object sizes per angular location for NCX and cav-3 are shown in Figure 4.2B and C. Higher magnification is shown in 2D and E and indicates constant object sizes on the top and bottom aspects of the cell.

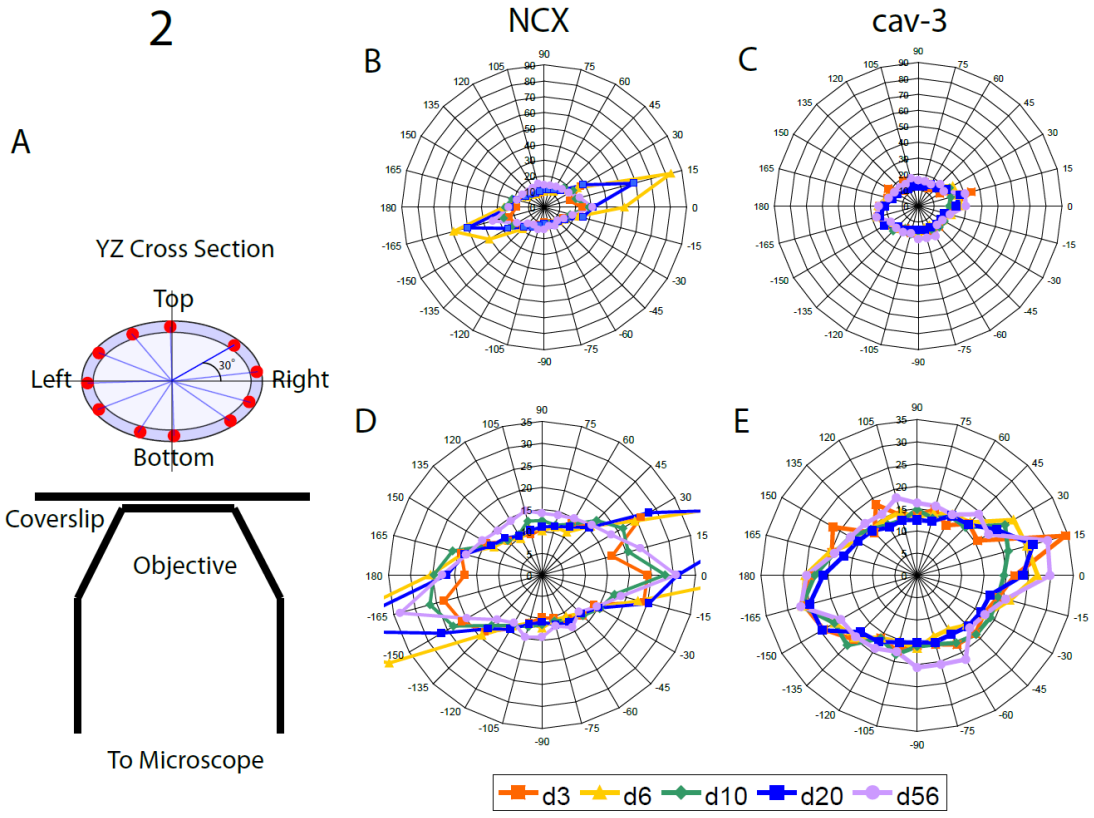

Figure 4.3 Cav-3 and NCX distributions in developing ventricular myocytes

Images of cav-3 (green) and NCX (red) labelled ventricular myocytes presented as (A) 800 nm thick xy surface sections, (B) middle xy section, and (C) 800 nm thick cross sections from 3d, 6d, 10d, 20d, and 56d old rabbits. Both surface and cross section images are maximum intensity projections. Scale bar is 5 µm.

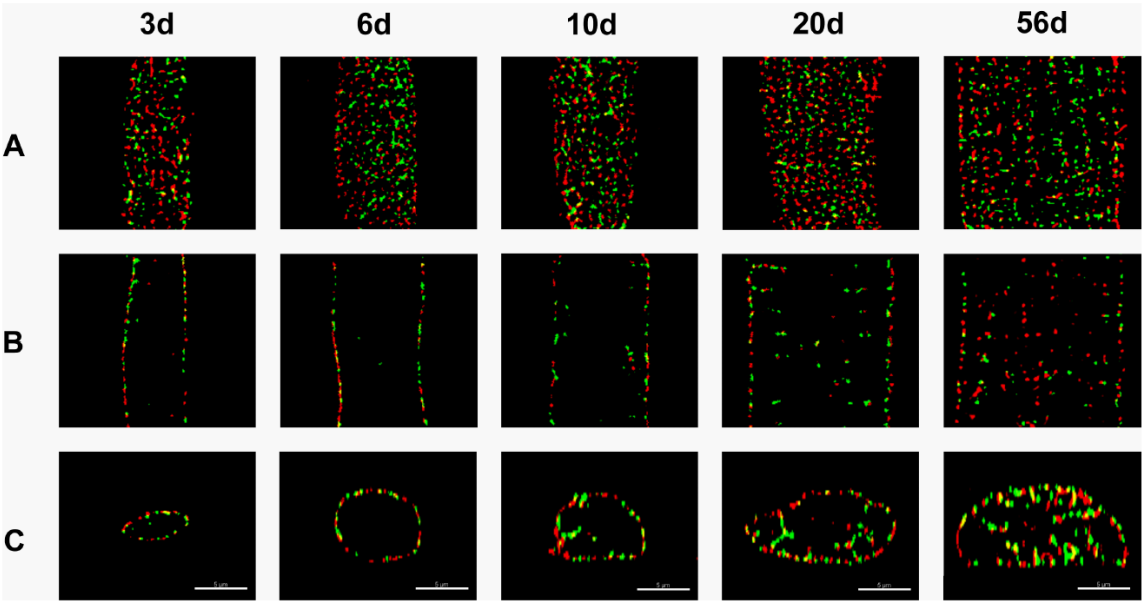

Figure 4.4 Compartmental colocalization

Colocalization analyses were applied to three cellular compartments to investigate possibly differing relationships between NCX and cav-3. Figure 4.4A indicates colocalization analysis from the entire cell without any image segmentation. Figures 4.4B and C indicate the colocalization in the individual peripheral and interior compartments, respectively, as defined in the methods. Only the 10, 20 and 56 days groups are shown in 4C since only these age groups had appreciable t-tubule development. Figure 4.4D shows the number of NCX, cav-3 and colocalized voxels found on the cell periphery relative to those found in the whole cell.

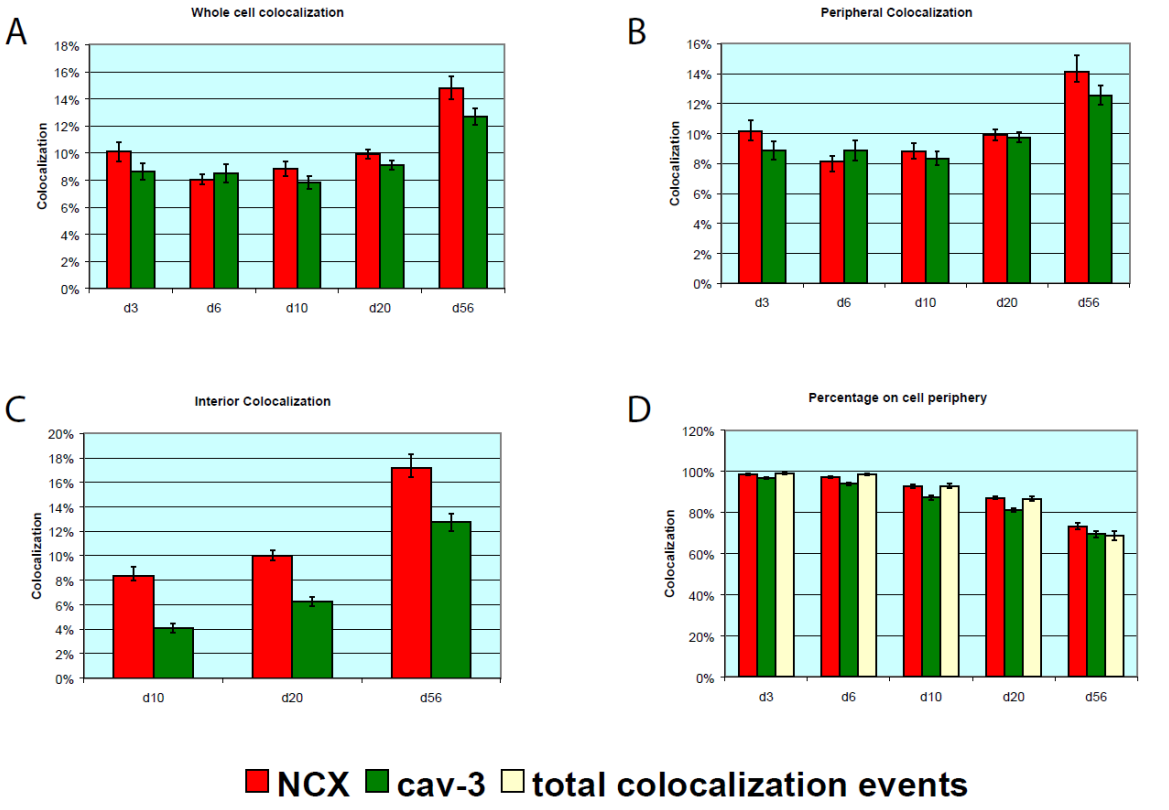

Figure 4.5 Peripheral object-specific colocalization

To investigate the colocalization specific to the peripheral compartment, object-specific colocalization analysis was applied. Figure 4.5A indicates the percentage of NCX and cav-3 objects on the cell periphery that contained one or more colocalized voxels. The remaining balance of objects contained no colocalization events and therefore has 0% colocalization. Figure 4.5B indicates the level of colocalization found if the 0% colocalization events were excluded from the calculation. This decreases the size of the denominator proportional to the number of voxels contained in the 0% colocalization objects and therefore increases the colocalization index. Only a small increase was found in Figure 4.5B when compared to Figure 4.4B indicating that the removed objects have relatively little mass. Figure 4.5C and 5D show cumulated object-specific colocalization indices from the 20 day group. The histogram bin-size has been set to 1 to show the presence of small ratios, peaks that can be seen at 100% (1:1), 50% (1:2), 66% (1:3) etc. Figures 4.5E and 4.5F show the quantification of highly colocalization objects (greater than 50% colocalization) by object count or by voxel count, respectively. Figure 4.5E shows the percentage of peripheral objects that contained more than 50% colocalization. Figure 4.5F indicates the percentage of peripheral colocalization voxels contained in object with greater than 50% colocalization as shown in Figure 4.5E.

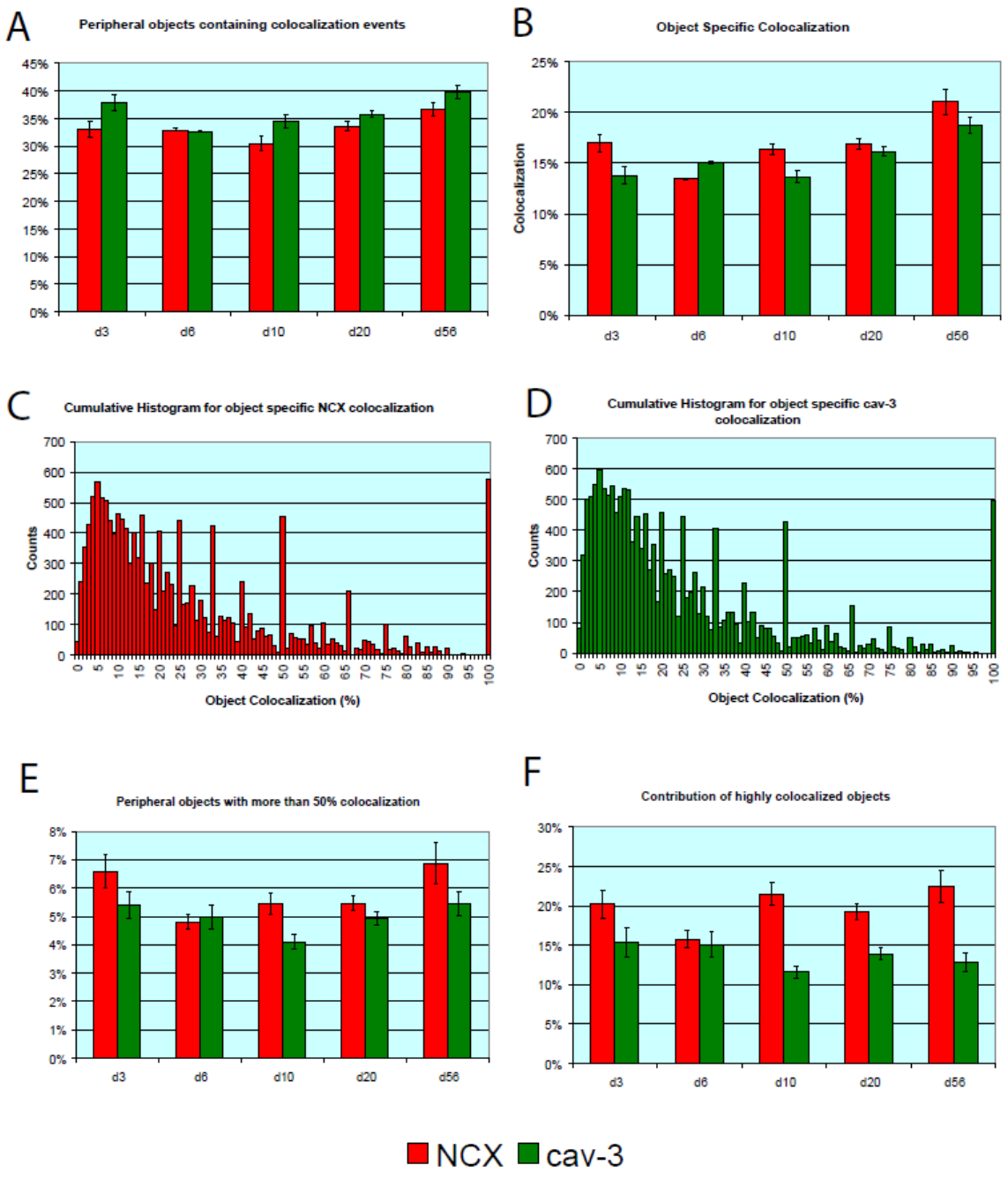
A
Peripheral objects containing colocalization events
45%
40%
35%
30%
25%
20%
15%
10%
5%
0%
d3
d6
d10
d20
d56
B
Object Specific Colocalization
Colocalization
25%
20%
15%
10%
5%
0%
d3
d6
d10
d20
d56
C
Cumulative Histogram for object specific NCX colocalization
Counts
700
600
500
400
300
200
100
0
0 5 10 15 20 25 30 35 40 45 50 55 60 65 70 75 80 85 90 95 100
Object Colocalization (%)
D
Cumulative Histogram for object specific cav-3 colocalization
Counts
700
600
500
400
300
200
100
0
0 5 10 15 20 25 30 35 40 45 50 55 60 65 70 75 80 85 90 95 100
Object Colocalization (%)
E
Peripheral objects with more than 50% colocalization
8%
7%
6%
5%
4%
3%
2%
1%
0%
d3
d6
d10
d20
d56
F
Contribution of highly colocalized objects
30%
25%
20%
15%
10%
5%
0%
d3
d6
d10
d20
d56
NCX
cav-3

Figure 4.6 Interior object-specific colocalization

Object-specific colocalization analysis was also applied to the interior compartment. Figure 4.6A shows the number of interior objects that contained one or more colocalized voxels. Figure 4.6B shows the object-specific colocalization where non-colocalized objects are excluded from the calculation. Figures 4.6C and 4.6D show cumulated object-specific colocalization analysis from the interior of the 20 day group. Figure 4.6E reports the number of objects found to contain more than 50% colocalization. Figure 4.6F reports the number of colocalized voxels accounted for in those objects containing more than 50% colocalization.

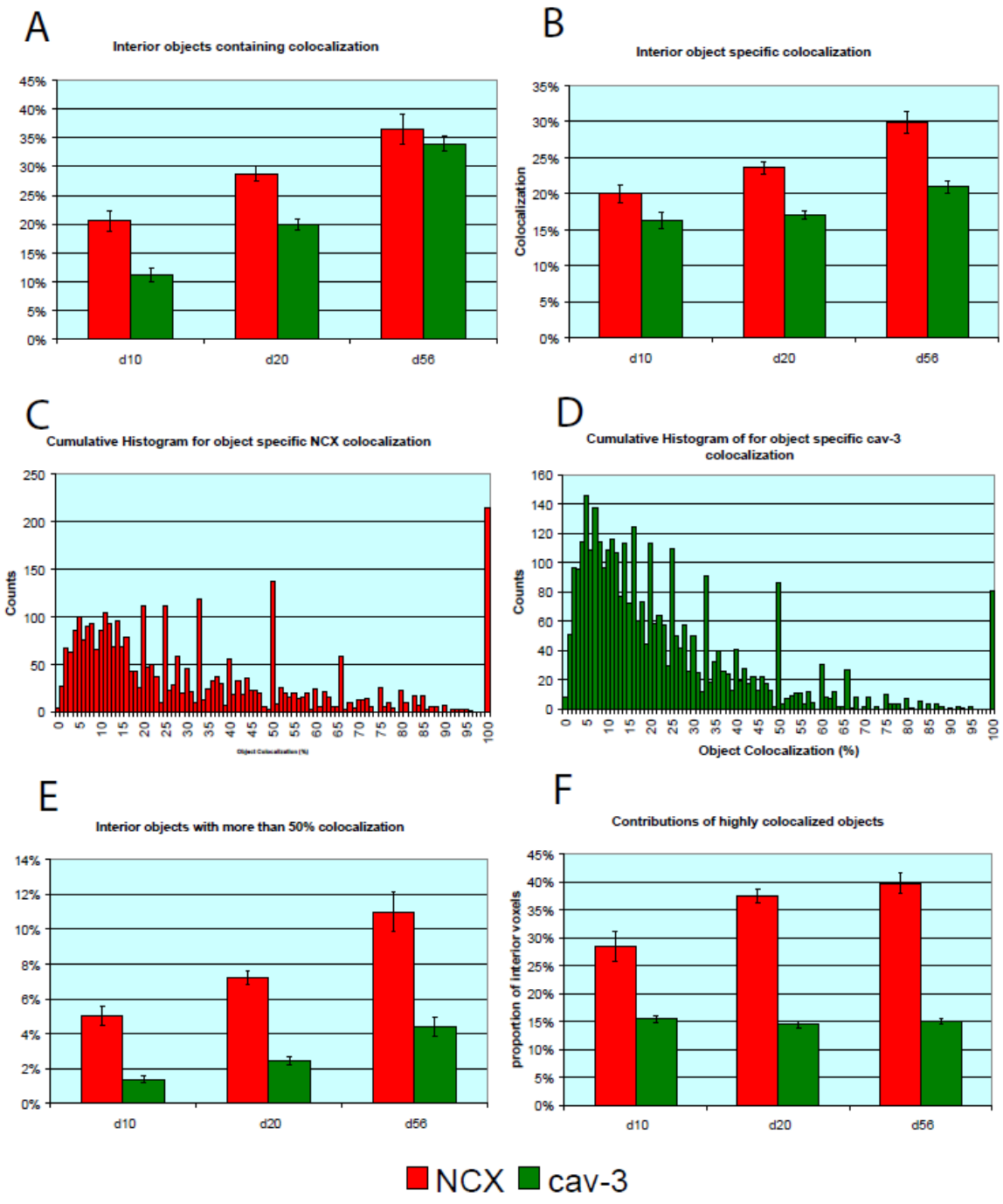
A
Interior objects containing colocalization
45%
40%
35%
30%
25%
20%
15%
10%
5%
0%
d10
d20
d56
B
Interior object specific colocalization
Colocalization
35%
30%
25%
20%
15%
10%
5%
0%
d10
d20
d56
C
Cumulative Histogram for object specific NCX colocalization
Counts
250
200
150
100
50
0
0 5 10 15 20 25 30 35 40 45 50 55 60 65 70 75 80 85 90 95 100
D
Cumulative Histogram of for object specific cav-3 colocalization
Counts
160
140
120
100
80
60
40
20
0
0 5 10 15 20 25 30 35 40 45 50 55 60 65 70 75 80 85 90 95 100
Object Colocalization (%)
E
Interior objects with more than 50% colocalization
14%
12%
10%
8%
6%
4%
2%
0%
d10
d20
d56
F
Contributions of highly colocalized objects
proportion of interior voxels
45%
40%
35%
30%
25%
20%
15%
10%
5%
0%
d10
d20
d56
NCX
cav-3

Figure 4.7 3-D distance analysis

Volume projection of surface connectivity between objects is shown in Figure 4.7A. Figure 4.7B shows a higher magnification of the connectivity grid created by the Delaney triangulation. Each object (large green circle) can have several neighbouring objects (small green circles) and the connecting path between two points serves as the basis for the distance calculation. Figure 4.7C shows a volume projection of peripheral NCX and cav-3 objects from the prospective of the camera as show in (A) by the red outlines. For clarity, (C) only shows the top half of the cell.

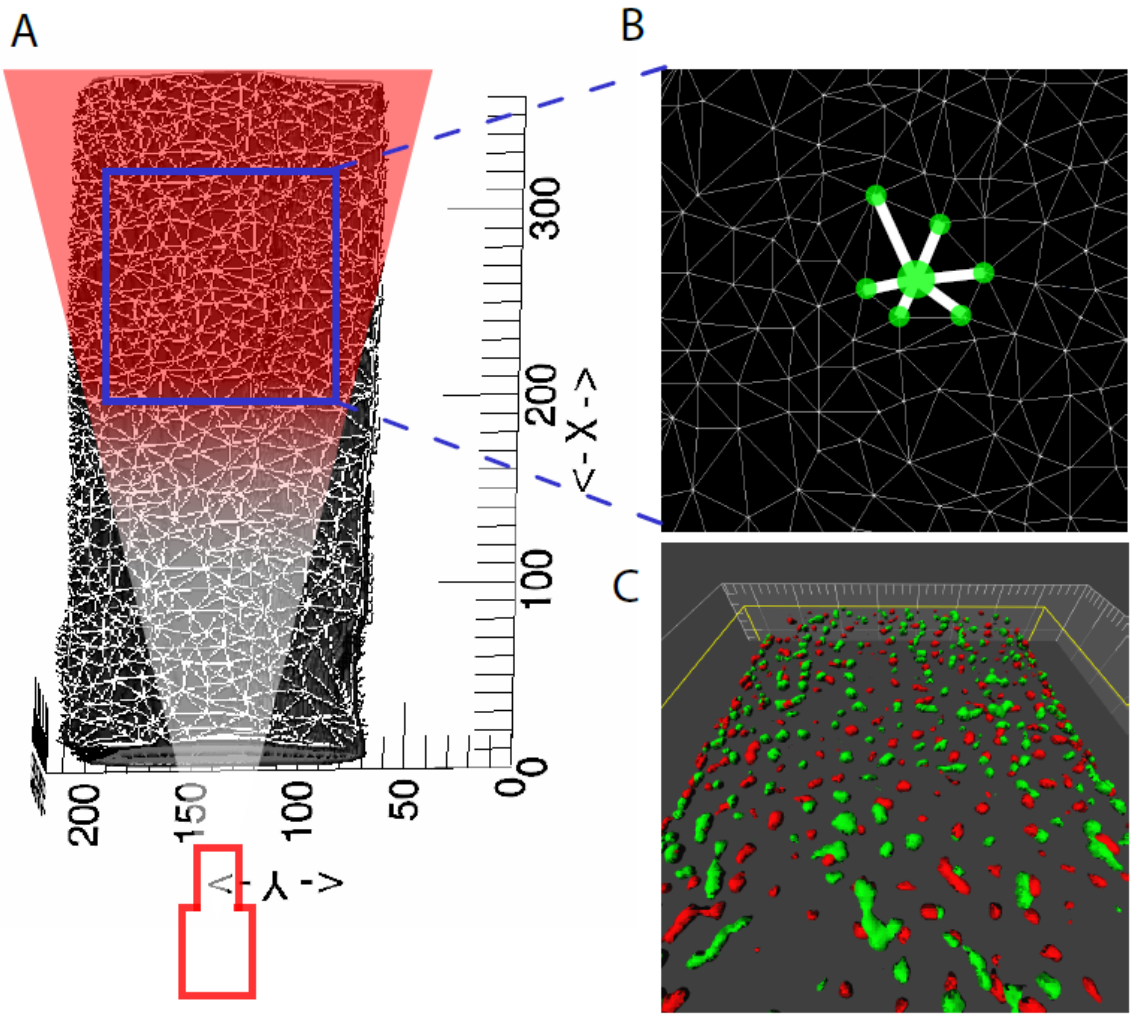

Figure 4.8 Distance to closest neighbour

Distance analysis was used to quantify the separation distances to the closest neighbouring object: between two NCX objects, two cav-3 objects and from a NCX object to a cav-3 object. Figure 4.8A shows NCX to NCX separation distances for the different developmental stages in closed circles (right curve) and NCX to cav-3 separation distances in open squares (left curve). Figure 4.8B show the cav-3 to cav-3 separation distances.

A

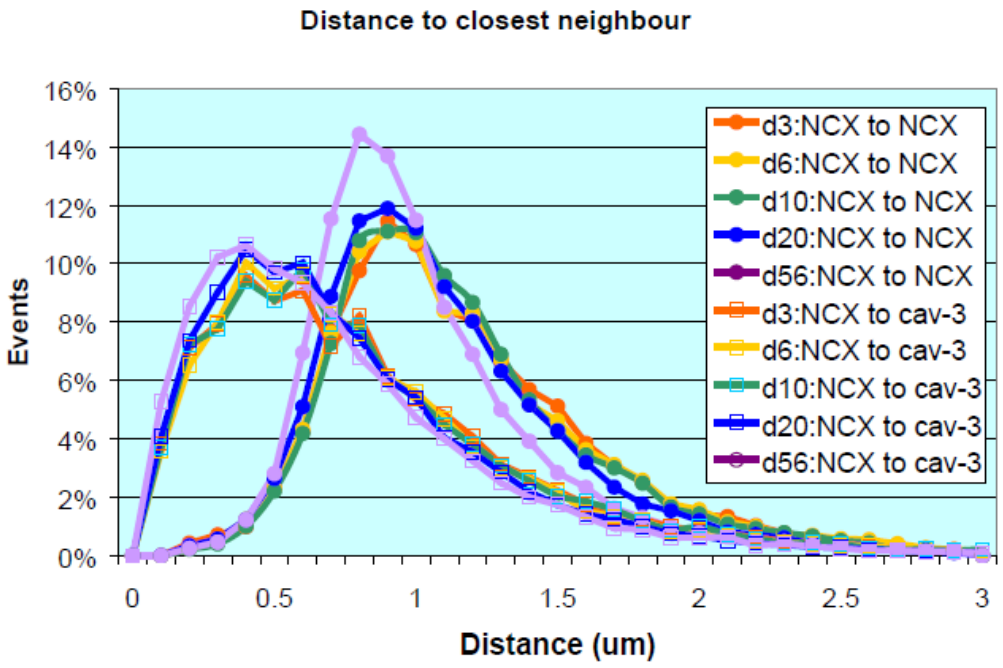
Distance to closest neighbour
16%
14%
12%
10%
8%
6%
4%
2%
0%
Events
0
0.5
1
1.5
2
2.5
3
Distance (um)
d3:NCX to NCX
d6:NCX to NCX
d10:NCX to NCX
d20:NCX to NCX
d56:NCX to NCX
d3:NCX to cav-3
d6:NCX to cav-3
d10:NCX to cav-3
d20:NCX to cav-3
d56:NCX to cav-3

B

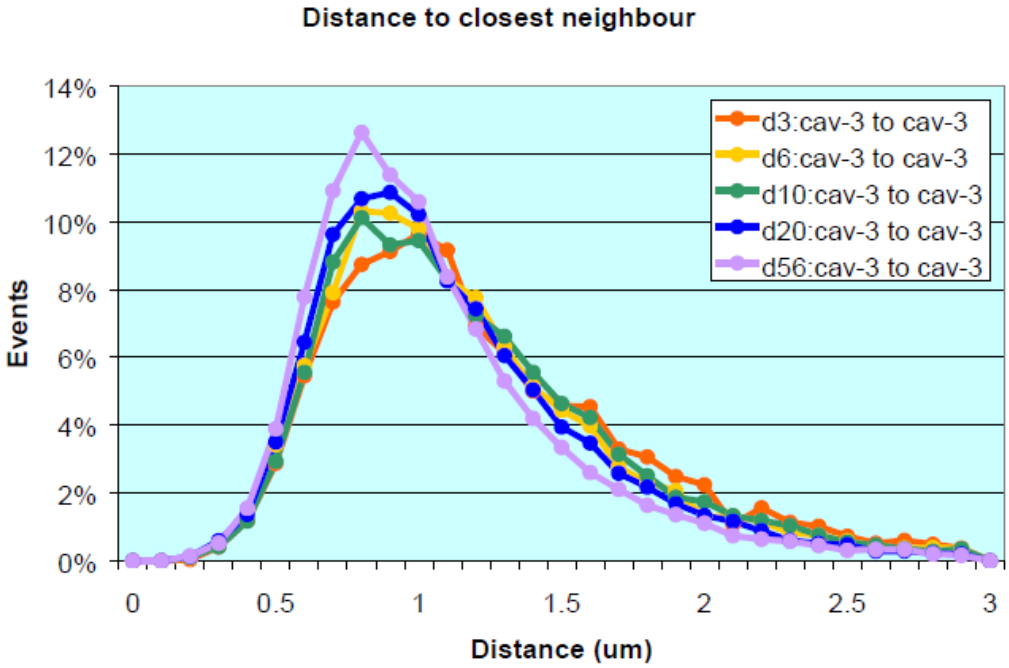
Distance to closest neighbour
14%
12%
10%
8%
6%
4%
2%
0%
Events
0
0.5
1
1.5
2
2.5
3
Distance (um)
d3:cav-3 to cav-3
d6:cav-3 to cav-3
d10:cav-3 to cav-3
d20:cav-3 to cav-3
d56:cav-3 to cav-3

Figure 4.9 Peripheral lateral and longitudinal separation

Lateral and longitudinal neighbours were defined as objects that were located ±15% from the lateral and longitudinal axis relative to the center node. The left columns (A, C, E) indicate lateral separation distances while the right columns (B, D, F) indicate longitudinal separations distances. NCX to NCX (A, B) and cav-3 to cav-3 (C, D) distances are shown in the top row and middle row, respectively. Figures 9E and 9F show the lateral and longitudinal separation distances between NCX and cav-3 objects.

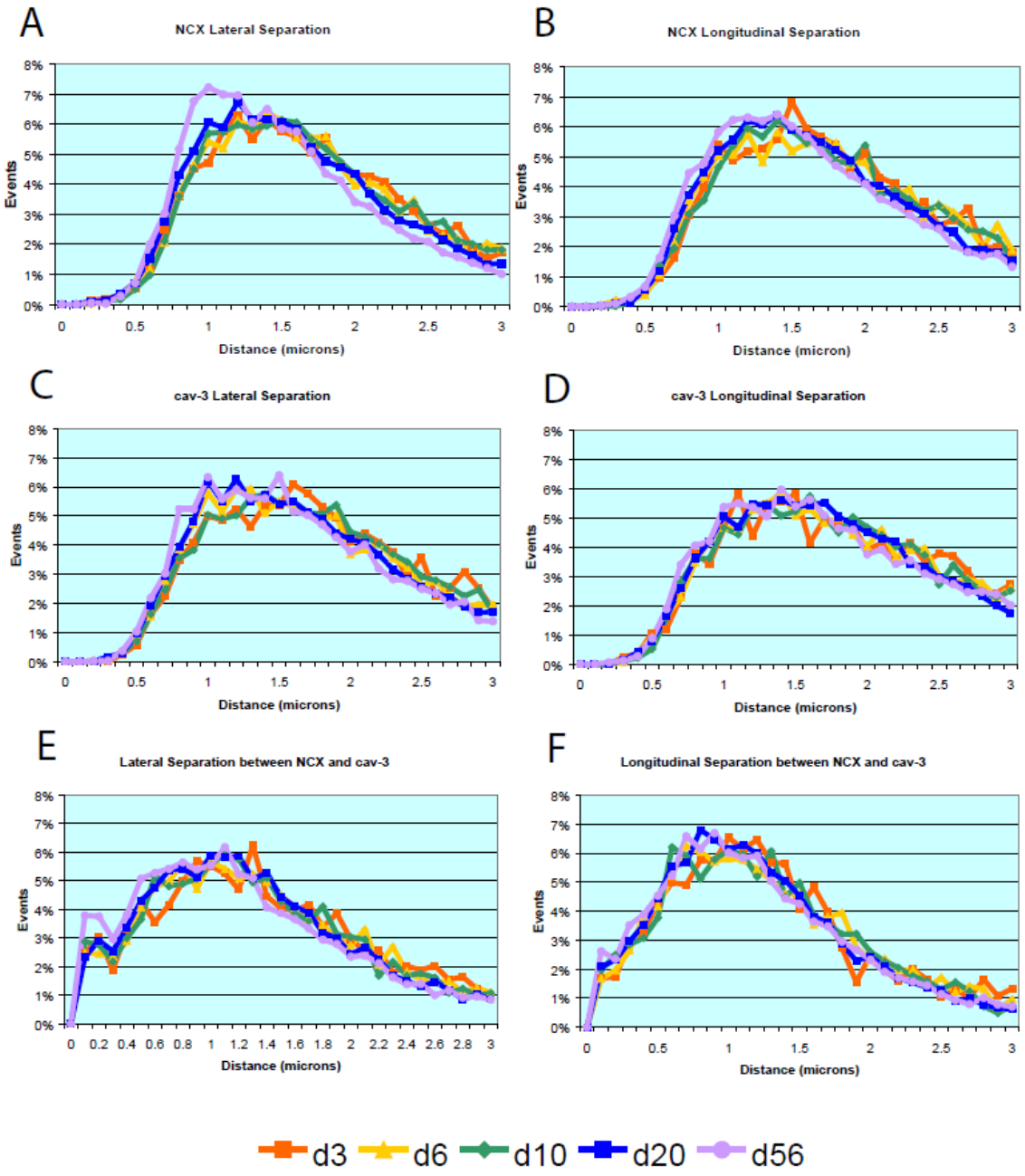
A
NCX Lateral Separation
Events
Distance (microns)
B
NCX Longitudinal Separation
Events
Distance (micron)
C
cav-3 Lateral Separation
Events
Distance (microns)
D
cav-3 Longitudinal Separation
Events
Distance (microns)
E
Lateral Separation between NCX and cav-3
Events
Distance (microns)
F
Longitudinal Separation between NCX and cav-3
Events
Distance (microns)
d3
d6
d10
d20
d56

Figure 4.10 Directionality of neighbouring objects

Distances to the closest neighbour (Figure 4.8) as well as lateral and longitudinal separation distance profiles (Figure 4.9) suggested that the distribution patterns of NCX and cav-3 objects on the periphery do not change with development. To take advantage of this property, object neighbour data were pooled and the angular relationship between neighbours was derived. Figures 4.10A and 4.10B show the relative angular relationship between NCX neighbours and cav-3 neighbours, respectively. Angle labels represent the direction of the neighbour relative the center object. The longitudinal direction is oriented vertically while the lateral direction is oriented horizontally in these graphs. Figure 4.10C shows cumulated data from all 5 age groups and is oriented the same as Figure 4.10A and Figure 4.10B. NCX to NCX distances are shown in red and cav-3 to cav-3 distances are shown in green. NCX to cav-3 separation distances are shown in yellow.

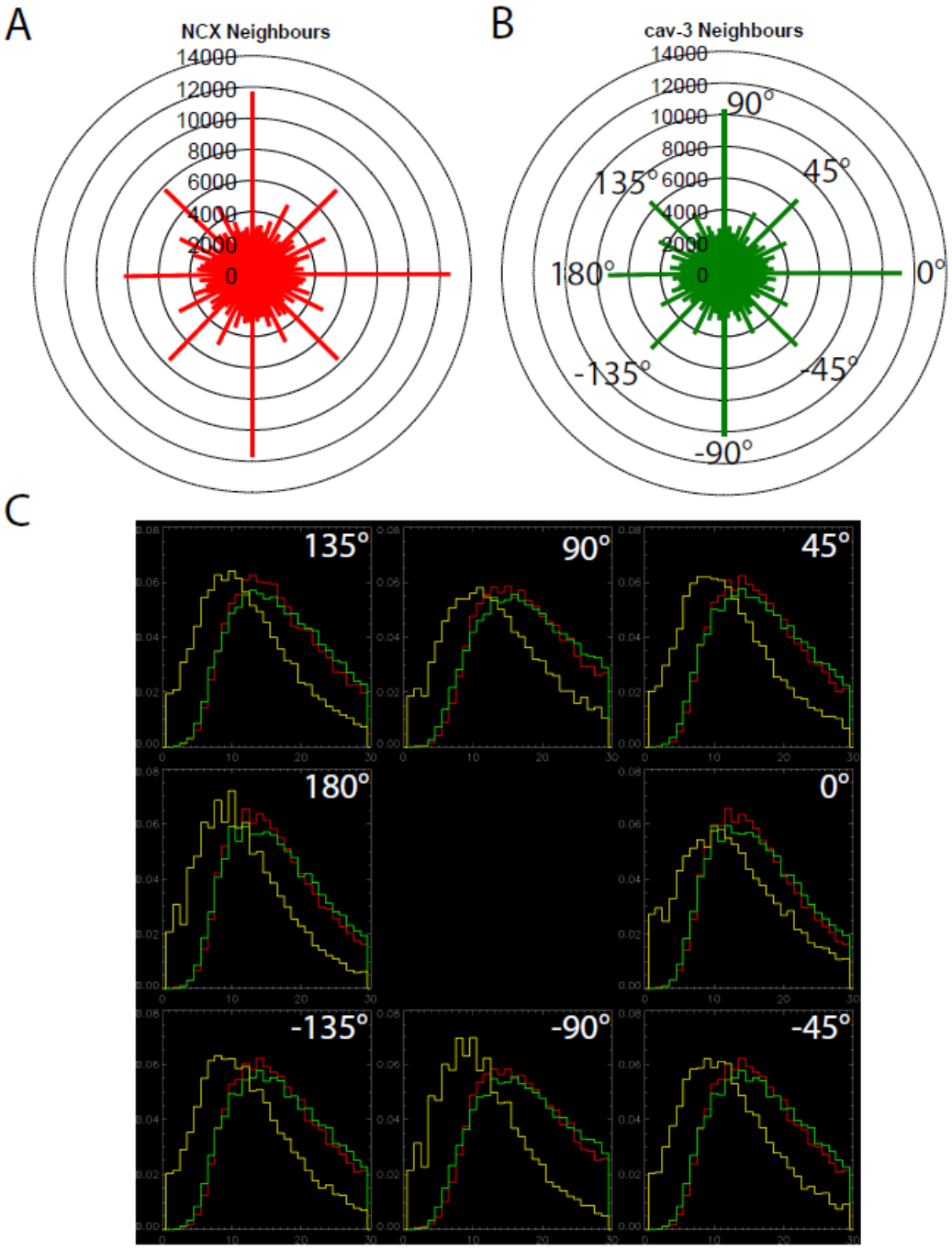
A
NCX Neighbours
14000
12000
10000
8000
6000
4000
2000
0
B
cav-3 Neighbours
14000
12000
10000
8000
6000
4000
2000
0
90°
45°
135°
180°
0°
-135°
-45°
-90°
C
135°
90°
45°
180°
0°
-135°
-90°
-45°

Figure 4.11 Interior separation distances

Separation distances were also determined from NCX and cav-3 objects directly beneath the peripheral compartment. The longitudinal separation for NCX to NCX is shown with square symbols while the lateral separation is shown with triangle symbols. The longitudinal separation of cav-3 to cav-3 is shown with diamonds while the lateral separation is shown with circles.

Figure 4.12 Noise Reduction

Cell outline extraction as described the manuscript is highly sensitive to extraneous non-cellular fluorescence as morphological closing tends to include rather than exclude non-cellular features. A single errant pixel can introduce large errors in the cell outline estimate. However, because the effects of errant pixels on the cell outline are systematic we were able to create a "anti-noise mask" that could be used to eliminate the effects of these errant pixels. Because the noise tends to be much smaller than the actual cell itself, morphological erosion can be used to eliminate objects that are smaller than a given diameter. By eroding cross-sectional images sequentially using a kernel (radius =1) and then dilating sequentially with the same kernel the anti-noise mask can be formed. The separation distance between the edge of the noise mask and the actual cell outline could be set by applying more dilations than erosions. In our analysis we used 7 erosion repeats and 10 dilations repeats to give us a separation distance between the cell surface and the noise mask of 3 pixels (some distance is required to avoid influencing the actual cell outline estimate). This anti-noise mask is then applied the original NCX and cav-3 images and a new cell outline is generated.

Top : A cross-sectional image of a 6 day myocytes with the raw cell outline shown in blue. White arrows showing image noise and its effect on the determined cell outline.

Middle: Generation of a noise mask; shown in white is the cell outline after 7 erosion repeats and shown in blue is the result after 10 dilation repeats. White arrows show the effect of the dilation repeats. The resulting cell mask excludes the noise present in the top figure.

Bottom: Final cell outline after masking applying the noise mask to original images. Cell outline is not unaffected by the image noise.

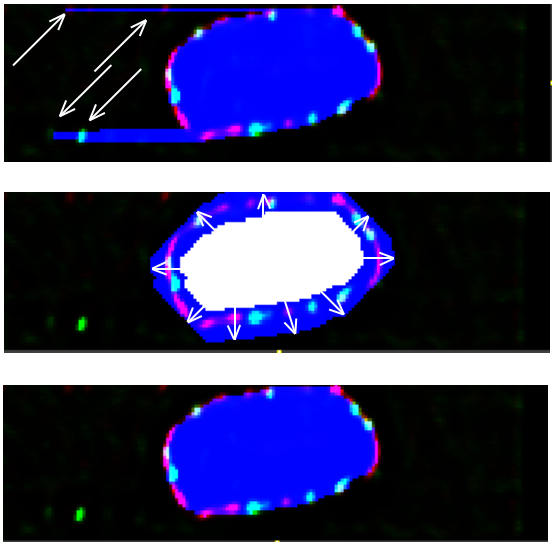

Figure 4.13 Three-Dimensional Distance Analysis:

Top: In order to limit the complexity of the calculations, a binary reference image was created from the 3D co-ordinates of the surface peel. This reference image had N columns and M rows, where N is equal to the circumference of the cell and M is equal to the length of the cell. Therefore, each X'Y' position in the reference image corresponds to a XYZ co-ordinate in the original image volume. The "pixel value" for each X'Y' co-ordinate in the reference image was determined by the location of the surface clusters of NCX or cav-3. For each cluster, its center of mass was determined and if the object is located on the surface a "1" would be placed in the appropriate X'Y' location in the reference image, such that, each surface object would be represented in the reference image by a single lit pixel.

Bottom: To determine the separation distance between any two particular surface objects one simply draws a connecting line between the two objects references on the X'Y' reference image and extracts a list of XYZ co-ordinates for the connecting voxels. The separation distance along the curvature of the cell is the sum of the individual separation distances between voxels

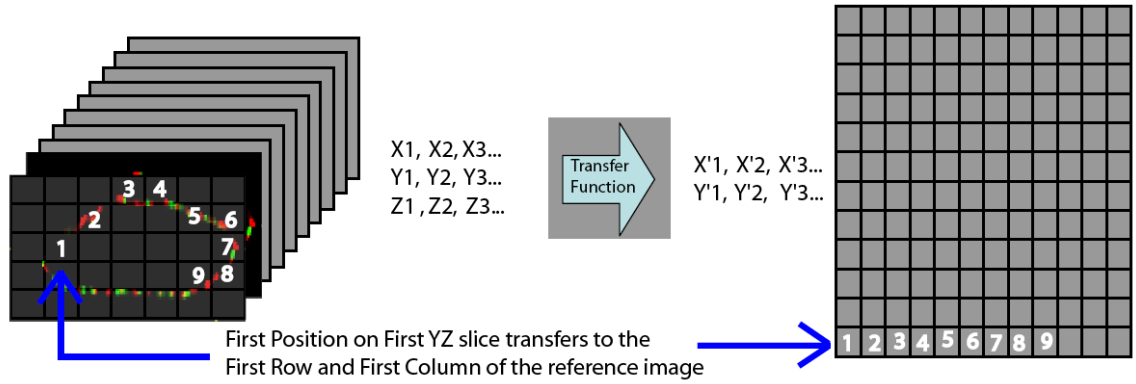
X1, X2, X3...
Y1, Y2, Y3...
Z1 , Z2, Z3...
Transfer Function
X'1, X'2, X'3...
Y'1, Y'2, Y'3...
First Position on First YZ slice transfers to the
First Row and First Column of the reference image
1 2 3 4 5 6 7 8 9

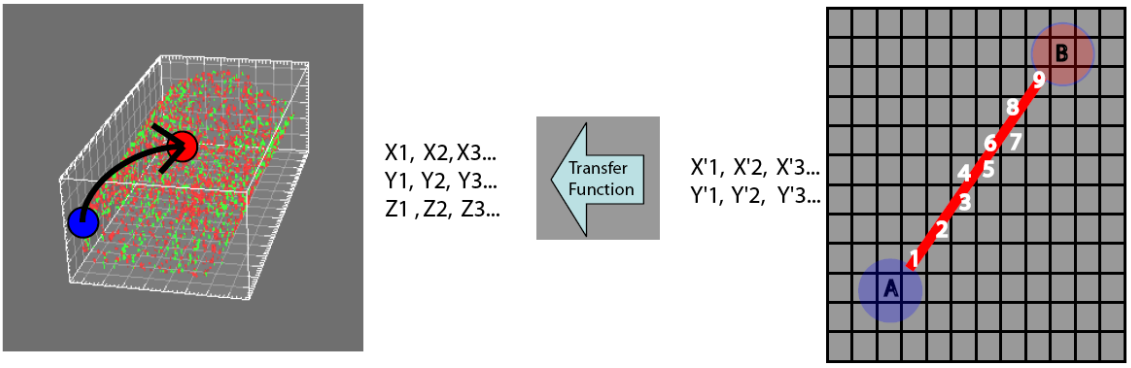
X1, X2, X3...
Y1, Y2, Y3...
Z1 , Z2, Z3...
Transfer Function
X'1, X'2, X'3...
Y'1, Y'2, Y'3...
A
B

Table 4.1 Statistical tests of colocalization indices

NCX whole cell colocalization

ANOVA RESULT		0			
age: mean (sterr)	d3	d6	d10	d20	d56
d3: 10.105 (0.7008)		0.0078	0.0458	0.4291	<0.0005*
d6: 8.063 (0.3508)			0.1563	<0.0005*	<0.0005*
d10: 8.812 (0.5400)				0.0172	<0.0005*
d20: 9.941 (0.3481)					<0.0005*
d56: 14.800 (0.8564)					

Peripheral NCX colocalization

ANOVA RESULT		0			
age: mean (sterr)	d3	d6	d10	d20	d56
d3: 10.183 (0.7093)		0.0087	0.0458	0.3544	<0.0005*
d6: 8.167 (0.3570)			0.2023	<0.0005*	<0.0005*
d10: 8.827 (0.5509)				0.0194	<0.0005*
d20: 9.900 (0.3684)					<0.0005*
d56: 14.133 (1.1052)					

cav-3 whole cell colocalization

ANOVA RESULT		0			
age: mean (sterr)	d3	d6	d10	d20	d56
d3: 8.648 (0.6193)		0.2058	0.1214	0.3073	<0.0005*
d6: 8.496 (0.6610)			0.4427	0.016	<0.0005*
d10: 7.833 (0.4525)				0.0148	<0.0005*
d20: 9.108 (0.3251)					<0.0005*
d56: 12.693 (0.6283)					

Peripheral NCX colocalization

ANOVA RESULT		0			
age: mean (sterr)	d3	d6	d10	d20	d56
d3: 8.860 (0.6223)		0.2313	0.1818	0.1903	<0.0005*
d6: 8.889 (0.6682)			0.4872	0.0117	<0.0005*
d10: 8.344 (0.4823)				0.0126	<0.0005*
d20: 9.751 (0.3767)					<0.0005*
d56: 12.562 (0.6931)					

Interior NCX colocalization

ANOVA RESULT		0			
age: mean (sterr)	d3	d6	d10	d20	d56
d10: 8.333 (0.7458)				0.0194	<0.0005*
d20: 9.998 (0.4525)					<0.0005*
d56: 17.157 (1.1360)					

Percentage NCX on cell periphery

ANOVA RESULT		0			
age: mean (sterr)	d3	d6	d10	d20	d56
d3: 98.455 (0.4391)		0.0625	<0.0005*	<0.0005*	<0.0005*
d6: 97.455 (0.4753)			<0.0005*	<0.0005*	<0.0005*
d10: 92.916 (0.7917)				<0.0005*	<0.0005*
d20: 87.199 (0.8240)					<0.0005*
d56: 73.314 (1.5044)					

Interior cav-3 colocalization

ANOVA RESULT		0			
age: mean (sterr)	d3	d6	d10	d20	d56
d10: 4.073 (0.3911)				<0.0005*	<0.0005*
d20: 6.267 (0.3648)					<0.0005*
d56: 12.732 (0.6878)					

Percentage NCX on cell periphery

ANOVA RESULT		0			
age: mean (sterr)	d3	d6	d10	d20	d56
d3: 96.740 (0.5541)		<0.0005*	<0.0005*	<0.0005*	<0.0005*
d6: 93.968 (0.6995)			<0.0005*	<0.0005*	<0.0005*
d10: 87.319 (1.0064)				<0.0005*	<0.0005*
d20: 81.277 (0.9329)					<0.0005*
d56: 69.517 (1.6096)					

Table 4.2 Statistical tests of peripheral object specific colocalization

Peripheral NCX objects with colocalization events (%)

ANOVA RESULT		0.0098			
age: mean (sterr)	d3	d6	d10	d20	d56
d3: 32.914 (1.6278)		0.2798	0.0917	0.4419	0.0323
d6: 32.895 (1.5674)			0.1602	0.1187	0.0021*
d10: 30.280 (1.6155)				0.0334	<0.0005*
d20: 33.486 (0.9419)					0.007
d56: 36.704 (1.1400)					

NCX object specific colocalization (%)

ANOVA RESULT		0			
age: mean (sterr)	d3	d6	d10	d20	d56
d3: 17.000 (0.8824)		<0.0005*	0.2688	0.3424	0.028
d6: 13.427 (0.4851)			<0.0005*	<0.0005*	<0.0005*
d10: 16.344 (0.5405)				0.3299	<0.0005*
d20: 16.931 (0.5212)					<0.0005*
d56: 21.095 (1.2512)					

Peripheral cav-3 objects with colocalization events (%)

ANOVA RESULT		0.0002			
age: mean (sterr)	d3	d6	d10	d20	d56
d3: 37.905 (1.4066)		<0.0005*	0.0427	0.0742	0.1737
d6: 32.619 (1.0062)			0.1681	0.0048*	<0.0005*
d10: 34.416 (1.2061)				0.1828	<0.0005*
d20: 35.784 (0.6963)					0.0030*
d56: 39.816 (1.2147)					

cav-3 object specific colocalization (%)

ANOVA RESULT		0			
age: mean (sterr)	d3	d6	d10	d20	d56
d3: 13.792 (0.8125)		0.3096	0.4484	0.0071	<0.0005*
d6: 15.039 (0.8719)			0.2766	0.014	<0.0005*
d10: 13.622 (0.5972)				<0.0005*	<0.0005*
d20: 16.124 (0.4543)					0.0009*
d56: 18.767 (0.7744)					

Percentage of NCX objects with more than 50% colocalization

ANOVA RESULT		0.0388			
age: mean (sterr)	d3	d6	d10	d20	d56
d3: 6.586 (0.5948)		0.0039*	0.0559	0.0441	0.475
d6: 4.815 (0.2779)			0.1722	0.1195	0.0064
d10: 5.445 (0.3854)				0.4177	0.0978
d20: 5.462 (0.2597)					0.0447
d56: 6.880 (0.7083)					

Contributions of highly colocalized NCX objects (peripheral)

ANOVA RESULT		0.0259			
age: mean (sterr)	d3	d6	d10	d20	d56
d3: 20.176 (1.7022)		0.0201	0.4228	0.3131	0.3082
d6: 15.755 (1.1428)			<0.0005*	0.0265	0.0049*
d10: 21.476 (1.4698)				0.1278	0.4909
d20: 19.213 (1.0143)					0.1223
d56: 22.457 (1.9977)					

Percentage of cav-3 objects with more than 50% colocalization

ANOVA RESULT		0.0532			
age: mean (sterr)	d3	d6	d10	d20	d56
d3: 5.405 (0.4630)		0.0801	0.0116	0.1056	0.3535
d6: 4.982 (0.4371)			0.1602	0.2206	0.0699
d10: 4.096 (0.2500)				0.0188	0.0034*
d20: 4.937 (0.2467)					0.1426
d56: 5.451 (0.4100)					

Contributions of highly colocalized cav-3 objects (peripheral)

ANOVA RESULT		0.3918			
age: mean (sterr)	d3	d6	d10	d20	d56
d3: 15.330 (1.8154)		0.2798	0.0636	0.2904	0.1658
d6: 15.100 (1.5986)			0.1276	0.4825	0.2232
d10: 11.564 (0.6802)				0.0238	0.2551
d20: 13.910 (0.7901)					0.2272
d56: 12.900 (1.1749)					

Table 4.3 Statistical tests of interior object specific colocalization

Interior NCX objects with colocalization events (%)

ANOVA RESULT		0
age: mean (sterr)	d20	d56
d10: 20.195 (1.6687)	<0.0005*	<0.0005*
d20: 27.716 (0.9691)		<0.0005*
d56: 35.927 (2.2024)		

NCX object specific colocalization (%)

ANOVA RESULT		0
age: mean (sterr)	d20	d56
d10: 20.022 (1.2415)	0.0183	<0.0005*
d20: 23.563 (0.9282)		<0.0005*
d56: 29.888 (1.4789)		

Interior cav-3 objects with colocalization events (%)

ANOVA RESULT		0.0001
age: mean (sterr)	d20	d56
d10: 11.138 (1.1720)	<0.0005*	<0.0005*
d20: 19.932 (0.9690)		<0.0005*
d56: 33.978 (1.2522)		

cav-3 object specific colocalization (%)

ANOVA RESULT		0.0006
age: mean (sterr)	d20	d56
d10: 16.288 (1.1773)	0.1861	<0.0005*
d20: 16.970 (0.5869)		<0.0005*
d56: 20.915 (0.8620)		

Percentage of NCX objects with more than 50% colocalization

ANOVA RESULT		0
age: mean (sterr)	d20	d56
d10: 5.039 (0.5659)	<0.0005*	<0.0005*
d20: 7.206 (0.3953)		<0.0005*
d56: 10.998 (1.1383)		

Contributions of highly colocalized NCX objects

ANOVA RESULT		0.0336
age: mean (sterr)	d20	d56
d10: 28.406 (4.0749)	0.0108	0.0127
d20: 37.472 (2.1359)		0.2029
d56: 39.730 (3.1366)		

Percentage of cav-3 objects with more than 50% colocalization

ANOVA RESULT		0
age: mean (sterr)	d20	d56
d10: 1.378 (0.2119)	<0.0005*	<0.0005*
d20: 2.458 (0.2161)		<0.0005*
d56: 4.426 (0.5345)		

Contributions of highly colocalized cav-3 objects

ANOVA RESULT		0.9821
age: mean (sterr)	d20	d56
d10: 15.386 (2.7095)	0.4505	0.4348
d20: 14.408 (1.2345)		0.4385
d56: 14.965 (1.7359)		

4.6. REFERENCES

1. Bers DM. Calcium cycling and signaling in cardiac myocytes. *Annu Rev Physiol.* 2008;70:23-49.

2. Huang J, Hove-Madsen L, Tibbits GF. Ontogeny of Ca^{2+}-induced Ca^{2+} release in rabbit ventricular myocytes. *Am J Physiol Cell Physiol.* 2008;294(2):C516-525.

3. Artman M, Ichikawa H, Avkiran M, Coetzee WA. Na^{+}/Ca^{2+} exchange current density in cardiac myocytes from rabbits and guinea pigs during postnatal development. *Am J Physiol.* 1995;268(4 Pt 2):H1714-1722.

4. Boerth SR, Zimmer DB, Artman M. Steady-state mRNA levels of the sarcolemmal Na^{+}-Ca^{2+} exchanger peak near birth in developing rabbit and rat hearts. *Circ Res.* 1994;74(2):354-359.

5. Artman M. Sarcolemmal Na^{+}-Ca^{2+} exchange activity and exchanger immunoreactivity in developing rabbit hearts. *Am J Physiol.* 1992;263(5 Pt 2):H1506-1513.

6. Vetter R, Studer R, Reinecke H, Kolar F, Ostadalova I, Drexler H. Reciprocal changes in the postnatal expression of the sarcolemmal Na^{+}-Ca^{2+}-exchanger and SERCA2 in rat heart. *J Mol Cell Cardiol.* 1995;27(8):1689-1701.

7. Harrell MD, Harbi S, Hoffman JF, Zavadil J, Coetzee WA. Large-scale analysis of ion channel gene expression in the mouse heart during perinatal development. *Physiol Genomics.* 2007;28(3):273-283.

8. Huang J, Hove-Madsen L, Tibbits GF. Na^{+}/Ca^{2+} exchange activity in neonatal rabbit ventricular myocytes. *Am J Physiol Cell Physiol.* 2005;288(1):C195-203.

9. Wetzel GT, Chen F, Klitzner TS. L- and T-type calcium channels in acutely isolated neonatal and adult cardiac myocytes. *Pediatr Res.* 1991;30(1):89-94.

10. Huang J, Xu L, Thomas M, Whitaker K, Hove-Madsen L, Tibbits GF. L-type Ca^{2+} channel function and expression in neonatal rabbit ventricular myocytes. *Am J Physiol Heart Circ Physiol.* 2006;290(6):H2267-2276.

11. Sedarat F, Lin E, Moore ED, Tibbits GF. Deconvolution of confocal images of dihydropyridine and ryanodine receptors in developing cardiomyocytes. *J Appl Physiol.* 2004;97(3):1098-1103.

12. Lines GT, Sande JB, Louch WE, Mork HK, Grottum P, Sejersted OM. Contribution of the Na^{+}/Ca^{2+} exchanger to rapid Ca^{2+} release in cardiomyocytes. *Biophys J.* 2006;91(3):779-792.

13. Frank JS, Mottino G, Reid D, Molday RS, Philipson KD. Distribution of the Na^{+}-Ca^{2+} exchange protein in mammalian cardiac myocytes: an immunofluorescence and immunocolloidal gold-labeling study. *J Cell Biol.* 1992;117(2):337-345.

14. Chen F, Mottino G, Klitzner TS, Philipson KD, Frank JS. Distribution of the Na^{+}/Ca^{2+} exchange protein in developing rabbit myocytes. *Am J Physiol.* 1995;268(5 Pt 1):C1126-1132.

15. Dan P, Lin E, Huang J, Biln P, Tibbits GF. Three-dimensional distribution of cardiac Na^{+}-Ca^{2+} exchanger and ryanodine receptor during development. *Biophysical journal.* 2007;93:2504-2518.

16. Razani B, Woodman SE, Lisanti MP. Caveolae: from cell biology to animal physiology. *Pharmacol Rev.* 2002;54(3):431-467.

17. Williams TM, Lisanti MP. The caveolin proteins. *Genome Biol.* 2004;5(3):214.

18. Bossuyt J, Taylor BE, James-Kracke M, Hale CC. Evidence for cardiac sodium-calcium exchanger association with caveolin-3. *FEBS Lett.* 2002;511(1-3):113-117.

19. Scriven DR, Klimek A, Asghari P, Bellve K, Moore ED. Caveolin-3 is adjacent to a group of extradyadic ryanodine receptors. *Biophys J.* 2005;89(3):1893-1901.

20. Cavalli A, Eghbali M, Minosyan TY, Stefani E, Philipson KD. Localization of sarcolemmal proteins to lipid rafts in the myocardium. *Cell Calcium.* 2007;42(3):313-322.

21. Scriven DR, Dan P, Moore ED. Distribution of proteins implicated in excitation-contraction coupling in rat ventricular myocytes. *Biophys J.* 2000;79(5):2682-2691.

5. COLOCALIZATION OF VOLTAGE-GATED SODIUM CHANNELS WITH THE NA^+/CA^{2+} EXCHANGER IN RABBIT CARDIOMYOCYTES DURING DEVELOPMENT[4]

5.1. INTRODUCTION

The established mechanism for excitation contraction coupling (ECC) in the adult cardiomyocyte is via depolarisation-triggered calcium entry through $Ca_v1.2$, also known as the voltage-gated L-type calcium channel. Activation of $Ca_v1.2$ mediates 'calcium-induced-calcium-release' or CICR [1]. In CICR a small calcium current (I_{Ca}) entering through $Ca_v1.2$ channels triggers the release of intracellular Ca^{2+} stored in the sarcoplasmic reticulum (SR) through the activation of the ryanodine receptor (RyR). RyR is a calcium-release channel on the SR. This release of SR calcium through the RyR elevates cytosolic calcium and activates cross bridge cycling and myocyte shortening.

Theoretically calcium release from the SR can also be triggered by reverse mode Na-Ca exchange. The Na-Ca exchanger (NCX) is a reversible antiporter exchanging 3 sodium ions for 1 calcium ion [2]. In most conditions the transsarcolemmal sodium and calcium gradients favour calcium extrusion by the NCX, and this is referred to as forward-mode NCX. However, reverse-mode NCX activity can generate sarcolemmal calcium entry if the membrane potential is strongly depolarized and/or the cytosolic sodium concentration is elevated [3].

One of the first reports of reverse-mode NCX mediated CICR came from LeBlanc and Hume in which a tetrodotoxin-sensitive calcium influx was identified in guinea pig cardiomyocytes suggesting a link between I_{Na} and NCX . It has been hypothesized that, despite the large peak sodium current, the rapid inactivation of I_{Na} prevents sufficient elevation in cytosolic sodium to induce reverse-mode NCX activity [4, 5]. However, if sodium channels and

[4] A version of this chapter has been submitted for publication. Cynthia Gershome, Eric Lin, Haruyo Kashihara, Leif Hove-Madsen and Glen F Tibbits. Colocalization of voltage-gated sodium channels with the Na^+/Ca^{2+} exchanger in rabbit cardiomyocytes during development.

NCX were functionally coupled in a restricted micro-domain then the sodium current could potentially elevate the sodium concentration sufficiently to activate reverse-mode NCX. This is often referred to as the 'fuzzy space' or restricted microdomain hypothesis. However, the significance and contribution of such I_{Na}-NCX coupling is not clear as other reports using cardiomyocytes from a variety of species show a more predominant effect of the calcium current in EC coupling [6-9].

The presence of a functional micro-domain with I_{Na}-NCX coupling may be more important in neonatal EC coupling because NCX densities are several fold higher [10, 11] and NCX plays a more prominent role than I_{Ca} [12-16]. We have also shown that NCX is distributed in punctuate clusters along the peripheral membrane, and that this distribution persists throughout development [17, 18]. This non-homogeneous distribution suggests that multiple NCX molecules may form functional units that act in concert to mediate EC coupling.

The stoichiometry of NCX transport renders the reversal potential of NCX intensely sensitive to cytosolic $[Na^+]$ and small changes in global $[Na^+]$ are expected to mediate large changes in the I_{NCX} [19]. In fact, modelling experiments have reported that a solitary sodium channel could be sufficient to induce reverse-mode NCX in a dyadic cleft if the influx is concomitant with greatly reduced sodium mobility [20]. Thus sodium channels localized within localized clusters of NCX are expected to have important functional consequences. The predominant cardiac sodium channel isoform is $Na_v1.5$, but isoforms more commonly associated with neuronal ($Na_v1.1$, 1.3, 1.6) and skeletal ($Na_v1.4$) tissues have also been reported in cardiomyocytes. The first report of $Na_v1.5$ localisation in rat cardiac myocytes suggested that $Na_v1.5$ was positioned along t-tubule membranes as well as along the intercalated disc regions of adjoining cells [21]. However, in these earlier reports the specificity of the antibody was questioned. Subsequently, in mouse heart $Na_v1.5$ was found to be localized predominately to the intercalated discs and $Na_v1.1$, $Na_v1.3$ and $Na_v1.6$ demonstrated expression along the t-tubular membranes [22, 23]. A recent study reported $Na_v1.1$-1.6 expression in cultured neonatal rat myocytes [24]. However, localisation of these isoforms relative to NCX has not yet been investigated as a function of development.

Therefore, the aim of this study was to investigate the relationship between NCX and various voltage-gated sodium channel isoforms in order to determine whether the prominent

NCX activity in neonatal myocytes is regulated by closely associated sodium channels. Western blot analysis showed that, of the sodium channel isoforms $Na_v1.1$-1.6, only $Na_v1.1$, 1.4 and 1.5 are expressed in detectable amounts in the developing rabbit heart. Moreover, $Na_v1.1$ and $Na_v1.4$ had more profound expression profiles in the neonate than in the adult whereas $Na_v1.5$ expression did not change significantly with development. The expression of $Na_v1.4$ and $Na_v1.5$ was sufficient in both age groups to determine the age-dependent changes in the co-localization of each isoforms with the NCX.

5.2. MATERIALS AND METHODS

Isolation of cardiac myocytes

Animals were cared for in accordance with the principles established by the Canadian Council on Animal Care (CCAC). The Simon Fraser University Animal Care Committee approved the use of animals and the experimental protocol used in this study in accordance with the CCAC regulations. Single ventricular myocytes were isolated from the hearts of New Zealand White rabbits of either sex from 3 and 56 days old (post-partum) by an enzymatic method as previously described [13, 25].

Antibodies

In our experiments, the distribution and localization of sodium channels by immunocytochemistry in some cases required different antibodies than the antibodies used to detect sodium channels in western blots. The antibodies employed in western blots react well with fully denatured proteins (unfolded) while they might not recognize the native conformation of the protein (folded) in immunocytochemistry techniques. Commercial antibodies used for Western blots were from the following sources: anti-$Na_v1.4$ (sc-28751) was from Santa Cruz Biotechnology (Santa Cruz, CA), anti-human $Na_v1.5$ and anti-$Na_v1.1$ (ASC-001) was from Alomone labs (Jerusalem, Israel). Monoclonal anti-actin (A3853) was from Sigma (St. Louis, MO). For immunocytochemistry we used anti-$Na_v1.4$ (pab0280, Covalab) which was also tested on western blots to confirm specificity. For $Na_v1.5$ immunolabelling, we used anti-$Na_v1.5$ (sc-22758, Santa Cruz), which recognizes 971-1140 amino acids in the internal region of human $Na_v1.5$. Anti-NCX.1 (MA3-926) was from Affinity Bioreagent (Golden, CO).

Immunoblot analysis

Cardiomyocytes were lysed with ice cold lysis buffer containing in mM: (25 Tris, 150 NaCl, 1 EGTA, 1 EDTA, 1 DTT, and 1% Triton X 100, pH 7.5) supplemented with protease inhibitor cocktail (Roche), phosphatase inhibitor cocktail (Sigma) and 1 mM PMSF. 80 μg total

protein from the clarified detergent soluble lysate was resolved on 7.5% SDS-PAGE gel and transferred onto PVDF membrane (Immobilon-FL, Millipore, Toronto, ON). The membranes were incubated overnight with primary antibodies, anti-$Na_v1.4$ (1:200), anti-$Na_v1.5$ (1:200), anti-$Na_v1.1$ (1:200) diluted in TBS. The immunoreactive bands were detected by immobilon HRP substrate (Millipore). Where the signals were weak, we also used SuperSignal West Femto Maximum sensitivity substrate by Pierce. Detection of the chemiluminescent signals was captured by G: BOX chemi HR16 (Syngene, Frederick, MD) which uses a CCD camera for imaging thereby increasing the sensitivity and dynamic range of capturing chemiluminescent signals. Densitometry values were obtained by using Genetools software, version 4 (Syngene). The immunoblots were normalized with actin to ensure equal loading.

Immunolabelling and image acquisition

Isolated cardiomyocytes were processed as described previously [18]. Fixed cells were blocked with 10% goat serum in PBS for one hour at room temperature to block non-specific sites. Cells were then incubated overnight with primary antibodies directed against canine NCX1.1 (anti-NCX1.1, Affinity Bioreagent), $Na_v1.4$ (polyclonal antibody, Covalab) and $Na_v1.5$ (polyclonal antibody, Santa Cruz). After extensive washing, cells were mounted with Prolong slow fade reagent (Molecular Probes, Invitrogen). Control experiments: Control cells were stained the same way as above but primary antibodies specific for $Na_v1.4$, $Na_v1.5$ and NCX were replaced with normal rabbit IgG serum and normal mouse serum. The control images were very dim and a general diffuse pattern was observed (Fig 5.7-8). To control for secondary antibody cross-reactivity, $Na_v1.4$ labelled cells were stained with the secondary antibody as that of NCX (i.e. $Na_v1.4$ + IgM) and vice versa (NCX + IgG). Control cells were also incubated with secondary antibodies only without the primary antibodies. All the control images were acquired with the same settings as that of the experimental images.

Images were acquired with a Zeiss LSM 5 Pascal laser scanning microscope through a 63 X /1.4 NA Plan Apochromat oil immersion objective. ZEN (Carl Zeiss, Inc) imaging software was used to acquire the images. The confocal pinhole was set for 1 Airy disk and voxel samples occurred at 93 nm by 93 nm by 200 nm. Images were subsequently deconvolved to improve image quality [26]. The maximum likelihood estimation algorithm provided by Huygens

Professional version 2.4.1 was used (Scientific Volume Imaging, Hilversum, The Netherlands). Empirical point spread functions were generated using 200 nm 'Tetraspeck' latex beads (Invitrogen). After deconvolution, images were transferred to custom image analysis procedures written in Interactive Data Language version (IDL- 7.0.6). T-tests were used for statistical comparisons and were conducted from inside IDL.

Image processing and analysis

Image thresholding

Variability in image thresholding can adversely affect image analysis results. Thresholding defines areas of the image that have sufficient image intensity to be considered for analysis. However, in images that contain objects with a variety of intensities, simple binary thresholding will overestimate the size of bright objects while underestimating the size of dim objects. We previously developed an iterative thresholding procedure which utilized object counting to determine a thresholding value that generates the maximum number of independent objects [17]. Iterative thresholding effectively limits the number of dimly lit objects that are removed by thresholding. However, in protein distributions that are less densely spaced, such as in $Na_v1.4$ and $Na_v1.5$, less thresholding 'intensity' is required to partition the objects. As a result iterative thresholding will result in over-estimated object sizes due to the retention in object 'shoulder regions' due to the inclusion of lower intensity voxels. Since colocalization analysis is strongly affected by differential object sizes, we applied a secondary thresholding step to further refine object size. For each object a secondary thresholding value equal to half of the maximum image intensity contained in the object was applied. Effectively this secondary thresholding value applies the resolution definition of Full-Width Half-Maximum to each individual object. A diagram to explain these effects is found in Fig 5.14.

Colocalization analysis

In this report we utilized both voxel-by-voxel colocalization analysis (traditional colocalization) as well as object-based colocalization approaches [17]. Traditional colocalization analysis is best suited to protein-protein distributions in which both proteins have the exact same relationship throughout the sample. It is best suited for distinguishing between complete colocalization and complete non-colocalization in the distributions. Object-specific colocalization analysis calculates the colocalization index between individual pairs of objects and allows the objects pairs to be sorted based on their internal colocalization. In protein distributions where objects are all the same size, object-specific colocalization can be used to investigate the reliability of the traditional colocalization index. In such a scenario, the object-specific approach can be used to identify object pairs that generate colocalization events simply due to object blurring. Such events will generate low object-specific colocalization indices since only a proportion of the object are in fact overlapped. However, objects that are perfectly colocalized will generate much higher object-specific colocalization indices and thus the contribution of these higher probability colocalization events to the traditional colocalization index can be quantified. This is illustrated diagrammatically in Fig 5.15.

Nearest Neighbour Separation distances

Colocalization analysis, both voxel based and object based approaches, are sensitive to object sizing. Two objects can be perfectly colocalized yet not return a 100% colocalization index if the one object is smaller than the other object. One way to circumvent this limitation is to directly calculate the separation distance between the two objects. For small sub-resolution objects, the actual location of objects can be estimated from the 'centre-of-mass' of the objects. Protein-protein distributions containing a larger proportion of sub-resolution separation distances are more likely to contain true colocalization events. Thus separation distance profiles allow an estimate of protein-protein colocalization independent of the effects of non-matching object sizes.

5.3. RESULTS

Expression of $Na_v1.4$, 1.5 and 1.1 proteins during development

From the western blot analyses a specific band at 260 kDa (Fig. 5.1*A*) was observed, consistent with robust $Na_v1.4$ expression in the neonatal myocyte and with significantly decreased intensity in the adult. Omission of the primary antibody but inclusion of the secondary antibody resulted in no detectable signals, confirming the specificity of the 260 kDa bands. Neuronal sodium channel $Na_v1.1$ was lowly expressed and followed a similar pattern as $Na_v1.4$ as we observed a significant decrease in the $Na_v1.1$ protein levels in the adult cardiomyocyte lysate (Fig. 5.1*B*). Specificity of bands for $Na_v1.1$ were also confirmed by omitting the primary antibody and probing the blots with secondary antibody. Western blot analysis was also performed for $Na_v1.5$ expression. Fig. 5.1*C* shows specific bands at 227 kDa. No statistically significant changes in $Na_v1.5$ protein levels were found as a function of development. Two antibody control experiments were conducted for $Na_v1.5$. Omission of the primary antibody but inclusion of the secondary antibody resulted in no detectable signals. A $Na_V1.5$-specific blocking peptide was also used in conjunction with the normal primary antibody and also resulted in no detectable signals. All immunoblots were normalised to actin expression which in our hands did not vary with development. Alternative loading controls such as β-actin, α-tubulin, connexin-43 and GAPDH were also tested, however, these proteins showed developmental variability.

Distribution and colocalization analysis of NCX and $Na_V1.4$/$Na_V1.5$ during development

Images of $Na_v1.4$ and $Na_v1.5$ co-labelling with NCX, after imaging processing, for 3d and 56d myocytes are shown in Fig. 5.2. Images of $Na_v1.4$/$Na_v1.5$ with NCX prior to image processing (i.e. prior to deconvolution and thresholding procedures) are shown in Fig 5.9-12. $Na_v1.4$ labelling in 3d myocytes was distributed along the cell periphery in punctuate clusters. In 56d myocytes $Na_v1.4$ was also found on the cell periphery and some t-tubular labelling was evident. Clear t-tubular labelling is not seen in Fig. 5.2 due to the aggressive two staged thresholding approach we developed in order to specifically separate closely positioned point sources on the cell periphery. Although the radii of the t-tubules are small, their lengths are

within the resolvable limits of confocal microscopy, thus aggressive thresholding underestimates the connectivity within the t-tubular network. Connectivity within the t-tubular network is more easily examined in the unprocessed images (Fig 5.10, 5.12). The $Na_v1.5$ distribution was visually similar to the $Na_v1.4$ distribution in both the 3d and 56d groups.

In three day old myocytes, all sodium channel antibodies that indicated labelling on the cell periphery also demonstrated peri-nuclear staining. We also immunolabelled 3d and 56d myocytes with Pan-19 antibody as a positive control. Pan-19 recognizes the epitope corresponding to residues 1501-1518 of rat $Na_v1.1$ which is conserved in all known isoforms of $Na_v1.X$. Pan-19 labelling results gave a similar nuclear staining pattern as $Na_v1.4$ and $Na_v1.5$ labelling (Fig 5.13). Although, non-specific staining of the nucleus may nevertheless be present, image segmentation procedures used in this study precludes the nuclear staining from interfering with the colocalization analysis of the peripheral compartment. $Na_v1.1$ immunolabelling on 3d and 56d myocytes is not included in this study due to insufficient labelling intensity. Even at low laser power settings photobleaching prevented the acquisition of 3D image stacks of sufficient quality.

In order to analyze the spatial distribution of the two isoforms quantitatively, colocalization analysis for each isoform with the NCX was performed at three levels. First, conventional colocalization analysis was performed. As shown in Fig. 5.3*A*, analysis of $Na_v1.4$-to-NCX colocalization revealed no significant ($p > 0.15$) change with development. In contrast, $Na_v1.5$-to-NCX colocalization significantly drops by 50% (from 34% to 18%) over this period of development ($p<0.001$). A comparison between the two neonatal groups indicated that $Na_v1.5$-to-NCX and $Na_v1.4$-to-NCX colocalization was not statistically different ($p >0.28$). The same comparison in the 56d group, however, found a statistically significant difference ($p<0.001$) as shown in Fig 5.3*A*.

When analyzing the percentage of NCX voxels also containing $Na_v1.X$, the NCX-to-$Na_v1.4$ colocalization drops by 42% from 17% to 12% colocalization and is statistically different ($p<0.01$) (Fig. 5.3*B*). NCX-to-$Na_v1.5$ drops by 50% from 20% to 10% during development and the difference is statistically significant ($p<0.001$). Comparison of the NCX-to-$Na_v1.4$ and NCX-

to-$Na_v1.5$ colocalization among the two neonatal groups showed no statistical difference ($p= 0.14$) while the same comparison was statistically different for the 56d group ($p<0.05$).

Object-specific colocalization analysis of NCX and $Na_V1.4$/$Na_V1.5$ during development

Due to the limited resolution of confocal microscopy, colocalization events using conventional analysis can be generated between two objects which are, in fact, well separated [26]. Indeed, traditional colocalization indices relate the total number of voxels for one label with the total number of voxels containing both labels (colocalized voxels), which renders the colocalization analysis sensitive to differences in the number of 'filled voxels' for each imaging channel. Thus, differences in the object sizes will artificially decrease the colocalization index, even in a situation where all NCX and $Na_v1.X$ objects are perfectly colocalized.

Estimated object sizes are dependent on image thresholding procedures and in this study two stages of automated image thresholding procedures were used. Theoretically, the estimated object sizes of subresolution point sources should only vary with the optical resolution, however, we have found that the iterative thresholding method (see Methods) estimates larger object sizes in lower density protein distributions. Therefore, this tendency of the iterative thresholding method is counteracted by a secondary thresholding method which utilizes the resolution definition of Full-Width-Half-Maximum (FWHM) to normalize object sizes by the maximum intensity contained in each object.

Fig. 5.4*A* shows an example of the estimated object sizes resulting from only the iterative thresholding procedure, while Fig. 5.4*B* shows the estimated object sizes after both iterative and FWHM thresholding is applied. Fig. 5.4*C* summarises the final median object sizes of NCX and $Na_v1.X$ objects at the 3 and 56 day stages. Notice that at both age stages, a NCX object is expected to only cover ~60% of a $Na_v1.X$ object due to the differences in object size, indicating that even if all NCX and $Na_v1.X$ objects were perfectly colocalized, the maximum $Na_v1.X$-to-NCX colocalization could not exceed ~60%. In contrast, NCX-to-$Na_v1.X$ colocalization is maximal at 100% because in a perfectly colocalized object pair, a $Na_v1.X$ object is expected to envelope an entire NCX object. However, the relative object densities indicate that total NCX-to-$Na_v1.X$ colocalization is not possible due to the greater abundance of NCX objects, and the

low NCX-to-$Na_v1.X$ colocalization shown in Fig. 5.4*D* does not result from the imbalance in object sizes but rather results, at least partially, from an imbalance in object densities.

The analysis shown in Fig. 5.4 demonstrates that the imbalance in object densities and object sizes make traditional colocalization measurements difficult to interpret since the colocalization index will reflect these differences as well as any changes is the actual colocalization relationship. Traditional colocalization analysis returns the proportion of voxels containing colocalization events. Therefore, to avoid the interference of mismatches in object size and mismatches in object densities, we utilized an object specific colocalization analysis in Fig. 5.5 in order to identify the number of $Na_v1.X$ and NCX objects that contain and do not contain colocalization events. At the object level, two objects can have any colocalization index between 0 and 100%. To simplify the description, we categorized objects into non-colocalized (0% colocalization), lowly colocalized (1-50% colocalization) and highly colocalized (51–100% colocalization) events. Fig. 5.5*A* shows the object-specific colocalization in $Na_v1.X$ objects while Fig. 5.5*B* shows the object-specific colocalization in NCX objects. This object-based colocalization analysis confirm that there is an age-dependent decrease in co-localisation of $Na_v1.5$ and NCX as the percentage of non-colocalized objects increase with age while the opposite is true for highly-colocalized objects (Fig. 5.5*A*). In contrast, there are no age-dependent changes in the percentage of colocalized $Na_v1.4$ and NCX objects however, the protein expression levels of both NCX and $Na_v1.4$ decreases significantly in an age-dependent manner.

Near neighbour separation of objects

As both traditional and object-specific colocalization indices are sensitive to object sizing, the third approach in our colocalization analysis estimated colocalization in a size-independent fashion, by reducing each object to a single co-ordinate by calculating their centre-of-mass. The distance separating each $Na_v1.4$ and $Na_v1.5$ object from their respective nearest NCX neighbour was then calculated and the profile of the separation distances is shown in Fig. 5.6*A*, *B* for $Na_v1.4$ and $Na_v1.5$, respectively. From this analysis, no age dependence is seen for the separation profiles between $Na_v1.4$ and NCX objects whereas $Na_v1.5$ objects grow farther from NCX objects with development. To simplify comparisons and analyze separation differences statistically, the proportion of events shorter than 300 nm was normalized to the total number of

events closer than 3 μm as shown in Fig. 5.6*C*. Using this analysis, the $Na_v1.4$-to-NCX separation distance was not statistically different ($p>0.07$) between the 3d and 56d groups while the separation distance for $Na_v1.5$-to-NCX was statistically larger in 56d than in 3d myocytes ($p<0.001$).

5.4. DISCUSSION

Sodium currents may increase reverse-mode NCX activity by inducing strong membrane depolarization and/or local sodium accumulation [3]. Previous reports from our laboratory indicated that neonatal rabbit myocytes are capable of mediating EC coupling through NCX-mediated calcium influx under moderately depolarising conditions (+10 mV) [14]. Under identical experimental conditions, adult rabbit myocytes show no significant NCX-mediated EC-coupling, consistent with the reliance of adult EC coupling on the L-type calcium channel for calcium-induced calcium release. In these studies, a voltage pre-pulse (-40 mV) was used to avoid contaminating the measured I_{Ca}, and I_{NCX} with a large I_{Na} and the membrane was not strongly depolarised. Therefore, these experimental conditions likely underestimate the role of NCX in both age groups, and to better understand changes in EC coupling occurring during development it is essential to elucidate the role of reverse-mode NCX. Towards this goal, this study investigated the expression and distribution of voltage-gated sodium channels in the developing myocytes and their colocalization with the NCX during development.

5.4.1. DEVELOPMENTAL CHANGES IN SODIUM CHANNEL EXPRESSION

Using western blot analysis to investigate which voltage-gated sodium channels were expressed in the developing myocardium, we demonstrate for the first time, the presence and quantitative expression pattern of the skeletal sodium channel isoform $Na_v1.4$ in neonatal vs. adult cardiomyocytes. Moreover, we observed that there is a decrease in both $Na_v1.4$ and $Na_v1.1$ protein levels during development while no statistically significant differences were seen in $Na_v1.5$ protein levels between neonatal and adult cardiomyocytes.

Although we found that both the $Na_v1.4$ and the $Na_v1.5$ sodium channel isoforms were highly expressed in the neonate heart, it is the density and proximity of these isoforms in relation to the NCX that will determine their functional contribution to the regulation of NCX-activity.

Thus, the total amount of sodium entering the cell is likely dictated by expression level of the sodium channel isoforms, whereas the amount of sarcolemmal calcium entry driven by reverse-mode NCX activity is dependent on the spatial distribution of the sodium channels. Therefore, to address age-dependent changes in the contribution of these isoforms to the regulation of NCX activity, we used confocal imaging to identify developmental changes in the distribution of $Na_v1.4$ and the $Na_v1.5$ isoforms and colocalization analysis to address their proximity to the NCX.

5.4.2. Numerical analysis of $Na_V1.4$ and $Na_V1.5$ distribution and colocalization with the NCX

Colocalization analysis can vary in levels of sophistication depending on the specific purposes of the study. Although the specific dimensions of subsarcolemmal sodium micro-domains are unknown, the functional association between sodium channels and NCX likely occurs at distances that are below the resolution of confocal imaging. To ensure of an accurate colocalization analysis at this scale, a sequence of image analysis techniques were used in this study, starting with conventional colocalization analysis based on the relationship between the total number of voxels for one label and the total number of voxels containing both labels (colocalized voxels). This approach is the most commonly used, even though the conclusions that can be drawn from this analysis are relatively insensitive to subtle changes in protein distribution [17] which may be functionally critical. For example, multiple protein distribution represented by a single colocalization index of 50% could reflect marginal colocalization between each and every object, but it could also reflect alternating objects being colocalized, with one object pair being perfectly colocalized while the next object pair is perfectly non-colocalized.

Therefore, to avoid potential misinterpretation of conventional colocalization analysis, in this study we employed two additional numerical approaches, consisting of an object-specific colocalization analysis and a nearest neighbour separation of objects analysis. In this analysis, image thresholding is a critical step in which object intensity spacing can affect the estimated size of the objects in a protein distribution. To counteract a potential bias of object size, a two stage thresholding procedure was used to increase the accuracy of the colocalization analysis

(Fig 5.14). Still, the interpretation of lowly colocalized objects is not straight forward for the object-specific colocalization analysis because NCX objects tended to be smaller than $Na_v1.X$ objects. Therefore, low object-specific colocalization indices may either reflect an increased separation distance or a decreased NCX object size. To resolve this problem, the final step in the colocalization analysis employed here, determined the distance between nearest neighbours of a $Na_V1.X$ and a NCX object based on the centre of mass for each object (Fig 5.15).

Developmental changes in sodium channel distribution and colocalization with NCX

Initial reports of $Na_v1.5$ localization in adult myocytes suggested that there would be easily identifiable intercalated discs indicated by intense $Na_v1.5$ labelling [22, 23]. Although some intercalated discs were identified in this study, it is clear from Fig. 5.2 that both $Na_v1.4$ and $Na_v1.5$ are distributed along the peripheral membrane of neonatal rabbit myocytes and that they are distributed along the peripheral and t-tubule membrane of adult rabbit myocytes. The fact that both $Na_v1.4$ and $Na_v1.5$ channels were found to be distributed in punctuate clusters also suggests that these proteins may function in multichannel units. Recently, $Na_v1.1$-1.6 expression and distribution has also been investigated in cultured neonatal rat myocytes in which a punctuate distribution was also found for each isoform without any obvious subcellular localisation [24]. Here we report a similar punctuate distribution of $Na_v1.1$, $Na_v1.4$ and $Na_v1.5$, in freshly isolated neonatal rabbit myocytes, but it should be kept in mind that some features may have been altered in the cultured cardiomyocytes due to the de-differentiation known to occur when cardiomyocytes are maintained in tissue culture [27].

It is also shown in the present study that the high expression levels of $Na_v1.4$ and $Na_v1.5$ occur together with a colocalization of the two isoforms with NCX in the neonate heart, which coincides with the prominence of reverse-mode NCX activity in neonatal EC-coupling reported in previous studies [12-16]. Moreover, we show that along with reduced NCX expression [10, 11], the adult myocyte also has decreased $Na_v1.4$ expression and an increased separation distance between $Na_v1.5$ and NCX, suggesting little or no sodium channel mediated regulation of NCX activity in the adult rabbit myocyte. The expression of $Na_v1.4$ and the spatial proximity between $Na_v1.4$ and NCX, as a function of development, highlights the complementary relationship between western blots and imaging techniques. Combined, the two techniques show that the

expression of both $Na_v1.4$ and of NCX decrease with development, but the spatial relationship between the two proteins is unchanged. Although neither technique can determine the specific number of proteins per functional unit, these findings are consistent with the decreased prominence of the reverse-mode NCX in the EC coupling of mature myocytes [12-16]. Given that $Na_v1.4$ expression decreases with development while the number of protein clusters remains constant, an implicit consequence of these results is that the number of channels per cluster decreases with development, thereby limiting the local increase in sodium that can be produced by a protein cluster in the adult rabbit heart.

5.4.3. CONTRIBUTION OF SODIUM CHANNELS TO REVERSE-MODE NCX

The object specific analysis found that most NCX objects, in either age group, did not coincide with a sodium channel object and it is not clear whether this subset of NCX objects participates in both forward-mode and reverse-mode NCX activity. Although voltage-gated sodium-channel-free NCX clusters are not likely to experience the same elevation in subsarcolemmal sodium concentrations as NCX clusters containing sodium channels, limited sodium mobility in the subsarcolemmal space may be sufficiently restricted to allow for functional coupling. Subsarcolemmal sodium mobility has yet to be measured directly, but pump currents from the sodium-potassium pump (NKA) and exchange currents from NCX have been used as bioassays of subsarcolemmal sodium levels [28, 29]. Thus, increases in subsarcolemmal sodium by NKA inhibition alters the reversal potential of NCX [30] which slows NCX-mediated relaxation [31, 32] and increases the size of voltage-induced calcium transients [31]. Moreover, inhibition of the sodium current in the presence and absence of NKA activity indicated that NKA can modulate the effects of the sodium current [33]. These studies are consistent with a reduced subsarcolemmal sodium mobility and the colocalization of proteins involved in Na^+ translocation including voltage-gated sodium channels, NCX and NKA.

It is not clear how sodium mobility is impeded in the subsarcolemmal space, but radial diffusion coefficients have been estimated to be 10^3-10^4 times lower than aqueous diffusion [34] and longitudinal diffusional coefficients have been estimated to be 100-200 times lower than in aqueous solutions [35]. One possible source of reduced sodium mobility is the dyadic cleft itself [20] in which a restricted space reduces the effective diffusional coefficient. In neonatal rabbit myocytes, electron micrographs have identified 300 nm sheets of SR membrane located ~20 nm

beneath the sarcolemma [36], which may contribute to reduce sodium mobility. Moreover, large fluctuations in ion concentration can be mediated by relatively few ions within small spaces, and if voltage-gated sodium channels and NCX colocalization events coincide with the 300 nm SR membrane sheets detected by EM then local sodium elevation could occur in a subsarcolemmal space of 300 x 300 x 20 nm. In this small space, opening of a single sodium channel passing 1.4 pA of current [37] for 1 ms (or ~8700 sodium ions) would increase the sodium concentration in this cleft by ~8 mM. Therefore, if sodium diffusion is sufficiently slow, ~10 sodium channels would be required to reach a saturating sodium concentration of 75 mM for the NCX [38] within each cleft. Our findings of a punctuate distribution pattern of $Na_v1.4$ and $Na_v1.5$, high expression levels of the two proteins, and colocalization of both proteins with NCX in neonatal rabbit ventricular myocytes are all consistent with localized subsarcolemmal areas with high $[Na^+]$ transients in neonatal rabbit hearts. Contrary to this, subsarcolemmal areas with high $[Na^+]$ transients sufficiently large to activate reverse-mode NCX are likely to be sparse or lacking in the adult rabbit heart as we find a decrease in $Na_v1.4$ and NCX expression with age and that $Na_v1.5$ and NCX grow apart with age. Moreover, the amplitude of local $[Na^+]$ transients are likely limited in the adult rabbit heart as the number of $Na_v1.4$ molecules per cluster decreases with age and a previous study has shown that subsarcolemmal SR membrane sheet-like structures are lacking in adult rabbit ventricular myocytes [36].

5.4.4. SCOPE OF IMAGE PROCESSING AND ANALYSIS IN QUANTIFICATION OF COLOCALIZATION OF PROTEINS

High-resolution imaging techniques such as wide-field deconvolution, confocal, 2-photon, and structured-illumination are becoming increasingly common. The increased resolution of these imaging techniques is expected to reveal additional levels of protein distribution complexities over more traditional imaging techniques. Many protein distributions which were previously thought to be homogenously distributed have now been shown to be punctuate in nature, strongly suggesting microdomain level organization of the plasma membrane. The sub-resolution size of these microdomains presents a challenge for confocal microscopy, even with the benefits of image restoration, however in this study we have shown that image processing techniques can be used to increase the specificity of colocalization analysis. While these image processing techniques do not change the fundamental limitations in resolution, they extend the

ability to describe these protein distributions. We and others have shown that centre-of-mass calculations can be used in the biological context to great advantage [17, 18, 39, 40].

5.4.5. CONCLUSION

In this study, we investigated the expression and localisation of voltage-gated sodium channel isoforms in the developing rabbit heart. Only $Na_v1.1$, $Na_v1.4$ and $Na_v1.5$ isoforms were found in appreciable amounts. The robust expression of $Na_v1.4$ and $Na_v1.5$ and their colocalization with the NCX in neonatal cardiomyocytes is consistent with a contribution of these channels to a prominent reverse-mode NCX activity in neonates. Colocalization between NCX and $Na_v1.5$ decreases with development and we show that this decrease in colocalization was not due to the changes in overall labelling density, or changes in object size but because individual NCX and $Na_v1.5$ events grow farther apart with development. This ability to determine the nature of increases or decreases in protein colocalization indices is expected to be widely extendable and may be especially useful in comparing normal and disease state protein distributions. On the other hand, our findings of a lower expression of $Na_v1.1$ and $Na_v1.4$ in adult myocytes, combined with the spatial separation of $Na_v1.5$ and the NCX are unfavourable to reverse-mode NCX activity in the adult rabbit heart.

5.5. FIGURES

Figure 5.1 Developmental expression of sodium channel isoforms in cardiomyocytes

(A), representative western blot demonstrating the expression levels of the skeletal ($Na_V1.4$) sodium channel isoform. Bar graphs represent data from 4 independent experiments, $^{**}P<0.01$. (B), representative western blot demonstrating the expression levels of the neuronal ($Na_V1.1$) sodium channel protein in the cardiomyocyte lysates. Bar graph represents data from 4 different experiments $^{**}P<0.01$. (C), representative western blot showing the expression of cardiac sodium channel ($Na_v1.5$) in developing cardiomyocytes. Bar graphs represent data from 4 different experiments. Results were calculated after band intensities were normalized to actin levels for A, B and C.

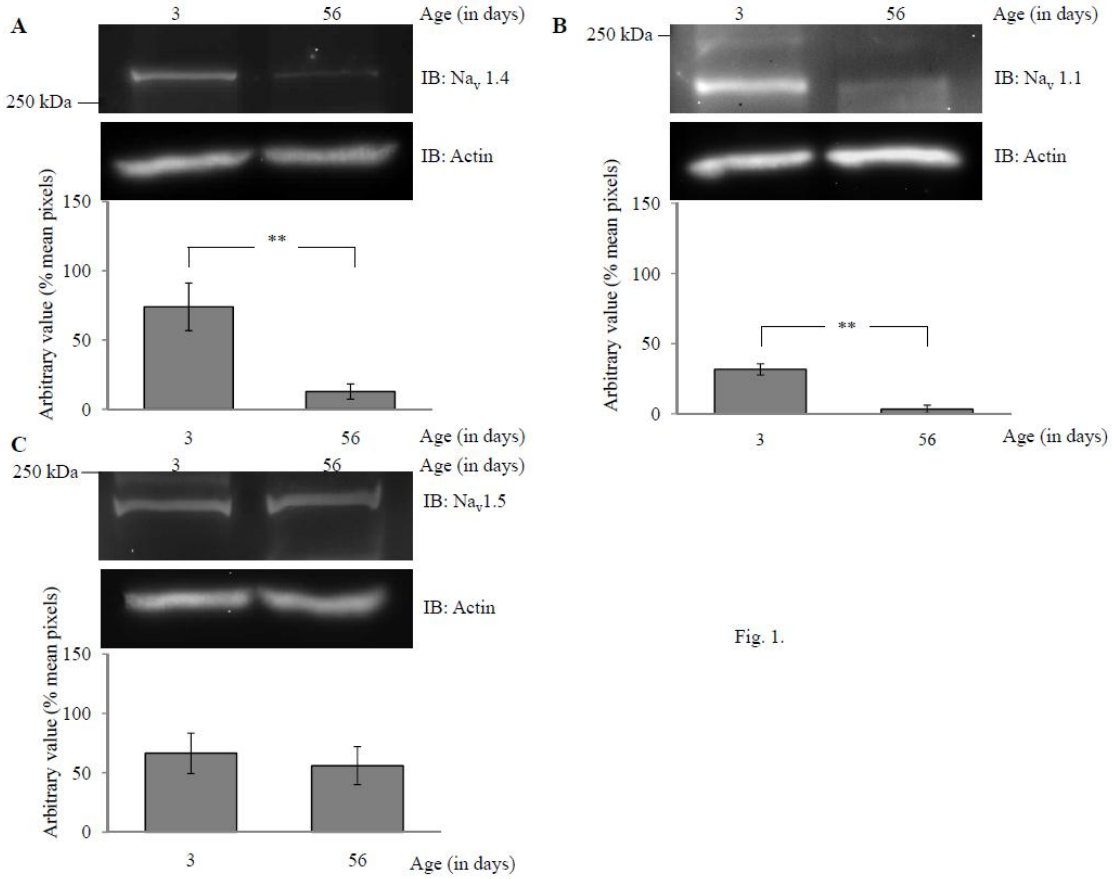

Fig. 1.

Figure 5.2 $Na_v1.4/Na_v1.5$ with NCX in developing cardiomyocytes

Representative confocal images showing the localization of $Na_v1.4/Na_v1.5$ with NCX in developing cardiomyocytes. The left side of each panel contains a longitudinal cross-sectional image while the right side of each panel contains a series of transverse cross-sections roughly aligned to the matching longitudinal image. $Na_v1.X$ is shown in red, NCX is shown in green and colocalization shown in yellow. The images have been deconvolved and thresholded as described in the text and are displayed with binary intensity, where pixels are either lit or unlit. Panels A and B are 3 day myocytes dual-labelled with $Na_v1.5$-NCX and $Na_v1.4$-NCX, respectively. Panels C and D are 56 day myocytes dual-labelled with $Na_v1.5$-NCX and $Na_v1.4$-NCX, respectively.

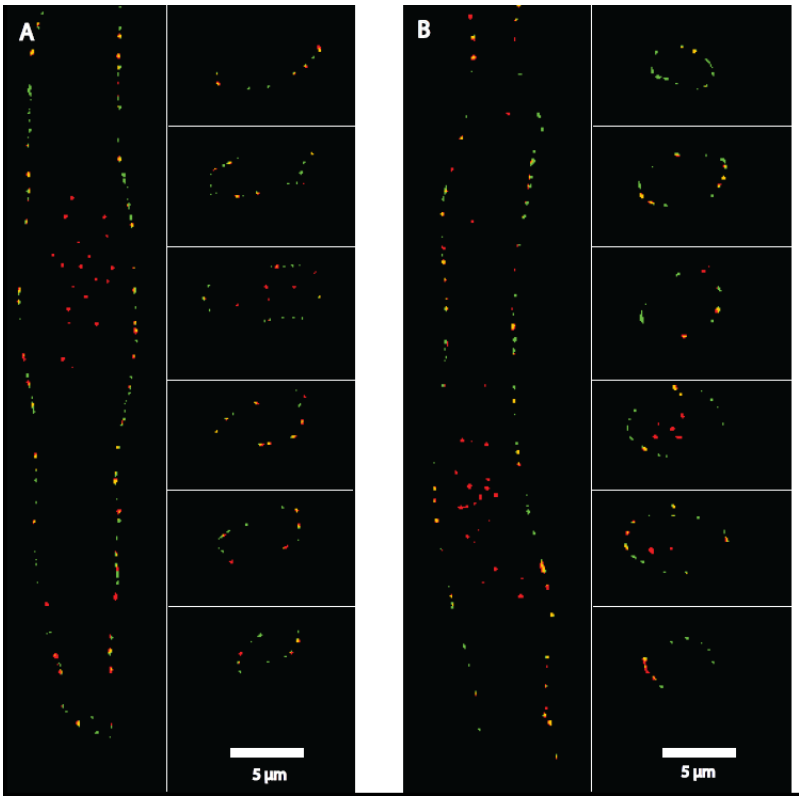
A
5 µm
B
5 µm

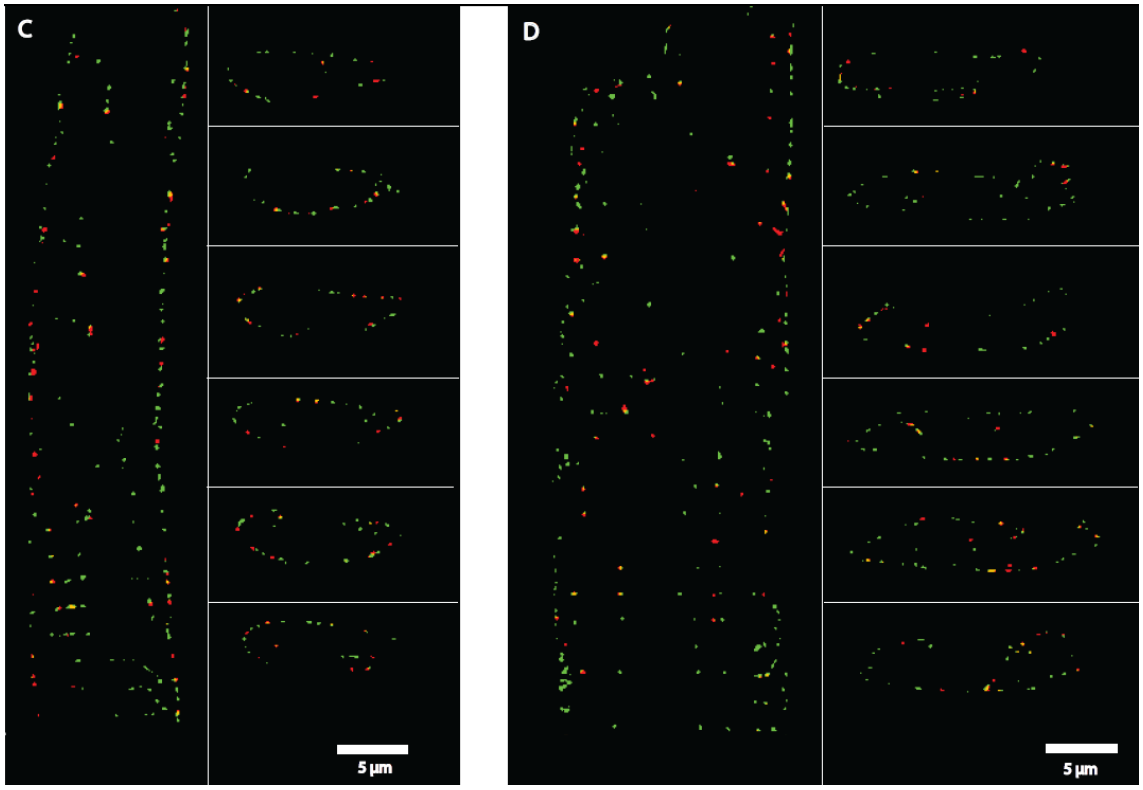
C
5 µm
D
5 µm

Figure 5.3 Traditional colocalization analysis

Traditional colocalization analysis makes a voxel-by-voxel analysis of coincident voxels. (A), $Na_v1.X$-to-NCX colocalization denotes the percentage of $Na_v1.X$ voxels that also contain NCX in the peripheral compartment. $^{*}P<0.05$ (B), NCX-to-$Na_v1.X$ colocalization denotes the percentage of NCX voxels that also contain a $Na_v1.X$ in the peripheral compartment. $^{*}P<0.05$. Results were calculated from image analysis of n=37 cells ($Na_v1.4$, 3 day), n= 38 cells ($Na_v1.4$, 56 day), n= 40 ($Na_v1.5$, 3 day), n=37 ($Na_v1.5$, 56 day) from 4 different experiments.

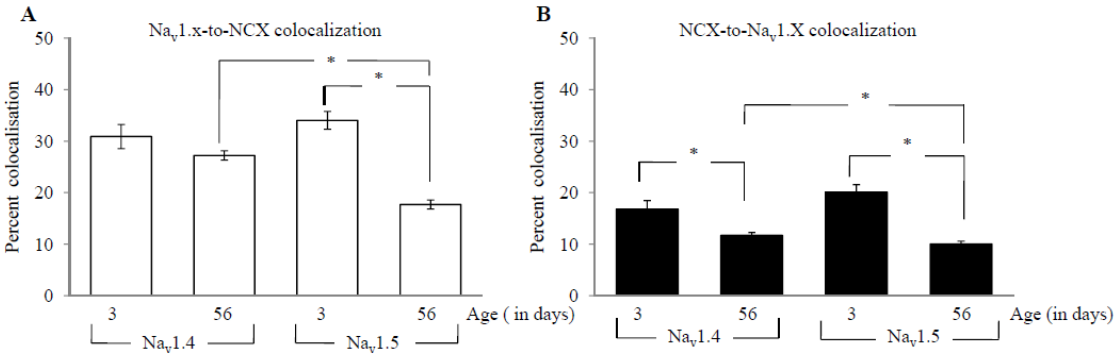

Figure 5.4 Object size and density analysis

Fig. 5.4. Object density can affect object size estimates. Panel (A) presents a line-histogram of the size distribution of NCX and $Na_v1.4$ objects after iterative thresholding. The $Na_v1.4$ object density is lower than the NCX density and requires less 'thresholding intensity' to separate neighbouring objects. This 'under-thresholding' results in the overestimation of $Na_v1.4$ object sizes. Panel (B) presents the object size distribution of NCX and $Na_v1.4$ objects after both iterative thresholding and Full-Width-Half-Maximum thresholding (FWHM) procedures have been applied. The FWHM thresholding step, which applies a secondary thresholding value based on the maximum object intensity, reduces the size discrepancy between NCX and $Na_v1.4$ objects. Panel (C) presents the median object size found after both iterative and FWHM thresholding procedures have been applied to each experimental group. Statistical tests indicated that all 4 groups contained a statistically significant difference between NCX and $Na_v1.X$ object sizes ($p<0.001$). Previous investigations found that the periodicity of NCX labelling does not change with development. Panel (D) uses the constant labelling density of NCX to express the labelling density of $Na_v1.x$ objects.

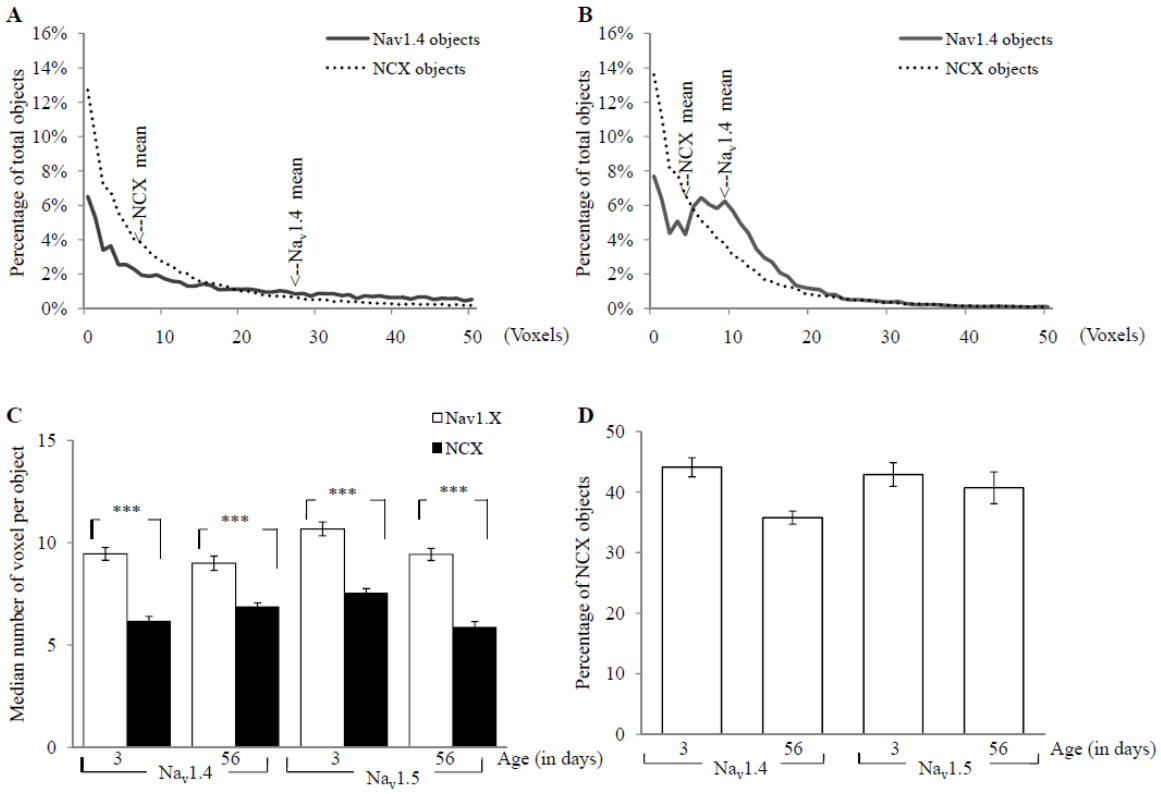
A
B
Nav1.4 objects
NCX objects
Percentage of total objects
<--NCX mean
<--Nav1.4 mean
(Voxels)
C
D
Nav1.X
NCX
Median number of voxel per object
Percentage of NCX objects
***
Age (in days)
Nav1.4
Nav1.5

Fig. 4.

Figure 5.5 Object specific colocalization results

Object specific analysis calculates the colocalization index in each object pair. The proportion of these object pairs that are non-colocalized (0%), lowly colocalized (1-50%) and highly colocalized (51-100%) are shown for (A), $Na_v1.X$ object-specific colocalization with NCX and for (B), NCX object-specific colocalization with $Na_v1.X$. $^{***}P<0.001$

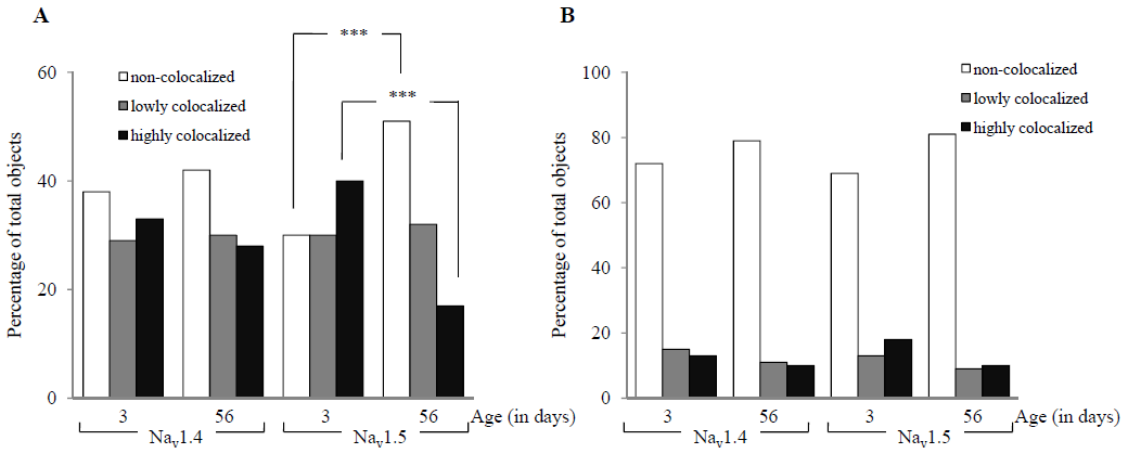

Figure 5.6 Separation distance analysis results

The distance separating two objects from different imaging channels can be used to estimate protein colocalization independent of heterogeneous object sizing. Objects are reduced to their centre of mass co-ordinate and their distance to the nearest neighbour is calculated. (A), graph represents the separation distances between $Na_v1.4$ and NCX objects. (B), graph represents the $Na_v1.5$-to-NCX separation distances in both age groups (C), Bar graph depicts the proportion of distance shorter than 300 nm between each experimental group and NCX. $^{***}P<0.001$.

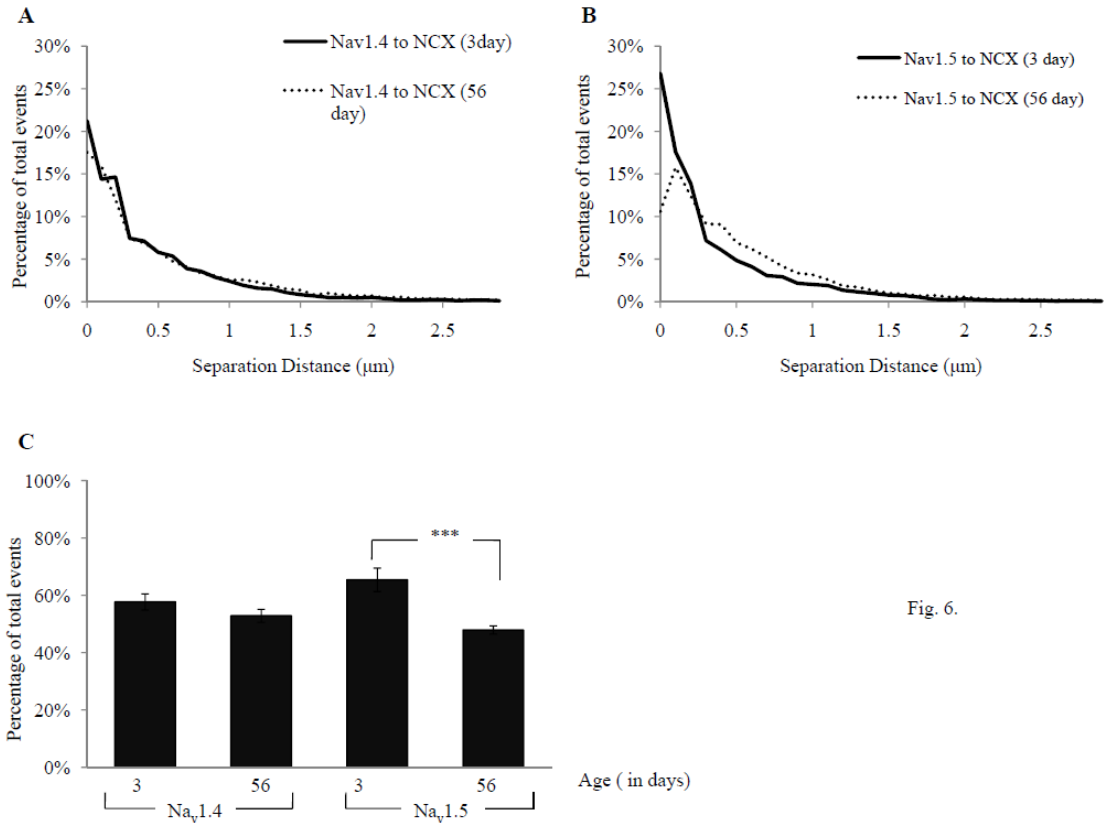

Fig. 6.

Figure 5.7 IgG control images (3 day)

Representative confocal image for control wherein rabbit polyclonal antibodies were replaced with normal rabbit IgG serum and mouse monoclonal antibody (NCX) was replaced with normal mouse serum in 3 day myocyte.

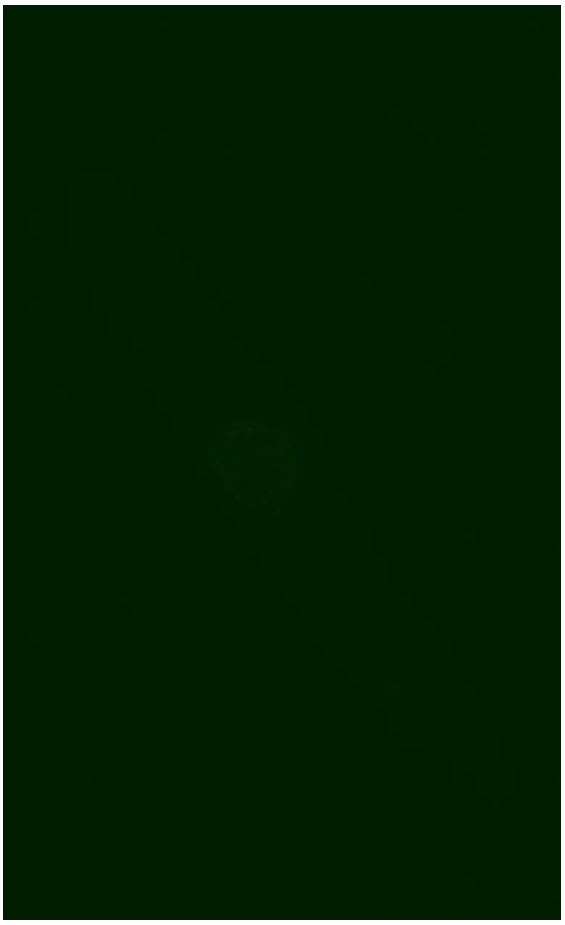

Figure 5.8 IgG control images (56 day)

Representative confocal image for control wherein rabbit polyclonal antibodies were replaced with normal rabbit IgG serum and mouse monoclonal antibody (NCX) was replaced with normal mouse serum in 56 day myocyte.

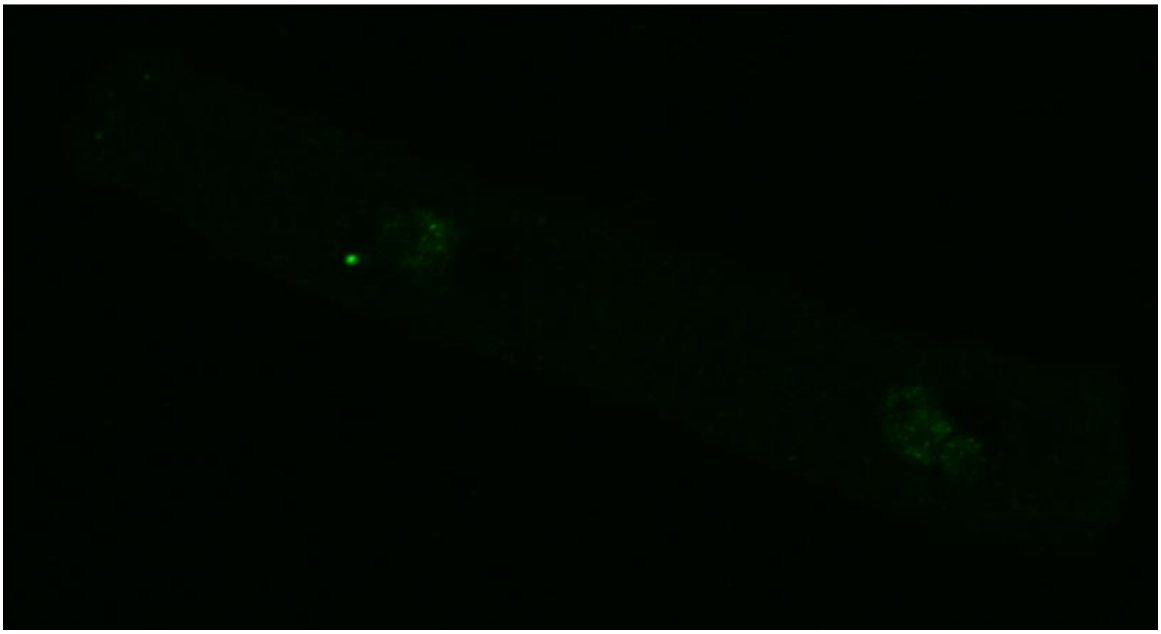

Figure 5.9 Images of $Na_v1.5$ and NCX before image processing (3 day)

Representative confocal image demonstrating the localization of $Na_v1.5$ and NCX before image processing in 3 day myocyte. Green channel represents $Na_v1.5$ labelling and red channel represent NCX labelling.

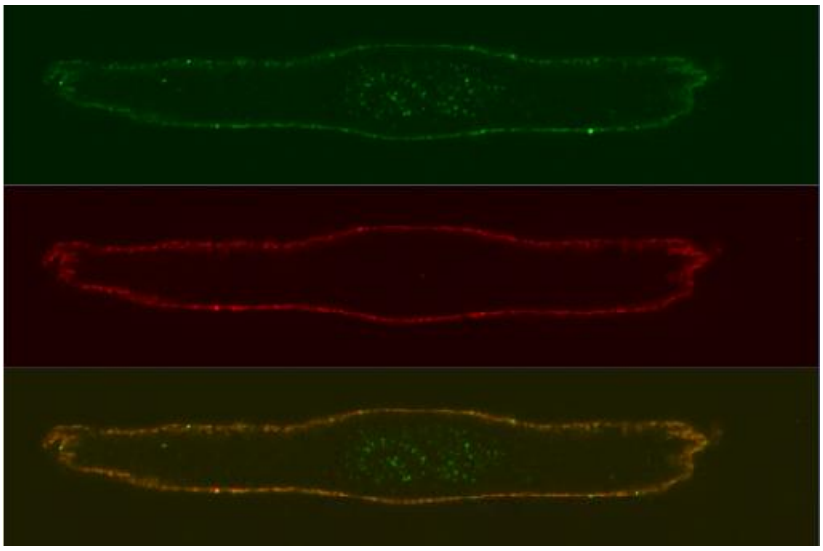

Figure 5.10 Images of $Na_v1.5$ and NCX before image processing (56 day)

Representative confocal image demonstrating the localization of $Na_v1.5$ and NCX before image processing in 56 day myocyte. Green channel represents $Na_v1.5$ labelling and red channel represent NCX labelling

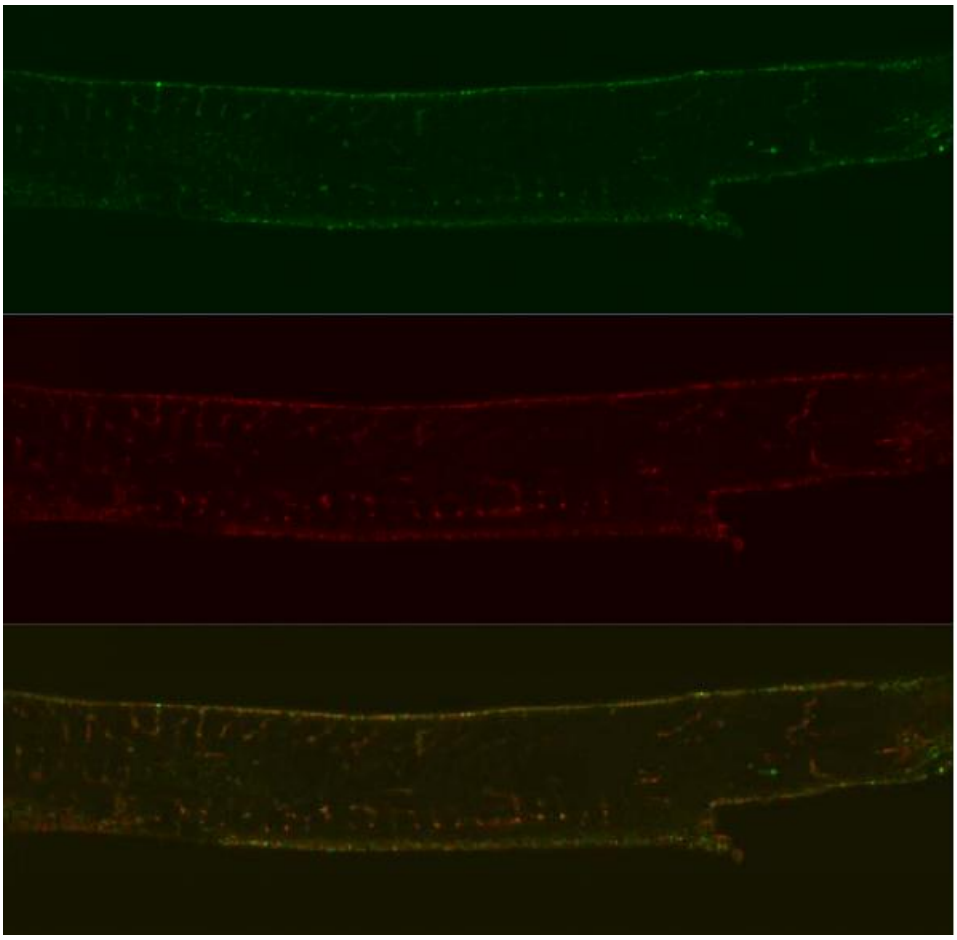

Figure 5.11 Images of $Na_v1.4$ and NCX before image processing (3 day)

Representative confocal images demonstrating the localization of Nav1.4 and NCX before image processing in 3 day myocyte . Green channel represents Nav1.4 labelling and red channel represent NCX labelling.

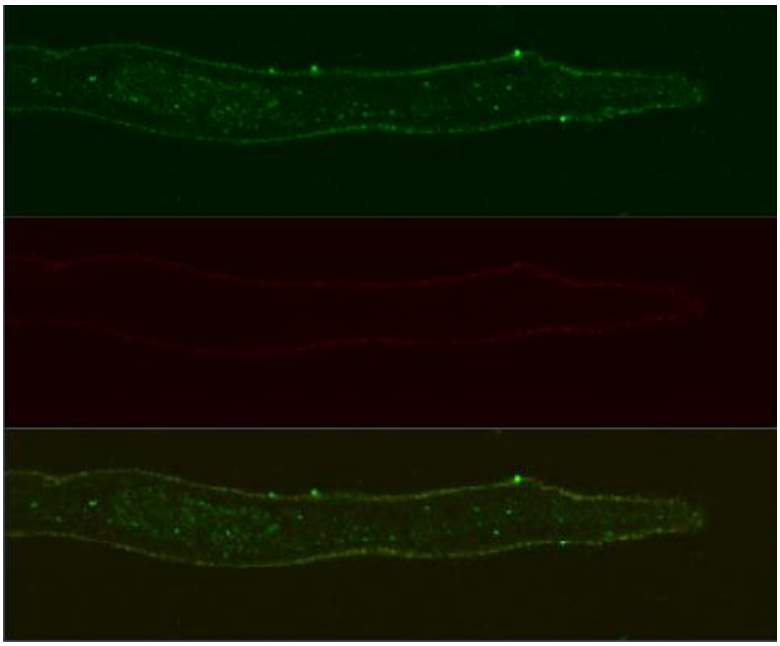

Figure 5.12 Images of $Na_v1.4$ and NCX before image processing (56 day)

Representative confocal images demonstrating the localization of $Na_v1.4$ and NCX before image processing in 56 day myocyte . Green channel represents $Na_v1.4$ labelling and red channel represent NCX labelling.

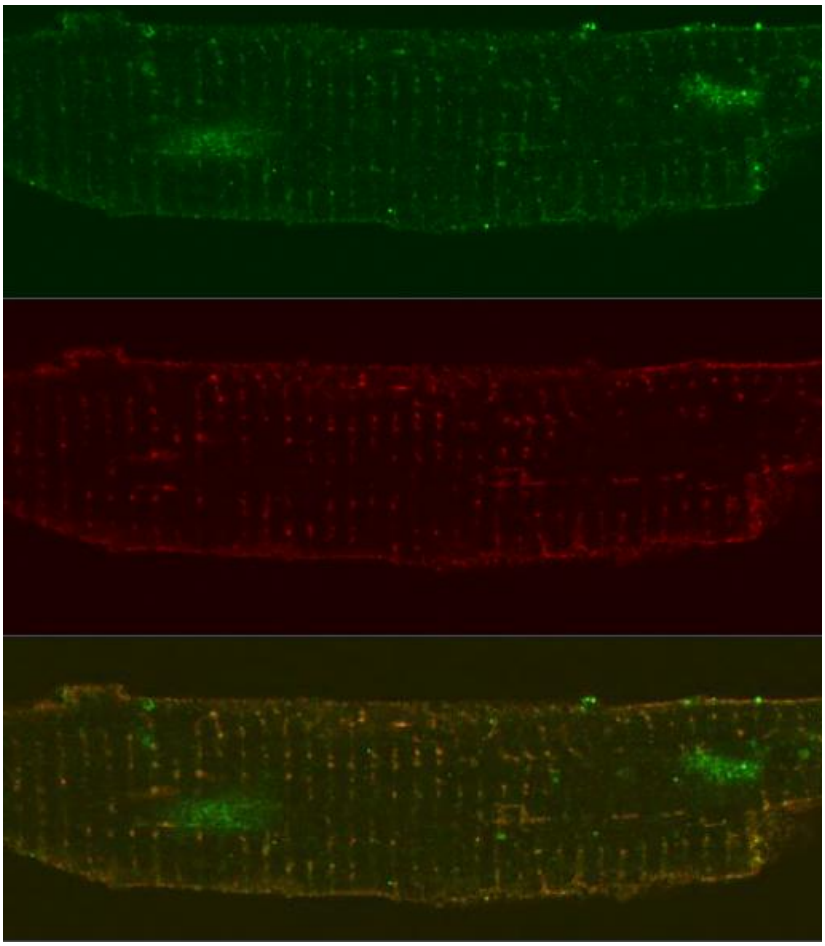

Figure 5.13 Pan 19 and NCX myocyte images

Representative confocal images of (A) 3 day myocyte and (B) 56 day myocyte immunolabelled with Pan-19 and NCX antibody

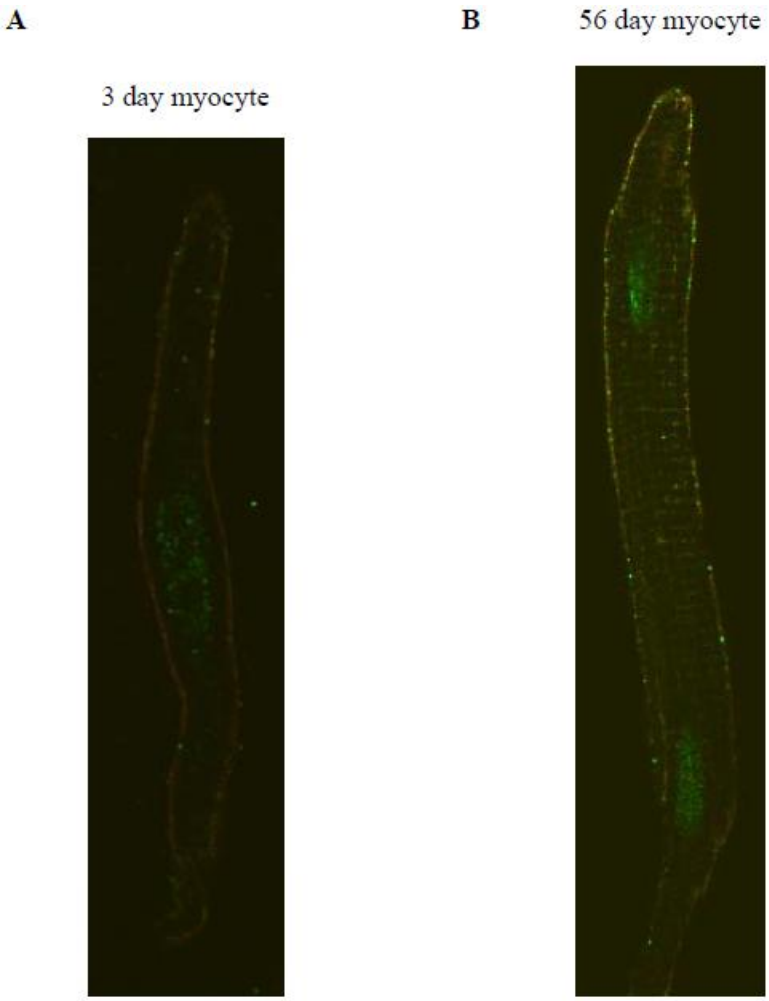

Figure 5.14 Pictorial representation of the effect of thresholding

(A), represents the effect of thresholding objects with increasing image intensity. (B), depicts the effect of increasing the thresholding. Higher thresholding (e.g. # 7) results in increased objects with brighter pixels. (C), represents the effect of iterative and FWHM thresholding on widely spaced objects. (D), while FWHM thresholding denser objects results in smaller object sizes.

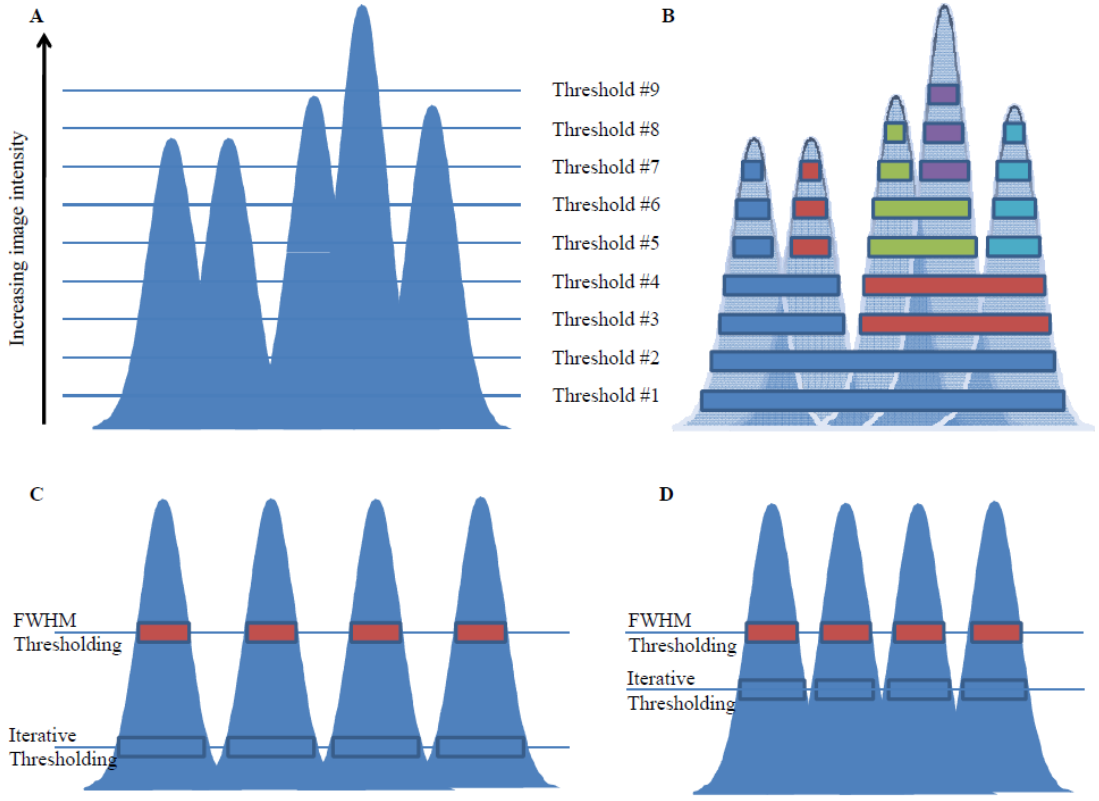

Figure 5.15 Object-specific colocalization and separation distance analysis

Object-specific colocalization indices reflect both relative object sizing and separation distances. Panels (A), (B), (C) all have the same 'green-to-orange' colocalization (same degree of orange overlap) however the distance between the centroids differs. Although Panel (C) and (D) have the same separation distance, panel (D) returns a higher colocalization index due to the presence of a larger orange object.

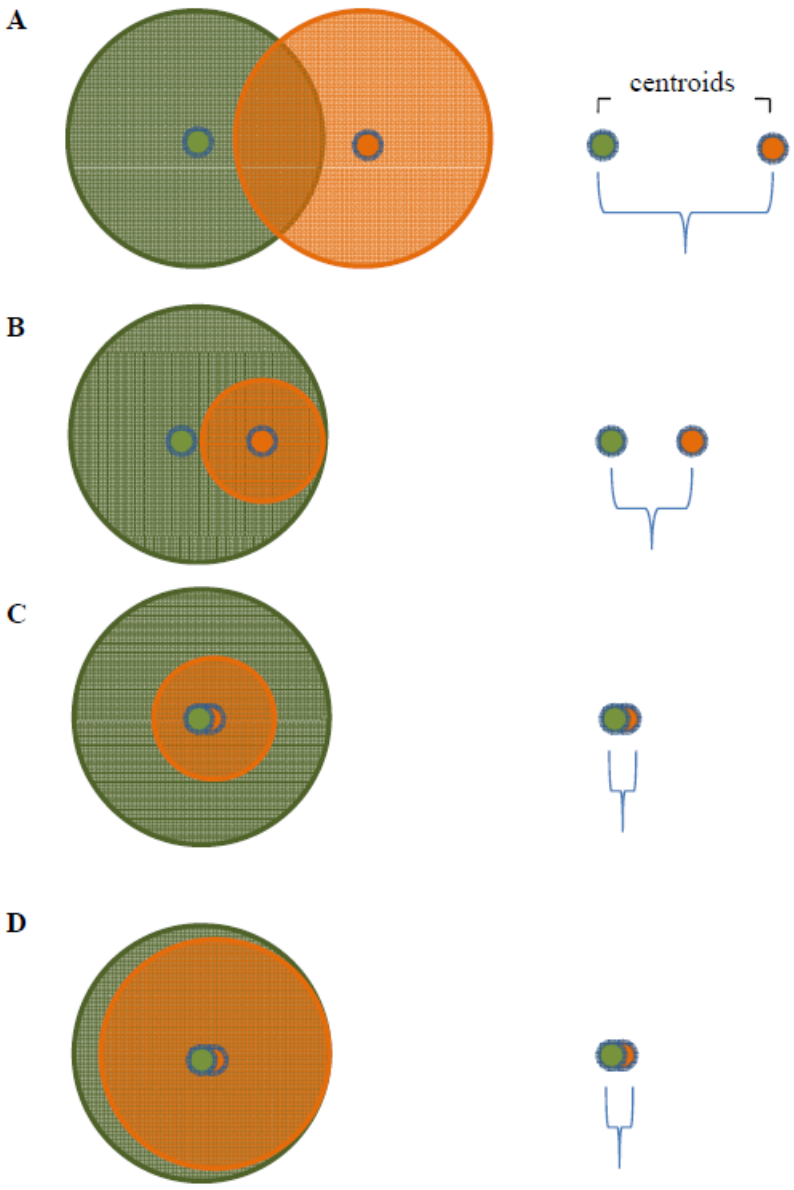

5.6. REFERENCES

1. Fabiato A. Time and calcium dependence of activation and inactivation of calcium-induced release of calcium from the sarcoplasmic reticulum of a skinned canine cardiac Purkinje cell. *The Journal of general physiology.* 1985;85:247-289.

2. Reeves JP, Hale CC. The stoichiometry of the cardiac sodium-calcium exchange system. *The Journal of biological chemistry.* 1984;259:7733-7739.

3. Bers DM, Despa S. Na^+ transport in cardiac myocytes; Implications for excitation-contraction coupling. *IUBMB life.* 2009;61:215-221.

4. Lederer WJ, Niggli E, Hadley RW. Sodium-calcium exchange in excitable cells: fuzzy space. *Science (New York, N.Y.* 1990;248:283.

5. Deschenes I, Trottier E, Chahine M. Implication of the C-terminal region of the alpha-subunit of voltage-gated sodium channels in fast inactivation. *The Journal of membrane biology.* 2001;183(2):103-114.

6. Sham JS, Cleemann L, Morad M. Gating of the cardiac Ca^{2+} release channel: the role of Na^+ current and Na^+-Ca^{2+} exchange. *Science (New York, N.Y.* 1992;255(5046):850-853.

7. Bouchard RA, Clark RB, Giles WR. Role of sodium-calcium exchange in activation of contraction in rat ventricle. *The Journal of physiology.* 1993;472:391-413.

8. Sipido KR, Carmeliet E, Pappano A. Na^+ current and Ca^{2+} release from the sarcoplasmic reticulum during action potentials in guinea-pig ventricular myocytes. *The Journal of physiology.* 1995;489 (Pt 1):1-17.

9. Grantham CJ, Cannell MB. Ca^{2+} influx during the cardiac action potential in guinea pig ventricular myocytes. *Circulation research.* 1996;79:194-200.

10. Artman M. Sarcolemmal Na^+-Ca^{2+} exchange activity and exchanger immunoreactivity in developing rabbit hearts. *The American journal of physiology.* 1992;263:H1506-1513.

11. Boerth SR, Zimmer DB, Artman M. Steady-state mRNA levels of the sarcolemmal Na^+-Ca^{2+} exchanger peak near birth in developing rabbit and rat hearts. *Circulation research.* 1994;74:354-359.

12. Wetzel GT, Chen F, Klitzner TS. Na^+/Ca^{2+} exchange and cell contraction in isolated neonatal and adult rabbit cardiac myocytes. *The American journal of physiology.* 1995;268:H1723-1733.

13. Huang J, Hove-Madsen L, Tibbits GF. Na^+/Ca^{2+} exchange activity in neonatal rabbit ventricular myocytes. *Am J Physiol Cell Physiol.* 2005;288:C195-203.

14. Huang J, Hove-Madsen L, Tibbits GF. Ontogeny of Ca^{2+}-induced Ca^{2+} release in rabbit ventricular myocytes. *Am J Physiol Cell Physiol.* 2008;294:C516-525.

15. Haddock PS, Coetzee WA, Artman M. Na^+/Ca^{2+} exchange current and contractions measured under Cl^--free conditions in developing rabbit hearts. *The American journal of physiology.* 1997;273:H837-846.

16. Haddock PS, Coetzee WA, Cho E, Porter L, Katoh H, Bers DM, Jafri MS, Artman M. Subcellular $[Ca^{2+}]_i$ gradients during excitation-contraction coupling in newborn rabbit ventricular myocytes. *Circulation research.* 1999;85:415-427.

17. Lin E, Hung VH, Kashihara H, Dan P, Tibbits GF. Distribution patterns of the Na^+-Ca^{2+} exchanger and caveolin-3 in developing rabbit cardiomyocytes. *Cell Calcium.* 2009;45:369-383.

18. Dan P, Lin E, Huang J, Biln P, Tibbits GF. Three-dimensional distribution of cardiac Na^+-Ca^{2+} exchanger and ryanodine receptor during development. *Biophysical journal.* 2007;93:2504-2518.

19. Despa S, Islam MA, Weber CR, Pogwizd SM, Bers DM. Intracellular Na^+ concentration is elevated in heart failure but Na/K pump function is unchanged. *Circulation.* 2002;105:2543-2548.

20. Lines GT, Sande JB, Louch WE, Mork HK, Grottum P, Sejersted OM. Contribution of the Na^+/Ca^{2+} exchanger to rapid Ca^{2+} release in cardiomyocytes. *Biophysical journal.* 2006;91:779-792.

21. Cohen SA. Immunocytochemical localization of rH1 sodium channel in adult rat heart atria and ventricle. Presence in terminal intercalated disks. *Circulation.* 1996;94:3083-3086.

22. Maier SK, Westenbroek RE, Yamanushi TT, Dobrzynski H, Boyett MR, Catterall WA, Scheuer T. An unexpected requirement for brain-type sodium channels for control of heart rate in the mouse sinoatrial node. *Proc Natl Acad Sci U S A.* 2003;100:3507-3512.

23. Maier SK, Westenbroek RE, Schenkman KA, Feigl EO, Scheuer T, Catterall WA. An unexpected role for brain-type sodium channels in coupling of cell surface depolarization to contraction in the heart. *Proc Natl Acad Sci U S A.* 2002;99:4073-4078.

24. Kaufmann SG, Westenbroek RE, Zechner C, Maass AH, Bischoff S, Muck J, Wischmeyer E, Scheuer T, Maier SK. Functional protein expression of multiple sodium channel a- and b-subunit isoforms in neonatal cardiomyocytes. *J Mol Cell Cardiol.* 2009.

25. Sedarat F, Xu L, Moore ED, Tibbits GF. Colocalization of dihydropyridine and ryanodine receptors in neonate rabbit heart using confocal microscopy. *American journal of physiology.* 2000;279(1):H202-209.

26. Sedarat F, Lin E, Moore ED, Tibbits GF. Deconvolution of confocal images of dihydropyridine and ryanodine receptors in developing cardiomyocytes. *J Appl Physiol.* 2004;97:1098-1103.

27. Bugaisky LB, Zak R. Differentiation of adult rat cardiac myocytes in cell culture. *Circulation research.* 1989;64:493-500.

28. Main MJ, Grantham CJ, Cannell MB. Changes in subsarcolemmal sodium concentration measured by Na-Ca exchanger activity during Na-pump inhibition and b-adrenergic stimulation in guinea-pig ventricular myocytes. *Pflugers Arch.* 1997;435:112-118.

29. Carmeliet E. A fuzzy subsarcolemmal space for intracellular Na^+ in cardiac cells? *Cardiovasc Res.* 1992;26:433-442.

30. Fujioka Y, Matsuoka S, Ban T, Noma A. Interaction of the Na^+-K^+ pump and Na^+-Ca^{2+} exchange via $[Na^+]_i$ in a restricted space of guinea-pig ventricular cells. *The Journal of physiology.* 1998;509 (Pt 2):457-470.

31. Su Z, Zou A, Nonaka A, Zubair I, Sanguinetti MC, Barry WH. Influence of prior Na^+ pump activity on pump and Na^+/Ca^{2+} exchange currents in mouse ventricular myocytes. *The American journal of physiology.* 1998;275(5 Pt 2):H1808-1817.

32. Terracciano CM. Rapid inhibition of the Na^+-K^+ pump affects Na^+-Ca^{2+} exchanger-mediated relaxation in rabbit ventricular myocytes. *The Journal of physiology.* 2001;533:165-173.

33. Su Z, Sugishita K, Ritter M, Li F, Spitzer KW, Barry WH. The sodium pump modulates the influence of I_{Na} on $[Ca^{2+}]_i$ transients in mouse ventricular myocytes. *Biophysical journal.* 2001;80:1230-1237.

34. Despa S, Bers DM. Na/K pump current and $[Na]_i$ in rabbit ventricular myocytes: local $[Na]_i$ depletion and Na buffering. *Biophysical journal.* 2003;84:4157-4166.

35. Despa S, Kockskamper J, Blatter LA, Bers DM. Na/K pump-induced $[Na]_i$ gradients in rat ventricular myocytes measured with two-photon microscopy. *Biophysical journal.* 2004;87:1360-1368.

36. Huang J, van Breemen C, Kuo KH, Hove-Madsen L, Tibbits GF. Store-operated Ca^{2+} entry modulates sarcoplasmic reticulum Ca^{2+} loading in neonatal rabbit cardiac ventricular myocytes. *Am J Physiol Cell Physiol.* 2006;290:C1572-1582.

37. Catterall WA, Goldin AL, Waxman SG. International Union of Pharmacology. XLVII. Nomenclature and structure-function relationships of voltage-gated sodium channels. *Pharmacol Rev.* 2005;57:397-409.

38. Miura Y, Kimura J. Sodium-calcium exchange current. Dependence on internal Ca and Na and competitive binding of external Na and Ca. *The Journal of general physiology.* 1989;93:1129-1145.

39. Chen-Izu Y, McCulle SL, Ward CW, Soeller C, Allen BM, Rabang C, Cannell MB, Balke CW, Izu LT. Three-dimensional distribution of ryanodine receptor clusters in cardiac myocytes. *Biophysical journal.* 2006;91(1):1-13.

40. Chen-Izu Y, Ward CW, Stark W, Jr., Banyasz T, Sumandea MP, Balke CW, Izu LT, Wehrens XH. Phosphorylation of RyR2 and shortening of RyR2 cluster spacing in spontaneously hypertensive rat with heart failure. *American journal of physiology.* 2007;293(4):H2409-2417.

6. CONCLUDING CHAPTER

6.1. INTRODUCTION

It is now well established that excitation-contraction (EC) coupling in the adult mammalian heart requires calcium-induced-calcium-release (CICR) to mediate contraction. In the adult heart, CICR is thought to be triggered exclusively by the calcium current (I_{Ca})[1]. One exception to this generalization may be EC coupling in the adult guinea pig heart, with some reports of sodium-calcium exchanger (NCX) mediated CICR (NCX-CICR)[2-4] in this species. Although NCX-CICR may exist in the guinea pig heart, the overall contribution of NCX-CICR in the adult calcium transient appears limited[5, 6]. Although many aspects of adult EC coupling have yet to be well defined, even less is known EC coupling in the developing myocardium. Normally, in the adult myocardium, the predominant role of NCX is in relaxation, where normal-mode NCX activity results in calcium efflux from the cytosol. However, neonatal myocytes appear to be able to elevate cytosolic calcium through the calcium influx or reverse-mode of NCX activity. Furthermore, current evidence indicates that the developing myocardium is more dependent on reverse-mode NCX activity than I_{Ca} in mediating transsarcolemmal calcium fluxes. Despite the prominence of NCX at early developmental stages, neonatal I_{Ca} is still an important component of developmental EC coupling.

In order for the neonatal myocardium to support significant amounts of NCX-CICR, early developmental stages are hypothesized to contain a variety of structural specializations. The prevalence of these specializations is expected to be higher at early developmental stages, when NCX-CICR is predominant, and then progressively decrease as I_{Ca}-CICR dominance emerges. NCX-CICR, in comparison to I_{Ca}-CICR, has a lower coupling efficiency and releases a smaller amount of SR calcium for a given amount of trigger calcium and the ability of NCX-CICR to dominate over I_{Ca}-CICR suggests that the I_{Ca}-CICR mechanism is functionally immature at early developmental stages. To determine the nature of the dysfunction, the first study investigates the physical separation between DHPR and RyR at different developmental stages.

NCX-CICR suggests that NCX is able to function as a surrogate calcium trigger in lieu of the traditional calcium current and suggests that NCX must be in close proximity to RyR. The second study investigates the colocalization relationship between NCX and RyR as a function of

development to determine the prevalence of these coupling events. At the single molecule level, NCX-mediated calcium entry is inherently slow, especially when compared to the single-channel conductance of a voltage-gated calcium channel. However this inherent rate-limitation may be less of a factor in conditions where NCX is highly expressed and organized into multi-molecular units. NCX expression is known to be robust at early developmental stages and may also be organized into punctate clusters by the presence of adapter proteins. Such organization of NCX would increase the local density of NCX and assist the role of NCX as a surrogate calcium trigger. To determine whether caveolin-3, the principle protein constituent of membrane caveolae may be participating in the organization of NCX as a function of development, the third study investigates the colocalization index between NCX and cav-3.

The rate of reverse-mode NCX activity is strongly modulated by increases in the intracellular sodium concentration. Early developmental stages may increase the efficacy of the NCX-CICR mechanism by coupling NCX to a transient sodium influx source. Although increased intracellular sodium favours calcium entry, increased intracellular sodium is also detrimental to calcium removal and myocyte relaxation. However, a transient increase in intracellular sodium would preferentially increase NCX-mediated calcium influx. Therefore, such an interaction would be expected to benefit increases in systolic calcium concentrations without detrimentally affecting diastolic calcium concentrations. In the fourth study, the expression of different sodium channel isoforms is evaluated and distribution of these channels in considered in relation to NCX.

6.2. DHPR AND RyR IN EXCITATION-CONTRACTION COUPLING

In adult myocytes, the majority of I_{Ca} is found within the t-tubular structures of the myocyte. Detubulation experiments have estimated that 80% of I_{Ca}[7] and 75% of dyadic associations[8] are found in the t-tubular membranes of the rat heart. T-tubules are hypothesized to facilitate the propagation of the action potential deep into the interior of the myocyte, ensuring contractile synchrony along the cross-section of the cell. Consistent with this hypothesis, many key EC coupling proteins have been localized to the t-tubular membrane area including L-type calcium channels, NCX and sodium channels[9-13].

Early electron microscopy studies reported a sparse SR network at early developmental stages[14] and found these myocytes to be devoid of t-tubular structures, leading investigators to believe that CICR does not occur early in development. Nevertheless, the neonatal SR network is able to store and release calcium[15-20]. I_{Ca} has been measured in neonatal myocytes and there are reports of increased I_{Ca}[21-23] as well as reports indicating a consistent I_{Ca} density with development[24, 25] and I_{Ca} is nevertheless present despite the paucity of the I_{Ca}-CICR mechanism[15, 16].

The neonatal phenotype of dysfunctional I_{Ca}-CICR suggests two basic but opposing possibilities. On one hand, the lack of an appreciable I_{Ca}-CICR response may indicate the insufficient proximity between the I_{Ca} calcium trigger and the RyR receiver. Because RyR is relatively insensitive to cytosolic calcium elevations, a larger distance of separation between DHPR and RyR at early developmental stages may effectively dilute the effects of the incoming I_{Ca} and fail to trigger SR calcium release. The neonatal I_{Ca}-CICR mechanism may be hampered by the lack of an effective calcium trigger. On the other hand, the proximity between DHPR and RyR may be constant with development. Instead, the lack of a significant I_{Ca}-CICR response may be indicative of insufficient SR calcium stores. Neonatal RyR may successfully detect and response to the incoming I_{Ca} but the underlying SR lumen may contain insufficient SR calcium loading to mediate a robust response. In this second scenario, the neonatal I_{Ca}-CICR is hampered by impaired limited calcium release.

To differentiate between these two opposing mechanisms, the colocalization relationship between DHPR and RyR was considered. When the proximity between DHPR to RyR was investigated in neonatal myocytes[12, 13] 44% of DHPR labelling, which is limited to the cell periphery, also contained RyR labelling[12, 13]. In the adult, the colocalization of DHPR with RyR increases to 63%, a change of over 40%. Thus, the number of DHPR events coinciding with RyR events increases with development, consistent with the hypothesis that increased I_{Ca}-CICR is correlated with increased DHPR-RyR proximity. Nevertheless, the colocalization relationship between DHPR and RyR is quite robust even at early developmental stages. This robust colocalization may suggest that the underlying I_{Ca}-CICR dysfunction at early developmental stages is related to limited SR calcium stores underlying the corresponding DHPR-RyR colocalization events.

The early reports of sparse SR development[14] at early developmental stages are, at first glance, contradictory to newer fluorescence based observations. Although there was an early report of diffuse RyR labelling in the neonate cardiomyocyte[17], well organized RyR labelling coinciding with what appear to be z-lines has since been identified in neonatal rat[26] as well as neonatal rabbit heart[11]. While this RyR labelling may seem inconsistent with the structural reports, RyR labelling only describes as subset of the SR network. While the colocalization index of DHPR-RyR increases with development, neonatal myocytes nevertheless contain 44% DHPR-RyR colocalization. Thus the optical measurements, in isolation, would suggest that DHPR and RyR are colocalized on the cell periphery, yet no functional contribution of I_{Ca}-CICR could be identified.

In addition to the two basic hypotheses outlined above, alternative hypotheses should also be considered. The dysfunctional I_{Ca}-CICR response in neonatal groups could also be related the amount of RyR labelling also containing DHPR labelling. 10% of RyR events in neonatal myocytes were found to also contain DHPR events[13]. In the adult, RyR-DHPR colocalization increases to 17%[13]. Thus it could be suggested that, early in development, fewer RyR channels are coupled to DHPR and contain less potential for I_{Ca}-CICR. However, it is obvious that the lack of t-tubular structures ensures that interior RyR population is corbular in nature, thus any potential interaction between I_{Ca} and RyR is limited to the cell periphery.

Visually, peripheral RyR and DHPR are strongly related and may be colocalized. The presence of an internal RyR distribution, yet no internal DHPR distribution, would suggest that the RyR-DHPR colocalization index in the neonate could be significantly higher if internal RyR events were excluded from the analysis. Thus, it is possible, that RyR-DHPR colocalization is equal to, or even higher than, adult RyR-DHPR colocalization. The optical measurements of the association between DHPR and RyR would then appear to conflict with the functional measurements of I_{Ca}-CICR. Since confocal resolution is approximately an order of magnitude greater than the dimension of the dyadic cleft, there will be the tendency for colocalization measurements to overestimate the actual relationship between DHPR and RyR. Sizable I_{Ca} in neonatal myocytes, yet an absence of I_{Ca}-CICR, suggests I_{Ca} is uncoupled to RyR calcium

release and either protein may be residing close to a potential dyadic cleft site without having the sufficient proximity for functional coupling.

Alternatively, DHPR may have the necessary proximity to RyR but lack functional coupling due to inherent differences in neonatal channels or required ancillary proteins. The biophysical properties of the RyR and calcium channel themselves appear to be consistent with development[24-26], thus functional uncoupling is unlikely to be attributed to the single channel properties. There are reports of differential expression of DHPR splice variants that occurs with development[24, 27], changing from a mixed IVS3A and IVS3B expression in the neonate to predominantly a IVS3B expression in the adult, however the functional significance of these splice variants is not yet established[28]. DHPR activity is known to be affected by the presence of accessory subunits and slice variants may affect subunit interaction[29]

Both RyR and DHPR are modulated by external factors. Developmentally, neonatal calcium currents but not adult calcium currents can be modulated by stimulation of β_2 adrenergic receptors (AR)[30, 31]. This β_2-AR response appears to be mediated by a pathway independent of global increases in PKA[32, 33], suggesting microdomain level regulation of I_{Ca}. A caveolar β_2-AR, but not β_1-AR, complex with DHPR has been reported[34].

The SR load is an important modulator of RyR release and higher luminal calcium concentrations are associated with an increased RyR sensitivity to cytosolic trigger calcium by modifying the mean open time of RyR[35-37]. SR calcium loads are reportedly higher in neonates than in adults when normalized to cell capacitances[18, 24] and caffeine SR calcium release experiments indicate robust calcium transients in neonatal myocytes[38, 39]. These results leave the possibility that neonatal RyR sensitivity could be equal to adult sensitivities and that there is sufficient SR calcium load to mediate a CICR response if I_{Ca} were to be coupled to the RyR/SR complex. Equal RyR sensitivity and the presence of SR calcium load could suggest that the apparent lack of DHPR and RyR coupling is due to insufficient proximity rather than fundamental differences in channel behaviour.

In adult myocytes, the link between I_{Ca} and I_{Ca}-CICR can be assessed by examining the time course of I_{Ca} for signs of calcium-dependent-inactivation (CDI). The binding of calcium to

a cytosolic calmodulin molecule mediates an increase in the rate of CDI, linking an intracellular calcium sensor to calcium channel function. An increased rate of inactivation has been correlated with increases in SR calcium load in adult myocytes but not in neonatal myocytes, indicating that despite the early colocalization index, neonatal I_{Ca} either does not reside in dyadic cleft or resides in a dyadic cleft without significant SR calcium load[24, 25].

In adult myocytes, the SR network and nuclear envelope is a single continuum and calcium is able diffuse along both networks[40]. Although neonatal RyR can be found in both the peripheral and interior compartments, the interconnectivity between these compartments is not yet known. Conceivably, peripheral RyR, found colocalized with either DHPR or NCX, could effectively sense incoming calcium yet have insufficient SR calcium load to contribute to global calcium transients. The caffeine transient could then be mediated by interior SR calcium stores physically uncoupled to the peripheral RyR population in neonatal myocytes. However, an uncoupled peripheral RyR population would suggest that the depletion of SR calcium load should not affect neonatal EC coupling. Yet, caffeine has been shown to strongly attenuate calcium transients in neonatal myocytes[19].

Interestingly, detubulation experiments have suggested that peripheral L-type channels in adult myocytes do not induce CICR. While CDI can be observed in myocytes with an intact t-tubular structure, upon detubulation, not only does a large component of the I_{Ca} disappear but the remaining I_{Ca} has altered inactivation properties[7]. Ionic diffusion is restricted in the t-tubular lumen ionic depletion and accumulation may occur during rapid stimulation[41]. Peripheral couplings may provide SR calcium loading in the absence of CICR activation[42]. However it is not known whether the peripheral calcium channel population is the analogous population as the neonatal peripheral population.

The adult peripheral population shows a smaller fractional I_{Ca} increase in response to β-adrenergic stimulation (isoproterenol)[43] as does the peripheral neonatal I_{Ca} population[44] suggesting that the peripheral population may be a specialized sub-population. Uncoupled peripheral I_{Ca} may be ideally suited to regulating SR calcium load due to the decreased rates of current inactivation. Uncoupled calcium channels are expected to mediate larger calcium influxes through longer mean open times than coupled channels undergoing CDI. The ability of

isoproterenol to 'rescue' cardiac function in detubulated myocytes suggests that peripheral calcium channels are nevertheless associated with RyR channels, albeit appear to have a weaker coupling efficiency under normal conditions[43] and may contribute to the cardiac reserve.

6.3. SODIUM-CALCIUM EXCHANGER (NCX) AND RYANODINE RECEPTOR (RYR) IN EXCITATION-CONTRACTION COUPLING

The lack of I_{Ca}-CICR in neonatal myocytes coincides with increased levels of NCX expression[19, 45-48] and a corresponding increase in the sensitivity of calcium transients to KB-R7943 (KB-R)[19], a NCX inhibitor. Under voltage-clamp, the presence of 15 μM nifedipine, a calcium channel blocker, does not alter the size of the calcium transient in neonates. However, this concentration of nifedipine in adults strongly attenuates the calcium transient[24]. This dose of nifedipine blocks ~98% of the I_{Ca}, suggesting that NCX is the predominant calcium influx mechanism in the neonate heart[19, 24, 47]. The lack of t-tubule development and reports of sparse SR development suggested that CICR mechanisms do not play a significant role in developmental EC coupling and the neonatal myocytes rely predominantly on transsarcolemmal calcium influx for contraction.

More recently, there are reports that NCX can mediate a CICR response in neonatal rabbit ventricular myocytes. Caffeine, which sensitizes RyR to luminal calcium load, effectively negates the SR load by releasing stored calcium[49]. Caffeine causes a partial reduction of the calcium transient in neonatal myocytes and 40% of the calcium transient was determined to be SR calcium release[19]. Adult myocytes, from most species except perhaps guinea pig cardiomyocytes, cannot mediate NCX-CICR and I_{Ca}-CICR accounts for the majority of the calcium transient. Thus robust NCX expression and a CICR response in the presence of calcium channel blockage suggest that NCX and NCX-CICR are the predominant EC coupling mechanisms at early developmental stages.

The ability of neonatal myocytes to display NCX-CICR is undoubtedly linked to the high NCX expression levels observed in early developmental stages. Nevertheless, it is still unexpected for a relatively slow exchanger mechanism to be able to mediate the large increase in

subsarcolemmal calcium necessary to induce SR calcium release. The unitary exchange current of NCX is predicted to be in the fA range[50] in this range of voltages and is ~3 orders of magnitude lower than the unitary current of $Ca_v1.2$, which is in the pA range[51].

CICR in cardiac EC coupling is a graded response, suggesting that RyR is activated by relatively high levels of subsarcolemmal calcium. Peak systolic calcium reaches ~1 μM, therefore, a graded CICR response implies that RyR is insensitive to this range of calcium concentrations. In the adult, it has been shown that the calcium influx resulting from the activation of a single calcium channel is sufficient to induce the activation of a calcium spark[52]. A sparklet, the calcium signal emanating from a single calcium channel is estimated to raise subsarcolemmal calcium to ~10 μM[53].

A calcium spark, the RyR response to a sparklet, likely corresponds to the recruitment of several RyR molecules[53]. At minimum, at least one RyR must be activated by NCX activity for there to be NCX-CICR. Each RyR has a length and width of 30 nm and a cross-sectional area of ~900 nm^2,[2, 54]. For 0.5 pA of current to pass through this area via NCX, there needs to be ~500 exchangers, packed at ~1 nm intervals to pass equivalent current as a single calcium channel. Thus, NCX expression must be high and organized into punctate clusters in order to mediate sufficiently high localized NCX densities to serve as a surrogate calcium trigger for I_{Ca}.

The NCX and RyR distributions were investigated using confocal microscopy and colocalization analysis[11]. Maximum colocalization between NCX and RyR was found in the youngest age group, with 14% colocalization between NCX and RyR in the 3d group. In adult myocytes, 10% of NCX was found to be colocalized with RyR. Although neonatal and adult colocalization indices were statistically different, the similarity of the neonatal index to the adult index is surprising considering the dramatic differences in NCX-CICR contributions as a function of development.

Colocalization results were broken down into peripheral and interior compartments since a large degree of corbular RyR labelling is found in the interior of even the youngest myocytes. The analysis indicated that, as expected, the majority of neonatal colocalization events are restricted to the cell periphery, consistent with membrane delimited NCX staining. Adult

myocytes had the majority of the colocalization events occurring within the t-tubular structure. Since the majority of dyadic clefts reside within the t-tubules, it is possible that NCX-CICR does not occur in the adult due to the colocalization of DHPR and RyR in the t-tubules. Although, the dominant factor in the absence of adult NCX-CICR is expected to be related to the decreased NCX expression.

The level of colocalization between NCX and RyR is perhaps unexpectedly small considering the contribution of NCX-CICR to the overall calcium transient. However, this colocalization index is similar to the RyR-to-DHPR colocalization index found in 20 day old myocytes from the previous DHPR-RyR study[13], in which only 17% of RyR appeared to be involved in I_{Ca}-CICR. This suggests that even in the high gain environment of I_{Ca}-CICR[19], only a small subset of RyR is directly involved in CICR initiation.

Because the NCX-CICR contribution in neonatal myocytes is not as high as the I_{Ca}-CICR contribution in adult myocytes, it is conceivable that NCX-CICR is mediated by only a small subset of NCX and RyR molecules. If only a small subset of NCX accounts for NCX-CICR, it suggests that any NCX-to-RyR coupling that does occurs, occurs with very high coupling efficiency; possibly much higher than I_{Ca} coupling efficiency. CICR gain is estimated by the total amount of SR calcium release normalized by the size of the trigger flux and NCX-induced calcium release is reportedly to have low global coupling efficiency relative to I_{Ca} coupling gain[19].

The imaging results imply that the vast majority of NCX events (~90%) are spatially well separated from RyR. Thus previous estimates of 40% NCX-CICR release must then be mediated by 10% of the NCX population. Thus, if this subpopulation of NCX does in fact mediate CICR, they must couple very strongly to RyR release (high dyadic coupling gain). Low global gain would then reflect the masking of these high gain NCX-to-RyR coupling sites by non-coupled NCX-activity. High NCX-to-RyR coupling efficiency would require very high localized NCX densities however the lack of NCX crystal structures prevents the estimation of maximal NCX packing densities.

As a rule, colocalization studies overestimate the true colocalization relationship[12]. Likely, even less NCX is coupled with RyR than what is estimated by the colocalization index suggesting even higher NCX-to RyR coupling gains and higher NCX packing densities. The low level of NCX-RyR colocalization suggests that NCX may not induce CICR in analogous fashion to adult I_{Ca}-CICR. The low colocalization index between NCX and RyR, yet the existence of a NCX-mediated CICR response suggests that NCX may induce CICR through 'long range' interactions.

The sensitivity of RyR to a cytosolic calcium trigger is known to be steeply dependent on luminal SR calcium load. It has been suggested that SR calcium load, when normalized to membrane capacitance, is larger in neonatal myocytes than in adult myocytes[18]. Thus, a higher SR calcium load could reduce calcium trigger requirements and help facilitate NCX-mediated CICR. However, it is difficult to conceptualize a membrane geometry and protein distribution patterns which would allow NCX to trigger CICR while simultaneously preventing calcium entry from DHPR from activating SR calcium release, suggesting that increased calcium load alone is not sufficient to account for the NCX-CICR mechanism.

It is possible that neonatal NCX-CICR benefits from the presence of SR membrane sheets which could provide a sufficiently large diffusional barrier to mediate 'long distance' NCX-RyR coupling. Previous EM results indicate that there are longitudinal SR sheets that run beneath the sarcolemma in neonatal myocytes[18] and could possibility function as a reflective boundary which would dramatically reduce the already low calcium diffusional coefficient[55]. Although such a mechanism could, in theory, couple NCX to RyR the same mechanism would also be expected to couple the reverse reaction; from RyR release to NCX mediated calcium efflux. Therefore, while a strong diffusional barrier could facilitate RyR release, it would also present the possibility of a NCX short-circuit, where released calcium is extruded to the extracellular space rather than participating in myofilament activation. Caffeine release experiments have indicated that NCX activity peaks earlier than the cytosolic calcium peak suggesting that NCX has privileged access to RyR calcium release[47]. RyR flux will outpace NCX extrusion, thus, NCX-CICR induced by this mechanism would still be able to induce contraction.

Because increased calcium load has such a strong sensitizing effect on RyR release, it has been suggested that calcium waves can be propagated by "sensitization wave fronts"[56], where loading of the SR allows RyR molecules ahead of the wave front to respond to a lower trigger calcium, thereby allowing the process of CICR to perpetuate. Since this mechanism does not require the colocalization between the calcium source site and the calcium release site, a related mechanism could be responsible for the NCX-CICR phenomenon. The sensitized calcium release hypothesis requires an overloaded SR load state to occur in the adult myocytes thus this mechanism may not necessarily be relevant to normal adult CICR function. However, the mechanism may be more effective in the neonate heart since the magnitude of the relative amount of calcium entering the cell and basal SR load are both higher in comparison to the adult[18]. A proportion of calcium entering through NCX may enter the SR lumen through SERCA activity thereby altering the sensitivity of RyR to cytosolic calcium.

Sensitized SR release may account for the observation of NCX-CICR, however, it may also account for the lack of a NCX-CICR response under certain conditions[17, 57]. These studies are notable because they also utilized a rabbit animal model with similar neonatal age groups. While these studies also found SR calcium stores, releasable by caffeine, their results led them to conclude that neonatal myocytes only have a minimal SR Ca^{2+} contribution and rely almost exclusively on trans-sarcolemmal calcium flux. A key distinction between the reports indicating NCX-CICR and those that do not, is the use of the voltage-clamp technique rather than the field stimulation technique.

In voltage-clamp, membrane depolarization is dictated through the voltage protocol, with a typical step-depolarization time of 400 ms[18-20, 24, 47]. In field-stimulation, a short 5-10 ms extracellular voltage pulse is applied through bath electrodes[58]. Field simulation induces an approximation of a normal action potential and the profile of this action potential is largely dependent on natural cellular currents. Under voltage clamp, adult rabbit ventricular myocytes have been shown to load predominately though I_{Ca}[18] and SR calcium load as determined by voltage-clamp or by field-stimulation are likely comparable in adult myocytes. This is because of I_{Ca} inactivation. Under voltage-clamp the majority of I_{Ca} is inactivated after 50 ms[24]. This inactivation ensures that longer step-depolarizations cannot increase the amount of calcium entering through I_{Ca}. Both step-depolarizations and induced action potentials are significantly

longer than 50ms and the limiting factor in adult myocytes, which load predominately via I_{Ca}, is the inactivation time course of I_{Ca}. Thus, adult myocytes are expected to have similar SR calcium loads regardless of whether this SR calcium load is established by voltage-clamp or by field-stimulation.

Neonatal myocytes have been shown to load predominately through NCX under voltage-clamp due to high levels of NCX expression[18]. Increased NCX expression is expected to cause voltage-clamped neonatal myocytes to load more SR calcium than neonatal myocytes loaded via field stimulation. This is because NCX will continue to influx calcium as long as it is thermodynamically favoured and the duration of the step depolarization is expected to have a direct effect on calcium entry. In an action potential, in which the membrane voltage is allowed to vary freely, robust NCX-mediated calcium entry is expected to shorten the action potential duration. Reverse-mode NCX activity generates an outward current with repolarizing effects[59]. Under voltage-clamp conditions, this repolarizing effect is counteracted by the patch-clamp amplifier. However in a native action potential, reverse mode NCX activity subsequently disfavours further reverse-mode activity via repolarization. The more NCX activity present in a cell, the stronger the repolarizing current will be with corresponding effects on action potential duration.

Thus, if NCX-CICR occurs through sensitized release, the shorter membrane depolarization time associated with field stimulation will correspond to a smaller SR calcium load and insufficient calcium loading may exist to facilitate NCX-CICR. However, under voltage clamp, the elevated SR calcium load may permit sensitized release to occur and may account for the NCX-CICR mechanism.

The effect of the length of the step-depolarization on SR calcium loading or on transsarcolemmal calcium flux can be considered further. Longer step depolarizations will favour I_{NCX} over I_{Ca} due to the non-inactivating characteristics of the NCX and inactivating characteristics of I_{Ca}[60]. The extent to which NCX is favoured is dependent on the length of the step depolarization. For all step depolarizations longer than the time course of I_{Ca}, the amount of calcium entry through I_{Ca} will be fixed. However, the balance between apparent NCX and I_{Ca} contributions can be altered by changing the length of the membrane depolarization. If the step

depolarization is limited to the time course of I_{Ca} then the estimated NCX contribution will be small. Increasing the duration of the step depolarization will be predicted to increase the NCX contribution. The estimated NCX contribution will continue to increase as long as calcium entry through NCX is thermodynamically favoured.

The effect of duration on the estimated NCX contribution in voltage clamp is important because NCX activity will always seek out its thermodynamic equilibrium. If the extracellular sodium concentration is fixed at 135 mM and if cytosolic sodium is fixed by a pipette sodium concentration of 10 mM then E_{Na} is predicted to be +67mV. If the extracellular calcium concentration is fixed at 2 mM and the myocyte is depolarized to +10mV, the concentration of cytosolic calcium necessary to drive the reversal potential of NCX (E_{NCX}) to equal +10mV can be back-calculated from $E_{NCX} = 3E_{Na}-2E_{Ca}$. Given these conditions, the calculation would predict that NCX will pass no net current when cytosolic calcium is elevated to 1.2 µM. Thus, if $[Na^+]_o$ = 135 mM, $[Na^+]i$ = 10 mM, $[Ca^{2+}]_o$ = 2 mM and $[Ca^{2+}]_i$ = 1.2 µM then E_{NCX} would equal +10 mV. The tendency for NCX to influx calcium until cytosolic calcium makes $E_{NCX} = E_m$, means that given a sufficiently long step depolarization NCX will always reach thermodynamic equilibrium.

The thermodynamic factors of NCX obviously do not change with increased or decreased NCX expression. While it may not occur with physiologically significant durations, it is thermodynamically possible that even a small NCX population can reach thermodynamic equilibrium given a sufficient duration. Conversely, in myocytes with strong NCX expression, the thermodynamic limit may be reached prior to the end of physiologically significant step durations. In such a scenario, the absence or inclusion of a sizable I_{Ca} will have no effect on the size of the calcium transient since a large NCX population would have sufficient time to compensate for any reduced calcium entry.

Calcium influx in the developing heart is reputedly mediated predominantly by reverse-mode NCX activity with the calcium entry through I_{Ca} having only an accessory role. However, it is important to reiterate the key caveat in this statement. Calcium entry through I_{Ca} can be blocked pharmacologically and yet neonate myocytes can still retain normal sized calcium transients, purportedly due to increased NCX expression, but this has only been demonstrated

when the membrane potential is controlled under voltage clamp conditions[61]. That is to say that NCX expression in neonatal myocytes is sufficiently large, such that, NCX activity can sufficiently replace the loss of I_{Ca} mediated calcium entry within the length of the step-depolarization. In the native action potential, I_{Ca} plays an important role in regulating the plateau phase of the action potential. I_{Ca} blockers nevertheless affect contractility by truncating the action potential duration, thereby limiting the amount of calcium that can enter the cell through reverse-mode NCX activity[61, 62].

6.4. NCX ORGANIZATION

Investigations of the NCX and RyR protein distributions revealed that NCX is organized in punctate clusters on the cell surface and that these punctate clusters have a regular periodicity that does not change with development. The NCX distribution has previously been described as homogenous in nature, suggesting that NCX is unlikely to be localized in functional microdomains[17, 63, 64]. However the phenomenon of NCX-CICR as well as the punctate labelling of NCX strongly suggests that multiple molecules of NCX exist in an organizational micro-domain. Multiple exchangers working in concert are expected to facilitate local elevations in subsarcolemmal [Ca^{2+}] and benefit the role of NCX as a trigger for RyR release.

Lipid rafts are cholesterol- and sphingolipid-enriched areas of the plasma membrane and are hypothesized to be an organization entity within the plasma membrane[65]. A subset of lipid rafts also contains caveolin proteins, some of which will also form into caveolae or 'little caves'. Caveolae are 50-100 nm diameter invaginations that appear to contain a variety of EC coupling proteins, such as L-type calcium channels, K^+ channels, Na^+ channels as well as NCX. Caveolae account for a significant proportion of the sarcolemmal area in rabbit ventricular myocytes and up to 32% of the total SL area is contained within caveolae[66].

Direct interactions between caveolin and other proteins are mediated by caveolin-binding motifs corresponding to the scaffolding domain of caveolin[67]. Analysis of the NCX primary structure identified 3 possible motifs, located on the large cytoplasmic regulatory f loop of NCX[68]. Co-immunoprecipitation experiments found evidence of a direct cav-3 to NCX interaction and cholesterol depletion experiments, using β-cycolodextrin, indicating that the

ability to co immunoprecipitate cav-3 with NCX could be inhibited with cholesterol depletion. Cholesterol depletion disrupts caveolae structure[69], further supporting the possibility of a direct cav-3 interaction with NCX.

In addition to a high localized NCX density, the ability of NCX to serve as a CICR trigger could also be potentiated by a functional coupling between NCX and a sodium source. One of the first ion channels to be found associated with caveolae in the heart is $Na_v1.5$, the cardiac "isoform" of voltage-gated sodium channels[70]. The link between $Na_v1.5$ and caveolae is believed to be important in the β-adrenergic regulated increase in I_{Na}[71]. To investigate a possible interaction between NCX and cav-3 immunolabelling and confocal microscopy techniques were applied to developing cardiomyocytes[10].

The image analysis techniques used to investigate the colocalization relationship between NCX and RyR allowed for ambiguity in the colocalization index due to the possible inclusion of 'fringe' pseudo-colocalization events[12]. Aggressive thresholding is one means of reducing pseudo-colocalization events; however aggressive thresholding can also remove legitimate cellular labelling. This study utilized an automated thresholding procedure that utilizes iterative procedures to examine the effects of under- and over-thresholding in each individual image to select a thresholding value that retains the maximum number of discrete objects in the image. A supplemental colocalization parameter, the object-specific colocalization index, which describes the specific overlap between each and every colocalized object pair allowed the identification of probable fringe colocalization events. These advancements revealed that nearly all colocalization events occurring between NCX and cav-3 can be attributed towards these fringe colocalization events. Furthermore, periodicity analysis indicated that the most frequent separation distance between NCX and cav-3 objects is 0.5 μm suggesting the NCX and cav-3 are not only seldom colocalized but appear to be spatially mutually exclusive.

Thus despite the presence of caveolin binding motifs in NCX and the apparent presence of NCX in caveolae as per co-immunoprecipitation and cholesterol depletion experiments, NCX and cav-3 do not appear to interact in intact cells. The colocalization relationship between NCX and cav-3 has also been investigated in adult rats with similar conclusions, where they also considered the effects of different lipid raft extraction methods[72]. Using a detergent-free method

of lipid rafts extraction, they found a plethora of integral membrane proteins in lower density sucrose fractions, including NCX and DHPR as well as NKA subunits, PMCA and the adenosine A_1 receptor. Using a more traditional detergent method, only DHPR and the adenosine receptors were found in lower density fractions thus suggesting that detergent-free methods may not successfully extract lipid rafts in cardiomyocytes[72]. Co-immunoprecipitation results indicated that neither NCX nor DHPR were associated with cav-3[72].

6.5. SODIUM CHANNELS AND NCX IN EC COUPLING

The stoichiometry of NCX makes the reversal potential, and therefore the driving force of NCX, sensitive to even small changes in cytosolic sodium concentration. This sensitivity may permit sodium influx mechanisms to regulate the activity of nearby exchangers[55]. In Chapter 5, sodium channel isoform expression and localization was investigated in 3 day and 56 day old myocytes. Western blot analysis for voltage-gated sodium channel ($Na_V1.X$) isoforms 1.1-1.6 indicated that $Na_v1.1$, $Na_v1.4$ and $Na_v1.5$ are expressed in rabbit cardiomyocytes. Expression of $Na_v1.1$ and $Na_v1.4$ decreases with development while no statistically significant changes in $Na_v1.5$ expression were found. Labelling intensity of $Na_v1.1$ was insufficient for further analysis however, $Na_v1.4$ and $Na_v1.5$ labelling was sufficiently intense to undergo detailed imaging studies. The study found that a subset of $Na_v1.4$ is colocalized with NCX and the association between these two proteins did not appear to change with development. The study also found a subset of $Na_v1.5$ is colocalized with NCX however this $Na_v1.5$-to-NCX relationship decreases with development. Using automated image analysis procedures, it was determined that the density of $Na_v1.5$ labelling, relatively to NCX labelling does not change with development. The decreased colocalization index between $Na_v1.5$ and NCX occurs due to an increase in distance separating $Na_v1.5$ and NCX events. Using these image analysis procedures it was also determined that the distance separating $Na_V1.4$ and NCX events does not change with development.

The results suggest that elevated NCX expression in neonates also correlates with increased $Na_v1.5$ and $Na_v1.4$ colocalization, consistent with the hypothesis that NCX and NCX-mediated CICR are the predominant EC coupling mechanisms at early developmental stages. The results also suggest that distribution of $Na_v1.4$, $Na_v1.5$ and NCX are co-ordinated as a

function of development. The relationship between these proteins may be mediated by ankyrins and the underlying spectrin cytoskeleton.

NCX has been suggested to interact with ankyrin-B with high affinity[73]. The interaction between NCX and ankyrin appears to exist in the detergent-soluble fraction of the rat heart[74]. A direct interaction between ankyrin-B and NCX is attributed to ANK repeats 16-18 and disruption of these regions affects expression and localization of NCX in cultured cardiomyocytes[75]. The inotropic effects of cardiac glycosides have been suggested to be mediated by the close proximity between NCX and NKA. Ankyrin-B has shown to bind with alpha 1 and alpha 2 NKA isoforms and colocalization experiments indicate that NCX is highly colocalized with NKA, suggesting that NCX and NKA are functionally coupled within an ankyrin-B complex[74].

An ankyrin G binding motif has been identified in loop 2 of voltage-gated sodium channels. This binding motif is 9 amino acids long and is conserved in Nav1.1-6 and was identified independently by two groups[76, 77]. The E1053K mutation in $Na_v1.5$ is associated with Brugada syndrome and this mutation appears to block Nav1.5 binding to ankyrin and disrupts surface expression[78]. Thus both NCX and Na_V isoforms may be organized by the ankyrin family of proteins.

$Na_v1.4$ is considered a TTX-sensitive isoform while $Na_v1.5$ is considered a TTX-resistant isoform, thus low (200 nM) and high (30 µM) concentrations of TTX may offer selective inhibition of these sodium currents. $Na_v1.4$ and $Na_v1.5$ colocalization in the neonate suggests that there is a $TTX_{200\ nM}$-sensitive NCX component as well as a $TTX_{30\ \mu M}$- sensitive NCX component to EC coupling. The imaging results do not indicate whether NCX objects colocalized with $Na_v1.4$ are also colocalized with $Na_v1.5$. The combined object density of both isoforms may equal NCX object density; however both isoforms indicate non-complete colocalization, suggesting that only some of NCX operates within close vicinity to sodium channels. Therefore functional experiments must determine the potentiating effects of $TTX_{200\ nM}$-sensitive and $TTX_{30\ \mu M}$-sensitive components of the sodium current on NCX function as well as the generalized effects of sodium entry.

One possibility of investigating these effects is to utilize field-stimulation techniques. Relative to the more laborious patch clamp approaches field stimulation is a high-throughput approach. However, field stimulation is purported to result in artifactual contractions[58]. Contractions induced by momentary current injections (current clamp) appear to be $TTX_{30\ \mu M}$-sensitive while field stimulated contractions are $TTX_{30\ \mu M}$ -insensitive. The strength of field stimulated contractions did not vary with stimulation duration, suggesting that field simulated contractions represent maximal strength contractions. The insensitivity of field stimulated contractions to TTX would suggest that the strength of the stimulation pulse is sufficient to directly activate voltage-gated calcium channels although it is unlikely that I_{Na} is completely inactive. Field stimulation applies extracellular field potentials such that opposite sides of the myocyte experience different potentials relative to the orientation of the cell to the bath electrodes, simultaneously creating both depolarized and hyperpolarized regions in the cell[79]. This voltage heterogeneity may desynchronize the activation $Na_v1.x$ and diffuse the depolarizing effects of I_{Na}. The lack of a TTX effect may make field simulation experiments difficult to interpret.

Because I_{Na} can affect NCX activity through membrane depolarization as well as through elevations in intracellular sodium, it may be difficult and convoluted to determine the specific contributions of $TTX_{200\ nM}$ -sensitive and $TTX_{30\ \mu M}$ -sensitive currents to NCX potentiation. Field stimulation and current clamp results are expected to be affected by the presence of TTX, regardless of the proximity of I_{Na} to NCX, due to the shortening of the action potential. A similar effect is seen in neonatal cardiomyocytes in the presence of nifedipine. Although neonatal myocytes can maintain normal sized calcium transients in the presence of nifedipine, neonatal myocytes are only nifedipine insensitive under voltage clamp conditions[60]. Voltage clamp injects a depolarizing current through the patch electrode, which in the native action potential is carried by the depolarizing calcium and sodium currents. Myocytes with high NCX expression can supplement the loss of calcium influx by nifedipine during a long step depolarization. However, under non-voltage clamp conditions, where the membrane voltage is allowed to vary, the loss of depolarizing membrane currents truncates the action potential duration and decreases contractility[62].

Field stimulation experiments may still be informative if neonatal, but not adult myocytes, can contract in the presence of nifedipine. Theoretically, NCX-CICR will make the largest physiological contribution if it occurs early in the action potential. Although calcium channels are expected to be active early in the action potential, strong depolarization is expected to degrade the driving force for calcium entry. Although nifedipine is expected to limit calcium entry later in the action potential, its effect on early NCX-CICR should be minimal. If neonatal myocytes can be field simulated in the presence of nifedipine it implies that the potentially large sodium current coupled to the large NCX expression can rapidly influx calcium and cause CICR.

If the TTX-S I_{Na} component is small relative to TTX-R I_{Na}, low TTX concentrations (~200 nM) may be able to selectively inhibit the TTX-S mediated NCX potentiation component, assuming that TTX-R I_{Na} is able to propagate normal membrane depolarization. If a normal action potential occurs in the presence of low TTX then any decrease in the calcium transient will result from decreased sodium accumulation in the vicinity of NCX. The imaging results predict that both $Na_v1.4$ and $Na_v1.5$ are colocalized with NCX in the neonate and if TTX-R is sizable, the current through $Na_v1.5$ may also mediate sodium accumulation near NCX. If the number of $Na_v1.4$-NCX and $Na_v1.5$-NCX couplings are equal, but current densities are unequal as required for the presence of a normal action potential in the presence of TTX_{low}, sodium accumulation as mediated by $Na_v1.4$ is expected to be very small. Thus, any significant decrease in the calcium transient by low dose TTX suggests a very strong coupling efficiency between TTX-S currents and NCX activity. In the scenario that the TTX-S I_{Na} component is larger than the TTX-S I_{Na} component then it is expected that the action potential profile will collapse in the presence of low TTX and it cannot be determined whether the decreased calcium transient results from reduced sodium accumulation or from decreased membrane depolarization. Nevertheless, if the effect of low TTX on the calcium transient is small, a recording of the membrane potential is required to confirm that the effect is occurring through the loss of sub-membrane sodium accumulation and not through a change in membrane depolarization.

Current clamp experiments will share many of the same limitations as field stimulation since TTX and nifedipine are both expected to alter the induced action potential. However, there are some distinctions. Current clamp/injection depolarizes the membrane homogeneously which results in higher peak membrane depolarizations due to concerted recruitment of sodium

channels. This should assist in detecting NCX-CICR responses due to greater cell averaged signal intensity. However, throughput is lower in current clamp relative to field stimulation. One key advantage of current clamp over field simulation is that current clamp can provide an action potential recording. This action potential recording, however, is expected to underestimate peak membrane depolarization due to the limited time resolution particularly when I_{Na} reaches its highest values. Therefore, current clamp experiments can determine whether the effect of low TTX in field-stimulation experiments is mediated through a decrease in sodium accumulation or mediated through changes in membrane depolarization.

To determine the contribution of TTX-S and TTX-R I_{Na} to NCX activity, it is necessary to remove sodium influx without altering the upstroke of the action potential. One possibility is to utilize the voltage clamp technique. A key limitation in voltage clamp is voltage-escape, which occurs when the patch electrode is unable to pass sufficient current to control the membrane potential. Voltage escape is a significant problem with native sodium currents due to their size and rapid time course. The phenomenon of voltage escape was an early criticism of I_{Na}-NCX-CICR in adult myocytes, such that, activation of I_{Na} at membrane potentials insufficient to activate I_{Ca} can cause the loss of voltage control, allowing the depolarizing current to activate I_{Ca} and CICR[80-82]. Depolarizations to -50 mV have been used in attempt to selectively activate I_{Na} and the NCX-CICR processes[4]. However, if voltage escape occurred, I_{Ca} induced by voltage escape would be misinterpreted as NCX-CICR. Likewise, pre-pulse experiments utilizing low step depolarization to voltage inactive the sodium current may also be affected by voltage escape[3]. Voltage escape at the prepulse would be expected to voltage inactive calcium channels as well sodium channels, thus subsequent depolarizations will underestimate the 'I_{Ca} only' component. Although sodium currents can be attenuated by reduced extracellular sodium or by sub-maximal activation of the sodium current, both options would also be expected to attenuate NCX-CICR.

Voltage escape occurs when the activation of sodium channels results in a depolarizing current that is larger than the repolarizing current available through the patch pipette. Activation of the sodium current at a low depolarizing potential allows rapid sodium entry to occur due to the large driving force. The intention of low depolarizing potentials is to avoid activation of I_{Ca}, however, given the natural tendency for stimulated cells to undergo strong depolarizations, an

alternative strategy may be to strongly depolarize the cell to the reversal potential of I_{Na}. The reversal potential of I_{Na} is +67 mV and at this potential voltage-gated calcium channels are active but mediate only small calcium currents due to small driving forces[24]. Under such a scheme, steady-state I_{Na} will also be limited due to negligible driving forces. Sodium entry into the cell is expected to be limited to the time required for the patch clamp amplifier to successfully complete the step depolarization. However, given the rapid time course of I_{Na} significant I_{Na} is expected. In the unlikely situation that the patch clamp amplifier is faster than I_{Na}, a short pre-pulse at -60 mV can be included to facilitate subsarcolemmal sodium accumulations through I_{Na}. In this general approach, injected currents and I_{Na} are in the same depolarizing direction, eliminating the possibility of voltage escape.

Voltage clamp allows the use of low and high concentrations of TTX to determine whether sub-sarcolemmal sodium accumulations are occurring with channel activation. While the effects of nifedipine should be minimal, significant nifedipine effects would indicate that I_{Ca} is occurring early in the action potential suggesting that the above assumptions should be revisited. If the voltage clamp is a suitable replacement for normal depolarization then low and high TTX should only remove the sub-sarcolemmal contributions of the respective currents.

6.6. SUMMARY

In this thesis, confocal microscopy and image analysis techniques were used to investigate the phenomenon of NCX-CICR present in neonatal myocytes. Colocalization between DHPR and RyR was investigated as a function of development and despite the lack of I_{Ca}-CICR in early developmental stages, a relatively high DHPR-RyR colocalization index was found. Modeling experiments determined that the reliability of colocalization analysis can be improved by the inclusion of image restoration techniques (deconvolution). Nevertheless despite the gains in imaging resolution, false-colocalization events can still occur.

The interpretation of colocalization indices is hampered by the simplicity of the calculation. At early developmental stages there are substantial amounts of RyR labelling in the interior of cardiomyocytes. Because these myocytes are devoid of t-tubules, only peripheral DHPR and NCX labelling have the possibility of colocalization. Therefore, colocalization

analysis conducted at the whole cell level is difficult to interpret. To prevent internal RyR labelling from diluting peripheral colocalization events, automated image analysis procedures were developed to allow the creation of a cell outline. This cell outline could then be used to calculate the colocalization index in the peripheral and interior compartments independently.

Image thresholding is an integral part of any quantitative imaging study. Given the importance of image thresholding to colocalization analysis, objective imaging thresholding parameters were obtained with automated image thresholding procedures. In dense protein distributions, like NCX and cav-3, iterative thresholding procedures allowed an objective estimation of the thresholding parameter. However, in low density protein distributions like $Na_V1.4$ and $Na_V1.5$, iterative thresholding overestimates object sizing. Thus, an additional layer of thresholding was used to normalize object size estimates against the microscope resolution. Using the resolution definition of full-width-half-maximum, individual objects identified by the iterative thresholding procedures were thresholded individually based on the maximum intensity valve found in each object.

The image analysis techniques, developed during the course of these studies, culminated in the use of "object-specific colocalization analysis" and "separation distance analysis" to supplement the traditional colocalization index. The ability to track object size and density and the separation distances between object pairs allows the traditional colocalization index to be examined in great detail. Changes in object size, changes in object density and changes in object separation can each be investigated independently. Thus, although none of these advancements in image analysis deals specifically with the limited resolution available in confocal microscopy, these new techniques nevertheless increase the ability to detect and investigate changing protein distributions.

The prevalence of NCX-CICR at early developmental stages suggests that neonatal ventricular myocytes contain a series of structural specializations that transiently permit the NCX-CICR mechanism to dominate over the I_{Ca}-CICR mechanism. Since neonatal myocytes contain a sizable I_{Ca} as well as sizable SR calcium stores, the presence of robust levels of DHPR-RyR colocalization at early developmental stages suggests that the minimal I_{Ca}-CICR response may be associated with an underlying dysfunction in the releasable SR content associated with

these DHPR-RyR colocalization events. Although a sizable SR calcium store exists in the neonate, I_{Ca} does not appear to be able to release a significant fraction of the internal calcium stores.

The studies found NCX to be highly localized in punctate clusters. These high density NCX events are likely a key factor in the ability of NCX to function as a surrogate CICR calcium trigger. However, the hypothesized protein partner caveolin-3 does not appear to participate in the sarcolemmal localization of NCX. Some of these NCX clusters were also found in close association with RyR. However, these NCX-RyR couplings are relatively rare in comparison to overall NCX labelling density and only about 10% of NCX also contains RyR at early developmental. The investigations of voltage-gated sodium channel isotype expression revealed a developmentally regulated expression of $Na_v1.4$, with three-fold higher expression in neonatal myocytes with respect to the adult myocytes. Although the expression of $Na_v1.4$ decreases with development, the colocalization relationship between NCX and $Na_v1.4$ does not appear to change with development. Expression levels of $Na_V1.5$ were equally robust at both neonatal and adult developmental stages. However, the colocalization relationship between NCX and $Na_V1.5$ decreases with development. Together, the results suggest that a significant proportion of NCX, between one-third and two-thirds of neonatal NCX, operate in close vicinity to voltage-gated sodium channels. Although many NCX-CICR structural specializations were identified in the course of these studies, the overall prevalence of these structures suggest that the modulation of cardiac contractility at early developmental stages is regulated through the modulation of transsarcolemmal calcium fluxes rather than modulation of the CICR response.

6.7. REFERENCES

1. Callewaert G. Excitation-contraction coupling in mammalian cardiac cells. *Cardiovascular research.* 1992;26(10):923-932.

2. Levi AJ, Spitzer KW, Kohmoto O, Bridge JH. Depolarization-induced Ca entry via Na-Ca exchange triggers SR release in guinea pig cardiac myocytes. *Am J Physiol.* 1994;266(4 Pt 2):H1422-1433.

3. Leblanc N, Hume JR. Sodium current-induced release of calcium from cardiac sarcoplasmic reticulum. *Science.* 1990;248(4953):372-376.

4. Lipp P, Niggli E. Sodium current-induced calcium signals in isolated guinea-pig ventricular myocytes. *J Physiol.* 1994;474(3):439-446.

5. Grantham CJ, Cannell MB. Ca2+ influx during the cardiac action potential in guinea pig ventricular myocytes. *Circ Res.* 1996;79(2):194-200.

6. Sipido KR, Carmeliet E, Pappano A. Na+ current and Ca2+ release from the sarcoplasmic reticulum during action potentials in guinea-pig ventricular myocytes. *J Physiol.* 1995;489 (Pt 1):1-17.

7. Brette F, Salle L, Orchard CH. Differential modulation of L-type Ca2+ current by SR Ca2+ release at the T-tubules and surface membrane of rat ventricular myocytes. *Circ Res.* 2004;95(1):e1-7.

8. Brette F, Salle L, Orchard CH. Quantification of calcium entry at the T-tubules and surface membrane in rat ventricular myocytes. *Biophys J.* 2006;90(1):381-389.

9. Scriven DR, Dan P, Moore ED. Distribution of proteins implicated in excitation-contraction coupling in rat ventricular myocytes. *Biophys J.* 2000;79(5):2682-2691.

10. Lin E, Hung VH, Kashihara H, Dan P, Tibbits GF. Distribution patterns of the Na+-Ca2+ exchanger and caveolin-3 in developing rabbit cardiomyocytes. *Cell Calcium.* 2009;45(4):369-383.

11. Dan P, Lin E, Huang J, Biln P, Tibbits GF. Three-dimensional distribution of cardiac Na+-Ca2+ exchanger and ryanodine receptor during development. *Biophys J.* 2007;93(7):2504-2518.

12. Sedarat F, Lin E, Moore ED, Tibbits GF. Deconvolution of confocal images of dihydropyridine and ryanodine receptors in developing cardiomyocytes. *J Appl Physiol.* 2004;97(3):1098-1103.

13. Sedarat F, Xu L, Moore ED, Tibbits GF. Colocalization of dihydropyridine and ryanodine receptors in neonate rabbit heart using confocal microscopy. *Am J Physiol Heart Circ Physiol.* 2000;279(1):H202-209.

14. Nassar R, Reedy MC, Anderson PA. Developmental changes in the ultrastructure and sarcomere shortening of the isolated rabbit ventricular myocyte. *Circ Res.* 1987;61(3):465-483.

15. Klitzner TS, Friedman WF. A diminished role for the sarcoplasmic reticulum in newborn myocardial contraction: effects of ryanodine. *Pediatr Res.* 1989;26(2):98-101.

16. Klitzner T, Friedman WF. Excitation-contraction coupling in developing mammalian myocardium: evidence from voltage clamp studies. *Pediatr Res.* 1988;23(4):428-432.

17. Haddock PS, Coetzee WA, Cho E, Porter L, Katoh H, Bers DM, Jafri MS, Artman M. Subcellular [Ca2+]i gradients during excitation-contraction coupling in newborn rabbit ventricular myocytes. *Circ Res.* 1999;85(5):415-427.

18. Huang J, Hove-Madsen L, Tibbits GF. SR Ca2+ refilling upon depletion and SR Ca2+ uptake rates during development in rabbit ventricular myocytes. *Am J Physiol Cell Physiol.* 2007;293(6):C1906-1915.

19. Huang J, Hove-Madsen L, Tibbits GF. Ontogeny of Ca2+-induced Ca2+ release in rabbit ventricular myocytes. *American journal of physiology.* 2008;294(2):C516-525.

20. Huang J, van Breemen C, Kuo KH, Hove-Madsen L, Tibbits GF. Store-operated Ca2+ entry modulates sarcoplasmic reticulum Ca2+ loading in neonatal rabbit cardiac ventricular myocytes. *Am J Physiol Cell Physiol.* 2006;290(6):C1572-1582.

21. Wetzel GT, Chen F, Klitzner TS. Ca2+ channel kinetics in acutely isolated fetal, neonatal, and adult rabbit cardiac myocytes. *Circ Res.* 1993;72(5):1065-1074.

22. Osaka T, Joyner RW. Developmental changes in calcium currents of rabbit ventricular cells. *Circ Res.* 1991;68(3):788-796.

23. Huynh TV, Chen F, Wetzel GT, Friedman WF, Klitzner TS. Developmental changes in membrane Ca2+ and K+ currents in fetal, neonatal, and adult rabbit ventricular myocytes. *Circ Res.* 1992;70(3):508-515.

24. Huang J, Xu L, Thomas M, Whitaker K, Hove-Madsen L, Tibbits GF. L-type Ca2+ channel function and expression in neonatal rabbit ventricular myocytes. *Am J Physiol Heart Circ Physiol.* 2006;290(6):H2267-2276.

25. Katsube Y, Yokoshiki H, Nguyen L, Yamamoto M, Sperelakis N. L-type Ca2+ currents in ventricular myocytes from neonatal and adult rats. *Can J Physiol Pharmacol.* 1998;76(9):873-881.

26. Perez CG, Copello JA, Li Y, Karko KL, Gomez L, Ramos-Franco J, Fill M, Escobar AL, Mejia-Alvarez R. Ryanodine receptor function in newborn rat heart. *Am J Physiol Heart Circ Physiol.* 2005;288(5):H2527-2540.

27. Diebold RJ, Koch WJ, Ellinor PT, Wang JJ, Muthuchamy M, Wieczorek DF, Schwartz A. Mutually exclusive exon splicing of the cardiac calcium channel alpha 1 subunit gene generates developmentally regulated isoforms in the rat heart. *Proc Natl Acad Sci U S A.* 1992;89(4):1497-1501.

28. Abernethy DR, Soldatov NM. Structure-functional diversity of human L-type Ca2+ channel: perspectives for new pharmacological targets. *J Pharmacol Exp Ther.* 2002;300(3):724-728.

29. Jurkat-Rott K, Lehmann-Horn F. The impact of splice isoforms on voltage-gated calcium channel alpha1 subunits. *J Physiol.* 2004;554(Pt 3):609-619.

30. Xiao RP, Cheng H, Zhou YY, Kuschel M, Lakatta EG. Recent advances in cardiac beta(2)-adrenergic signal transduction. *Circ Res.* 1999;85(11):1092-1100.

31. Xiao RP, Avdonin P, Zhou YY, Cheng H, Akhter SA, Eschenhagen T, Lefkowitz RJ, Koch WJ, Lakatta EG. Coupling of beta2-adrenoceptor to Gi proteins and its physiological relevance in murine cardiac myocytes. *Circ Res.* 1999;84(1):43-52.

32. Collis LP, Srivastava S, Coetzee WA, Artman M. beta2-Adrenergic receptor agonists stimulate L-type calcium current independent of PKA in newborn rabbit ventricular myocytes. *Am J Physiol Heart Circ Physiol.* 2007;293(5):H2826-2835.

33. Ding G, Wiegerinck RF, Shen M, Cojoc A, Zeidenweber CM, Wagner MB. Dopamine increases L-type calcium current more in newborn than adult rabbit cardiomyocytes via D1 and beta2 receptors. *Am J Physiol Heart Circ Physiol.* 2008;294(5):H2327-2335.

34. Balijepalli RC, Foell JD, Hall DD, Hell JW, Kamp TJ. Localization of cardiac L-type Ca(2+) channels to a caveolar macromolecular signaling complex is required for beta(2)-adrenergic regulation. *Proc Natl Acad Sci U S A.* 2006;103(19):7500-7505.

35. Fabiato A, Fabiato F. Calcium release from the sarcoplasmic reticulum. *Circ Res.* 1977;40(2):119-129.

36. Laver DR. Ca2+ stores regulate ryanodine receptor Ca2+ release channels via luminal and cytosolic Ca2+ sites. *Biophys J.* 2007;92(10):3541-3555.

37. Sitsapesan R, Williams AJ. Regulation of current flow through ryanodine receptors by luminal Ca2+. *J Membr Biol.* 1997;159(3):179-185.

38. Balaguru D, Haddock PS, Puglisi JL, Bers DM, Coetzee WA, Artman M. Role of the sarcoplasmic reticulum in contraction and relaxation of immature rabbit ventricular myocytes. *J Mol Cell Cardiol.* 1997;29(10):2747-2757.

39. Miller MS, Friedman WF, Wetzel GT. Caffeine-induced contractions in developing rabbit heart. *Pediatr Res.* 1997;42(3):287-292.

40. Wu X, Bers DM. Sarcoplasmic reticulum and nuclear envelope are one highly interconnected Ca2+ store throughout cardiac myocyte. *Circ Res.* 2006;99(3):283-291.

41. Shepherd N, McDonough HB. Ionic diffusion in transverse tubules of cardiac ventricular myocytes. *Am J Physiol.* 1998;275(3 Pt 2):H852-860.

42. Brette F, Despa S, Bers DM, Orchard CH. Spatiotemporal characteristics of SR Ca(2+) uptake and release in detubulated rat ventricular myocytes. *J Mol Cell Cardiol.* 2005;39(5):804-812.

43. Brette F, Rodriguez P, Komukai K, Colyer J, Orchard CH. beta-adrenergic stimulation restores the Ca transient of ventricular myocytes lacking t-tubules. *J Mol Cell Cardiol.* 2004;36(2):265-275.

44. Osaka T, Joyner RW. Developmental changes in the beta-adrenergic modulation of calcium currents in rabbit ventricular cells. *Circ Res.* 1992;70(1):104-115.

45. Artman M. Sarcolemmal Na(+)-Ca2+ exchange activity and exchanger immunoreactivity in developing rabbit hearts. *The American journal of physiology.* 1992;263(5 Pt 2):H1506-1513.

46. Boerth SR, Zimmer DB, Artman M. Steady-state mRNA levels of the sarcolemmal Na(+)-Ca2+ exchanger peak near birth in developing rabbit and rat hearts. *Circulation research.* 1994;74(2):354-359.

47. Huang J, Hove-Madsen L, Tibbits GF. Na+/Ca2+ exchange activity in neonatal rabbit ventricular myocytes. *American journal of physiology.* 2005;288(1):C195-203.

48. Qu Y, Ghatpande A, el-Sherif N, Boutjdir M. Gene expression of Na+/Ca2+ exchanger during development in human heart. *Cardiovascular research.* 2000;45(4):866-873.

49. Kong H, Jones PP, Koop A, Zhang L, Duff HJ, Chen SR. Caffeine induces Ca2+ release by reducing the threshold for luminal Ca2+ activation of the ryanodine receptor. *Biochem J.* 2008;414(3):441-452.

50. Hilgemann DW. Unitary cardiac Na+, Ca2+ exchange current magnitudes determined from channel-like noise and charge movements of ion transport. *Biophys J.* 1996;71(2):759-768.

51. Tsien RW, Hess P, McCleskey EW, Rosenberg RL. Calcium channels: mechanisms of selectivity, permeation, and block. *Annu Rev Biophys Biophys Chem.* 1987;16:265-290.

52. Altamirano J, Bers DM. Voltage dependence of cardiac excitation-contraction coupling: unitary Ca2+ current amplitude and open channel probability. *Circ Res.* 2007;101(6):590-597.

53. Cheng H, Lederer WJ. Calcium sparks. *Physiol Rev.* 2008;88(4):1491-1545.

54. Stern MD, Song LS, Cheng H, Sham JS, Yang HT, Boheler KR, Rios E. Local control models of cardiac excitation-contraction coupling. A possible role for allosteric interactions between ryanodine receptors. *J Gen Physiol.* 1999;113(3):469-489.

55. Lines GT, Sande JB, Louch WE, Mork HK, Grottum P, Sejersted OM. Contribution of the Na+/Ca2+ exchanger to rapid Ca2+ release in cardiomyocytes. *Biophys J.* 2006;91(3):779-792.

56. Keller M, Kao JP, Egger M, Niggli E. Calcium waves driven by "sensitization" wave-fronts. *Cardiovascular research.* 2007;74(1):39-45.

57. Chen F, Ding S, Lee BS, Wetzel GT. Sarcoplasmic reticulum Ca(2+)ATPase and cell contraction in developing rabbit heart. *J Mol Cell Cardiol.* 2000;32(5):745-755.

58. Bokenes J, Sjaastad I, Sejersted OM. Artifactual contractions triggered by field stimulation of cardiomyocytes. *J Appl Physiol.* 2005;98(5):1712-1719.

59. Armoundas AA, Hobai IA, Tomaselli GF, Winslow RL, O'Rourke B. Role of sodium-calcium exchanger in modulating the action potential of ventricular myocytes from normal and failing hearts. *Circ Res.* 2003;93(1):46-53.

60. Wetzel GT, Chen F, Klitzner TS. Na+/Ca2+ exchange and cell contraction in isolated neonatal and adult rabbit cardiac myocytes. *Am J Physiol.* 1995;268(4 Pt 2):H1723-1733.

61. Klitzner TS, Chen FH, Raven RR, Wetzel GT, Friedman WF. Calcium current and tension generation in immature mammalian myocardium: effects of diltiazem. *J Mol Cell Cardiol.* 1991;23(7):807-815.

62. Go A, Srivastava S, Collis L, Coetzee WA, Artman M. Negative inotropic effect of nifedipine in the immature rabbit heart is due to shortening of the action potential. *Pediatr Res.* 2005;57(3):399-403.

63. Chen F, Mottino G, Klitzner TS, Philipson KD, Frank JS. Distribution of the Na+/Ca2+ exchange protein in developing rabbit myocytes. *Am J Physiol.* 1995;268(5 Pt 1):C1126-1132.

64. Frank JS, Mottino G, Reid D, Molday RS, Philipson KD. Distribution of the Na(+)-Ca2+ exchange protein in mammalian cardiac myocytes: an immunofluorescence and immunocolloidal gold-labeling study. *J Cell Biol.* 1992;117(2):337-345.

65. Anderson RG. The caveolae membrane system. *Annu Rev Biochem.* 1998;67:199-225.

66. Levin KR, Page E. Quantitative studies on plasmalemmal folds and caveolae of rabbit ventricular myocardial cells. *Circ Res.* 1980;46(2):244-255.

67. Okamoto T, Schlegel A, Scherer PE, Lisanti MP. Caveolins, a family of scaffolding proteins for organizing "preassembled signaling complexes" at the plasma membrane. *J Biol Chem.* 1998;273(10):5419-5422.

68. Bossuyt J, Taylor BE, James-Kracke M, Hale CC. Evidence for cardiac sodium-calcium exchanger association with caveolin-3. *FEBS Lett.* 2002;511(1-3):113-117.

69. Hailstones D, Sleer LS, Parton RG, Stanley KK. Regulation of caveolin and caveolae by cholesterol in MDCK cells. *J Lipid Res.* 1998;39(2):369-379.

70. Yarbrough TL, Lu T, Lee HC, Shibata EF. Localization of cardiac sodium channels in caveolin-rich membrane domains: regulation of sodium current amplitude. *Circ Res.* 2002;90(4):443-449.

71. Shibata EF, Brown TL, Washburn ZW, Bai J, Revak TJ, Butters CA. Autonomic regulation of voltage-gated cardiac ion channels. *J Cardiovasc Electrophysiol.* 2006;17 Suppl 1:S34-S42.

72. Cavalli A, Eghbali M, Minosyan TY, Stefani E, Philipson KD. Localization of sarcolemmal proteins to lipid rafts in the myocardium. *Cell Calcium.* 2007;42(3):313-322.

73. Li ZP, Burke EP, Frank JS, Bennett V, Philipson KD. The cardiac Na+-Ca2+ exchanger binds to the cytoskeletal protein ankyrin. *J Biol Chem.* 1993;268(16):11489-11491.

74. Mohler PJ, Davis JQ, Bennett V. Ankyrin-B coordinates the Na/K ATPase, Na/Ca exchanger, and InsP3 receptor in a cardiac T-tubule/SR microdomain. *PLoS Biol.* 2005;3(12):e423.

75. Cunha SR, Bhasin N, Mohler PJ. Targeting and stability of Na/Ca exchanger 1 in cardiomyocytes requires direct interaction with the membrane adaptor ankyrin-B. *J Biol Chem.* 2007;282(7):4875-4883.

76. Lemaillet G, Walker B, Lambert S. Identification of a conserved ankyrin-binding motif in the family of sodium channel alpha subunits. *J Biol Chem.* 2003;278(30):27333-27339.

77. Garrido JJ, Giraud P, Carlier E, Fernandes F, Moussif A, Fache MP, Debanne D, Dargent B. A targeting motif involved in sodium channel clustering at the axonal initial segment. *Science.* 2003;300(5628):2091-2094.

78. Mohler PJ, Rivolta I, Napolitano C, LeMaillet G, Lambert S, Priori SG, Bennett V. Nav1.5 E1053K mutation causing Brugada syndrome blocks binding to ankyrin-G and expression of Nav1.5 on the surface of cardiomyocytes. *Proc Natl Acad Sci U S A.* 2004;101(50):17533-17538.

79. Cheng DK, Tung L, Sobie EA. Nonuniform responses of transmembrane potential during electric field stimulation of single cardiac cells. *Am J Physiol.* 1999;277(1 Pt 2):H351-362.

80. Sham JS, Cleemann L, Morad M. Gating of the cardiac Ca2+ release channel: the role of Na+ current and Na(+)-Ca2+ exchange. *Science.* 1992;255(5046):850-853.

81. Bouchard RA, Clark RB, Giles WR. Role of sodium-calcium exchange in activation of contraction in rat ventricle. *J Physiol.* 1993;472:391-413.

82. DelPrincipe F, Egger M, Niggli E. L-type Ca2+ current as the predominant pathway of Ca2+ entry during I(Na) activation in beta-stimulated cardiac myocytes. *J Physiol.* 2000;527 Pt 3:455-466.